

## **Abstract**

CHEHAB, GHASSAN RIAD. Characterization of Asphalt Concrete in Tension Using a ViscoElastoPlastic Model. (Under the direction of Dr. Y. Richard Kim)

The objective of the research presented herein is to develop an accurate and advanced material characterization procedure to be incorporated in the Superpave performance models system. The procedure includes the theoretical models and its supporting experimental testing protocols necessary for predicting responses of asphalt mixtures subjected to tension loading. The model encompasses the elastic, viscoelastic, plastic and viscoplastic components of asphalt concrete behavior. Addressed are the major factors affecting asphalt concrete response such as: rate of loading, temperature, stress state in addition to damage and healing. Modeling strategy is based on modeling strain components separately and then adding the resulting models to attain a final integrated ViscoElastoPlastic model. Viscoelastic response, including elastic component, is modeled based on Schapery's continuum damage theory comprising of an elastic-viscoelastic correspondence principle and work potential theory. As for the viscoplastic response, which includes the plastic component, its characterization stems from Uzan's strain hardening model. The testing program required for developing the models consists of complex modulus testing for determination of material response functions, constant crosshead rate testing at low temperatures for viscoelastic modeling, and repetitive creep and recovery testing for viscoplastic modeling. The developed model is successful in predicting responses up to localization when microcracks start to coalesce. After that, fracture process zone strains detected using Digital Image Correlation are used to extend

the model's ability in predicting responses in the post-localization stage. However, once major macrocracks develop, the currently developed model ceases to accurately predict responses. At that state, the theory of fracture mechanics needs to be integrated with the current continuum damage-based model.

**CHARACTERIZATION OF ASPHALT CONCRETE IN TENSION USING A  
VISCOELASTOPLASTIC MODEL**

by

**G Hassan Riad Chehab**

A dissertation submitted to the Graduate Faculty of  
North Carolina State University  
in partial fulfillment of the  
requirements for the Degree of  
Doctor of Philosophy

**DEPARTMENT OF CIVIL ENGINEERING**

Raleigh, North Carolina

2002

**APPROVED BY:**

---

Dr. Y.R. Kim  
Chair of Advisory Committee

---

Dr. M.N. Guddati

---

Dr. A.A. Tayebali

---

Dr. F.G. Yuan

## **Dedication**

I dedicate this dissertation to my loving mother Samar. Your “tips” and ever-supportive voice whispering in my head “Dr. Chehab, Dr. Ghassan Chehab” made me persistent in pursuing my dream...your dream.

## **Biography**

I first saw light on July 8, 1974 in Beirut, Lebanon. As I remember, it was cloudy that day and a contractor was paving our local road. It was that smell, the ugly smell of asphalt, that probably made me spend four PhD years trying to make it last longer. The longer pavements last I thought, the less often they need to be repaved.

My mom, Samar Itani, married my father, Riad Chehab, and gave me the name Ghassan. Thus my name is Ghassan Riad Chehab. Ghassan attended Rawdah High School where he spent all his years except for the 4<sup>th</sup> grade (Winneteka Ave. Elementary School, Los Angeles) and 7<sup>th</sup> grade (Noble Junior High School, Los Angeles) when he had to leave because of the war. In spite of all the battles that were occurring in Lebanon at the time: civil war, Israeli invasion, etc., he always managed to stay focused and be ranked among the elite in his class. Studying under candles, he passed the Lebanese Baccalaureate Degree (emphasis on Math) with distinction in 1992 and was accepted by the American University of Beirut to study Civil Engineering.

During his four years in college, he managed to be on the Dean's Honor List in each semester. He completed his training in Dubai, UAE, working on the Trade Center Roundabout Interchange with CCC. Ghassan graduated with distinction in 1996 and received a graduate assistantship to complete his Masters studies in Engineering Management under the supervision of Dr. Assem Abdul-Malak. 1996 was a special year because it was God's will that Ghassan and Lina Arnaout be joined in a blessed marriage. In 1998, Ghassan graduated with his Master's thesis entitled: "Purchasing and Payment Policies for Building Construction Materials"

During that time, Ghassan also worked with his father as a design and supervising engineer, where he designed and supervised seven residential and office buildings in the Greater Beirut Metropolitan area. He is a licensed engineer by the Lebanese Syndicate of Engineers and the Ministry of Transportation and Public Works. After finishing his Masters degree, Ghassan went again to the United States to pursue his Ph.D. degree at North Carolina State University.

At NC State, Ghassan received a research assistantship to study and work in the field of transportation materials with the major emphasis being on the modeling of asphalt concrete. With the aid of God, and the support of his advisor Dr. Richard Kim, he was able to complete his course work, conduct quality experimental and analytical research, and serve as a lab instructor, in four grilling years that were full of emotional, psychological and physical distresses. It was only on December 26, 2001 when his precious daughter Samar came to life that his mind let go of all the stresses that were accompanying him. Ghassan finally earned his Doctoral degree in Civil Engineering in July, 2002 with a cumulative GPA of 4.0, a smiling face, two proud parents, an exhausted wife and a lucky daughter.

Some of Ghassan's other achievements are:

- Harriri Foundation Scholarship (1992-1997),
- Ward K. Parr Scholarship (Association of Asphalt Paving Technologists) (2001),
- Induction to Tau Beta Pi and Phi Kappa Phi honor societies,

- North Carolina State University Award and Certificate of Ethics and Leadership (2001),
- Listed on Strathmore's Who's Who (2002),
- Publications in ASCE Proceedings (2000), Transportation Research Record (2000), and Journal of Asphalt Paving Technologies (2002),
- Presentations at the TRB conference in Washington DC (2000), and the AAPT conference in Colorado Springs, CO (2002), and
- Active memberships in ACI, ASCE, ITE, and AAPT.

As for the future, Ghassan lives day by day, without long term planning. He will weigh opportunities as they come; however, he does prefer to work in research and academia.

## Acknowledgements

All thanks and praise are due to God the most gracious the most merciful. He has been with me throughout this long journey and helped me in completing what is presented to you herein.

I can not find enough words to express my deep and sincere gratitude to my mother. She was the one who stood by me, inspired me and helped me get over all the obstacles I faced in my life. I do not want to specify more otherwise this section will turn into a tragedy. Her efforts in raising an excellent man were unsurpassed, and her guiding tips were endless; she has made me who I am. I can never do anything to return her countless favors. Based on her contributions, I think Sammoora deserves to be an honorary author of this thesis.

Who can forget my dad, “Abu Ghassan”? He has been the role model in my life. He is the one who insisted that I exert my full potential and reach the heights which circumstances had forced him to back up from. He is the one who planted this strong perseverance in my soul, and showed me endless trust and support. He has been very generous; his lips never knew the word “no”. I am grateful to have him as a father. I will try hard to always use my middle name, “Riad”, instead of that cruel middle initial, “R”.

Oh, my brother you have been great. Mahmoud I will never forget how you used to bring me the As-safir newspaper and Knafe breakfast every morning when I was overburdened with study. Thanks for all those music tapes and CD’s you compiled for me during my stay here in Raleigh. Thanks for the Big Mac’s you used to bring me when you worked at McDonald’s. You were my spokesperson in Lebanon: thanks for the

lobbying that you did to provide me with financial support! You are a delightful brother; I wish you a prosperous life. I am lucky to have you as the one and only brother.

The question that poses itself now is: well, what's the wife's contribution? Put simply, without Lina there would have not been a Dr. Chehab. I am not an easy husband when I am in my best state; so imagine how I am when I have exams, lab machines not working, data contradicting all man-made theories, and upon receiving that email from Dr. Kim in the evening telling me he needs that 30 page report by next morning (of course with the PowerPoint slides)! You do not want to talk to me at such a time. But Lina had to and did so with grace, patience, and acceptance with a voice that never failed to show sympathy, support, inspiration, and hope for better days ahead. I can not imagine how I would have stayed a single semester without her being beside me. In fact, I was so close to giving up and going back to Lebanon before she convinced me of the opposite at a restaurant I pass by everyday now with confidence and hope. I struggled but she was with me all the way; she was the one that held my hand when I fell down; she was the one that showed me the light when I was lost in the dark, but unfortunately there she was exhausted when I finished. I promise you a better future Lina; I really do. We both deserve it.

Protocol and tradition say that I should write something nice about my advisor, so here it goes. My admiration to Dr. Kim as a professor, advisor, researcher and mentor displays itself by my decision to change my area of study from construction management to transportation materials. It was in that pavement design class, which you taught me in the Fall semester of 1998, when lightning struck and turned my attention towards asphalt research and opened a wide door of opportunities.

Throughout the years to follow, you have been an exemplary guide, a motivator, and a mentor. I really feel that I can communicate very easily with you, I know what you have to say before you say it. You have given me confidence, authority, room for decision making and most importantly trust. The trust that you gave me made me so comfortable in doing what I do best. It is that trust you give your students that made me hold the utmost respect and gratitude towards you. Now, that I have reached the finish line, I realize why you always pushed me to do better; why I never heard the words: wow, very good work, excellent job, etc. from you. It is your philosophy for motivation I guess; you knew I can go a long way and you wanted me to go as far as possible. I appreciate that Dr. Kim; although it was at times very tough and frustrating. I know how much energy and resources you have invested in your students; I hope you get a payback you deserve.

I want to thank Dr. Richard Schapery for his enormous input into this research. I also want to thank my committee members: Dr. Tayebali, Dr. Guddati, and Dr. Yuan for their help and time they spent in serving on my committee. In addition, I want to acknowledge my group members for their help and support. Firstly, I want to thank Dr. Jo Daniel who spent a lot of her time teaching me what she knows and in helping me when I get stuck. She really left a big void when she graduated and left for UNH. Her flying back to attend my defense is just one illustration of the true friendship and respect we have for each other. Other fellow members who have left their marks in my life include: Emily McGraw, the carrier of bad news to Lina, Kristy Alford who was a companion in worrying about our Wolfpack team, Youngguk Seo, my late night CFL buddy, Sungho Mun, my Matlab consultant, and Zhen Feng, our network administrator

and my next door neighbor. Additional thanks go to Liza Runey who helped in preparing the specimen fabrication protocols. I also want to extend my regards to my friends Ali Turmus, Mounir Bohsali, Amr Bohsali, Tarek Sinno, and others who give me back my life during the weekends.

Finally, I want to thank Dr. David Johnston, the director of graduate studies in the CE department for his efforts in solving my endless problems, in addition to Barbara Nichols, Edna White and Pat Rollins for their administrative help. Thanks to Dr. Sami Rizkallah for providing a professional yet friendly atmosphere at the CFL lab. Special thanks go to the engineers and staff at IPC who crossed the globe to fix my cursed testing machine, not forgetting Bill Dunleavy, Larry Dufour, and Jerry Atkinson for their technical assistance at NC State.

# Table of Contents

<b>LIST OF TABLES</b> .....	xv
<b>LIST OF FIGURES</b> .....	xvii
<b>1 INTRODUCTION</b> .....	<b>1</b>
1.1 RESEARCH OBJECTIVE.....	1
1.2 RESEARCH APPROACH.....	3
1.3 OUTLINE OF RESEARCH PRESENTED.....	4
<b>2 THEORETICAL BACKGROUND AND LITERATURE REVIEW</b> .....	<b>6</b>
2.1 INTRODUCTION.....	6
2.2 THEORY OF VISCOELASTICITY.....	7
2.2.1 <i>Definitions</i> .....	7
2.2.2 <i>Correspondence Principle</i> .....	9
2.2.3 <i>Uniaxial Constitutive Model Using Work Potential Theory</i> .....	12
2.3 TIME-TEMPERATURE SUPERPOSITION WITH GROWING DAMAGE IN TENSION.....	17
2.3.1 <i>Introduction</i> .....	17
2.3.2 <i>Structure of the Constitutive Equations:</i> .....	18
2.3.3 <i>Application to uniaxial loading:</i> .....	19
2.3.4 <i>Stress-strain data</i> .....	21
2.3.5 <i>Strength data</i> .....	21
2.4 BRIEF OVERVIEW OF THE VISCOPLASTIC MODEL APPROACH.....	23
<b>3 SPECIMEN PREPARATION AND TESTING PROGRAMS</b> .....	<b>25</b>
3.1 INTRODUCTION.....	25
3.2 SPECIMEN PREPARATION.....	25
3.2.1 <i>Asphalt Mixtures</i> .....	25
3.2.2 <i>Specimen Preparation</i> .....	29

3.3 TESTING PROGRAM .....	31
3.3.1 Testing Systems.....	31
3.3.2 Test Methods.....	34
<b>4 SPECIMEN GEOMETRY STUDY .....</b>	<b>42</b>
4.1 INTRODUCTION.....	42
4.2 SPECIMEN SIZES STUDIED .....	43
4.2.1 Specimens for Air Void Distribution Study.....	43
4.2.2 Specimens for Mechanical Tests and End Effect Study.....	45
4.3 MATERIALS AND SPECIMEN FABRICATION .....	46
4.3.1 Materials.....	46
4.3.2 Compaction.....	46
4.4 AIR VOID DISTRIBUTION STUDY .....	48
4.4.1 Air Void Measurement Techniques.....	48
4.4.2 Discussion of Results .....	52
4.5 END EFFECT ANALYSIS (END PLATES EFFECT) .....	57
4.6 EFFECT OF GEOMETRY AND GAGE LENGTHS ON RESPONSES FROM MECHANICAL TESTS .....	61
4.6.1 Description of Tests .....	61
4.6.2 Data Analysis.....	63
4.6.3 Effect of Gage Length on Material Responses .....	75
4.7 CONCLUSION .....	80
<b>5 DETERMINATION AND INTERCONVERSION AMONG LINEAR VISCOELASTIC RESPONSE FUNCTIONS.....</b>	<b>83</b>
5.1 INTRODUCTION.....	83
5.2 ANALYTICAL REPRESENTATION OF LVE MATERIAL PROPERTIES.....	84
5.2.1 Complex Modulus.....	84
5.2.2 Relaxation Modulus and Creep Compliance.....	86
5.3 CONSTRUCTION OF LVE MATERIAL PROPERTY MASTERCURVE.....	88
5.3.1 Time-Temperature Superposition Principle for LVE behavior .....	89
5.4 INTERCONVERSION AMONG VISCOELASTIC RESPONSE FUNCTIONS .....	99
5.4.1 Conversion from Complex Modulus to Relaxation Modulus.....	100

5.4.2 Conversion from Complex Modulus to Creep Compliance.....	105
<b>6 VALIDATION AND APPLICATION OF TIME-TEMPERATURE</b>	
<b>SUPERPOSITION PRINCIPLE IN THE DAMAGED STATE.....</b>	<b>109</b>
6.1 INTRODUCTION.....	109
6.2 SAMPLE PREPARATION AND TESTING EQUIPMENT .....	110
6.3 TESTING PROGRAM .....	111
6.3.1 Complex Modulus Test .....	111
6.3.2 Constant Crosshead-Rate Tests.....	111
6.4 EXPERIMENTAL RESULTS AND ANALYSIS .....	113
6.4.1 Complex Modulus Test .....	113
6.4.2 Constant Crosshead-Rate Test .....	114
6.5 APPLICATIONS USING TIME-TEMPERATURE SUPERPOSITION WITH GROWING	
DAMAGE .....	137
6.5.1 Reduction of Testing Program: Application to Repeated Creep and	
Recovery Test .....	137
6.5.2 Superposition of Strength and Corresponding Strain .....	143
6.5.3 Prediction of Stress-Strain Curves for Constant Crosshead Rate Tests	
.....	149
6.5.4 Constructing Characteristic Curve at Reference Temperature.....	154
<b>7 MODELING OF VISCOELASTIC AND VISCOPLASTIC BEHAVIOR IN</b>	
<b>TENSION STATE .....</b>	<b>156</b>
7.1 INTRODUCTION.....	156
7.1.1 Brief Overview of Modeling Approach.....	156
7.2 MODELING OF VISCOELASTIC BEHAVIOR.....	158
7.2.1 Testing Conducted .....	158
7.2.2 Determination of Material Constant ' $\alpha$ ' .....	159
7.2.3 Effect of Using Time vs. Reduced Time in Calculating Pseudostrains	
and Damage Parameters.....	165
7.2.4 Validity of Using $S^*$ as a Damage Parameter.....	167
7.3 VISCOELASTIC MODEL: C VS. S APPROACH.....	170
7.3.1 Theoretical Formulation.....	171
7.3.2 Determination of Relationships for Model Development .....	173
7.3.3 Problems Associated with the C vs. S Approach .....	175

7.4 VISCOELASTIC MODEL: C vs. S* APPROACH.....	177
7.4.1 Theoretical Formulation.....	177
7.4.2 Determination of Relationships for Model Development.....	178
7.4.3 Validation of the Viscoelastic strain Model .....	181
7.5 MODELING OF VISCOPLASTIC BEHAVIOR .....	185
7.5.1 Determining Viscoplastic Strains at the End of Creep and Recovery Cycles .....	186
7.5.2 Theoretical Formulation and Testing Program .....	190
7.5.3 Testing Results.....	196
7.5.4 Validation of the Viscoplastic Model.....	201
7.6 FORMULATION AND VALIDATION OF THE VISCOELASTOPLASTIC MODEL	207
7.7 EXTENSION OF THE VISCOELASTOPLASTIC MODEL BEYOND LOCALIZATION	
.....	226
7.7.1 LVDT vs. DIC Strains.....	226
7.7.2 Model Development Using DIC .....	231
<b>8 CONCLUSIONS AND FUTURE WORK.....</b>	<b>235</b>
8.1 CONCLUSIONS .....	235
8.2 FUTURE WORK .....	236
8.2.1 Post-Fracture Characterization .....	236
8.2.2 Confining Pressure Effect.....	236
8.2.3 Evaluation Testing.....	236
8.2.4 Sensitivity Analysis .....	237
<b>REFERENCES.....</b>	<b>238</b>
<b>APPENDIX A: SPECIMEN PREPARATION.....</b>	<b>242</b>
A.1 MIXTURE INFORMATION.....	242
A.2 SPECIMEN PREPARATION PROTOCOLS.....	247
A.2.1 BATCHING .....	247
A.2.2 MIXING.....	248
A.2.3 COMPACTION .....	251
A.2.4 CORING.....	254
A.2.5 SAWING .....	255
A.2.6 AIR VOIDS MEASUREMENT .....	256
A.2.7 GLUING SPECIMENS.....	259
A.2.8 REMOVING ADHESIVE.....	261
A.2.9 CLEANING END PLATES.....	261

<b>APPENDIX B: PHOTOGRAPHS.....</b>	<b>263</b>
B.1 SPECIMEN FABRICATION.....	263
B.2 TESTING SYSTEMS .....	267
B.3 SPECIMEN GEOMETRY .....	269
B.4 MEASUREMENT INSTRUMENTATION .....	271
<b>APPENDIX C: MACHINE COMPLIANCE AND MEASUREMENT</b>	
<b>INSTRUMENTATION .....</b>	<b>275</b>
C.1 INTRODUCTION .....	275
C.2 TESTING PROGRAM.....	276
<i>C.2.1 Testing Machines</i> .....	277
<i>C.2.2 Deformation Measurements</i> .....	277
<i>C.2.3 Materials</i> .....	278
<i>C.2.4 Test Methods</i> .....	278
C.3 MACHINE COMPLIANCE.....	279
C.4 MEASUREMENT INSTRUMENTATION: LVDTs, SIGNAL CONDITIONERS, AND MOUNTING ASSEMBLY.....	282
<i>C.4.1 Effect on Phase Angle Measurement</i> .....	282
C.5 ELECTRONIC NOISE .....	292
C.6 DRIFT IN STRAIN MEASUREMENT.....	295

## List of Tables

Table 3.1	Complex modulus test parameters .....	35
Table 3.2	Average values and variation coefficients of complex modulus results .....	37
Table 3.3	Crosshead strain rates used for the monotonic tests.....	39
Table 4.1	Error (%) in vertical strain due to end effect .....	60
Table 4.2	Geometries used for mechanical testing .....	61
Table 4.3	Gage lengths used for all geometries .....	62
Table 4.4	Frequencies and stress levels for complex modulus testing .....	63
Table 4.5	ANOVA table for $ E^* $ and $\phi$ for all geometries .....	76
Table 4.6	ANOVA table for effect of diameter and h/d on constant crosshead-rate test parameters.....	76
Table 4.7	ANOVA table for the effect of gage length on $ E^* $ and $\phi$ .....	82
Table 4.8	ANOVA Table for effect of gage length on constant crosshead-rate test parameters .....	82
Table 5.1	$E^*$ to $E(t)$ interconversion methods .....	104
Table 6.1	Test Parameters at 25°C .....	139
Table 6.2	Test Parameters at 35°C .....	139
Table 6.3	Testing conditions at -20 and -30°C.....	143
Table 6.4	Failure modes.....	146
Table 7.1	A and q values for 5°C monotonic tests obtained through different techniques .....	176
Table 7.2	S4 testing parameters .....	193

Table 7.3	S5 testing parameters .....	195
Table 7.3b	Percent viscoelastic and viscoplastic strain as a function of temperature and strain rate .....	212
Table 7.4	Strain rates corresponding to reduced strain rates in Figure 7.45.....	213
Table A.1	Maryland Mixture Stockpile and Aggregate Data .....	243
Table A.2	AASHTO MP1 grading for 12.5-mm MD mix binder .....	244
Table A.3	Mixing and compaction temperatures .....	244
Table A.4	12.5 mm mixture verification results .....	245
Table A.5	Final 12.5 mm MD mixture design .....	245
Table C.1	Summary of LVDT types .....	278
Table C.2	Noise amplitude for different LVDT types .....	294
Table C.3	Frequency sweep results from aluminum and asphalt specimens ...	294
Table C.4	Extent of drift in strains for the different combinations tested.....	297

## List of Figures

Figure 2.1	(a) Stress–strain behavior for mixture under LVE cyclic loading (b) Stress-pseudo strain behavior for same data .....	11
Figure 3.1	Gradation chart for NC 12.5-mm Superpave mix .....	26
Figure 3.2	Gradation chart for MD 12.5-mm Superpave mix .....	29
Figure 3.3	Stresses and strains from $E^*$ testing .....	36
Figure 3.4	Crosshead and on-specimen 75 mm GL LVDT strains for a monotonic test conducted at 25 <sup>0</sup> C and 0.0135 strains/sec .....	38
Figure 3.5	Stress and strain response for a creep test (courtesy of Daniel 2001) .....	40
Figure 3.6	Typical creep compliance curve (courtesy of Daniel 2001) .....	40
Figure 4.1	Comparison of air void measurement techniques for different sections: SSD vs. Parafilm, (b) Corelok vs. Parafilm, (c) SSD vs. Corelok. ....	54
Figure 4.2	Air void variation inside: (a) 150 x 175: AV%=5.8; (b) 150 x 175: AV%=5.0 (c) 150 x 140: AV%=7.0 (Dimensions in mm, AV in % measured using the Parafilm method) .....	58
Figure 4.3	Vertical strain from FEM analysis for $ E^* =3500$ MPa and $\nu=0.35$ ....	59
Figure 4.3b	Positioning of LVDTs .....	62
Figure 4.4	Dynamic moduli and phase angles .....	66
Figure 4.5	$ E^* $ and $\phi$ for 75x150 and 100x150 (50 mm GL).....	66
Figure 4.6	Effect of diameter on $\phi$ : a) 1 Hz, b) 5 Hz, c) 10 Hz, d) 20 Hz .....	69
Figure 4.7	Effect of H/D on $\phi$ : a) 1 Hz, b) 5 Hz, c) 10 Hz, d) 20 Hz .....	70
Figure 4.8	Effect of diameter on $ E^* $ : a) 1 Hz, b) 5 Hz, c) 10 Hz, d) 20 Hz .....	71
Figure 4.9	Effect of H/D on $ E^* $ : a) 1 Hz, b) 5 Hz, c) 10 Hz, d) 20 Hz .....	72

Figure 4.10	Average stress-strain curves from constant crosshead-rate test for all geometries.....	73
Figure 4.11	Average stress/strain curves from constant crosshead-rate test for 75x150 and 100x150.....	73
Figure 4.12	Effect of gage length on $ E^* $ : a) 100x150, b) 75x150, c)100x200.....	78
Figure 4.13	Comparison of stress-strain curves for 75x150 for 2 gage lengths....	79
Figure 5.1	Components of the Complex Modulus .....	86
Figure 5.2	Wiechert Model: where $\eta_m$ is the coefficient of viscosity and $E_m$ is the stiffness for the $m^{\text{th}}$ term .....	88
Figure 5.3	Kelvin Model: where $\eta_m$ is the coefficient of viscosity and $D_m$ is the compliance for the $m^{\text{th}}$ term.....	89
Figure 5.4	Storage modulus as a function of (a) frequency and (b) reduced frequency .....	93
Figure 5.5	Log shift factor as a function of temperature obtained by constructing the storage modulus mastercurve at 25°C.....	94
Figure 5.6	$ E^* $ as a function of (a) frequency before shifting and (b) reduced frequency at 25°C after shifting .....	95
Figure 5.7	Phase angle as a function of (a) frequency before shifting and (b) reduced frequency at 25°C after shifting .....	96
Figure 5.8	Figure 5.8. (a) Individual creep curves for different replicates and temperatures, (b) average creep mastercurves constructed from creep and $E'$ shift factors .....	98
Figure 5.9	Log shift factors determined by constructing creep and $E'$ mastercurves .....	99
Figure 5.10	Individual phase angle mastercurves for replicate specimens Along with the fitted sigmoidal mastercurve .....	104
Figure 5.11	Relaxation modulus mastercurves obtained from different interconversion techniques .....	105

Figure 5.12	Interconversion from E* to D(t): direct and through E(t) along with creep mastercurves from testing.....	108
Figure 6.1	Log shift factor vs. temperature from complex modulus tests .....	113
Figure 6.2	Stress-strain plot at -10°C (1 specimen at each rate).....	115
Figure 6.3	Stress-strain curves at 5°C (Crosshead strain rate and replicate number indicated next to each curve).....	115
Figure 6.4	Stress-strain curves at 25°C (2 replicates at each rate except for 0.0015).....	116
Figure 6.5	Stress-strain curves at 40°C (1 replicate per strain rate).....	116
Figure 6.6	Difference between crosshead and on-specimen 75 mm GL LVDT strains for a monotonic test conducted at 25°C and 0.0135 strains/sec .....	118
Figure 6.7	Detection of strain localization for a strain rate of 0.00003 at 5°C	119
Figure 6.8	Plate uneven displacement (just after 200 seconds) and effect on superposition for a test at a strain rate of 0.00003 at 5°C.....	119
Figure 6.9	On-specimen LVDT strain deviation from pure power law (linear on log-log scales) and effect on superposition for the same test presented in Figures 6.7 and 6.8.....	120
Figure 6.10	Secant modulus from constant crosshead strain rate tests conducted at -10°C and relaxation modulus mastercurve at a reference temperature 25°C.....	124
Figure 6.11	Secant modulus from constant crosshead strain rate tests conducted at 5C and relaxation modulus mastercurve at a reference temperature 25C.....	124
Figure 6.12	Determining stress for a strain of 0.005 for different crosshead rate tests at different temperatures.....	128
Figure 6.13	Crossplot of stress and log time for a strain of 0.005; (b) crossplot of stress and log reduced time at 25°C for a strain of 0.005 after applying the LVE shift factor.....	129

Figure 6.14	(a) and (b): Crossplots for 0.00015 LVDT strain before and after shift respectively; (c) and (d): Crossplots for 0.0006 LVDT strain before and after shift respectively; (e) and (f): Crossplots for 0.003 LVDT strain before and after shift respectively; (g) and (h): Crossplots for 0.006 LVDT strain before and after shift respectively; (i) and (j): Crossplots for 0.01 LVDT strain before and after shift respectively; (k) and (l): Crossplots for 0.02 LVDT strain before and after shift respectively.....	130-135
Figure 6.15	(a) Crossplots for selected LVDT strains; (b) Crossplots for crosshead LVDT strains .....	136
Figure 6.16	(a) Stress-reduced time history of 25 and 35°C creep and recovery tests plotted at reference temperature 25°C; (b) Corresponding stress- time history at testing temperatures 25 and 35°C.....	140
Figure 6.17	(a) Strain-reduced time history of 25 and 35°C creep and recovery tests plotted at testing temperatures; (b) Corresponding strain-reduced time history at reference temperature 25°C.....	141
Figure 6.18	(a) Strain- time history of 25 and 35°C creep and recovery tests plotted at testing temperatures (log-log scale); (b) Corresponding strain-reduced time history at reference temperature 25°C (log-log scale).....	142
Figure 6.19	Relationship between crosshead and specimen LVDT strain rates at 25 <sup>0</sup> C .....	145
Figure 6.20	Strength mastercurve as a function of reduced strain rate (crosshead and LVDT) at 25°C.....	147
Figure 6.21	Mastercurve of specimen strain at peak stress as a function of reduced LVDT strain rate at 25°C.....	148
Figure 6.22	Mastercurve of crosshead strain at peak stress as a function of reduced crosshead strain at 25C.....	148
Figure 6.23	Methodology for predicting stresses for constant crosshead strain rates using stress-reduced time crossplots .....	151
Figure 6.24	Predicted and actual stress-strain curves for a crosshead strain rate of 0.0135 at 25°C.....	152

Figure 6.25	Actual and predicted stress-strain curves at 0.000012 strains/sec at 5°C.....	152
Figure 6.26	Actual and predicted stress-strain curves at 0.0005 strains/sec at -10°C.....	153
Figure 6.27	Actual and predicted stress-strain curves at 0.07 strains/sec at 40°C.....	153
Figure 6.28	Characteristic curves at 5 and 25°C for various constant crosshead rates.....	155
Figure 6.29	Characteristic curves for various constant crosshead rates at 5 and 25°C shifted to reference temperature of 25°C.....	155
Figure 7.1	Strain decomposition from creep and recovery test.....	157
Figure 7.2	Stress-strain curves for monotonic tests at 5°C.....	159
Figure 7.3	(a) C vs. S*; (b) C vs. S curves for $\alpha=1/n-1$ .....	161
Figure 7.4	(a) C vs. S*; (b) C vs. S curves for $\alpha=1/n$ .....	162
Figure 7.5	(a) C vs. S*; (b) C vs. S curves for $\alpha=1+1/n$ .....	163
Figure 7.6	(a) C vs. S*; (b) C vs. S curves for $\alpha=2+1/n$ .....	164
Figure 7.7	Pseudostrains for 2 monotonic tests at 5°C calculated using time and reduced time.....	166
Figure 7.8	C vs. S for 2 monotonic tests at 5°C corresponding to pseudo strains calculated using time and reduced time .....	166
Figure 7.9	Comparison of S* as calculated from Equations (7.5) and (7.6).....	169
Figure 7.10	Relationship between S and S* using monotonic test data at 25°C..	169
Figure 7.11	C vs. S and C vs. S* for a monotonic test at 25°C .....	170
Figure 7.12	Characteristic C vs. S curves from monotonic testing at 5°C shifted to a reference temperature of 25°C.....	174
Figure 7.13	$dS/d\xi$ , from the localized slope method and from direct	

	differentiation, as a function of $\epsilon_R$ for a test at 5°C and a constant crosshead rate of 0.00002.....	175
Figure 7.14	C vs. S* for tests at 5°C plotted at a reference temperature 25°C....	179
Figure 7.15	S* vs. Lebesgue norm for tests at 5°C plotted at a reference temperature 25°C .....	180
Figure 7.16	Predicted viscoelastic strain vs. actual strain at -10°C and a rate of 0.0005.....	183
Figure 7.17	Predicted viscoelastic strain vs. actual strain at 5°C and a rate of 0.008.....	183
Figure 7.18	Predicted viscoelastic strain vs. actual strain at 5°C and a rate of 0.000025.....	184
Figure 7.19	Predicted viscoelastic strain vs. actual strain at 40°C and a rate of 0.00009.....	184
Figure 7.20	Typical strain response from a repetitive creep and recovery test till failure.....	189
Figure 7.21	Recovery strains for cycles of a repetitive creep and recovery test (corresponds to strain history shown in the previous figure, plotted on a log-log scale where start time of each recovery period is set to zero.....	190
Figure 7.22	Schematic of a stress history of an S4 test.....	192
Figure 7.23	Schematic of a stress history of an S5 test.....	194
Figure 7.24	Stress history of an S4 test conducted at 25°C .....	197
Figure 7.25	Strain history of an S4 test conducted at 25°C.....	197
Figure 7.26	Stress history of an S5 test conducted at 25°C.....	198
Figure 7.27	Stress history of an S5 test conducted at 25°C.....	198
Figure 7.28	Plot of cumulative strain as a function of loading time for S4 tests...	199
Figure 7.29	Plot of cumulative strain as a function of stress for S5 tests.....	200

Figure 7.30	Incremental viscoplastic strain as a function of loading time for S4 tests .....	203
Figure 7.31	Incremental viscoplastic strain as a function of loading time for S4 tests (log-log scale).....	203
Figure 7.32	Incremental viscoplastic strain as a function of stress for S5 tests....	204
Figure 7.33	Incremental viscoplastic strain as a function of stress for S5 tests (log-log scale).....	204
Figure 7.34	Predicted vs. measured incremental strains for data from S4 and S5 tests .....	205
Figure 7.35	C vs. S curves for constant crosshead rate tests based on total measured strains at a reference temperature of 25°C .....	206
Figure 7.36	C vs. S curves for constant crosshead rate tests based on total measured strains – predicted VP strains at a reference temperature of 25°C.....	206
Figure 7.37	Predicted viscoplastic, viscoelastic, and total strain at -10°C and $\dot{\epsilon}$ rate of 0.0005.....	208
Figure 7.38	Predicted viscoplastic, viscoelastic, and total strain at 5°C and $\dot{\epsilon}$ rate of 0.008.....	209
Figure 7.39	Predicted viscoplastic, viscoelastic, and total strain at 5°C and $\dot{\epsilon}$ rate of 0.00003.....	209
Figure 7.40	Predicted viscoplastic, viscoelastic, and total strain at 25°C and $\dot{\epsilon}$ rate of 0.0135.....	210
Figure 7.41	Predicted viscoplastic, viscoelastic, and total strain at 5°C and $\dot{\epsilon}$ rate of 0.000012.....	210
Figure 7.42	Predicted viscoplastic, viscoelastic, and total strain at 25°C and $\dot{\epsilon}$ rate of 0.0005.....	211
Figure 7.43	Predicted viscoplastic, viscoelastic, and total strain at 40°C and $\dot{\epsilon}$ rate of 0.0009.....	211

Figure 7.44	Percent viscoelastic and viscoplastic strains for different reduced strain rates at 25°C .....	214
Figure 7.45	Percent viscoelastic and viscoplastic strains as a function of reduced strain rate at 25°C .....	215
Figure 7.46	Actual and predicted stress-strain curves at -10°C and 0.0005 $\epsilon$ /sec .....	217
Figure 7.47	Actual and predicted stress-strain curves at 5°C and 0.008 $\epsilon$ /sec.....	217
Figure 7.48	Actual and predicted stress-strain curves at 5°C and 0.000035 $\epsilon$ /sec.....	218
Figure 7.49	Actual and predicted stress-strain curves at 5°C and 0.00003 $\epsilon$ /sec (Replicate 1).....	218
Figure 7.50	Actual and predicted stress-strain curves at 5°C and 0.00003 $\epsilon$ /sec (Replicate 2).....	219
Figure 7.51	Actual and predicted stress-strain curves at 5°C and 0.00003 $\epsilon$ /sec (Replicate 3).....	219
Figure 7.52	Actual and predicted stress-strain curves at 5°C and 0.000025 $\epsilon$ /sec .....	220
Figure 7.53	Actual and predicted stress-strain curves at 5°C and 0.00002 $\epsilon$ /sec.....	220
Figure 7.54	Actual and predicted stress-strain curves at 5°C and 0.000012 $\epsilon$ /sec .....	221
Figure 7.55	Actual and predicted stress-strain curves at 5°C and 0.00001 $\epsilon$ /sec .....	221
Figure 7.56	Actual and predicted stress-strain curves at 25°C and 0.0135 $\epsilon$ /sec.....	222
Figure 7.57	Actual and predicted stress-strain curves at 25°C and 0.0045 $\epsilon$ /sec .....	222

Figure 7.58	Actual and predicted stress-strain curves at 25°C and 0.0005 $\epsilon$ /sec (Replicate 1).....	223
Figure 7.59	Actual and predicted stress-strain curves at 25°C and 0.0005 $\epsilon$ /sec (Replicate 2).....	223
Figure 7.60	Actual and predicted stress-strain curves at 25°C and 0.0005 $\epsilon$ /sec (Replicate 3).....	224
Figure 7.61	Actual and predicted stress-strain curves at 40°C and 0.07 $\epsilon$ /sec.....	224
Figure 7.62	Actual and predicted stress-strain curves at 40°C and 0.0078 $\epsilon$ /sec...	225
Figure 7.63	Actual and predicted stress-strain curves at 40°C and 0.0009 $\epsilon$ /sec...	225
Figure 7.64	75x140 mm specimen with 100 mm GL LVDTs with 50x100 mm DIC superposed image showing FPZ (Courtesy of Seo).....	228
Figure 7.65	Comparison between DIC and LVDT strains for a monotonic test at 25°C and 0.0005 $\epsilon$ /sec (Courtesy of Seo).....	229
Figure 7.66	Comparison between DIC and LVDT strains for a monotonic test at 5°C and 0.00003 $\epsilon$ /sec (Courtesy of Seo).....	229
Figure 7.67	DIC 50x100 mm DIC image showing strain distribution during: (a) pre-peak and (b) localization (As colors change from blue to green to red, the value of vertical strain increases) (Courtesy of Seo).....	230
Figure 7.68	LVDT and DIC strains for a test at 5°C and 0.00003 $\epsilon$ /sec.....	232
Figure 7.69	C vs. S* curve using LVDT and DIC strains .....	233
Figure 7.70	S* vs. Lebesgue norm of stress using LVDT and DIC strains .....	233
Figure 7.71	Measured and predicted $\sigma$ - $\epsilon$ curves using LVDT strains and LVDT with a switch to DIC strains .....	234
Figure A.1	12.5 mm MD mixture trial compaction data.....	246
Figure B.1	Compactor mold and extension collar.....	263
Figure B.2	ServoPac gyratory compactor.....	264

Figure B.3	Coring and sawing machines .....	265
Figure B.4	Gluing gig .....	266
Figure B.5	MTS testing setup .....	267
Figure B.6	UTM testing system .....	268
Figure B.7	Geometries used for mechanical testing .....	269
Figure B.8	Specimens cut and cored for air void distribution study .....	270
Figure B.9	Wrapping a specimen with Parafilm.....	271
Figure B.10	GTX LVDT (Left) and XSB LVDT (Front).....	272
Figure B.11	CD LVDTs .....	273
Figure B.12	Different LVDT mounting mechanisms on a horizontal plate to check strain drift .....	274
Figure C.1	Stress and strain measurements for constant crosshead-rate test.....	283
Figure C.2	Comparison of ram and LVDT dynamic modulus and phase angle measurements.....	284
Figure C.3	Measurement of deformations at each joint along the loading train of the MTS loading machine .....	285
Figure C.4	Machine compliance evaluated at different temperatures and crosshead strain rates for UTM machine .....	286
Figure C.5	Adjusted and unadjusted phase angle measurements for various machine, LVDT, and mount type combinations .....	287
Figure C.6	Different LVDT mount types on aluminum specimen .....	288
Figure C.7	Phase angle measurements from aluminum specimen tested with MTS .....	289

# **1 Introduction**

## ***1.1 Research Objective***

Stated in simplest terms, mechanistic pavement modeling is composed of two main models: the material characterization model and the structural response model. Without these two components, modeling of pavements is reduced to a simplistic empirical approach. While the role of the structural response model is to predict stresses and strains in the pavement, which are later used for distresses and performance prediction, it is the material characterization model that provides the material properties needed for the structural response model. Hence, from this it is seen that accurate and advanced asphalt concrete characterization is essential and vital for realistic performance prediction of asphalt concrete pavements.

While coupling of distresses is seldom considered when predicting the initiation and evolution of pavement distresses, in reality the presence of one distress type can accelerate or decelerate the initiation and development of another distress type. Coupling of distresses will become feasible if the material characterization model is developed to implicitly incorporate all distresses at the material level. The major distresses that are usually considered in asphalt pavement are rutting, fatigue cracking, thermal cracking, and reflective cracking. In a survey submitted to nation-wide transportation agencies, rutting was ranked as the most critical distress followed by fatigue cracking. Briefly stated, rutting is the accumulation of permanent vertical strains in the asphalt pavement layers; while, fatigue cracking is either the initiation of a crack at the bottom of the

asphalt layer and its subsequent propagation to the surface or its initiation at the surface and propagation to the bottom.

The overall objective of this research, which is a part of project NCHRP 9-19, is to develop an advanced and accurate asphalt material characterization procedure to be incorporated in the Superpave performance models system. This procedure will include the necessary models and the necessary supporting test protocols for determining the required material parameters. The focus of the research presented herein is to develop the protocols for tensile testing needed to determine material parameters that are generally related to fatigue cracking distresses (distresses caused by mechanical strains). On the other end, a research group at the University of Maryland will develop testing protocols and model parameters for the compression state, which is related to rutting. The resulting models and test protocols will eventually be combined to produce a generalized material characterization model that is able to address both types of distresses, rutting and fatigue.

Thermal cracking will be addressed in the distress model through thermal strains; while ABAQUS software will be used to predict the reflective cracking (cracking initiating and propagating from a concrete sublayer) based on the given boundary condition problem.

The basic requirements for this material characterization model are (Superpave Models Team Report 1999):

- It must be applicable to a full range of loading conditions experienced in a pavement including temperature and loading rate.
- It must encompass all possible components of asphalt concrete response:
  - \* Elastic,

- \* Viscoelastic,
  - \* Plastic,
  - \* Viscoplastic, and
  - \* Fracture
- It must address the major factors affecting asphalt concrete response, which are in decreasing order of significance:
    - \* Strain rate/time of loading,
    - \* Temperature,
    - \* Stress state,
    - \* Damage and healing, and
    - \* Anisotropy, aging, moisture, and others.

The study on anisotropy was performed by our partner-research group working at ASU, while aging and moisture will be addressed in the future.

### ***1.2 Research Approach***

The modeling approach selected for characterizing asphalt concrete must address two fundamental topics:

- Constitutive law: Relationship between stress, strain and time
- Failure Criteria /material strength

As known, asphalt concrete behaves differently depending on temperature and rate of loading. Its behavior may vary from elastic and linear viscoelastic at low temperatures or fast loading rates to non-linear viscoelastic and viscoplastic at high temperatures or slow loading rates. Therefore, the modeling strategy adopted is to model each behavior

separately. The separation of the response into components is done best using creep and recovery tests, with sufficient loading and unloading times to permit isolation of time dependence. In this research, the elastic strain is combined with the viscoelastic strain and referred to as viscoelastic strain; while, plastic and viscoplastic strains are also combined together and referred to as viscoplastic strain. The resulting characterization model will be referred to as the ViscoElastoPlastic model.

The viscoelastic modeling approach selected in this research is based on Schapery's continuum damage model. The model, originally developed for modeling solid rocket propellant, is based on a thermodynamic formulation with viscoelastic and viscoplastic constitutive equations and internal state variables related to material micro-cracking. Kim (Kim et al. 1997, Lee and Kim 1998a) has recently applied the approach to the prediction of fatigue in asphalt. However, this work was only done at low and moderate temperatures where viscoplastic strains are not present. Moreover, the approach has not yet been used to model macro-fracture and failure in the full post-peak portion of the material response. It is hoped that the model can be extended or generalized to predict the fracture portion of the response. Some of Uzan's work on viscoplasticity, especially the strain hardening model, was referenced in developing the viscoplastic model.

### ***1.3 Outline of Research Presented***

While Chapter 2 presents the theoretical formulation necessary for developing the ElastoViscoPlastic model, Chapter 3 discusses materials, specimen fabrication, testing setup and experimental testing details incorporated in the research. Because specimens used in the testing need to be representative of the material being tested and yield responses that can be considered independent of aggregate size and specimen boundary

conditions a comprehensive specimen geometry study is included in Chapter 4. The study focuses on air void and strain distributions inside Superpave gyratory compacted specimens.

Chapter 5 is dedicated to presenting methods for determining and inter-converting of viscoelastic material response functions, which are the building blocks of any representative characterization model. Chapter 6 tackles a challenging task in the presentation of a technique to validate the applicability of time-temperature superposition as damage in the specimen grows. The chapter also explores potential applications and benefits, most important of which is the reduction of required number of tests needed for development of testing protocols. Finally, Chapter 8, which could be considered as the fruit of this research, presents the development of the ElastoViscoPlastic model. Firstly,, the viscoelastic model is developed followed by the viscoplastic model. The models are validated first independently and later together after they are integrated. Appendices A and B contain supporting figures and fabrication protocols, while Appendix C presents an important study that sheds light on machine and measurement instrumentation problems and their effects on testing results and analyses.

## **2 Theoretical Background and Literature Review**

### ***2.1 Introduction***

The research approach that is presented in this research began with the work of Kim and Little (1990) based on Schapery's earlier work on viscoelasticity. Kim and Little successfully applied Schapery's (1981) nonlinear viscoelastic constitutive theory for composite materials with distributed damage to sand asphalt concrete under cyclic loading. In that model, a viscoelastic problem is transformed to an elastic case by replacing physical strains by pseudo strains based on the extended elastic-viscoelastic correspondence principle (Schapery 1984). A damage parameter based on a microcrack growth law and pseudo strain values is used to describe the effect of growing damage on the deformation behavior of the material.

Schapery (1990) developed the work potential theory for elastic materials with growing damage based on the thermodynamics of irreversible processes. The theory uses an internal state variable formulation to describe the structural changes with damage growth and was also extended to viscoelastic media. This theory was successfully applied to asphalt concrete under monotonic loading (Park et al. 1996) and cyclic loading (Lee 1996, Kim et al. 1997, Lee and Kim 1998a). Daniel (2001) later used the theory to develop a characterization model using monotonic testing that can be used to characterize behavior under cyclic loading. However, all the aforementioned work was done at loading rates and temperatures where only elastic and viscoelastic behaviors prevailed, with negligible if any viscoplasticity present.

Once viscoplastic behavior becomes a significant constituent of the overall asphalt concrete response, the viscoelastic models cease to characterize the asphalt behavior completely (Chehab 2002). To accurately characterize asphalt concrete behavior at any testing condition; i.e., loading rate and temperature, it becomes necessary to develop a model that can handle viscoplastic behavior when present. The viscoplastic model presented in this research will be based on the works of Uzan (1996) and Schapery (1997).

This chapter commences with the presentation of the theory of viscoelasticity, including the elastic-viscoelastic correspondence, work potential theory and the constitutive model developed by Lee (1996). Next, the theoretical derivation necessary for showing the validity of the time-temperature superposition principle to asphalt concrete with growing damage in the tension state is presented (Chehab 2002). The chapter ends with an overview of the theory of viscoplasticity adopted in developing the ViscoElastoPlastic model in this research.

## ***2.2 Theory of Viscoelasticity***

### **2.2.1 Definitions**

Viscoelastic materials such as asphalt concrete exhibit time or rate dependence, meaning that the material response is not only a function of the current input, but the current and ***past*** input history. The response of a linear viscoelastic body to any input history is described using the convolution integral. A system is considered to be a linear system ***if and only if*** the conditions of homogeneity and superposition are satisfied:

- Homogeneity:  $R \{AI\} = A R \{I\}$  and (2.1)

- Superposition:  $R \{I_1+I_2\} = R \{I_1\} + R \{I_2\}$  (2.2)

where  $I, I_1, I_2$  are input histories,  $R$  is the response, and  $A$  is an arbitrary constant.

The brackets  $\{ \}$  indicate that the response is a function of the input history. The homogeneity, or proportionality condition essentially states that the output is directionally proportional to the input, e.g., if the input is doubled, the response doubles as well. The superposition condition states that the response to the sum of two inputs is equivalent to the sum of the responses from the individual inputs.

For linear viscoelastic materials, the input-response relationship is expressed through the hereditary integral:

$$R = \int_{-\infty}^t R_H(t, \tau) \frac{dI}{d\tau} d\tau \quad (2.3)$$

where  $R_H$  is the unit response function. With a known unit response function, the response to any input history can be calculated. The lower limit of the integration can be reduced to  $0^-$  (zero minus, just before time zero) if the input starts at time  $t=0$  and both the input and response are equal to zero at  $t<0$ . The value of  $0^-$  is used instead of  $0$  to allow for the possibility of a discontinuous change in the input at  $t=0$ . For notational simplicity,  $0$  is used as the lower limit in all successive equations and should be interpreted as  $0^-$  unless specified otherwise. Equation (2.3) is applicable to an aging system in which the time zero is the time of fabrication rather than the time of load application.

In this research, it is assumed that the asphalt concrete behavior is that of a non-aging system; thus Equation (2.3) reduces to:

$$R = \int_0^t R_H(t - \tau) \frac{dI}{d\tau} d\tau \quad (2.4)$$

For the uniaxial loading, the non-aging, linear viscoelastic stress-strain relationships are:

$$\sigma = \int_0^t E(t - \tau) \frac{d\varepsilon}{d\tau} d\tau \quad (2.5)$$

$$\varepsilon = \int_0^t D(t - \tau) \frac{d\sigma}{d\tau} d\tau \quad (2.6)$$

where  $E(t)$  is the relaxation modulus and  $D(t)$  is the creep compliance, both of which are referred to as unit response functions.

### 2.2.2 Correspondence Principle

Schapery (1984) proposed the extended elastic-viscoelastic correspondence principle, which is applicable to both linear and nonlinear viscoelastic materials. He suggested that constitutive equations for certain viscoelastic media are identical to those for the elastic cases, but stresses and strains are not necessarily physical quantities in the viscoelastic body. Instead, they are *pseudo* variables in the form of convolution integrals.

According to Schapery, the uniaxial pseudo strain ( $\varepsilon^R$ ) is defined as:

$$\varepsilon^R = \frac{1}{E_R} \int_0^t E(t - \tau) \frac{d\varepsilon}{d\tau} d\tau \quad (2.7)$$

where  $\varepsilon$  is uniaxial strain,

$E_R$  is a reference modulus set as an arbitrary constant,

$E(t)$  is the uniaxial relaxation modulus,

$t$  is the time of interest; and

$\tau$  is an integration constant.

Using the definition of pseudo strain in Equation (2.7), Equation (2.5) can be rewritten as:

$$\sigma = E_R \varepsilon^R \quad (2.8)$$

A correspondence can be found between Equation (2.8) and a linear elastic stress-strain relationship (Hooke's Law). The power of the pseudo strain can be seen in Figure 2.1. Figure 2.1(a) shows the stress strain behavior for controlled-stress cyclic loading within the material's linear viscoelastic range (such as in a complex modulus test). Because the material is being tested in its linear viscoelastic range, no damage is induced and the hysteretic behavior and accumulating strain are due to viscoelasticity only. Figure 2.1(b) shows the same stress data plotted against the calculated pseudo strains. All of the cycles collapse to a single line with a slope of 1.0 ( $E_R=1.0$ ). The use of pseudo strain simplifies the modeling approach significantly by allowing for the separation of viscoelastic (time-dependant) behavior from any accumulated damage.

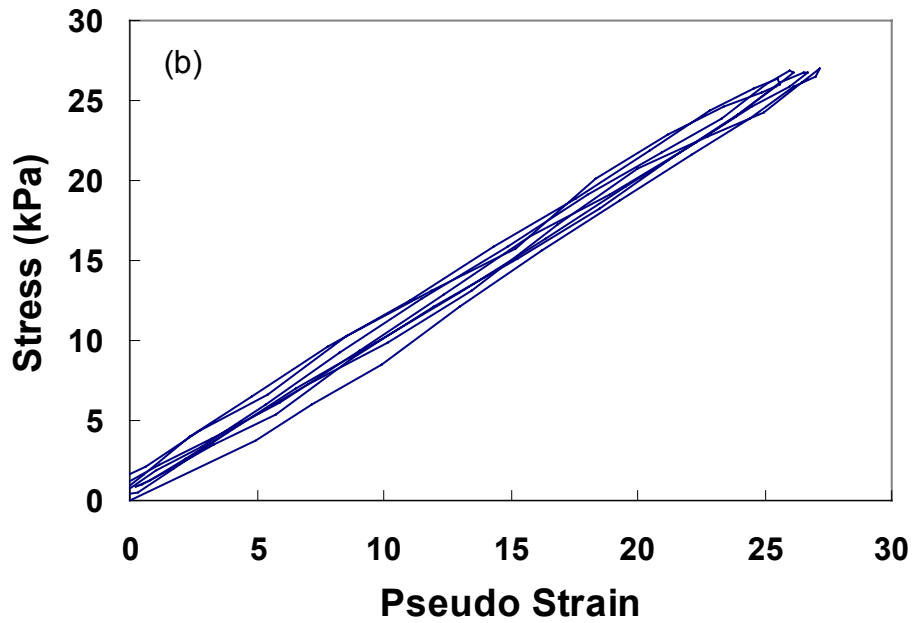
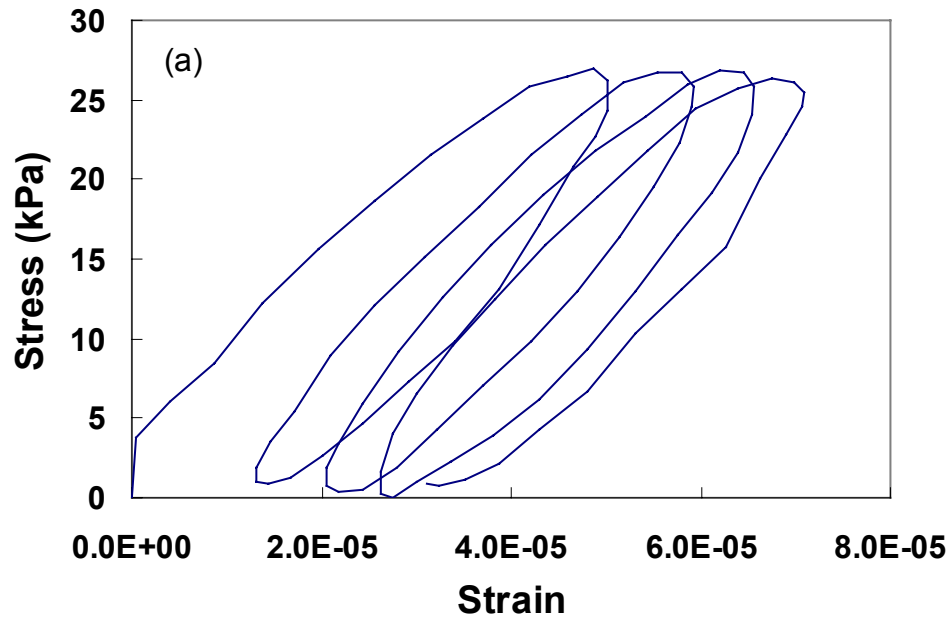


Figure 2.1. (a) Stress–strain behavior for mixture under LVE cyclic loading; (b) Stress–pseudo strain behavior for same data (Courtesy of Daniel 2001)

### 2.2.3 Uniaxial Constitutive Model Using Work Potential Theory

The constitutive model that is used as the basis of this research was developed by Kim and Lee (Lee 1996, Kim et al. 1997, Lee and Kim 1998a). The model utilizes the elastic-viscoelastic correspondence principle to eliminate the time dependence of the material. Work potential theory (Schapery 1990) is then used to model both the damage growth and healing in the material. The term damage is defined as all structural changes except linear viscoelasticity that result in the reduction of stiffness or strength as the material undergoes loading. Microdamage healing includes everything except linear viscoelastic relaxation that contribute to the recovery of stiffness or strength during rest periods and can include such things as fracture healing, steric hardening, and nonlinear viscoelastic relaxation.

Schapery (1990) developed a theory using the method of thermodynamics of irreversible processes to describe the mechanical behavior of elastic composite materials with growing damage. Three fundamental elements comprise the work potential theory:

1. Strain energy density function

$$W = W(\varepsilon_{ij}, S_m) \quad (2.9)$$

2. Stress-strain relationship

$$\sigma_{ij} = \frac{\partial W}{\partial \varepsilon_{ij}} \quad (2.10)$$

3. Damage evolution law

$$-\frac{\partial W}{\partial S_m} = \frac{\partial W_s}{\partial S_m} \quad (2.11)$$

where  $\sigma_{ij}$  and  $\varepsilon_{ij}$  are stress and strain tensors, respectively.  $S_m$  are internal state variables and  $W_s = W_s(S_m)$  is the dissipated energy due to structural changes. Using Schapery's

elastic-viscoelastic correspondence principle (CP) and rate-type damage evolution law (Schapery 1984 and 1990, Park et al. 1996), the physical strains,  $\varepsilon_{ij}$ , are replaced with pseudo strains,  $\varepsilon_{ij}^R$ , to include the effect of viscoelasticity. The use of pseudo strain as defined in Equation (2.7) accounts for all the time-dependent effects of the material through the convolution integral. Thus, the strain energy density function  $W=W(\varepsilon_{ij}, S_m)$  transforms to the pseudo strain energy density function:

$$W^R=W^R(\varepsilon_{ij}^R, S_m) \quad (2.12)$$

Schapery's correspondence principle cannot be used to transform the elastic damage evolution law to use with viscoelastic materials because both the available force for growth of  $S_m$  and the resistance against the growth of  $S_m$  in the damage evolution law are rate-dependent for most viscoelastic materials (Park et al. 1996). Therefore, a form similar to power-law crack growth laws is used to describe the damage evolution in a viscoelastic material:

$$\dot{S}_m = \left( -\frac{\partial W^R}{\partial S_m} \right)^{\alpha_m} \quad (2.13)$$

where  $\dot{S}_m$  is the damage evolution rate,  $W^R$  is the pseudo strain energy density function, and  $\alpha_m$  are material constants.

Using Schapery's work potential theory and CP, Lee and Kim (1998b) developed a mode of loading-independent constitutive model that describes the fatigue and microdamage healing of asphalt concrete under cyclic loading. Lee and Kim (1998b) used uniaxial tensile cyclic tests with various loading amplitudes to study the mechanical behavior of asphalt concrete. They were able to account for the hysteretic behavior due to both loading-unloading and repetitive loading in the linear viscoelastic range using

pseudo strains. In damage-inducing testing, they observed that the slope of the stress – pseudo strain loop decreases as loading continues in both controlled stress and controlled strain testing. The change in the slope of the loop represents the reduction in the stiffness of the material as damage accumulates. To represent the change in slope, Lee and Kim (1998b) used the secant pseudo stiffness,  $S^R$ , defined as:

$$S^R = \frac{\sigma_m}{\epsilon_m^R} \quad (2.14)$$

where  $\epsilon_m^R$  is the peak pseudo strain in each stress-pseudo strain cycle, and  $\sigma_m$  is the stress corresponding to  $\epsilon_m^R$ . A normalization constant  $I$  had to be introduced to account for sample to sample variation and for its effect on pseudostiffness (Lee 1996). The normalized pseudostiffness thus becomes:

$$C = \frac{S^R}{I} \quad (2.15)$$

It is beneficial to compare uniaxial constitutive equations for elastic and viscoelastic materials with and without damage to show how the correspondence principle reduces the viscoelastic model to a corresponding elastic counterpart:

$$\text{Elastic Body without Damage:} \quad \sigma = E_R \epsilon \quad (2.16)$$

$$\text{Elastic Body with Damage:} \quad \sigma = C(S_m) \epsilon \quad (2.17)$$

$$\text{Viscoelastic Body without Damage:} \quad \sigma = E_R \epsilon^R \quad (2.18)$$

$$\text{Viscoelastic Body with Damage:} \quad \sigma = C(S_m) \epsilon^R \quad (2.19)$$

where  $E_R$  is a constant and  $C(S_m)$  is a function of internal state variables (ISV's)  $S_m$  that represent the changing stiffness of the material due to microstructure changes such as accumulating damage or healing. In Equation (2.16),  $E_R$  is Young's modulus. A correspondence is seen between the elastic and viscoelastic constitutive equations; that is, the viscoelastic equations take the same form as the elastic ones with pseudo strain replacing physical strain.

Since all the tests that will be done in this research for the purpose of viscoelastic behavior characterization will be in strain control, particularly constant crosshead-rate tests, the constitutive equations reduce to:

$$W_m^R = \frac{I}{2} C(S) (\varepsilon_m^R)^2 \quad (2.20)$$

$$\sigma_m = IC(S) \varepsilon_m^R \quad (2.21)$$

The function  $C$  represents  $S^R$ , as can be seen from Equations (2.15) and (2.20). The evolution law becomes:

$$\dot{S}_m = \left( -\frac{\partial W_m^R}{\partial S_m} \right)^{\alpha_m} \quad (2.22)$$

To characterize the function  $C$  in Equation (2.21), the damage evolution law and experimental data are used. With the measured stresses and calculated pseudo strains,  $C$  values can be determined through Equation (2.15). To find the characteristic relationship between  $C$  and  $S$ , the values of  $S$  must be obtained through Equation (2.22). The form of Equation (2.22) as presented is not suitable for finding  $S$  because it requires prior knowledge of the  $C(S)$  function through Equation (2.20). Lee (1996) uses the chain rule

presented in Equation (2.23) to eliminate S from the right hand side of the evolution equation and obtain S in the exact form shown in Equation (2.24):

$$\frac{dC}{dS} = \frac{dC}{dt} \frac{dt}{dS} \quad (2.23)$$

$$S = \int_0^t \left[ \frac{I}{2} \frac{dC}{dt} (\varepsilon_m^R)^2 \right]^{(1+\alpha)} dt \quad (2.24)$$

Since both the function C and  $\varepsilon_m^R$  are dependent upon time t, a numerical approximation can be used with the measured data to obtain S as a function of time:

$$S(t) \cong \sum_{i=1}^N \left[ \frac{I}{2} (\varepsilon_{mi}^R)^2 (C_{i-1} - C_i) \right]^{(1+\alpha)} (t_i - t_{i-1})^{\frac{1}{(1+\alpha)}} \quad (2.25)$$

Depending on the characteristics of the failure zone at a crack tip,  $\alpha=(1+1/n)$  or  $\alpha=1/n$ , where n is the slope of the linear viscoelastic response function plotted as a function of time in a logarithmic scale. If the material's fracture energy and failure stress are constant, then  $\alpha=(1+1/n)$ . On the other hand, if the fracture process zone size and fracture energy are constant,  $\alpha=1/n$ . This has been observed by Schapery for rubber, and by Lee and Kim (1998a, 1998b) for asphalt concrete (Lee 1996, Daniel 2001).

The relationship between C and S can be found by performing regression on the data. Lee (1996) found that the function follows the form:

$$C_1(S_1) = C_{10} - C_{11}(S_1)^{C_{12}} \quad (2.26)$$

The regression coefficient  $C_{10}$  is close to 1.0, as would be expected at a negligible damage level ( $S_1$  goes to zero) because the material is in the linear viscoelastic range of behavior and there exists a one-to-one relationship between stress and pseudo strain (i.e.,  $E^R=1$ ).

## ***2.3 Time-Temperature Superposition with Growing Damage in Tension***

### **2.3.1 Introduction**

It has been shown in earlier research that asphalt concrete in its linear viscoelastic state is a thermorheologically simple material. That is, time-temperature superposition can be applied given that the material is in its undamaged state. As such, data from complex modulus testing conducted within linear viscoelastic limits at different frequencies and temperatures should yield a single continuous mastercurve for dynamic modulus and phase angle as a function of frequency at a given reference temperature by horizontally shifting individual curves along the frequency axis.

However, for comprehensive material modeling, laboratory testing often extends to the damaged state where micro- and macro-cracks in the asphalt concrete matrix start to develop. If it can be shown that time-temperature superposition holds for the damaged state (i.e., the effect of both temperature and time can be expressed through reduced time at a reference temperature) the laboratory testing required for comprehensive material characterization can be significantly reduced.

Schapery (Park et al. 1997) has shown that solid propellant, which consists of a rubber matrix that is highly-filled with hard particles, has been found to be thermorheologically simple (TRS) not only when it is linearly viscoelastic, but also when it is strongly nonlinear due to micro-cracking. The shift factor is independent of the amount of damage. Experimental studies of macro-crack growth in solid propellant at several temperatures have demonstrated that the shift factor for this crack growth is identical to that for linear viscoelastic behavior (Schapery 1978). The physical basis for this behavior is that the time and temperature dependence of deformation and all crack

growth in the rubber and at interfaces originates from the rubber, which is itself TRS. With this motivation and the fact that TRS behavior of asphalt concrete exists in its linear range, experiments will have to be conducted to determine if TRS extends to behavior with micro-cracking and viscoplasticity. By examining the basic structure of the underlying constitutive equations, one can identify a convenient test history and data reduction method for determining if asphalt concrete is TRS. Both deformation and failure behavior will be addressed in the following section.

### 2.3.2 Structure of the Constitutive Equations:

Using abbreviated notation, the total strain  $\varepsilon$  (including viscoplastic strain) and stress  $\sigma$  tensors are related as follows for non-aging materials (Schapery 1999):

$$\varepsilon = - \partial G / \partial \sigma \quad (2.27)$$

where  $G=G(\sigma, \mathbf{S}, T)$  is the Gibbs free energy,  $T$  is temperature and  $\mathbf{S}$  represents the set of all thermodynamic state variables that account for local effects on all scales (molecular motions, micro-deformations, micro-cracking and macro-cracking (if any)). The set of evolution equations for  $\mathbf{S}$  is:

$$\frac{d\mathbf{S}}{dt} = \mathbf{f}(\sigma, \mathbf{S}, T) \quad (2.28)$$

where  $\mathbf{f}$  comes from the intrinsic viscous behavior of asphalt concrete. There are as many equations in Equation (2.28) as  $\mathbf{S}$  variables. In principle, therefore, Equation (2.28) may be solved to express  $\mathbf{S}$  as a function of  $\sigma$  and  $T$  histories. This result may then be substituted into Equation (2.27) to provide strain in terms of stress and temperature histories. A TRS material is one in which all effects of  $T$  in Equation (2.28) appear as a common factor, which we denote as  $1/a_T$ . In this case, Equation (2.28) reduces to:

$$\frac{d\mathbf{S}}{d\xi} = \mathbf{F}(\sigma, \mathbf{S}) \quad (2.29)$$

where  $d\xi = dt/a_T$  for constant or transient temperature; in the latter case,

$$\xi = \int_0^t dt/a_T, \text{ and} \quad (2.30)$$

$$\xi = \frac{t}{a_t} \quad (2.31)$$

while Equation (2.31) applies in the former case. The effect of temperature in Equation (2.27) is assumed to produce only thermal expansion strain,  $\varepsilon_T$  say. Thus, we may write

$$\varepsilon_\sigma \equiv \varepsilon - \varepsilon_T = -\partial G_\sigma / \partial \sigma \quad (2.32)$$

where  $\varepsilon_\sigma$  is the “strain due to stress” and  $G_\sigma = G_\sigma(\sigma, \mathbf{S})$ . Also,  $\mathbf{S}$  comes from the solution of Equation (2.29). It is important to observe that all time-dependant behavior for non-aging TRS materials comes from Equation (2.29), and only reduced time, not physical time, appears. Thus, physical time enters mechanical behavior of non-aging asphalt concrete only through external inputs if Equations (2.29) and (2.32) are applicable.

### 2.3.3 Application to Uniaxial Loading:

A convenient series of tests that may be used to check for TRS behavior consists of a series of constant crosshead rates to failure at a series of constant temperatures using cylindrical bars; they should be sufficiently long that the stress state is essentially uniaxial. With such tests, the theory is needed to determine how to check for TRS behavior from analysis of the stress-strain data. In practice, the overall specimen strain, or local strain using for example LVDTs, may not increase at a constant rate even if a constant crosshead rate is specified, as discussed in Appendix C. A power law in time may better describe the local or global axial strain (due to stress),

$$\varepsilon_{\sigma} = k't^n \quad (2.33)$$

where  $n$  is assumed constant, but  $k'$  is a variable because a series of different crosshead rates are imposed. Rewriting this strain input in terms of reduced time,

$$\varepsilon_{\sigma} = k\xi^n \quad (2.34)$$

where:

$$k = k'a_T^n \quad (2.35)$$

If  $n=1$ , then  $k$  is the “reduced strain rate”; although  $k$  is not really reduced strain rate when  $n \neq 1$ , we shall still use this name for ease of discussion.

Next, customizing Equations (2.29) and (2.32) to uniaxial stress-strain behavior and inverting Equation (2.32), The following is obtained:

$$\sigma = g(\varepsilon_{\sigma}, \mathcal{S}) \quad (2.36)$$

Also, Equation 2.37 is derived:

$$d\mathcal{S}/d\xi = h(\varepsilon_{\sigma}, \mathcal{S}) \quad (2.37)$$

after inserting Equation (2.36) in Equation (2.29). Given Equation (2.34) and solving (in principle) Equation (2.37) for  $\mathcal{S}$ , we obtain stress in the form:

$$\sigma = \hat{g}(\xi, k, n) \quad (2.38)$$

in which both  $\xi$  and  $k$  are “reduced” variables. In order to analyze data for TRS behavior, it is helpful to eliminate  $k$  in favor of  $\varepsilon_{\sigma}$  using Equation (2.37). Thus, Equation (2.38) may be written as:

$$\sigma = \hat{f}(\varepsilon_{\sigma}, \xi, n) \quad (2.39)$$

### 2.3.4 Stress-Strain Data

Equation (2.39) provides the basis for checking stress-strain data for TRS behavior. It shows that if the material is TRS and if the strain history is that in Equation (2.34), then plots of  $\sigma$  (or  $\log \sigma$ ) versus  $\log t$  at any given constant  $\varepsilon_\sigma$  (and for a set of temperatures) may be shifted by amounts of  $\log a_T$  to form a master curve. These constant-strain curves are constructed by making cross-plots of the original stress-strain data taken at constant  $k'$ . In other words, for each  $\varepsilon_\sigma$  the dependence on time and temperature is the same as for a linear viscoelastic material; in the latter case, it is helpful to shift curves of  $\sigma/\varepsilon_\sigma$  because this quantity is independent of  $\varepsilon_\sigma$ . It should be noted that we have not assumed the material non-linearity for all strain histories is a function of only current strain; it is the special history in Equation (2.33) that produces the behavior in Equation (2.39).

### 2.3.5 Strength Data

In principle, Equation (2.39) or the much more general version, Equations (2.29) and (2.32), apply on a local scale even with strain localization if the strains do not change significantly on a scale comparable to a suitably defined average aggregate particle dimension. In the case of Equation (2.39), the stress state must be essentially uniaxial. Alternatively, these equations may be used on a global scale, even with strain localization, because  $S$  can be used, in principle, to account for localization; thus, in Equation (2.39)  $\sigma$  may be axial force divided by initial cross-sectional area while  $\varepsilon_\sigma$  is crosshead-based strain for both pre-peak and full post-peak behavior.

Let us first assume the failure behavior is “ductile” in that specimens do not break until after a maximum stress is reached. For each rate  $k'$  and temperature  $T$ , the maximum stress is given by the condition  $d\sigma/dt=0$ . In terms of Equation (2.38) this implies that:

$$d\hat{g}/d\xi = 0 \quad (2.40)$$

Thus, solving Equation (2.40) the reduced time at the maximum in  $\sigma$ , say  $\sigma_m$ , is

$$\xi_m = \text{function}(k, n) \quad (2.41)$$

and the corresponding strain, Equation (2.34), is

$$\varepsilon_m = k\xi_m^n = \text{function}(k, n) \quad (2.42)$$

Similarly, from Equation (2.38), the “ductile” strength is

$$\sigma_m = \text{function}(k, n) \quad (2.43)$$

Equations (2.42) and (2.43) show that, for the TRS material model employed, the strain at maximum stress and maximum stress may be expressed as master curves in terms of reduced strain rate, Equation (2.35).

If a specimen breaks before a maximum,  $d\sigma/dt=0$ , is reached, then the failure is usually called “brittle.” In this case, we may interpret failure to be the result of at least one crack that propagates the full specimen width. Taking one of the  $S$  variables as crack length, say  $S$  then when  $S$  reaches a critical size,  $S_c$ , brittle failure occurs. The latter corresponds to the specimen width or, more commonly, a size beyond which crack growth is dynamic. Denote the stress and strain at this time  $\xi_c$  by  $\sigma_c$  and  $\varepsilon_c$ , respectively.

Solution of Equation (2.37) for  $S$ , given Equation (2.34), gives for  $\xi \leq \xi_c$ ,

$$S = \text{function}(\xi, k, n) \quad (2.44)$$

This equation came from a quasi-static analysis; unstable crack growth corresponds to predicting  $S \rightarrow \infty$  at some finite time  $\xi_c$ ; if the growth is not dynamic, then  $S \sim$  specimen width at  $\xi = \xi_c$ . In either case, Equation (2.44) implies  $\xi_c = \text{function}(k, n)$  at the time of brittle failure. In turn, Equations (2.34) and (2.38) imply

$$\varepsilon_c = \text{function}(k, n) \quad (2.45)$$

$$\sigma_c = \text{function}(k, n) \quad (2.46)$$

Thus, master curves in reduced strain rate may be developed, just as for ductile failure. However, the functional form of these curves will be different because they reflect different physical processes. Finally, it should be noted that except for this section on theory, the strain-due-to-stress is denoted by  $\varepsilon$  instead of  $\varepsilon_\sigma$  in the following chapters.

#### ***2.4 Brief Overview of the Viscoplastic Model Approach***

The modeling strategy followed in this research calls for the separation of the constituent responses in an asphalt concrete mixture under loading, and modeling each separately. Background about the characterization of the viscoelastic (including elastic) behavior has been already discussed in the previous section. For viscoplastic (including plastic) response, Uzan's strain hardening model (Uzan et al. 1985) in addition to further work by Schapery (1999) will be the foundation of the model to be developed in this research.

The first step in modeling the viscoplastic response is to conduct cyclic creep and recovery tests to separate the component strains and obtain the viscoplastic strain component. Equation (2.47) serves as the foundation of the viscoplastic model, where viscoplastic strain is assumed to follow a strain-hardening model of the form:

$$\dot{\epsilon}_{VP} = \frac{g(\sigma)}{\eta_{vp}} \quad (2.47)$$

where  $\dot{\epsilon}_{VP}$  is the viscoplastic strain rate, and  $\eta_{vp}$  is the material's coefficient of viscosity.

Assuming that  $\eta$  is a power law in strain (Uzan et al. 1985), Equation (2.47) becomes:

$$\dot{\epsilon}_{VP} = \frac{g(\sigma)}{A\epsilon_{vp}^p} \quad (2.48)$$

where A and p are model coefficients. The background of the viscoplastic theory was presented briefly here because it will be discussed in much more detail in Chapter 8 when presenting the theoretical formulation for developing the ViscoElastoPlastic model.

## **3 Specimen Preparation and Testing Programs**

### ***3.1 Introduction***

The study on specimen geometry and machine and measurement instrumentation utilized a mixture different than that used for the development of the ViscoElastoPlastic model and its prerequisite tasks. As for testing programs, there are tests common to all tasks and others that are task specific. Presented in this chapter are the two mixtures used in addition to the common testing programs adopted throughout the research.

### ***3.2 Specimen Preparation***

#### **3.2.1 Asphalt Mixtures**

The two mixtures used in this research are the North Carolina 12.5 mm Superpave mixture and the Maryland 12.5 mm Superpave mixture. The former mix was used for the specimen geometry study (Chapter 4) in addition to the machine and measurement instrumentation study (Appendix C). On the other hand, the latter mixture was used for determining the viscoelastic material properties (Chapter 5), validation of time-temperature superposition principle for the damaged state (Chapter 6) and for the development of the ViscoElastoPlastic model (Chapter 7). More emphasis will be placed on the Maryland mixture since it is the one used for modeling purposes.

##### ***3.2.1.1 North Carolina 12.5mm Superpave Mix***

The NC 12.5 mm mix is based on the Superpave mix design that was used for the SPS-9 project on US 1 in Sanford, North Carolina. The maximum nominal aggregate size was 12.5 mm. The aggregate blend used consisted of 95.5% by mass granite aggregates

obtained from three stockpiles from Lemon Springs, NC, 3.5% natural sand (Rambeaut sand), and 1% baghouse fines. The gradation for the blend is presented in Figure 3.1. The asphalt binder used was PG 70-22 obtained from the Citgo Asphalt Company in Paulsboro, New Jersey. The optimum asphalt content, as determined by the Superpave volumetric mix design, was 5.2% by mass. Mixing and compaction temperatures were 166°C and 153°C respectively. Compaction was done using the Superpave gyratory compactor. More details on compaction are presented in Chapter 4.

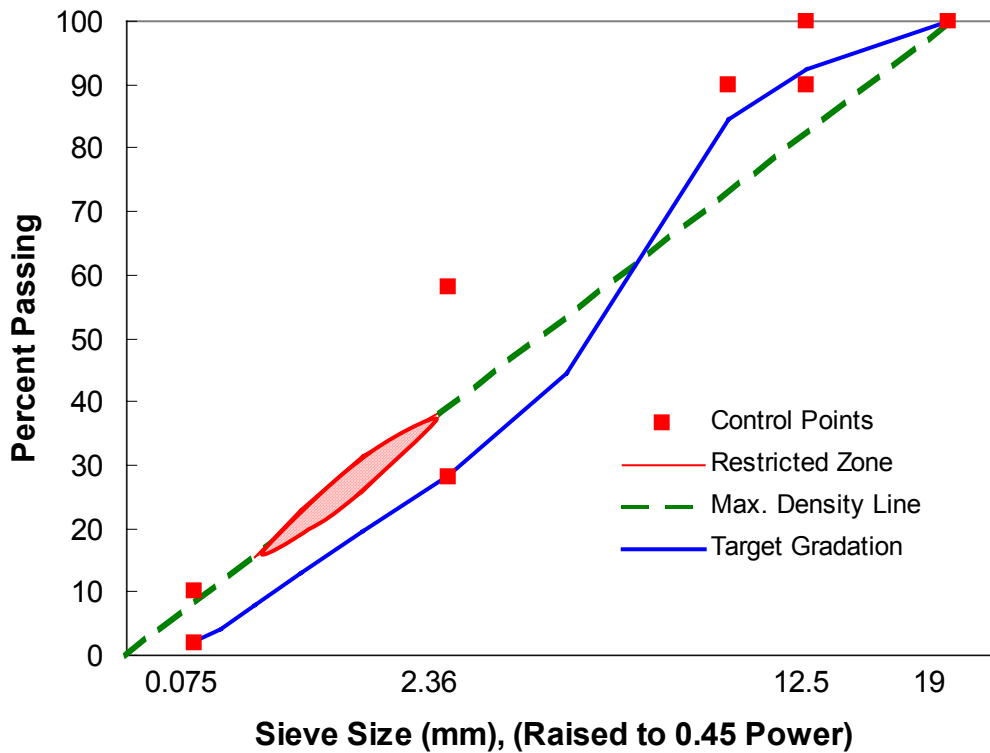


Figure 3.1. Gradation chart for NC 12.5-mm Superpave mix

### *3.2.1.2 Maryland 12.5 mm Superpave Mix*

The Maryland 12.5 mm Superpave mixture is a standard mixture used extensively as a surface course mixture in Maryland, and was selected for use in laboratory experiments in the Superpave Support and Performance Models Management project, including those for the development of the characterization model. The Superpave mixture uses 100 percent crushed limestone from Maryland and an unmodified PG 64-22 binder. The mix design was done at the University of Maryland; more details about component materials and mix design procedures are documented in the volumetric design report (Superpave Models Team 1999(b)).

#### Aggregates

The Superpave mixture was produced with limestone aggregate from Redland Genstar's Frederick Maryland quarry. Material from seven stockpiles were used to produce the mixtures. Additionally, fines obtained from the dust collection system of a hot mix plant at the quarry were included to increase the filler content of the mixture to that typical of plant production. Aggregate properties are presented in Table A.1 in Appendix A.

#### Asphalt Binder

The asphalt binder used in the Superpave mixture was an unmodified PG 64-22 obtained from the Paulsboro, New Jersey terminal of the Citgo asphalt refining company. An extensive testing program was performed to characterize the rheological properties of the binder over a wide range of temperatures using both conventional and Superpave tests. Table A.2 summarizes AASHTO MP1 (1998) grading data for the binder obtained

from the manufacturer's certification report (Citgo 1998). Mixing and compaction temperatures are presented in Table A.3 (Citgo 1998).

### Mix Design

The optimum binder content for the MD 12.5 mm mixture was determined using sequential trial batches to estimate the design asphalt content. Specimens were fabricated using the Maryland State Highway Administration (MSHA) provided aggregate gradations, adjusted with additional minus 0.075 mm material to represent plant production. Using an initial trial asphalt content estimated from the preliminary MSHA design, two specimens were then compacted in the Superpave gyratory compactor to 174 gyrations and average volumetric properties were calculated for a design level of 109 gyrations. From these compacted specimens, the optimum asphalt content and volumetric properties at the optimum asphalt content were estimated using the method described in Asphalt Institute Publication SP-2 (Asphalt Institute 1996). If the estimated optimum asphalt content differed from the trial asphalt content by more than 0.3 percent, the estimated optimum asphalt content was then used as the trial asphalt content of a second iteration of the procedure; however, this mix required only one iteration. Table A.4 summarizes the results of the iterative verification process. The final design and volumetric properties for the mixture is presented in Tables A.5. Figures 3.2 and A.1 present gradation and gyratory compaction data for the 12.5 mm mixture.

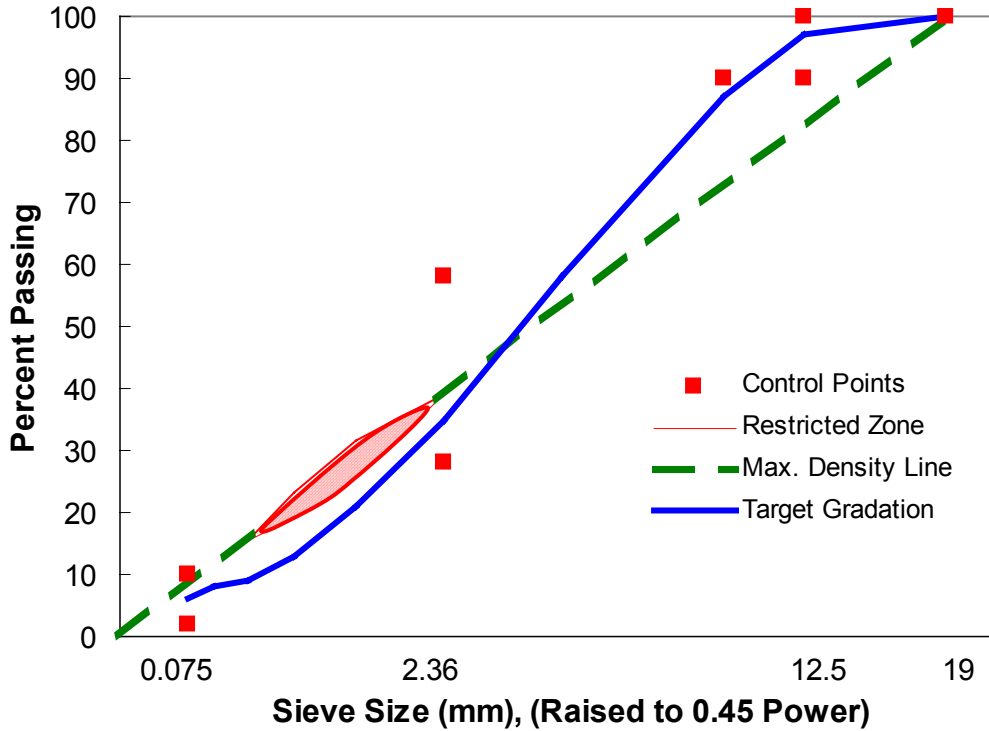


Figure 3.2. Gradation Chart for MD 12.5 mm Superpave mix

The final design of the mixture meets all of the current Superpave criteria except the requirement on the filler to effective asphalt content ratio. The design value of 1.3 exceeds the current Superpave maximum limit of 1.2. Guidance recently issued by the Superpave Lead States recommends that the upper limit for the filler to effective asphalt content ratio be increased to 1.6, and it is likely that AASHTO MP2 will be modified in the future to increase the upper limit to 1.6 (McGennis 1999).

### 3.2.2 Specimen Preparation

Based on an extensive specimen geometry study for tests in tension, the 75x150 mm geometry yielded the best strain and air void distribution and thus was selected for use in this research. More details about the study are presented in Chapter 4. The specimen was obtained after coring and cutting from a 150x175 mm Superpave gyratory-

compacted specimen. Procedures and protocols for sieving, batching, mixing, compacting, cutting and coring are provided in Appendix A. Pictures of machines and equipment are provided in Appendix B (Figures B.1 to B.3).

After measurement of air voids, which should be  $4.0 \pm 0.5$  % (Chapter 4), the specimen is stored in a Zip-Loc bag inside a closed cabinet at room temperature to minimize aging. Shelf life is limited to less than two weeks. Before testing, the specimen is placed in a gluing gig where it is glued to end plates while ensuring proper alignment. Step-by-step procedures for gluing and detaching the specimens from the end plates and cleaning them are also presented in Appendix A.

A specimen was not to be tested before 24 hours have elapsed from time of gluing. Moreover, the specimen is kept inside the environmental chamber, where the temperature of the inside of a dummy specimen containing an inserted probe is monitored. Specimens were tested half an hour after thermal equilibrium was reached. Typically three replicates were tested; however, as availability of materials became a problem, two replicates were tested, with an additional one required if there was significant deviation in results from the initial two specimens.

Specimens made from NC 12.5 mm mixes were fabricated at North Carolina State University, NCSU; while specimens fabricated from the Maryland 12.5 mm mix were fabricated at Arizona State University, ASU, and later shipped to NCSU. The decision behind choosing to fabricate the Maryland specimens at ASU instead of at NCSU is attributed to the fact that research results obtained from experimental testing using the same mix will be conducted at three different labs; and hence, consistency in fabrication

becomes important. However, the fabrication protocols presented in Appendix A were still followed at ASU labs.

### ***3.3 Testing Program***

This section will provide a quick overview about the testing machines, measurement instrumentation, and data acquisition systems utilized in this research. Basic information about particular tests conducted will also be presented.

#### **3.3.1 Testing Systems**

Two testing systems were utilized in this research. Both consisted of a servo-hydraulic closed loop testing machine, 16-bit National Instruments data acquisition card, and similar LVDTs (Linear Variable Differential Transducers).

##### ***3.3.1.1 Testing Machines***

Two servo-hydraulic universal testing machines were used. The first one was an MTS-810 testing system with a 100 kN capacity; while the other was a UTM-25 having a 25 kN capacity and manufactured by IPC, Industrial Process Controls in Australia. Both machines were capable of applying load over a wide range of frequencies (from 0.1 to 20 Hz) and loading rates in both displacement and load control at temperatures ranging from -10°C up to 40°C. The MTS machine had a function generator, micro-profiler, capable of producing the required testing waveforms efficiently; while the UTM was fully computer controlled. The two machines were calibrated against each other by testing an aluminum specimen in frequency sweep using the same types of LVDTs. Pictures of the testing setups are presented in Figures B.5 and B.6.

### *3.3.1.2 Temperature Control*

The temperature control system of the MTS utilized nitrogen liquid for cooling; while the UTM's was refrigeration-based. Both utilized heating elements for achieving high temperatures. Both temperature control systems were able to provide temperatures required for most of the testing (-10°C to 40°C). Some tests were done at -20 and -30°C; those temperatures were only achieved by the MTS testing system. The **same** asphalt dummy specimen with a temperature probe inserted in it was used with both machines to ensure consistency in testing temperature.

### *3.3.1.3 Measurement System*

The measurement system for both testing systems were fully computer controlled and capable of measuring and recording a minimum of 16 channels simultaneously. These channels were assigned to various sensors. Of these 16 channels, 12 were dedicated to sample deformation measurements (four for radial and eight for vertical – four each for two different gage lengths). The other four channels were used for the load cell, temperature sensor, pressure sensor, and the actuator LVDT.

### Data Acquisition

For data acquisition, a 16-bit National Instruments board was used in both systems. Data acquisition programs were prepared using LabView software for data collection and analysis. The rate of data acquisition for sinusoidal loading was 100 data points per cycle. The data acquisition rate for the constant strain rate test varied depending on the rate, but was at least 5 points per second for the slowest rates.

### Deflection Measurement

The values of vertical and radial deformation shall be measured with linear variable differential transformers (LVDTs).

The GTX 5000 spring loaded LVDTs were used to measure radial deformations. Those LVDTs are used to maintain positive contact with the specimen throughout the loading period. Four LVDTs were spaced 90 degrees apart along the circumference and at mid-height of the specimen.

As for the measurement of vertical deflection, both GTX 5000 and CD 100 LVDTs were used, depending on the type of test. Four LVDTs were used to measure deflections for a specific gage length, either 75 or 100 mm; this is referred to as the primary gage length. Two other LVDTs were used to measure deflections for a different gage length, which is referred to as the secondary gage length. This allows for the detection of the instance of localization. All LVDTs were placed to measure deflections in the mid-portion of the specimen. The LVDTs are attached to the specimen using guided mounts attached to targets glued to the specimen surface.

### Load Measurement

Loads are measured using electronic load cells. The MTS is equipped with 22,000 and 2,500 lb. load cells; while the UTM is equipped with a 25 kN (5,000 lb.) load cell. Appendix C discusses the issues of measurement instrumentation in extensive detail.

### 3.3.2 Test Methods

Tests conducted in this research include complex modulus ( $E^*$ ) testing, constant crosshead rate testing, creep, in addition to repetitive creep and recovery tests. All tests were done in both machines, but the repetitive creep and recovery tests were conducted in the MTS machine due to better control of the zero load during recovery.

#### 3.3.2.1 Complex Modulus Test

The complex modulus test is conducted in stress-control within the linear viscoelastic range. This test is used to obtain a viscoelastic fingerprint of the specimen being tested and to determine the shift factors for the undamaged state by constructing a dynamic modulus mastercurve. Sinusoidal loading in tension and compression sufficient to produce total strain amplitude of about 70 micro-strains is applied at six different frequencies. Limiting the microstrains to 70 ensures linear viscoelastic behavior (more study needs to be done to verify this assumption, as explained in later chapters).

The testing commences with 10 Hz preconditioning loads and the rest of the frequencies are then applied from the fastest to the slowest. The load amplitude is adjusted based on the material stiffness, temperature, and frequency to keep the strain response within the linear viscoelastic range. After each frequency, a five-minute rest period is allowed for specimen recovery before the next loading block is applied. Using tension and compression with mean stress of zero minimizes the accumulated strain at the end of cycling, which in turn minimizes the possibility of damage and needed rest period between frequencies. For mastercurve construction, tests were conducted at four temperatures  $-10$ ,  $5$ ,  $25$  and  $40^\circ\text{C}$ . Testing conditions for the complex modulus test are summarized in Table 3.1.

Because the weight of the specimen and end plate become significant relative to the stiffness of the material at 40°C, accumulated compressive strain may result during the test. In such cases, the tensile load amplitude applied should be greater than the compressive, and enough rest period needs to be given for strain recovery before any subsequent testing. It is worthy noting that at 40°C, the research group noticed that when locking the ball joint to the specimen top end plate, shear stresses are being transferred to the specimen causing distortion. To prevent that, specimens that are to be tested at 40°C are connected to the locking joint at room temperature and then conditioned to the testing temperature under the controlled stress mode to eliminate the stress build-up in the specimen due to the temperature change.

Table 3.1. Complex modulus test parameters

Frequency (Hz)	Cycles	Load (kN)				Following Rest Period (sec)
		Temperature (C)				
		-10	5	25	40	
Preconditioning 10	100	+/-2.2	+/-1.5	+/-0.55	+/-0.15	300
20	200	+/-4.7	+/-3.25	+/-1.2	+/-0.35	300
10	100	+/-4.5	+/-3.0	+/-1.0	+/-0.28	300
3	100	+/-4.3	+/-2.75	+/-0.7	+/-0.15	300
1	60	+/-4.05	+/-2.35	+/-0.45	+/-0.13	300
0.3	30	+/-3.8	+/-2.05	+/-0.3	+/-0.11	300
0.1	15	+/-3.45	+/-1.55	+/-0.25	+/-0.1	300

Stress and strain data are fitted to cosine wave functions using least squares method. Dynamic modulus and phase angle are then calculated using fitted data from the last six cycles, where steady state condition is achieved. Stresses and strains for an E\* test

are shown in Figure 3.3, and results from testing are documented in Table 3.2. These relationships are as follows:

$$\sigma = \sigma_0 + \sigma_1 \cos(2\pi ft + \phi_1), \quad (3.1)$$

$$\varepsilon = \varepsilon_0 + \varepsilon_1 t + \varepsilon_2 \cos(2\pi ft + \phi_2), \quad (3.2)$$

$$|E^*| = \frac{\sigma_0}{\varepsilon_0}, \text{ and} \quad (3.3)$$

$$\phi = \phi_2 - \phi_1. \quad (3.4)$$

where  $\sigma$  and  $\varepsilon$  = stress and strain respectively,

$t$  and  $f$  = time and frequency respectively,

$\sigma_0, \sigma_1, \varepsilon_0, \varepsilon_1, \varepsilon_2, \phi_1,$  and  $\phi_2$  = regression constants, and

$|E^*|$  and  $\phi$  are dynamic modulus and phase angle respectively.

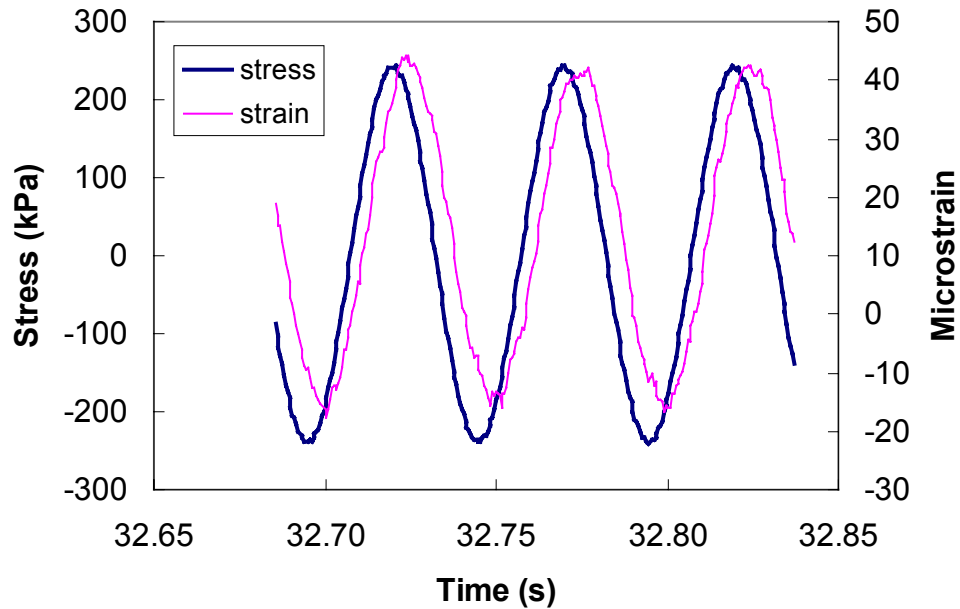


Figure 3.3 Stresses and strains from  $E^*$  testing

Table 3.2. Average values and variation coefficients of complex modulus results

Temperature	Frequency	Dynamic Modulus (Mpa)			Phase Angle (Deg)		
		Average	Std. Dev.	Coeff. Of Corr.	Average	Std. Dev.	Coeff. Of Corr.
-10	20	28228	207	0.7	2.7	1.7	62.9
	10	27598	100	0.4	4.1	1.5	36.7
	3	26008	173	0.7	5.3	1.6	29.4
	1	24295	15	0.1	6.4	2.3	35.4
	0.3	22602	15	0.1	7.6	1.8	24.2
	0.1	20720	377	1.8	8.6	1.8	21.4
5	20	19722	2226	11.3	8.2	1.5	18.3
	10	18483	2039	11.0	10.2	1.4	13.6
	3	16010	1781	11.1	12.7	2.2	17.2
	1	13826	1594	11.5	15.0	2.1	14.1
	0.3	11411	1357	11.9	17.7	1.8	10.1
	0.1	9364	1329	14.2	21.5	2.9	13.6
25	20	7685	955	12.4	24.8	1.5	6.1
	10	6399	875	13.7	28.1	1.7	6.0
	3	4299	676	15.7	33.9	1.5	4.5
	1	2873	481	16.7	38.1	1.1	2.8
	0.3	1760	327	18.6	41.5	1.2	2.9
	0.1	1117	216	19.3	42.8	1.3	3.1
40	20	1951	234	12.0	40.3	5.5	13.7
	10	1406	161	11.5	45.2	1.2	2.7
	3	841	113	13.5	43.9	2.9	6.5
	1	539	76	14.1	41.0	3.9	9.5
	0.3	358	51	14.3	36.5	2.2	6.0
	0.1	275	68	24.8	32.4	3.4	10.4

### 3.3.2.2 Constant Crosshead Rate Tests

The constant crosshead rate test is also known as a monotonic test and the two terms are used interchangeably. Constant crosshead rate tests were conducted in tension mode till failure of the specimen at different crosshead rates. Testing temperatures varied from -30°C to 40°C. Instead of testing several replicates for each condition, additional conditions were tested. This strategy deemed to be preferable for proving the validity of the time-temperature superposition principle. The strain rates at each temperature were selected based on specific conditions mandated by the procedure followed in proving the

time-temperature principle. The procedure adopted for selecting the strain rates is presented in Chapter 6. The constant crosshead testing conditions are presented in Table 3.3.

A typical stress response curve is shown in Figure 3.4 along with the on-specimen and actuator LVDT strain measurements. Due to the machine compliance, the on-specimen LVDT measurements follow a power curve up until failure while actuator strain rate is constant. More details about machine compliance and the difference between LVDT and actuator strains will be discussed thoroughly in a separate chapter.

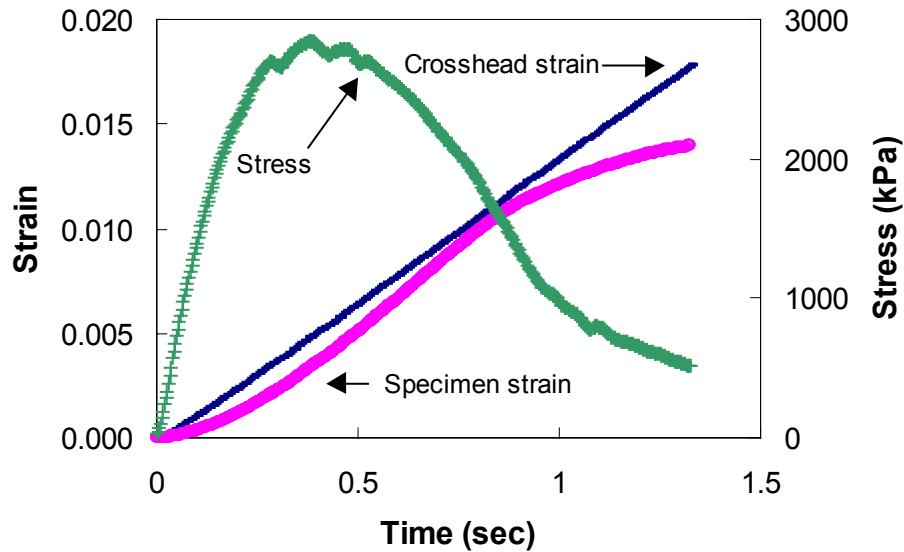


Figure 3.4. Crosshead and on-specimen 75 mm GL LVDT strains for a monotonic test conducted at 25°C and 0.0135 strains/sec

Table 3.3. Crosshead strain rates used for the monotonic tests (number of replicates in parentheses)

Temperature (°C)					
-30	-20	-10	5	25	40
0.007	0.005	0.000019	0.00001	0.0005 (3)	0.0009
0.01	0.01	0.0005	0.000012	0.0015	0.0078
	0.2	0.0135	0.00002	0.0045 (3)	0.07
			0.000025	0.0135 (2)	
			0.00003 (3)		
			0.000035		
			0.000056 (2)		
			0.0005		
			0.008		

### 3.3.2.3 Creep Compliance Test

In the creep compliance test a constant load is applied from zero at a very fast rate and held constant for a specific period of time usually not more than 100 seconds to stay within the linear viscoelastic range. The creep compliance is calculated using the quasi-elastic method to approximate the linear viscoelastic convolution integral (Kim et al. 1995):

$$D(t) = \frac{\varepsilon(t)}{\sigma(t)} \quad (3.5)$$

where  $D(t)$  is the creep compliance,  $\varepsilon(t)$  is the strain, and  $\sigma(t)$  is the applied stress. The appropriate load level for creep compliance testing is determined by testing a specimen with increasing load levels, each of which is followed by a low magnitude reference load to determine the linear viscoelastic range. This procedure is described further by McGraw

(2000). Figures 3.5 and 3.6, (courtesy of Daniel 2001), show the stress and strain response from a creep test and a typical creep compliance curve respectively.

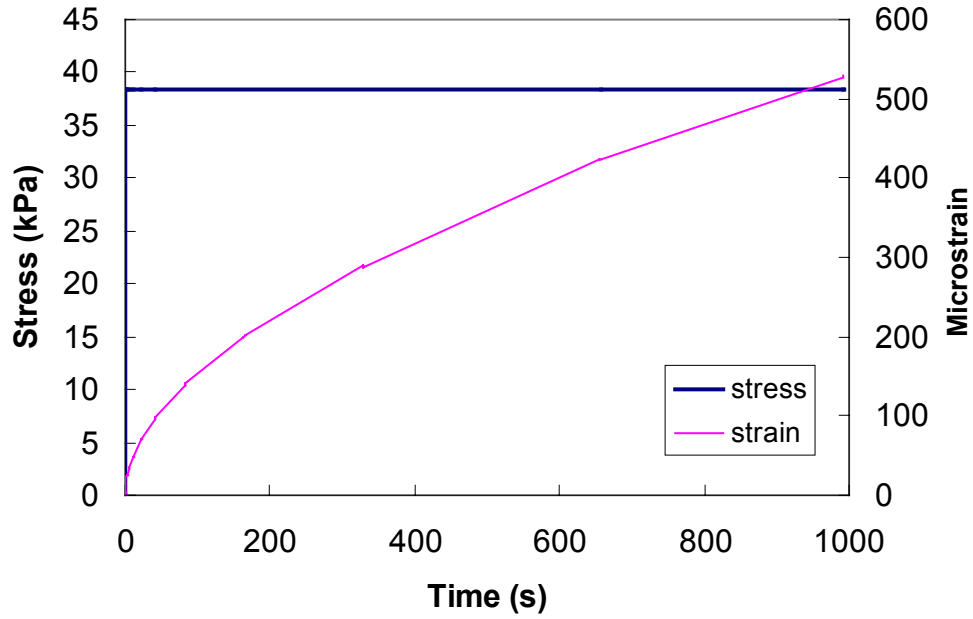


Figure 3.5 Stress and strain response for a creep test (Daniel 2001)

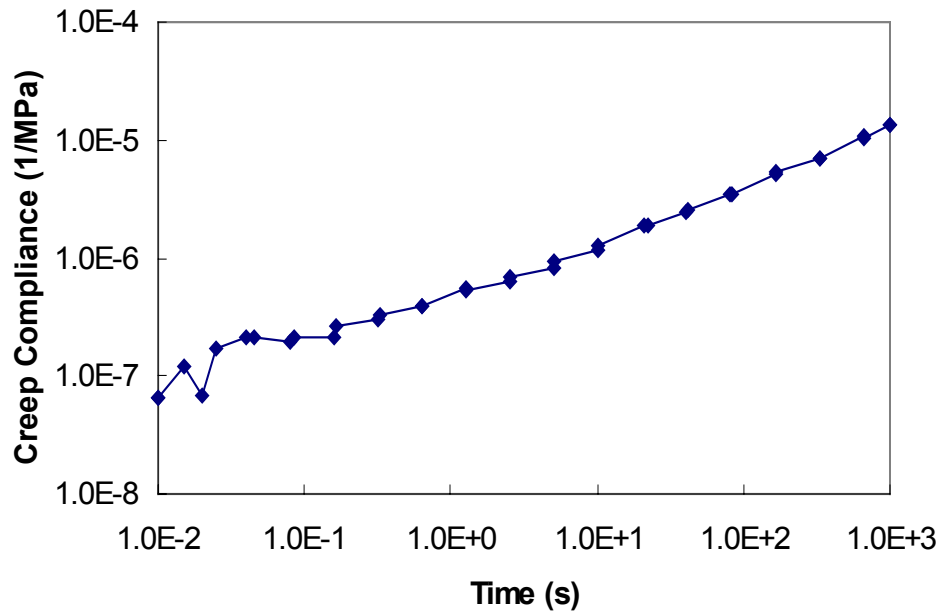


Figure 3.6. Typical creep compliance curve (Daniel 2001)

#### *3.3.2.4 Repetitive Creep and Recovery Tests*

The repetitive creep and recovery test stems from the creep compliance test, where several cycles of creep loading blocks are applied in between which rest periods are programmed. In this research the repetitive creep and recovery tests are applied in tension up to the failure of the specimen; and are exclusively used for the separation of strain components of the strain response, which is needed for the characterization of viscoplastic behavior. Details about the creep load amplitude and duration for each cycle in addition to the subsequent rest period duration are documented in Chapter 7.

## 4 Specimen Geometry Study

### 4.1 Introduction

Reliable material characterization and performance prediction testing of asphalt concrete requires specimens that can be treated as statistically homogeneous and representative of the material being tested. The recent development of Superpave Gyrotory Compactor (SGC) and its acceptance at state highway agencies make it important to develop the testing test protocols for the material characterization model based on SGC compacted specimens. The focus of this chapter is to select the proper SGC specimen geometry that can be used for tensile testing.

The specimen selected for material characterization testing should be representative of the material being tested. Material properties, most importantly air voids, should be consistent throughout. Moreover, material responses under mechanical tests should be consistent and independent of aggregate size and specimen boundary conditions. In that sense, if the representative volume element requirements (RVE) are to be followed (Superpave Models Team 1999), then according to ASTM D-3497 (1985):

- The minimum ratio of maximum aggregate size to diameter should be 1:4, and
- The minimum ratio of diameter to height should be 1:2.

Since the maximum aggregate size of most mixes is up to 19 mm, the minimum specimen diameter would have to be 75 mm with a corresponding height of 150 mm. An alternative geometry is 100 mm diameter and 150 mm height. The latter geometry has been selected for compression testing; therefore, there is a great advantage in using it for tension testing since that will standardize the geometry used in all kinds of testing.

However, the diameter to height ratio is 1.5, which violates the RVE condition. If a ratio of 2 is to be met, then the height will have to be 200 mm. Since a specimen with a height of 200 mm can not be fabricated monolithically using the Superpave Gyrotory Compactor, such a specimen would require gluing of specimens to each other (stacking), which could be problematic in tension testing.

Based on the presented discussion, it was apparent that more study should be done before a decision on the appropriate geometry can be made. Issues that have to be considered are:

- Air voids distribution inside specimens compacted by the Superpave Gyrotory Compactor (SGC).
- Effect of glued end plates on the uniformity of stress-strain states inside the specimen (End effect).
- Effect of geometry (diameter and height to diameter ratio) and gage length on material responses (values and consistency) from mechanical tests.

## ***4.2 Specimen Sizes Studied***

### **4.2.1 Specimens for Air Void Distribution Study**

Both literature and experience have shown that specimens compacted using gyrotory compactors tend to have non-uniform air void distribution both along the diameter and height (Harvey et. al 1994). To obtain a uniform air void distribution within a specimen for testing, it will have to be cored from a larger compacted specimen with the top and bottom sections cut off.

A brief preliminary study was done on 75-mm diameter cylinders cored from 100 and 150-mm diameter specimens to compare their air void distribution. The study revealed that in the case of 100 mm compacted specimens, sections in the middle of the 75-mm core had higher air void content than those at the top and bottom. This was opposite to the distribution found in 75-mm diameter cores from 150 mm diameter specimens.

This finding and the fact that the SGC had been originally designed for compacting 150-mm diameter specimens suggest that 100-mm diameter specimens are not being compacted as effectively as those with 150 mm diameter. In order to get better compaction using the 100-mm mold, the following modifications may have to be made to the current compaction method:

- The angle of gyration, set to 1.25 degrees currently, needs to be increased since that will lead to higher shear stresses and consequently a greater depth to which compaction is effective.
- The compaction pressure, set to 600 kPa, needs to be increased.

Since the main objective of this study is to identify proper sample geometry for tension testing using the current Superpave specifications, it was decided to prepare 150-mm diameter specimens for further analysis. This is especially advantageous for DOT s, since their labs already fabricate 150-mm diameter specimens for the Superpave volumetric mix design.

#### *4.2.1.1 150 x 175 mm Specimens*

In all, twenty one specimens with 150-mm diameter, 175-mm height were prepared. For this geometry, sections used for testing were 75-mm diameter and 150-mm

high, and 100-mm diameter and 150-mm high obtained after coring and cutting the original specimen. Eighteen of the twenty one specimens were cored to 75 mm diameter. Twelve of those were prepared for six different masses of mix, and the other six were prepared at the target mass (yielding 4% air void content for the 75 x 150 core). The last three specimens were cored to 100-mm diameter for 4% air voids in the 100x150 core.

#### *4.2.1.2 150 x 140 mm Specimens*

Since not all compactors have the ability to compact 175-mm high specimens, another geometry of 150-mm diameter and 140-mm height was investigated. For this purpose, nine specimens were prepared. The section proposed to be used for testing in this geometry will be 75-mm in diameter and 115 mm in height and obtained by coring the original specimen and cutting 12.5 mm off of the top and bottom edges.

#### **4.2.2 Specimens for Mechanical Tests and End Effect Study**

For mechanical tests, end-effect analysis and gage length study, four geometries corresponding to two diameters and two height-to-diameter ratios (H/D) were used. The geometries were 75x150 and 100x150 obtained from 150x175 SGC specimens. Another geometry used was 100x200. Since the Superpave Gyratory Compactor can not accommodate 200-mm height, the specimen was fabricated by gluing two 100-mm diameter, 25 mm thick sections to the top and bottom of a 100x150 specimen (stacking). The fourth geometry was 75x115 obtained from 150x140 mm SGC specimen. Figure B.7. is a schematic showing how specimens for testing were obtained from SGC specimens.

### ***4.3 Materials and Specimen Fabrication***

#### **4.3.1 Materials**

All specimens used in the study were prepared from the North Carolina 12.5 mm Superpave mix.

#### **4.3.2 Compaction**

All specimens were compacted using the Australian Superpave Gyratory compactor, ServoPac. It is a servo-controlled compactor that applies a static compressive vertical force, while simultaneously applying a gyratory motion to the cylindrical mold. The compactor settings used in this study were in accordance with Superpave specifications.

Due to the height limitation of the mold, a tapered collar was fabricated to extend the effective internal height of the mold to accommodate mixes required to prepare 150-mm diameter, 175-mm high specimens (Figure B.1). However, even with the collar, the mold could not contain all the mix if it was to be poured into the mold all at once. Several techniques were adopted to fit the mix in the mold:

1. Compacting in three lifts: In this technique, a quarter of the mix is introduced into the mold and compacted in five gyrations. Then, a second quarter is introduced into the mold and compacted for twenty gyrations. Finally, the rest of the mix is introduced into the mold and compacted to height.
2. Rodding: In this technique, half of the mix is introduced into the mold, and the surface is rodded twenty times. Then, the second half is introduced and compacted to height.

For some specimens, 60% of the mix is first introduced, while for others 40% is first introduced.

3. Introduction of mix in four quarters: In this technique, the mix is introduced in four quarters into the mold and then compacted to the required height. After each quarter is poured, a spatula is used to scrape the sides of the mold and level the surface. Doing so creates more space for the succeeding quarter.

The study on air void distribution, which is detailed later, revealed that compacting in three lifts yields a large gradient in air void distribution along the height, with high air void content at the interfaces. Such non-uniformity would create weak zones at the interfaces; hence, large deformation and probably misleading failure in the specimen could occur when subjected to tensile load. Moreover, if LVDTs were mounted to the middle section of the specimen, this deformation may occur unrecorded. In addition, this technique requires that the compactor be setup differently for each lift, and the mold taken out twice while compacting. This procedure consumes appreciable time while compacting, during which the temperature of the mix drops significantly. For these reasons, this technique was dropped from the study.

The second technique yielded a better gradient although there was a high air void content at the rodded interface. The third technique yielded a gradient similar to the second with reduced peaks of air void content at the interfaces. Therefore, the third technique was adopted for incorporation in the finalized compaction procedure for the 175-mm high specimens.

## 4.4 Air Void Distribution Study

### 4.4.1 Air Void Measurement Techniques

The procedure used for calculating air voids of asphalt concrete specimens is ASTM D3203, where:

$$AV(\%) = 1 - \frac{\text{Bulk Specific Gravity}}{\text{Maximum Theoretical Specific Gravity}} \quad (4.1)$$

Since specimens in this study have to be cored and cut, resulting sections will vary in geometry, cylinders versus disks versus rings, and in surfaces, as compacted surfaces versus cut. Figure B8 shows how the specimens were cored and cut to obtain sections used for the air void study. To obtain true distribution gradients, the effects of difference in geometry and surface on air void measurements have to be considered.

While determining the maximum specific gravity of the mix is straightforward (ASTM D2041), determining the bulk specific gravity for each section type is more complicated; different techniques will have to be used for drawing different comparisons. The following is a description and brief evaluation of each of the three techniques used in the study. Detailed step-by-step procedures for each technique are documented in Appendix A. The effect of each technique on air void measurements is discussed in the following section.

#### 4.4.1.1 Saturated Surface-Dry (SSD)

This technique is the one most commonly used. According to ASTM D2726, this method is valid for specimens that do not have a porous structure or inter-connecting voids or absorb more than 2% of water by volume or both. The bulk specific gravity can

be determined by measuring the mass of the specimen in dry condition, while submerged in water, and in its SSD condition (Equation 4.2):

$$G_{sb} = \frac{W_a}{(W_{ssd} - W_w)} \quad (4.2)$$

where  $W_a$  is the weight in air,  $W_{ssd}$  is the weight saturated surface dry and  $W_w$  is the weight submerged in water.

While this method is fast and simple, it has a major drawback when used for sections with significant surface pores. When the specimen is submerged in the water tank, pores at the surface will not be considered as air voids because they are connected to the water medium. The SSD method proves handy in measuring air voids of cylinders and disks with cut surfaces.

#### 4.4.1.2 Parafilm

This technique is usually used for specimens with a porous structure. According to ASTM D1188, asphalt concrete specimens have to be covered with Parafilm membrane to make the specimen impermeable to water (Figure B9). The bulk specific gravity is determined after measuring the mass of specimen in its dry condition, dry while wrapped with Parafilm, and submerged in water while wrapped in Parafilm. The following equation is used to determine the bulk specific gravity when wrapped with Parafilm:

$$G_{sb} = \frac{W_a}{\left[ (W_{awp} - W_{wwp}) - \frac{(W_{awp} - W_a)}{SG_p} \right]} \quad (4.3)$$

where  $W_a$  is the weight of the unsealed specimen in air,  $W_{awp}$  is the weight of the specimen wrapped in air,  $W_{wwp}$  is the weight of the specimen wrapped and submerged in

water, and  $SG_p$  is the specific gravity of the wrapping medium. When the wrapping medium is Parafilm  $SG_p$  is 0.9.

Since the surface is sealed, this method is advantageous when used to determine air void contents of sections having as-compacted surfaces as well as for ring sections. The disadvantage of this method lies in the case where there are large surface intrusions and irregularities; the Parafilm membrane will bridge over those pores and thus they will apparently be regarded as air voids. There are special techniques to try to force the membrane to line these surfaces as much as possible, but the bridging effect can not be completely eliminated. In some instances, the membrane is torn allowing water to penetrate inside the specimen, and thus, lower the measured air void content. In general, this method can cause poor repeatability if extra care is not exercised because measurements obtained are highly sensitive to the wrapping technique.

#### *4.4.1.3 Corelok Vacuum Sealing*

The Corelok Vacuum sealing machine, manufactured by Instrotek, utilizes an automatic vacuum chamber with specially designed puncture resistant, resilient bags to seal the specimen's surface against water penetration. The specimen, up to 150-mm in diameter, is put in a plastic bag and then placed in the vacuum chamber. After vacuum is applied and the plastic bag sealed, air is allowed back in causing the plastic membrane to collapse on itself and line the specimen's surface.

The advantage of this method is that the membrane lines the outer surface closely and completely seals the specimen. Since there is minimal operator effort involved, this method is fairly repeatable. The major drawback of this method with the current bag sizes used is that it is not efficient in sealing small disks, rings and specimens of large

dimensions. More experimentation needs to be done regarding the choice of bag size used for each type of those sections. Equation 4.3 is used to determine the bulk specific gravity of the specimen when using the vacuum sealing method.

Expecting that the SSD method yield a lower air void content than the actual, while the Parafilm method yield a higher one, both methods were used for measuring the air void content of all the sections. In that way, the boundary limits within which the actual value lies are known. Moreover, any problem or error encountered in an individual measurement using one method can be detected when checking against that value obtained using the other method. The Corelok method was applied to a limited number of sections towards the end of the study due to the recent availability of the device.

It is worth noting that for specimens containing moisture, both ASTM D2726 and D1188 procedures require that the specimen be placed in the oven for twenty-four hours at 110°C before measuring its mass in the dry condition. This requirement created a problem in this study, since drying will consume a considerable amount of time due to the repetitive wet coring and sawing tasks involved. Moreover, when dealing with specimens that are to be used for testing, oven drying can alter the properties of the specimens. It has been documented that drying the specimens using a 30-psi air pressure gun yields moisture contents very close to those using oven-drying (Harvey et al. 1994). This technique was evaluated for sections with as-compacted surfaces and for those with cut surfaces. On average, both types of sections had additional moisture content of 0.05% when dried by the air gun. Consequently, the air void measurements (SSD) of sections with as-compacted surfaces decreased by 0.07%, while those with cut surfaces decreased

by 0.05%. Since the difference in measurements between the two techniques is insignificant, drying with 30-psi air pressure was adopted for the study.

#### **4.4.2 Discussion of Results**

##### *4.4.2.1 Effects of Air Void Measurement Techniques*

To get a true understanding on the variation of air voids inside SGC specimens, it is imperative to study the effect of section surface and geometry on air void measurements obtained by the three techniques described earlier. The Corelok method should give the closest value to the actual because it does a better job of following the contour of surface pores and preventing water from penetrating inside. On this basis, measurements obtained using the Corelok could be used as a reference to compare SSD and Parafilm measurements. Comparisons between those methods for various sections are presented in Figure 4.1.

##### Sections with as-compacted surfaces

As seen in Figure 4.1(a), values of air void contents of whole specimens (as-compacted surfaces) fall above the line of equality indicating that Parafilm measurements are higher than those of SSD for this type of surface. Figures 4.1(b) and 4.1(c) show that the Corelok values are in between those of SSD and Parafilm, but are closer to the latter. Until the Corelok device is widely available, either the Parafilm or the SSD could be used depending on absorption and condition of the surface pores.

### Ring Sections

Again, as seen in Figure 4.1(a), the Parafilm technique yields higher air voids than SSD. This difference is greatest among all sections, because in addition to the effect of the as-compacted surface, the rings have a relatively large surface area and small thickness; and hence, allow more water penetration to internal pores. To eliminate those effects, the Parafilm method should be used when comparing air voids of ring sections to other sections of different geometries. As mentioned earlier, the Corelok method could not be accurately used to seal ring sections.

### Sections with Cored and Cut Surfaces

For those sections, values obtained by the Corelok method almost match those obtained by the SSD method (Figure 4.1(c)). This is probably due to the absence of wide gaps, interconnecting pores and irregularities that are usually the gates for water intrusion. Values obtained using the Parafilm were slightly greater than those obtained using the other methods (Figures 4.1(a) and 4.1(b)). This is probably due to the bridging effect of Parafilm over some small surface pores, which are on the other hand smoothly lined when vacuum-sealed. Therefore, when comparing between sections with cut and cored surfaces it is preferable to use the SSD method; however, when comparing those sections with sections of other surfaces or to rings it is preferable to use the Parafilm method.

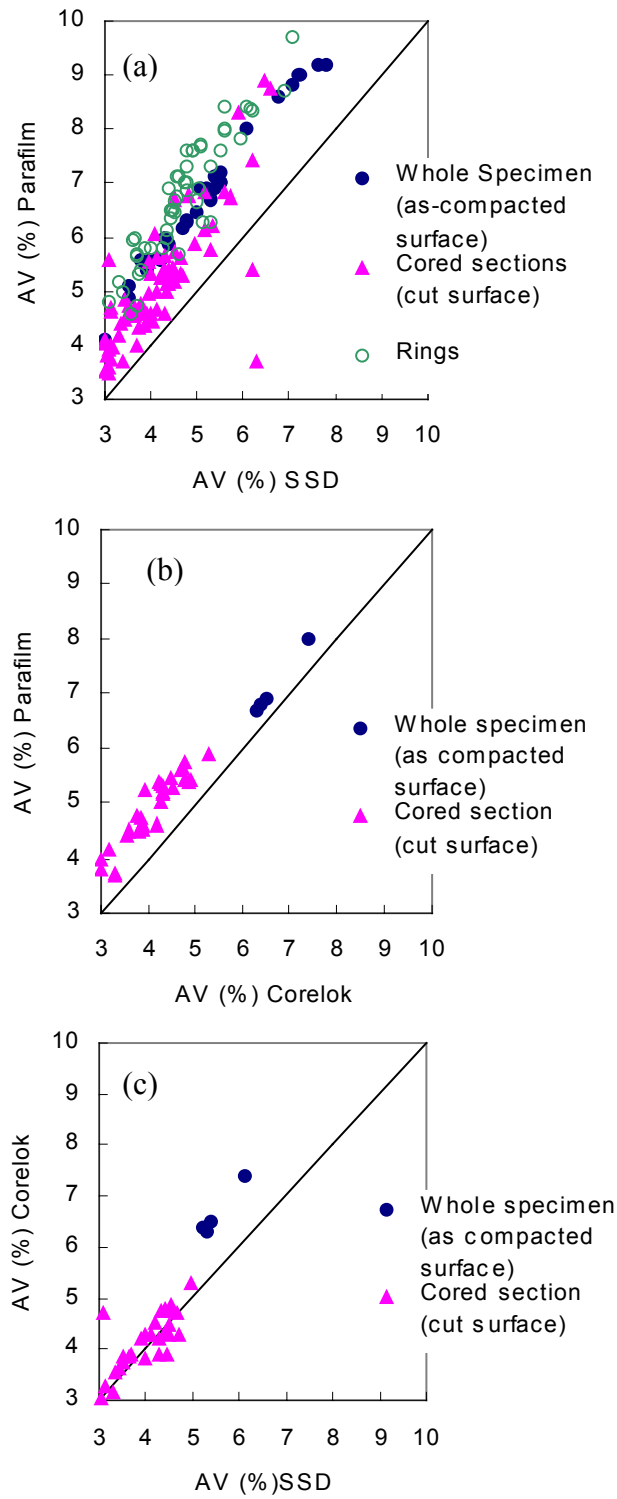


Figure 4.1. Comparison of air void measurement techniques for different sections: (a) SSD vs. Parafilm, (b) Corelok vs. Parafilm, (c) SSD vs. Corelok.

#### *4.4.2.2 Air Void Distribution in SGC Compacted Specimens*

As detailed earlier, air void content measurements were done on different cut and cored sections for each geometry to inspect air void distribution inside SGC specimens. Presented in Figures 4.2(a-c), are the values obtained based on the average for all specimens of the same geometry. It is worthy to note that there was a close match of air void content values for whole specimens of the same geometry and mass. This indicates that mixing, compaction, and air void measurement procedures were consistent throughout the study. Analysis of the results led to the following conclusions:

##### 150 x 175 mm Specimens

For this geometry, the distribution of air voids was studied based on a 75-mm core of the specimen. For specimens cored to a 100-mm diameter, only the variation along the height of the core was studied.

- The highest air void content exists in the 150 x 175 ring followed by the 150 x 150 ring, the 75 x 175 core, and then the 75 x 150 core. This supports our belief that air void content tends to be high in the areas adjacent to the mold walls and top and bottom; hence, coring and cutting is inevitable to obtain a representative volume element for testing.
- It seems that the air voids content of the 150 x 175 ring has a higher effect on the air void content of the whole specimen than the 75 x 175 core does. This is true because the former represents about 75% by volume and by mass of the whole specimen. Therefore, one should be careful when relating the air void content of the whole specimen to that of the inside core.

- The difference in air void between the 75x 150 core and the whole specimen ranges from 2.2 to 2.7%, the average being 2.5% (measured in Parafilm).

#### **Variation along the height of the 150 x 150 ring**

- The middle section has higher air void content than both the top and bottom sections. This is common to all specimens of this geometry (Figure 4.2a).
- When considering each specimen individually, there is no clear trend for the variation in air void content between the top and bottom sections. However, if the average variation for all specimens is considered, then the bottom sections appear to be more compacted.

#### **Variation along the height of the 75 x 150 core**

The top and bottom sections of the core have the highest air voids, while their adjacent sections have the least (Figures 4.2a). The difference between the air void content of the edges and their adjacent sides, around 1.5%, is appreciable and of concern. This variation is true although the top and bottom 12.5 mm edges had already been cut off from the 150 x 175 original specimen. This indicates that probably a thicker edge section should be cut off.

#### **Variation along the height of the 100 x 150 core**

The difference in air voids content between the sections is smaller than that for the 75x150 core. Except for the section adjacent to the bottom one, air voids are somewhat evenly distributed among the five sections (Figure 4.2b).

## **150 x 140 Specimens**

The same trend that appeared in 150 x 175 specimens was common to 150 x 140 specimens (Figure 4.2c). Still, air voids are high at the top and bottom and near the mold walls. The difference in air void content between the original specimen and the inside core still averages 2.5%, implying a pattern; however, this may not hold true for other geometries and mixes.

As for the variation along the height of the 75 x 115 core, the trend is similar to that of the 75 x 150 mm cored from 75 x 175 specimens. The difference in air voids between the top or bottom and its adjacent section is less than that of the 75 x 150. Hence, using a taller specimen does not provide more uniformity in the inside core of the specimen if the same thickness is cut off from top and bottom. For the 150 x 115 ring section, as seen in Figure 4.2(c), the middle section has the highest air voids, a pattern also seen in the previous geometry.

### ***4.5 End Effect Analysis (End Plate Effect)***

Specimens tested in tension must be glued to metal end plates. The glued interface restricts the horizontal movement and hence creates non-uniformity in the vertical strains. Since this effect varies from one geometry to the other; it is important to address this issue when comparing material responses of different geometries. To shed more light on how vertical strains vary along the height of a glued specimen, specimens were modeled by a 2-Dimensional finite element mesh. A finite element analysis using ABAQUS software was conducted based on a linear elastic model for three stiffness conditions:  $E^*=9000\text{Mpa}$  and  $\nu=0.2$ ,  $E^*=6000\text{Mpa}$  and  $\nu=0.3$ , and  $E^*=3500\text{Mpa}$  and  $\nu=0.35$ .

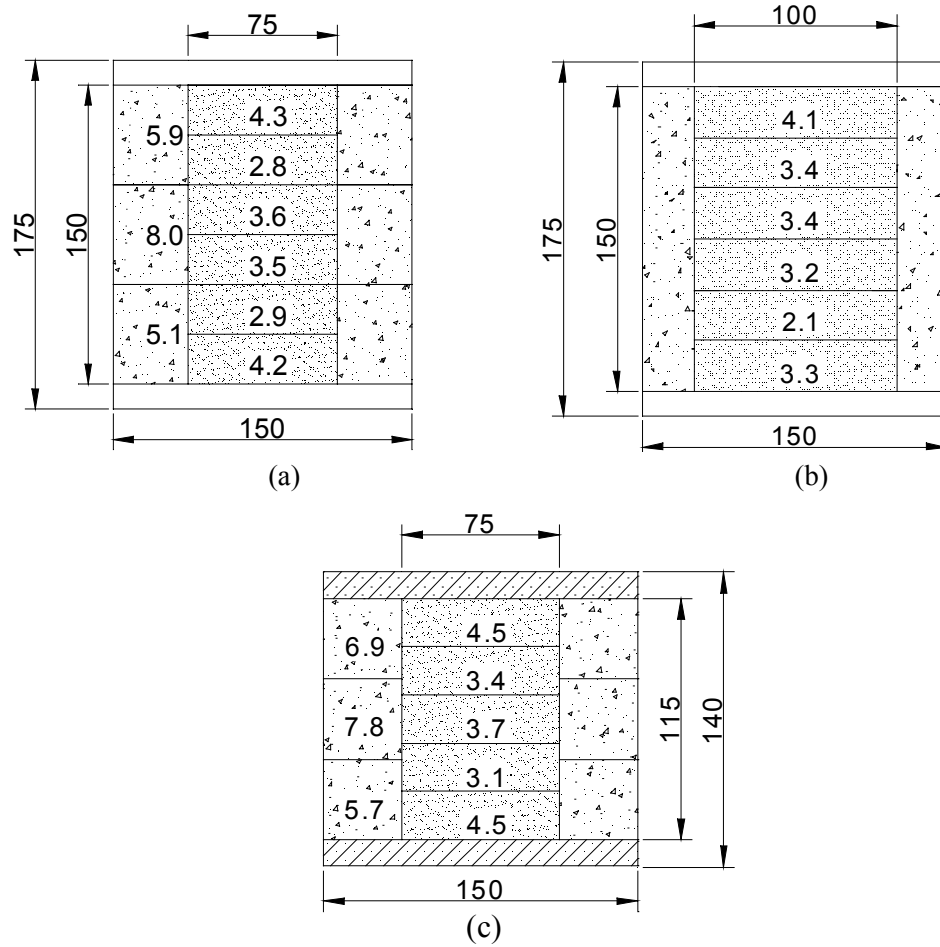


Figure 4.2. Air void variation inside: (a) 150 x 175: AV%=5.8; (b) 150 x 175: AV%=5.0 (c) 150 x 140: AV%=7.0 (Dimensions in mm, AV in % measured using the Parafilm method).

As seen from Figure 4.3, strains of a glued specimen are lower than the case of an unglued specimen (no end effect). This difference varies from one geometry to the other and is greatest for the 100x150. Only for specimens with a height to diameter ratio of 2 (100x200 and 75x150) do the strains of glued specimens reach the value of those for unglued specimens; and this occurs at the mid-height of the specimen. The glue between the stacked sections of the 100x200 does not seem to considerably affect the strain

uniformity along the height, probably because its stiffness is similar to the stiffness conditions set for the asphalt concrete in the analysis.

Considering the non-uniformity in strains, one can predict that larger gage lengths would read smaller strain values for the same specimen. Therefore, it is important that for comparing material responses of different geometries the error involved due to glue effect be similar for all. This would ensure that the difference in material response between different geometries is attributed to the effect of geometry and not to the end (glue) effect. Based on finite element analysis, the error in strain measurement due to the end effect for the chosen set of gage lengths is presented in Table 4.1.

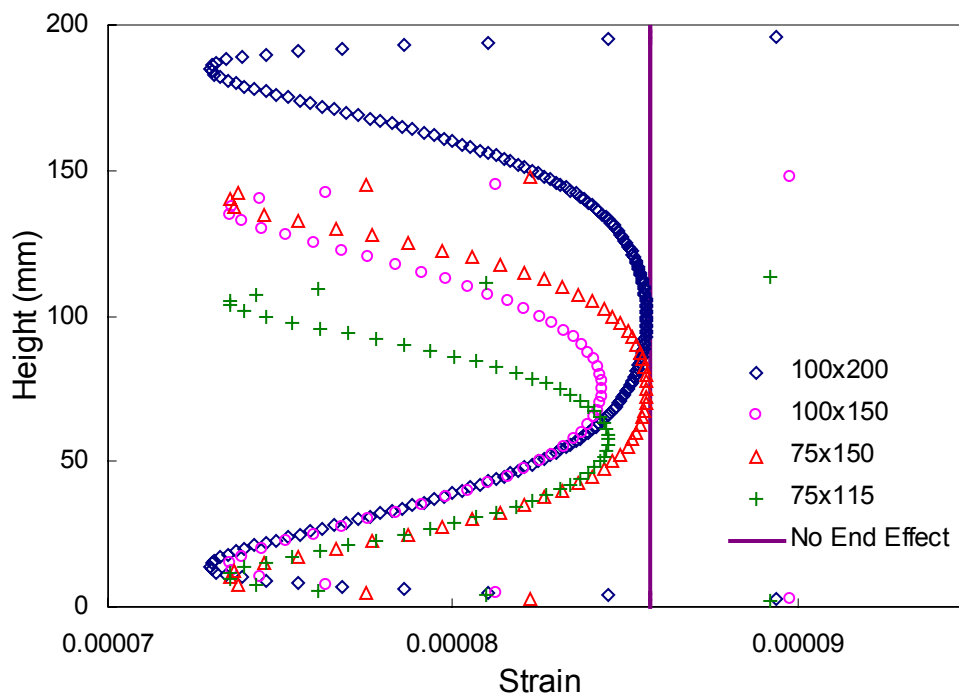


Figure 4.3. Vertical strain from FEM analysis for  $|E^*|=3500$  MPa and  $\nu=0.35$

Table 4.1 Error (%) in vertical strain due to end effect

Conditions	Geometry						
	Gage Length	75x150	100x150	Gage Length	75x115	Gage length	100x200
<b>E=3500 MPa</b>	<b>75 mm</b>	-1.1	-3.4	<b>57.5 mm</b>	-3.1	<b>90 mm</b>	-0.9
<b>v=0.35</b>	<b>50 mm</b>	-0.5	-2.4	<b>40 mm</b>	-2.2	<b>50 mm</b>	-0.3
<b>E=6000 MPa</b>	<b>75 mm</b>	-1.0	-3.0	<b>57.5 mm</b>	-2.8	<b>90 mm</b>	-0.8
<b>v=0.3</b>	<b>50 mm</b>	-0.5	-2.2	<b>40 mm</b>	-2.0	<b>50 mm</b>	-0.3
<b>E=9000 MPa</b>	<b>75 mm</b>	-0.8	-2.1	<b>57.5 mm</b>	-2.0	<b>90 mm</b>	-0.6
<b>v=0.2</b>	<b>50 mm</b>	-0.4	-1.6	<b>40 mm</b>	-1.5	<b>50 mm</b>	-0.2

The gage lengths were selected based on 2 rules of thumb: half the height, and height minus diameter. As observed from the table the error varies for different geometries, gage lengths, and stiffness conditions. As one would expect, the smaller the gage length the smaller the error. Therefore, it is advantageous to use a small gage length; on the other hand, it is also important that it be large enough to be representative of the material response.

The set of gage lengths chosen for the calculation of error from the FEM analysis were later adopted to measure strains by LVDTs from actual mechanical tests. In doing so, the comparisons between material responses of different geometries could be made with the prior knowledge of the approximate error involved due to the end effect.

It is important to keep in mind that the error as presented in Table 4.1 is calculated based on the linear elastic model assuming homogeneity and isotropy of the material. Actual error may be different because of the viscoelastic properties and heterogeneity of asphalt concrete mixtures.

#### ***4.6 Effect of Geometry and Gage Lengths on Responses from Mechanical Tests***

As noted earlier, mechanical tests were conducted to study the effect of diameter, height-to-diameter ratio, and gage length on measured material responses. For that purpose, four geometries corresponding to two diameters and two height-to-diameter ratios were selected.

##### **4.6.1 Description of Tests**

Specimens were preconditioned by applying fifty haversine loading cycles at 10 Hz and 120 kPa. After preconditioning, two mechanical tests were conducted for the four geometries (Table 4.2): a complex modulus test at different frequencies followed by a constant crosshead-rate test until failure. A rest period of two hours was given between the two tests. Only those specimens with air voids of 4 +/-0.5% were used for testing; three replicates were used for each geometry. Tests were done in the uniaxial tension mode at 20°C using the servo-hydraulic loading machine, UTM-25. Displacements were measured using eight LVDTs corresponding to two gage lengths mounted to the middle portion of each specimen (Figure 4.3(b), Table 4.3). Using four LVDTs (for each gage length) at right angles from each other minimizes the variation of strains within each specimen.

Table 4.2. Geometries used for mechanical testing

<b>H/D</b>	<b>Diameter</b>	
	75 mm	100 mm
<b>1.5</b>	75x115	100x150
<b>2</b>	75x150	100x200

Table 4.3. Gage lengths used for all geometries

	<b>75x115</b>	<b>75x150</b>	<b>100x150</b>	<b>100x200</b>
<b>Gage Length 1 (4 LVDTs)</b>	40 mm	50 mm	50 mm	50 mm
<b>Gage Length 2 (4 LVDTs)</b>	57.5 mm	75 mm	75 mm	90 mm

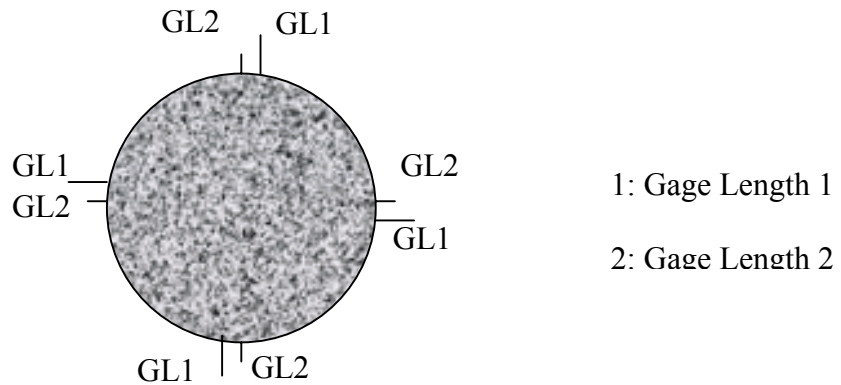


Figure 4.3(b) Positioning of LVDTs

The complex modulus test was conducted in stress control at 5 different frequencies for 100 cycles each. Stress levels were chosen so that axial deformation be limited to about 50 micro-strains (Table 4.4); this would ensure that responses are within the linear viscoelastic range. Five minutes of rest period were given between subsequent frequency applications to allow for material relaxation.

Table 4.4. Frequencies and stress levels for complex modulus testing

Frequency (Hz)	Stress Level (kPa)
20	360
10	340
5	320
2	260
1	240

Only measurements from the last 6 cycles of each frequency were used for the calculation of the dynamic modulus and phase angle. The measured stress and strain data were smoothed by fitting the following functions:

$$\text{Stress: } \sigma = \sigma_0 + \sigma_1 \cos(2\pi ft + \phi),$$

$$\text{Strain: } \varepsilon = \varepsilon_0 + \varepsilon_1 t + \varepsilon_2 \cos(2\pi ft + \phi_2),$$

where:  $f$  is the frequency,

$t$  is the time, and

$\sigma_0$ ,  $\sigma_1$ ,  $\varepsilon_0$ ,  $\varepsilon_1$ ,  $\varepsilon_2$ ,  $\phi$  and  $\phi_2$  are parameters determined by regression.

As for the constant crosshead-rate test, the loading rate was 0.0004 units per second. Two hours of rest period were given after the complex modulus test to allow for sufficient material relaxation before the subsequent test was performed.

#### 4.6.2 Data Analysis

To study the effect of diameter, height to diameter ratio and gage length on material responses, a graphical analysis was conducted on the average of these responses for the different conditions (geometry, gage length). A statistical analysis followed the

graphical analysis to study the significance of any observed differences or trends for the average material responses. The parameters studied were:

- Complex modulus test (for 5 frequencies):
  - Dynamic modulus,  $|E^*|$
  - Phase angle,  $\phi$
- Constant crosshead-rate test:
  - Slope of linear pre-peak portion of stress/strain curve
  - Peak stress
  - Strain at Peak Stress
  - Stress at 1% strain
  - Stress at 2.5 % strain

It is worth noting that in the constant crosshead-rate test, it is the overall pattern of the stress/strain curve that is important in graphically analyzing any effects due to geometry or gage length. The parameters listed above were used to aid in comparing the curves statistically.

Since the specimen air void content varied from one test specimen to the other, it was necessary to study any effect the air void content could have on material responses. For the complex modulus test, it was observed that the dynamic modulus decreased with increasing air void content, while the phase angle was not affected. The effect on dynamic modulus was determined using linear regression at each frequency and for every geometry individually. The slope of the linear fit was then used to adjust the dynamic moduli to a common air void content of 4.0 percent.

As for the constant crosshead-rate test, the peak stress was not affected by the air void content, and hence the values were not adjusted; other parameters were also not adjusted.

#### *4.6.2.1 Graphical Analysis of Testing Results*

As mentioned earlier, the graphical analysis is a subjective graphical comparison of the average responses for different conditions.

#### Complex Modulus Test

The dynamic moduli and phase angles for the four geometries and phase angles are plotted in Figure 4.4 (57.5 mm gage length for 75x115 and 50 mm gage lengths for the other geometries). As expected,  $|E^*|$  increases with increasing frequency, while phase angle decreases. It can be observed that the average dynamic modulus of the 100x200 specimens is higher than that for the rest of the geometries. The dynamic moduli of the other geometries are comparable for low frequencies but deviate at 10 Hz and 20 Hz. The 75x150 geometry tends to have the lowest  $|E^*|$  values. As for phase angle, the 75x115 geometry has the highest values, and the 75x150 has the lowest. It is interesting to see that at 10 and 20 Hz the phase angles for all the geometries except the 75x115 match closely. Since the 75x150 and 100x150 are of particular importance, their responses are plotted in Figure 4.5. In general, the two geometries exhibit comparable responses; however,  $|E^*|$  for the 100x150 at high frequencies is higher than that for the 75x150, and the phase angle for the former at 2 and 5 Hz is higher than that for 75x150.

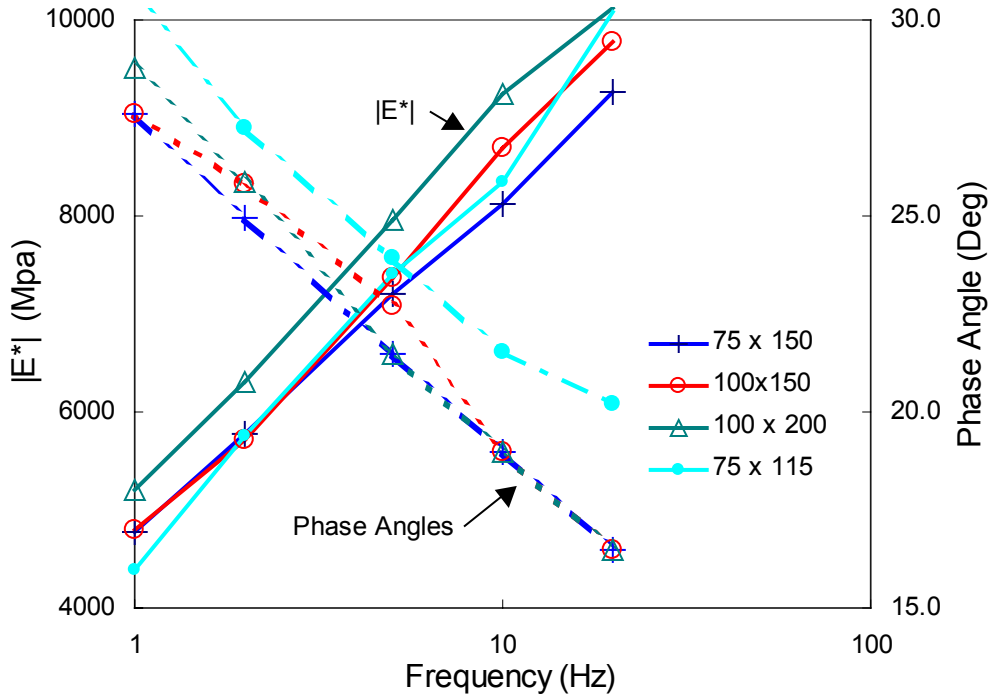


Figure 4.4. Dynamic moduli and phase angles (50 mm GL for all geometries except 75x115, 57.5 GL)

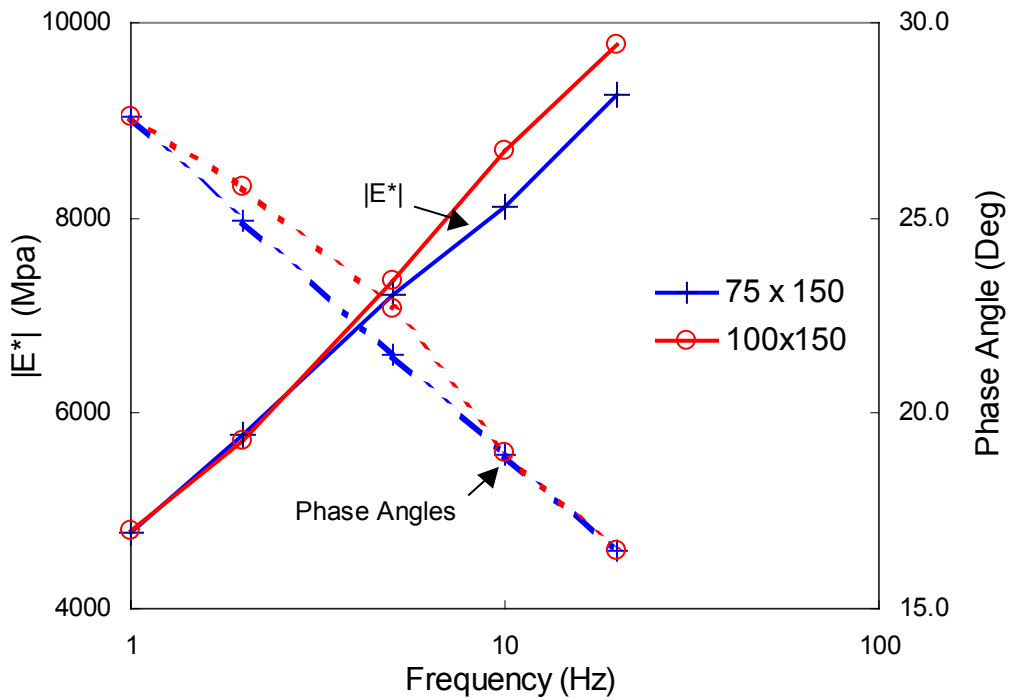


Figure 4.5.  $|E^*|$  and  $\phi$  for 75x150 and 100x150 (50 mm GL)

Referring to the finite element analysis results documented earlier, the fact that the strains for the 75x150 geometry were highest among all the geometries could explain why the actual dynamic modulus for the 75x150 is the lowest. The 100x200 geometry exhibited the highest dynamic moduli, although it had a strain distribution similar to that of the 75x150 (from FEM analysis); this may be attributed to the effect of glue between the stacked sections. It is possible that this glue interface, which lies outside the range of the LVDTs, is deforming and hence relieving the strain in the asphalt concrete in the middle of the specimen. Consequently, the LVDTs will measure strains that are lower than those in the case of monolithic specimens.

Figures 4.6 and 4.7 respectively show the effect of diameter and height-to-diameter ratio on phase angle at each frequency; while Figures 4.8 and 4.9 respectively show the effect of diameter and height-to-diameter ratio on dynamic modulus (57.5 mm gage length for 75x115 and 50 mm for the other geometries).

From these figures, it is evident that the phase angle decreases as diameter and height to diameter increase; however, this decrease is small relative to the variation between specimens, and its significance has yet to be seen from the statistical analysis. As for the dynamic modulus, it increases with increasing diameter and with increasing height to diameter ratio except at 20 Hz where it decreases with increasing height to diameter ratio. From the plots, there is an evident diameter and height to diameter effect on  $|E^*|$ , but again, whether this effect is significant or not has to be determined by statistical analysis.

### Constant Crosshead-Rate Test

It is important that the curves for stress versus strain as measured from the LVDTs for the different geometries be comparable. While this comparison is subjective, parameters that could be compared somewhat easily are the peak stress and its corresponding strain in addition to the slope of the linear pre-peak portion of the curve. The curves, based on average values of replicates, are plotted for all geometries in Figure 4.10 for the specified gage lengths. Again, since the 75x150 and 100x150 are of particular importance, their stress/strain curves are plotted together in Figure 4.11.

Comparing the curves, it can be concluded that the slopes of all the curves are comparable except for the 75x115, which exhibits low strength. The peak stresses for the 100x150 and 100x200 match closely, while those for the other geometries are far off. As for strains corresponding to the peak stresses, they match closely for all the geometries.

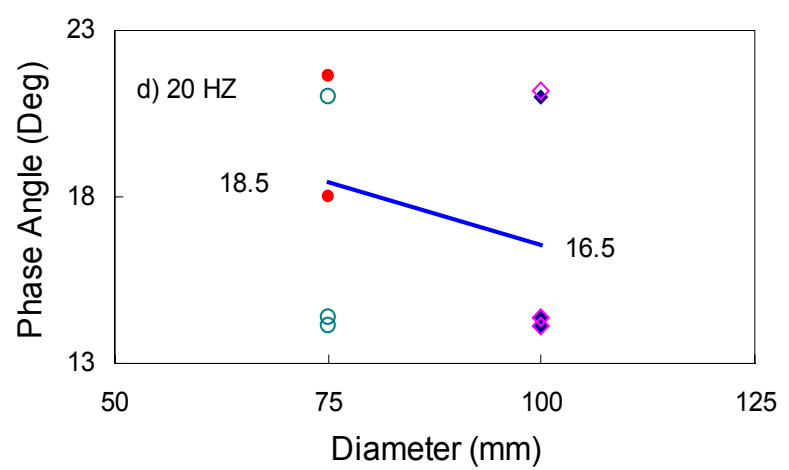
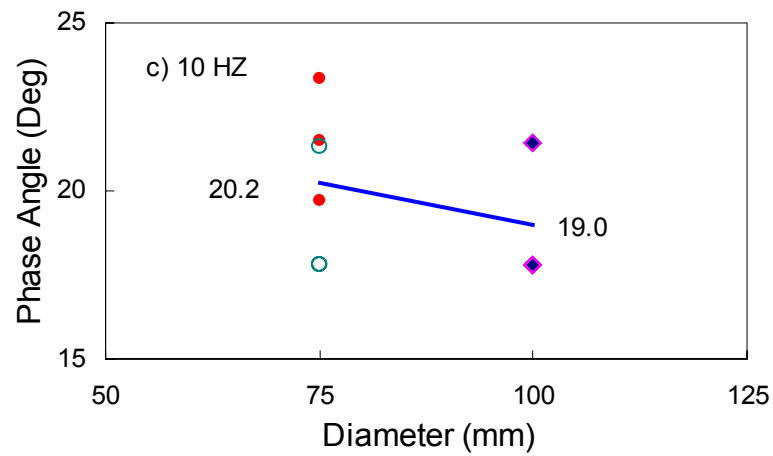
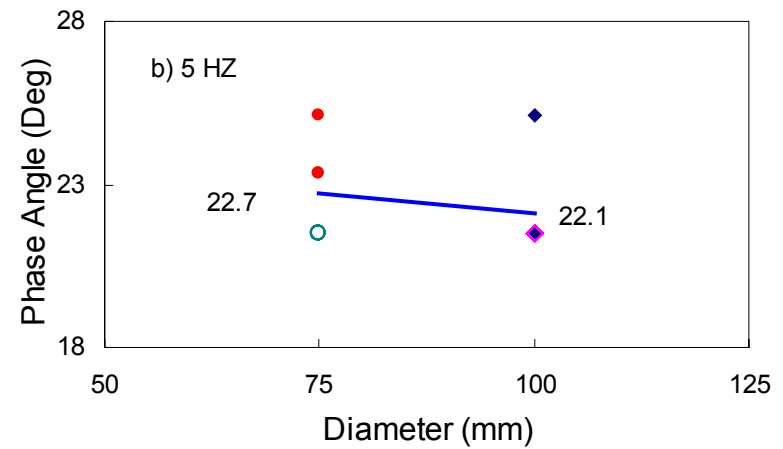
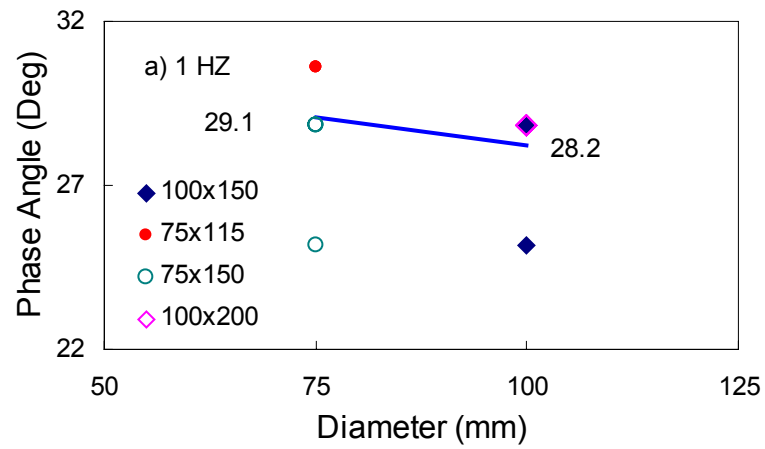
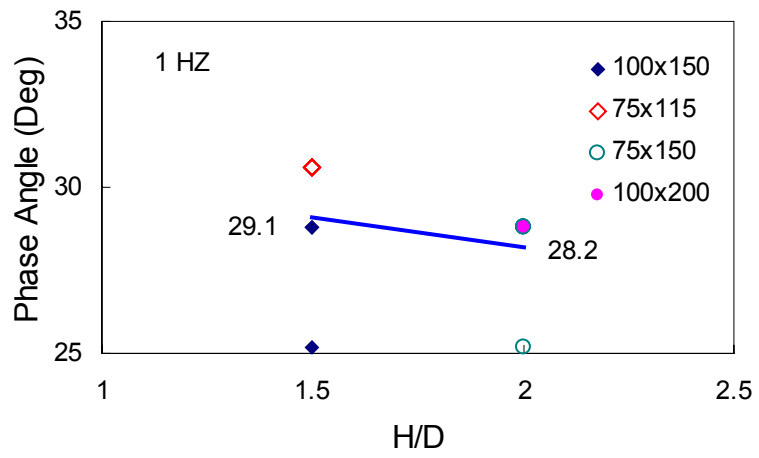
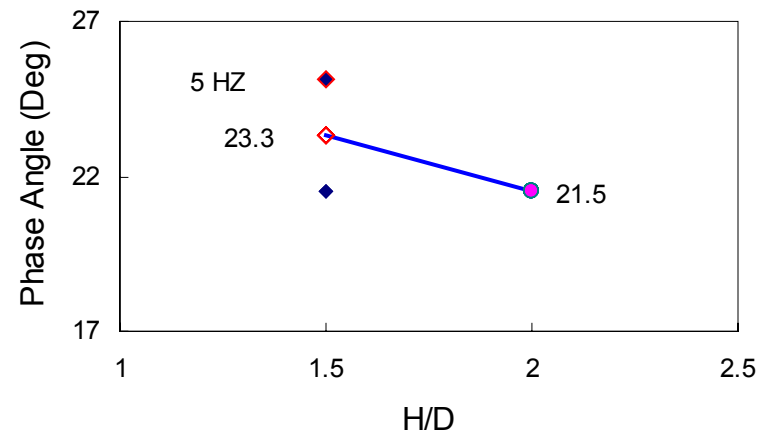


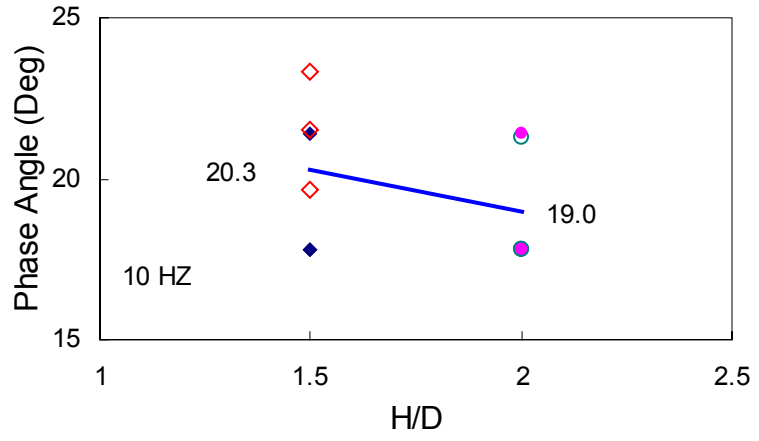
Figure 4.6. Effect of diameter on  $\phi$ : a) 1 Hz, b) 5 Hz, c) 10 Hz, d) 20 Hz



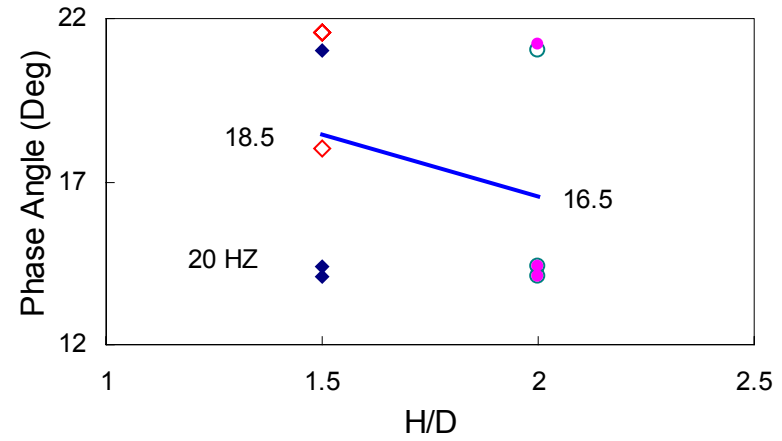
a)



b)

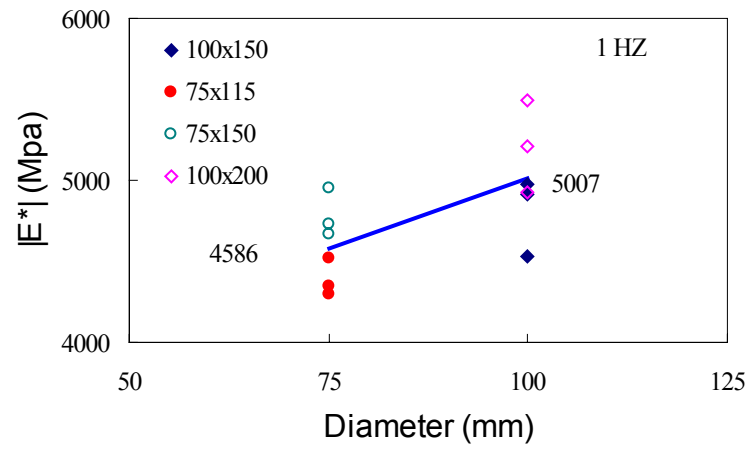


c)

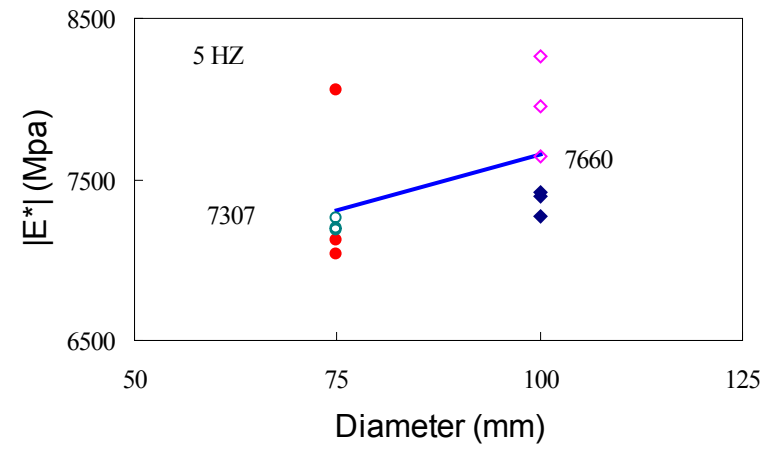


d)

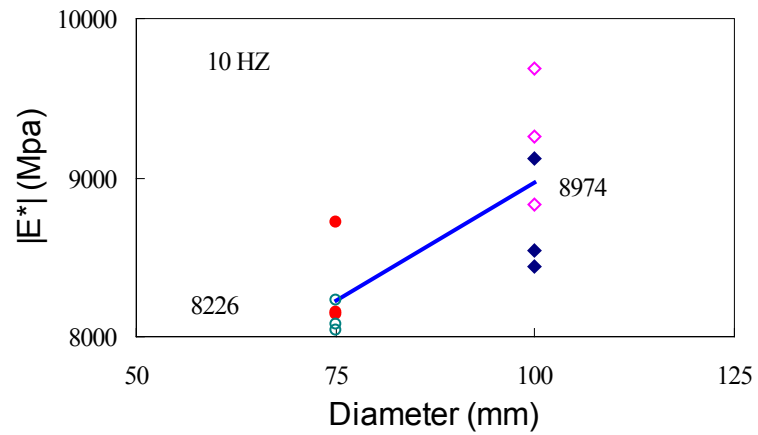
Figure 4.7. Effect of H/D on  $\phi$ : a) 1 Hz, b) 5 Hz, c) 10 Hz, d) 20 Hz



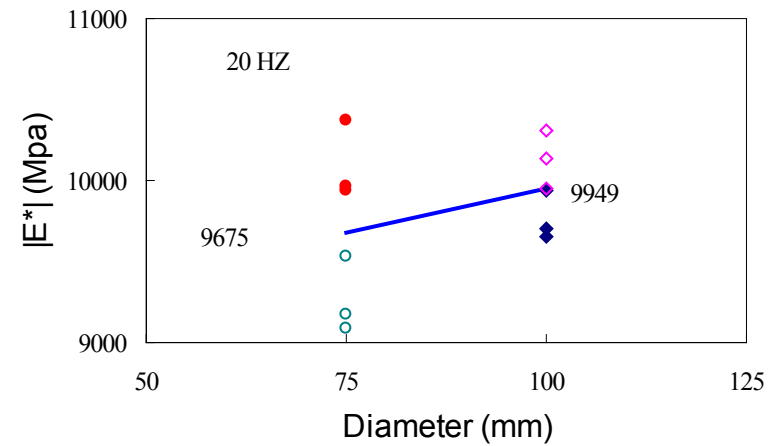
a)



b)



c)



d)

Figure 4.8. Effect of diameter on  $|E^*|$ : a) 1 Hz, b) 5 Hz, c) 10 Hz, d) 20 Hz

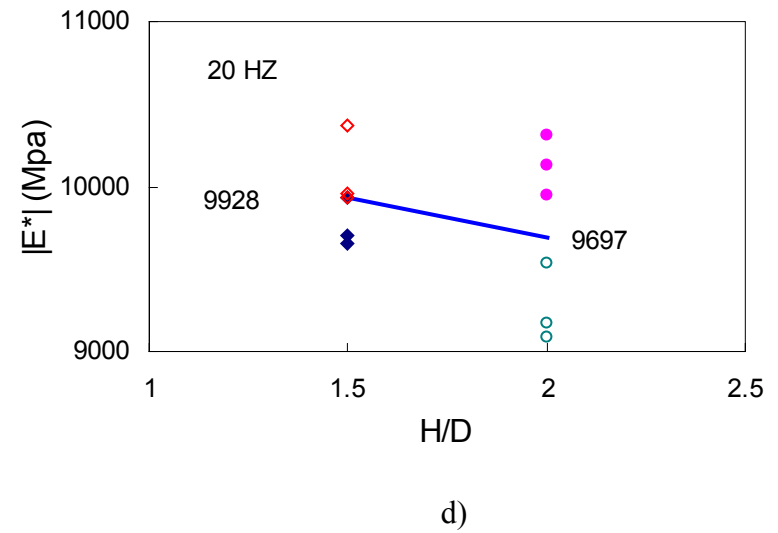
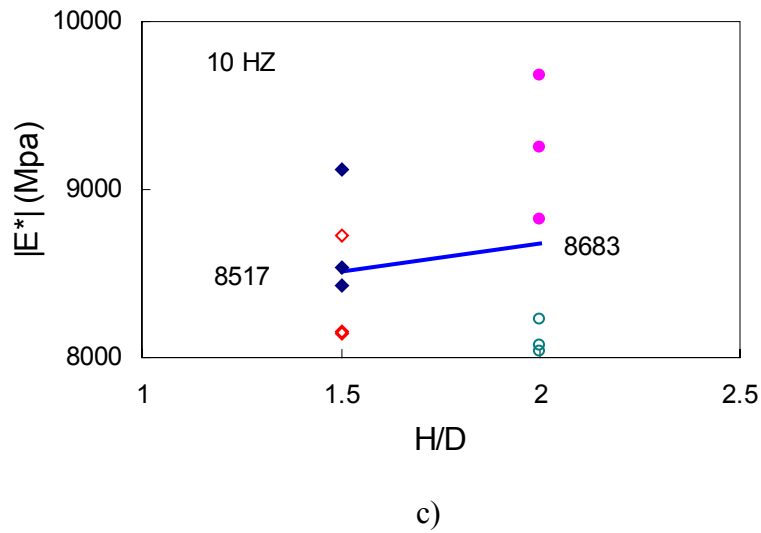
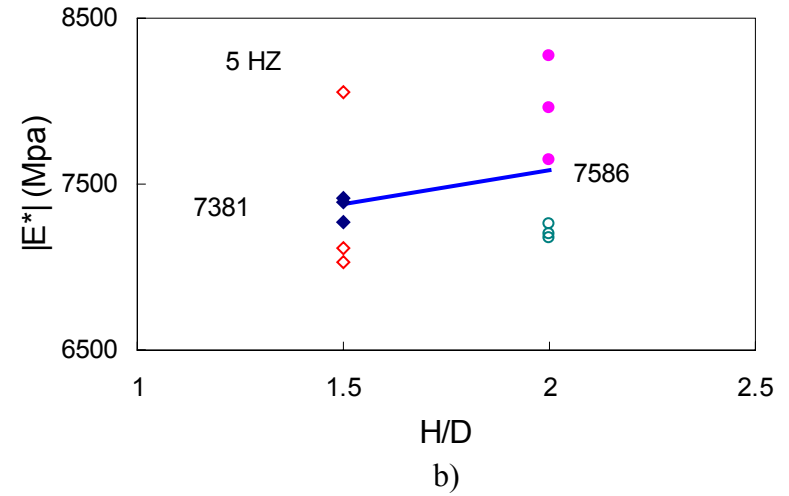
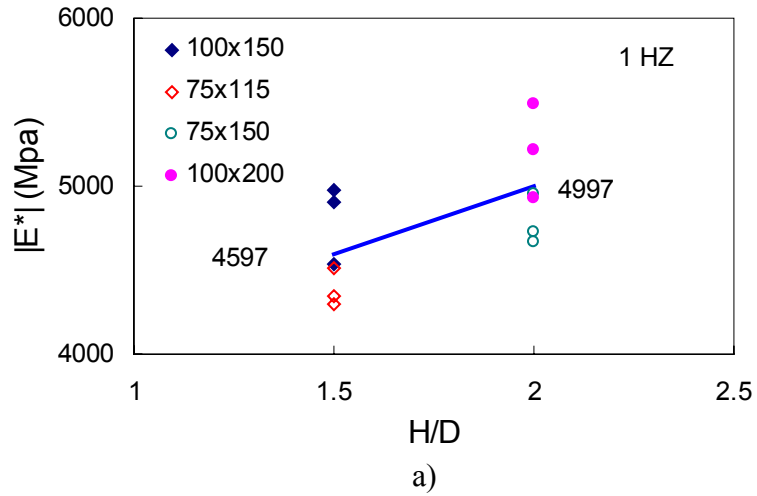


Figure 4.9. Effect of H/D on  $|E^*|$ : a) 1 Hz, b) 5 Hz, c) 10 Hz, d) 20 Hz

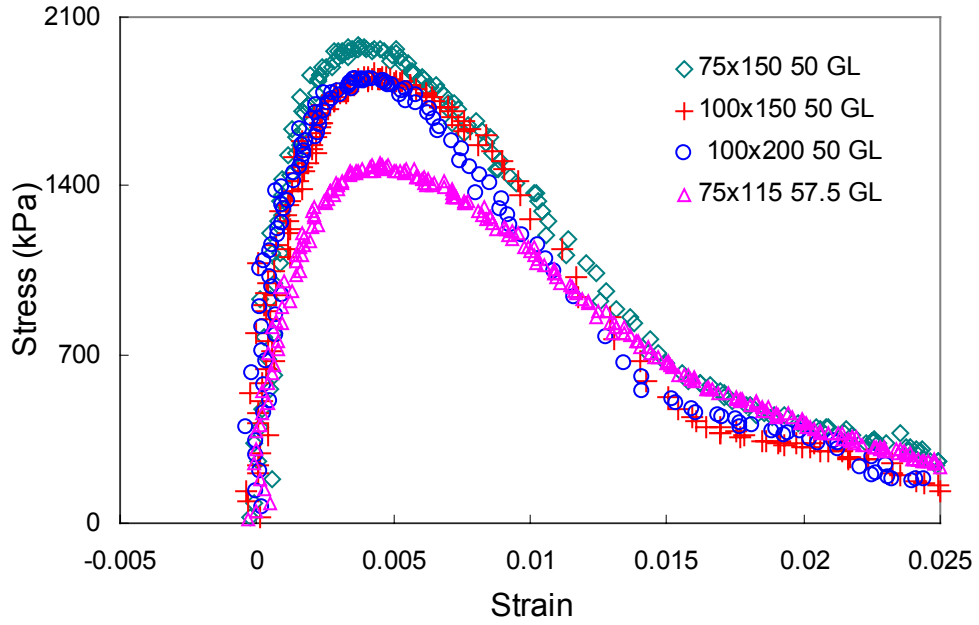


Figure 4.10. Average stress/strain curves from constant crosshead-rate test for all geometries

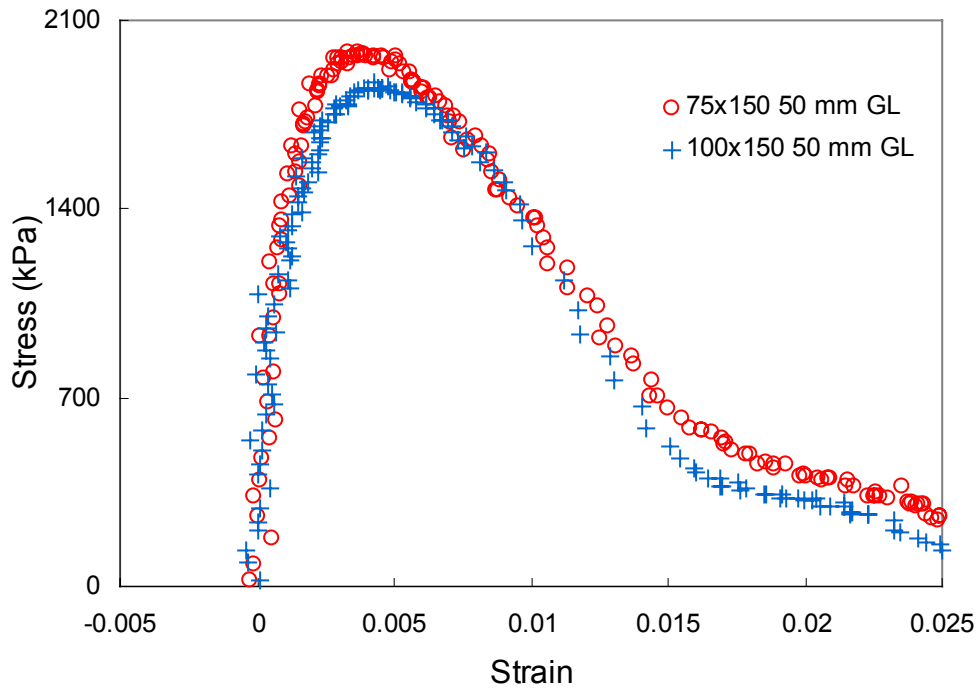


Figure 4.11. Average stress/strain curves from constant crosshead-rate test for 75x150 and 100x150

#### 4.6.2.2 Statistical Analysis of Testing Results

Before drawing any conclusions on how the material responses are affected by diameter and height to diameter ratio, statistical analysis has to be conducted to test the significance of these conclusions. For instance, before stating that the diameter affects  $|E^*|$  based on the comparison of the average values for the different geometries, it is important to compare that effect with the total specimen to specimen variation of  $|E^*|$ .

For that purpose, a two-factor analysis of variance, based on 95 percent confidence level, was conducted to study the effect of diameter and height to diameter ratio for responses obtained from the 50 mm gage lengths (57.5 mm for 75x115). If it were realized that there is an interaction between those two factors, a one-factor analysis would be conducted to study the effect of each. An effect is deemed significant if the p-value is less than 5%.

#### Complex Modulus Test

For the complex modulus test, the effects on  $|E^*|$  and  $\phi$  were evaluated for all frequencies individually. Results are summarized in Table 4.5. It can be concluded from the statistical analysis that not all trends detected graphically were significant. When the effect is statistically significant, it is in line with the graphical observation. However, since only at two frequencies there is an effect of H/D, the P-value of 2.7 which is close to 5 % makes it is safe to assume that the phase angle is independent of the effect of geometry.

### Constant Crosshead-Rate Test

The parameters evaluated in this test are the slope, peak stress and corresponding strain, stress at 1 percent strain and stress at 2.5 percent strain. Stresses beyond 2.5 percent strain were not evaluated because all the curves match closely in that region. The results of the statistical analysis are presented in Table 4.6.

Statistically, the low value of the peak stress for the 75x115 geometry has contributed to the significance of the effect of diameter and height to diameter ratio on peak stress for 75-mm diameter and H/D of 1.5. Other than that, it can be concluded that the stress/strain curves of the other geometries are statistically comparable, which supports the conclusions drawn from the graphical analysis.

#### **4.6.3 Effect of Gage Length on Material Responses**

Due to the non-uniformity of vertical strains along the height of glued specimens, as determined from the finite element analysis for linear elastic conditions, it is expected that LVDTs with different gage lengths measure different values for strain for the same specimen and during the same mechanical test. In particular, the larger the gage length, the lower the strain value, assuming that the LVDT is connected to the middle portion of the specimen. This difference in measured strain, which could yield to a difference in material response, had yet to be confirmed from actual mechanical tests.

Table 4.5. ANOVA table for  $|E^*|$  and  $\phi$  for all geometries

Complex Modulus Parameters						
Parameter	Frequency Hz	Interaction	Effect of Increasing H/D	P-value (%)	Effect of Increasing Diameter	P-value (%)
$ E^* $	1	None	Increases	1	Increases	1
	2	None	None	7	None	13
	5	None	None	16	None	28
	10	None	None	41	Increases	1
	20	Yes	D=75 mm, decreases	0.7	H/D=2, increases	1
$\phi$	1	None	Decreases	2.7	None	22
	2	None	None	30	None	32
	5	None	Decreases	2.7	None	22
	10	None	None	30	None	32
	20	Yes	None	38	None	38

Table 4.6. ANOVA table for effect of diameter and h/d on constant crosshead-rate test parameters

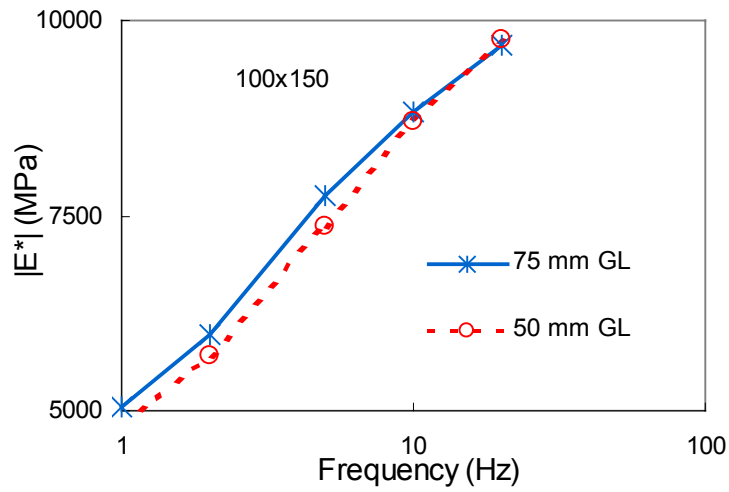
Constant Crosshead-Rate Test					
Parameter	Interaction	Effect of Increasing H/D	P-value (%)	Effect of Increasing D	P-value (%)
Slope	None	None	92	None	93
Peak Stress	Yes	D=75, increases	1	H/D=1.5, increases	1
Strain at Peak Stress	None	None	61	None	94
Stress at 1% Strain	None	None	51	None	22
Stress at 2.5 % strain	None	None	25	Decreases	1

To confirm the effect of gage length on material responses, eight LVDTs corresponding to two gage lengths were used for strain measurement during the complex modulus test and constant crosshead-rate test, as described earlier. As in the case of diameter and height to diameter ratio and for the same material responses, this effect was evaluated graphically and statistically.

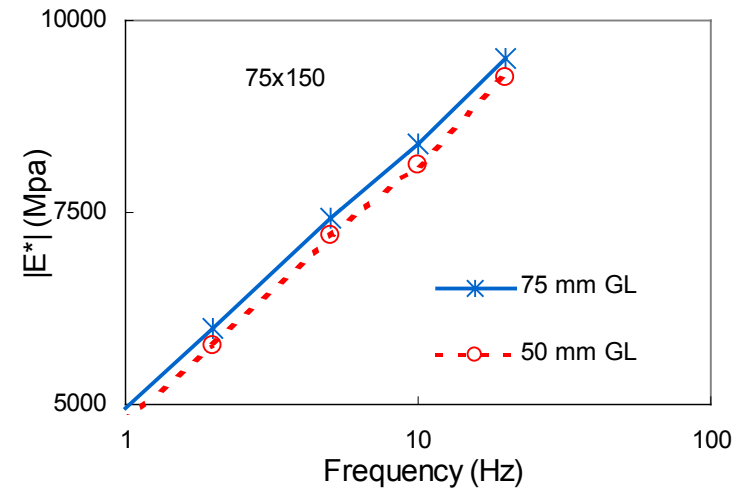
#### *4.6.3.1 Graphical Analysis:*

By comparing the average phase angle values for the different geometries, it was concluded that the gage length does not affect phase angle at any frequency. However, this was not the case for dynamic modulus. Figure 4.12 provides a comparison of average  $|E^*|$  for three geometries at all frequencies. As expected, because elements away from the center of the specimen exhibit less strain,  $|E^*|$  values for the larger gage length were higher than those for the smaller. This difference is proportional to the error in strain as determined previously from the finite element analysis. It is interesting to note that the two gage lengths in the case of 100x200 specimens yield almost the same values for  $|E^*|$ .

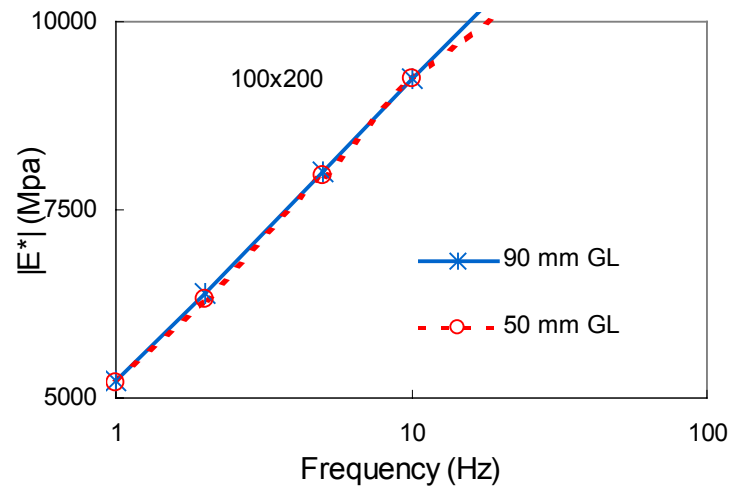
In the case of the constant crosshead-rate test, it is seen that the stress/strain curves for the different gage lengths almost overlap in the pre-peak region; that is, the slope, peak stress and strain match closely (Figure 4.13). It is only in the post-peak region that the curves diverge. This is attributed to strain localization and onset of macro-cracking that occurs near the middle portion of the specimen at failure. If this difference between the curves is found to be statistically significant, than using two gage lengths in testing could aid in determining the onset of macro-cracking in specimens, an instance that is usually hard to determine especially if macro-cracks originate from the inside of the specimen.



a)



b)



c)

Figure 4.12. Effect of gage length on  $|E^*|$ : a) 100x150, b) 75x150, c) 100x200

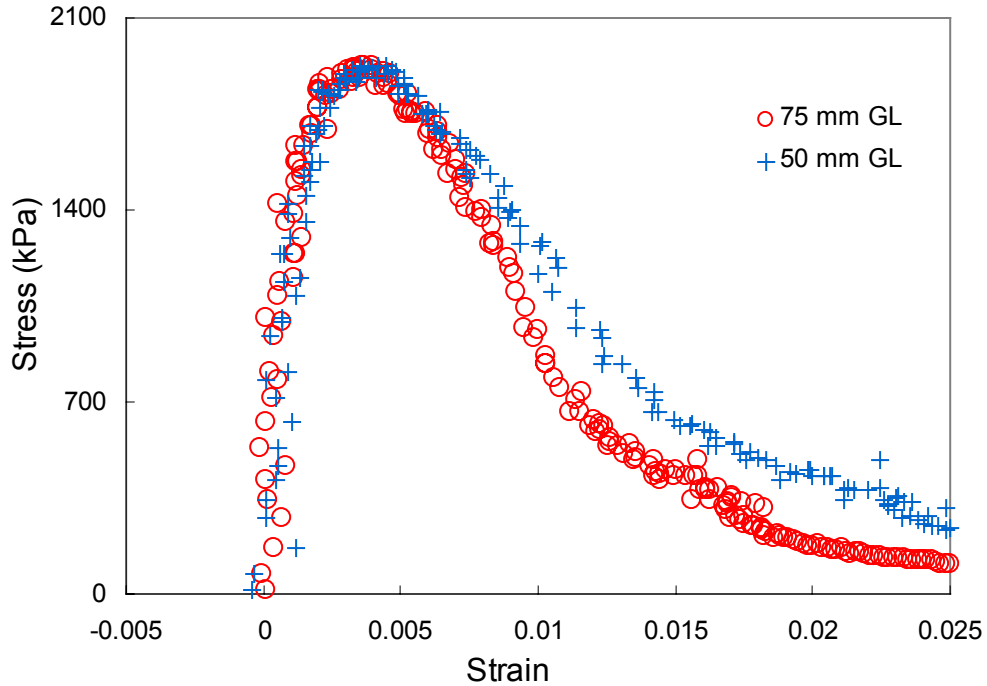


Figure 4.13. Comparison of stress/strain curves for 75x150 for 2 gage lengths

#### 4.6.3.2 Statistical Aysis

Finally, a two-factor analysis of variance was conducted to study the effect of gage length and frequency on  $|E^*|$  and  $\phi$ . Although the effect of frequency on those parameters is known, it was incorporated to increase the number of replicates used. Results are tabulated in Table 4.7.

It can be concluded that the larger the gage length, the larger the dynamic modulus. As for phase angle, it is unaffected. These conclusions support earlier conclusions drawn from the graphical comparison. For the constant crosshead-rate test, a two-factor analysis of variance was also conducted. Results are presented in Table 4.8. The results support the previous graphical conclusions that the gage length does not affect the slope and peak strain but affects stresses in the post-peak regions; larger gage length measure lower strains for a certain stress value (lower stress for a certain strain).

#### **4.7 Conclusion**

For the asphalt mixture used, it is observed that the top and bottom edges, in addition to sections adjacent to the mold walls, of SGC compacted specimens have higher air void content than the other sections of the specimen; thus, it is imperative for the specimens used in testing to be cored and cut from larger size compacted specimens. The similar variation along the height of all the candidate geometries make it hard to favor one over the other.

The effect of glued end plates on the uniformity of strains, as demonstrated in the finite element analysis, varies from one geometry to the other and can be revealed by comparing the dynamic modulus of a particular geometry measured for two different gage lengths. Strains are large in the middle portion of the specimen and decrease as the elements become closer to the ends. This effect is the smallest for geometries of H/D of 2 and becomes higher for H/D of 1.5.

The gage length used for vertical strain measurement has to be small enough to minimize the error attributed to the end effect as discussed above. In the mean time, this length should be large enough to measure representative material responses independent of aggregate size. Using 2 gage lengths in constant crosshead-rate tests can detect the onset of macro-cracking in specimens.

Considering the results from mechanical tests, both the high values for phase angle and low values for fracture strength corresponding to the 75x115 imply that it is being affected by the specimen boundary conditions; hence, it is ruled out of the selection. As for the 100x200 specimen, its selection has two disadvantages: complexity in fabrication, and possible effect of glue between stacked sections on material responses.

For the 75x150 and 100x150, both exhibit similar stress/strain curves under the monotonic test, especially in the pre-peak region. Any difference between the curves in the post-peak region is small and statistically insignificant. Under the complex modulus test, the  $|E^*|$  values were very close at low frequencies but diverged at 10 and 20 Hz. Statistically, differences attributed to the diameter and H/D were found to be significant at certain frequencies and not for others. As for phase angles, values for the two geometries were comparable both graphically and statistically.

Based on these findings, it can be concluded that the 75x150, which meets the “traditional” RVE requirements (1:4, diameter to maximum aggregate size (for 12.5 and 19 mm mixes), and 1:2 H/D), is a more conservative geometry to adopt for tensile testing. Either a 75 mm or a 100 mm gage length can be used for axial strain measurement. However, if larger size aggregate mixes are to be used; or if it is important that the same geometry be adopted for compression and tension testing, then it is reasonable to adopt the 100x150 geometry. In both cases, the test specimen would have to be cut and cored from a larger size SGC specimen. It is worthy to note that this conclusion may not be universally applicable to other mixes and for other Superpave gyratory compactors.

Table 4.7. ANOVA table for the effect of gage length on  $|E^*|$  and  $\phi$

Effect of Increasing Gage Length in Complex Modulus Test						
Geometry	Interaction with Frequency		Parameter			
	$ E^* $	$\phi$	$ E^* $	P-value (%)	$\phi$	P-value (%)
75x115	None	None	Increases	2	None	69
75x150	None	None	Increases	0.1	None	23
100x150	None	None	Increases	2	None	52
100x200	None	None	None	59	None	77

Table 4.8. ANOVA Table for effect of gage length on constant crosshead-rate test parameters

Effect of Increasing Gage Length in Constant Crosshead-Rate Test									
Geometry	Interaction with H/D (For all parameters)	Parameter							
		Slope	P-value (%)	Strain at Peak Stress	P-value (%)	Stress at 1% Strain	P-value (%)	Stress at 2.5 % Strain	P-value (%)
75x115, 75x150	None	None	75	None	82	None	10	Decreases	1
100x150, 100x200	None	None	82	None	35	Decreases	4	Decreases	2

## **5 Determination and Interconversion among Linear Viscoelastic Response Functions**

### ***5.1 Introduction***

Several viscoelastic response functions can be used to characterize the linear viscoelastic behavior of asphalt concrete. They are: relaxation modulus, creep compliance, and complex modulus. The importance of determining those response functions, or linear viscoelastic properties, is not limited to the characterization of asphalt concrete in the linear viscoelastic range, LVE, but also for the characterization of the viscoelastic behavior beyond that range where asphalt concrete exhibits non-linearity and damage behavior. Additionally, a response function can serve as a viscoelastic fingerprint for specimens that are being used in any mechanical test. Those fingerprints may be used to evaluate the specimen-to-specimen variation and/or to determine if the material is damaged or not.

The viscoelastic response functions can be obtained through mechanical tests conducted in the LVE range. Additionally, from the theory of viscoelasticity it can be shown that all LVE material properties are inter-related and thus any property can be obtained if another is known. While the creep compliance test and complex modulus test can be easily conducted, the relaxation test is more difficult to conduct and requires a high capacity robust testing machine. Therefore, it is often the case where the relaxation modulus is obtained through interconversion of creep compliance or complex modulus functions. Interconversion can also be necessary where one material function can not be determined over the entire range of the domain needed from a single test type. For

example the relaxation modulus or creep compliance can not be determined at very short times; in this case, the complex modulus is determined for that range and then converted to relaxation modulus or creep compliance. The mathematical interrelationships between the linear viscoelastic material functions have been covered in previous research (Park et al. 1999). Only those inter-relationships that were needed in this research are presented in this chapter.

## **5.2 Analytical Representation of LVE Material Properties**

Whether a LVE material property is determined through testing or through interconversion techniques, a representative analytical representation should be established so that accurate material characterization can be achieved.

### **5.2.1 Complex Modulus**

The complex modulus is composed of two components: dynamic modulus  $|E^*|$  and phase angle  $\phi$ . In the previous chapter, details of the complex modulus test from which the values of these components can be obtained were outlined. In complex domain, the complex modulus is composed of real and imaginary components, the storage and loss moduli respectively, and is presented as follows:

$$E^* = E' + iE'' \quad (5.1)$$

where  $E'$  = storage modulus,

$E''$  = loss modulus, and

$i = (-1)^{1/2}$ .

The dynamic modulus is the amplitude of the complex modulus and is defined as follows:

$$|E^*| = \sqrt{(E')^2 + (E'')^2} \quad (5.2)$$

The values of the storage and loss moduli are related to the dynamic modulus and phase angle as follows:

$$E' = |E^*| \cos \phi, \text{ and} \quad (5.3)$$

$$E'' = |E^*| \sin \phi \quad (5.4)$$

Figure 5.1 shows the relationship between the aforementioned components. As the material becomes more viscous, the phase angle increases and the loss component of the complex modulus increases. A phase angle of  $90^\circ$  indicates purely viscous behavior. On the other hand, as phase angle decreases there is greater elastic behavior and a larger contribution from the storage modulus. A phase angle of zero indicates a purely elastic material.

The dynamic modulus at each frequency is calculated by dividing the stress amplitude ( $\sigma_{amp}$ ) by the strain amplitude ( $\epsilon_{amp}$ ) at steady state sinusoidal loading, as follows:

$$|E^*| = \frac{\sigma_{amp}}{\epsilon_{amp}} \quad (5.5)$$

The phase angle,  $\phi$ , is related to the time lag,  $\Delta t$ , between the stress input and strain response and the frequency of testing:

$$\phi = 2\pi f \Delta t \quad (5.6)$$

where  $f$  is the loading frequency. As the testing temperature decreases or the rate of loading (frequency) increases, the dynamic modulus increases and the phase angle decreases due to the time dependence or viscoelasticity of the material.

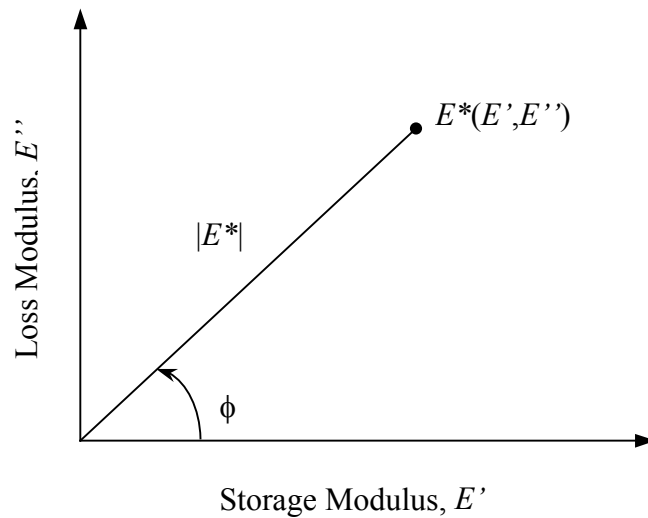


Figure 5.1. Components of the Complex Modulus

### 5.2.2 Relaxation Modulus and Creep Compliance

The creep compliance is the ratio of strain response to constant stress input, while the relaxation modulus is the ratio of stress response to constant strain input. If asphalt concrete was purely elastic, then creep compliance,  $D(t)$ , and relaxation modulus,  $E(t)$ , would be the reciprocal of each other. However due to the viscoelastic nature of asphalt concrete, this is true only in Laplace transform domain. While the creep compliance can be determined from the creep test, as detailed in Chapter 3, the relaxation modulus is determined in this research through interconversion from other LVE material functions.

Successive research by (Kim et al. 1995) based on earlier works of Schapery have led to refined analytical representation of the creep compliance and relaxation modulus using Prony series.

### 5.2.2.1 Relaxation Modulus

The Prony series representation of the relaxation modulus is of the following form:

$$E(t) = E_{\infty} + \sum_{m=1}^M E_m e^{-t/\rho_m} \quad (5.7)$$

where  $E_{\infty}$ ,  $\rho_m$ , and  $E_m$  are long time equilibrium modulus, relaxation time, and Prony regression coefficients respectively. Physically, this representation is related to the Wiechert (or Generalized Maxwell) model (Figure 5.2). The regression coefficients can be obtained by assuming the relaxation times for selected collocation points of time (Schapery, 1961). Formulating Equation (5.7) in column vectors ( $\{\mathbf{A}\}$  and  $\{\mathbf{C}\}$ ) and matrix  $[\mathbf{B}]$ , the regression coefficients are determined using the following equation:

$$\underbrace{E(t_n) - E_{\infty}}_{\{\mathbf{A}\}} = \underbrace{\sum_{m=1}^M \exp(-t_n / \rho_m)}_{[\mathbf{B}]} \underbrace{E_m}_{\{\mathbf{C}\}}, n=1, \dots, N. \quad (5.8)$$

The non-negative coefficients,  $\{\mathbf{C}\}$ , are solved for using the imbedded linear programming function provided by **MATLAB** using the following rearranged form with constraints forcing the coefficients to be positive while still satisfying Equation (5.8):

$$\text{MINIMIZE } |[\mathbf{B}]\{\mathbf{C}\} - \{\mathbf{A}\}| \text{ SUCH THAT } \{\mathbf{C}\} \geq 0. \quad (5.9)$$

### 5.2.2.2 Creep Compliance

Prony series representation of the creep compliance is of the following form:

$$D(t) = D_0 + \sum_m^M D_m [1 - e^{-t/\tau_m}] \quad (5.10)$$

where  $\tau_m$  is retardation time,  $D_m$  is a regression coefficient, and  $D_0$  is the initial creep compliance at time zero. As in the case of relaxation modulus, the collocation method is applied to determine the regression coefficients. The presented Prony series representation of creep compliance relates, in physical terms, to the Kelvin (or Generalized Voigt) model (Figure 5.3).

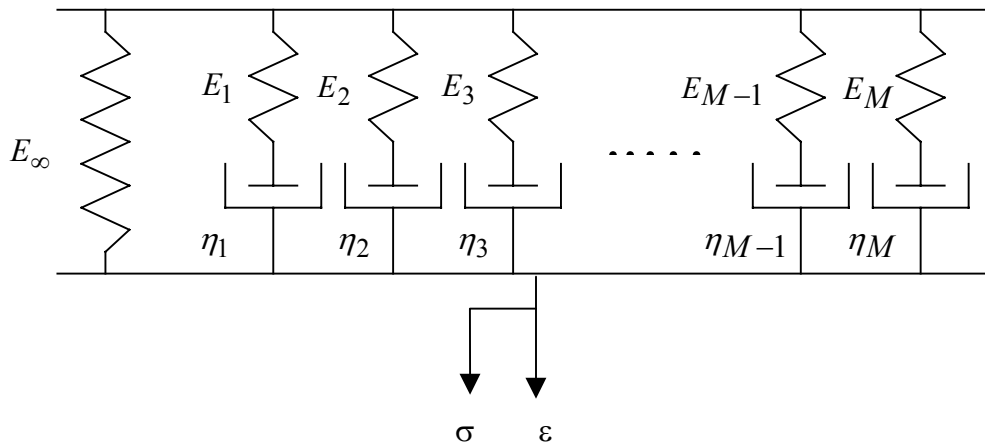


Figure 5.2. Wiechert Model: where  $\eta_m$  is the coefficient of viscosity and  $E_m$  is the stiffness for the  $m^{\text{th}}$  term

### 5.3 Construction of LVE Material Property Mastercurve

The aforementioned representations of the LVE response functions (material properties) were for a given time range at a fixed temperature. However, it is often the case where the material property is to be determined over a wider range of time/frequency domain. Due to testing constraints and the risk of exceeding the LVE range, it may not be always possible to conduct mechanical tests over that wide range of time domain. In such scenarios, the mechanical tests are performed at several temperatures with different testing parameters, such as load level, at each temperature.

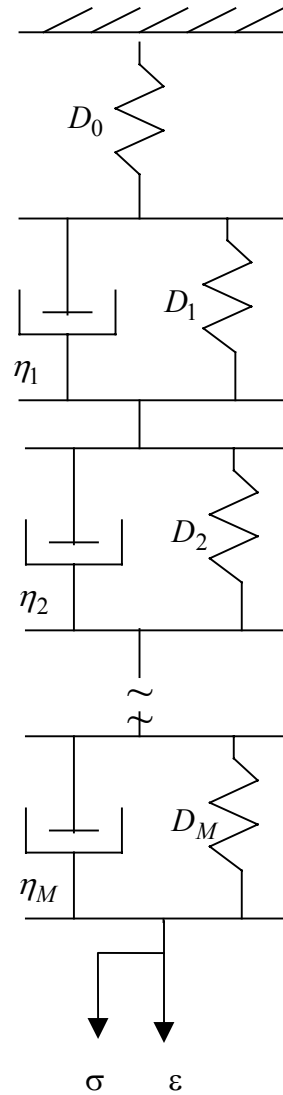


Figure 5.3. Kelvin Model: where  $\eta_m$  is the coefficient of viscosity and  $D_m$  is the compliance for the  $m^{\text{th}}$  term

### 5.3.1 Time-Temperature Superposition Principle for LVE behavior

Asphalt concrete is a viscoelastic material that exhibits time and temperature dependency, and, except at low temperatures, viscoplastic non-recoverable strain. It is also known that when in its linear viscoelastic range, asphalt concrete is thermorheologically simple (TRS); that is, the effects of time or frequency and temperature can be expressed through one joint parameter. As such, the same material

property values can be obtained either at low temperatures and long times or at high testing temperatures but short times. The viscoelastic material property (e.g., relaxation modulus and creep compliance) as a function of time (or frequency), at various temperatures can be shifted along the horizontal time axis (log scale) to form a single characteristic mastercurve of that property as a function of reduced time at a desired reference temperature.

Thus, for the relaxation modulus at a certain time and temperature:

$$E(t, T) = E(\xi) \quad (5.11)$$

where  $\xi = \frac{t}{a_T}$  (5.12)

$t$  = time before shifting for a given temperature, T,

$\xi$  = reduced time at reference temperature  $T_0$ , and

$a_T$  = shift factor for temperature T.

The well-known WLF equation developed by William, Landal, and Ferry (1955) estimates the shift factor as:

$$\log a_T = \log \frac{t_T}{t_{T_0}} = \frac{c_1(T - T_0)}{c_2 + T - T_0} \quad (5.13)$$

where  $c_1$  and  $c_2$  are constants dependant on the reference temperature  $T_0$  expressed in degree Kelvin. The WLF equation can only be applied to temperatures above the glass transition temperature, which is around  $-30^\circ\text{C}$  for asphalt. In this research, the WLF equation was not used; instead, the shift factors were determined experimentally through graphical shifting of storage modulus curves and were later refined through error minimization using fitting techniques. More details are provided later.

Theoretically, the time-temperature shift factors, which are a function of the material itself, should be the same regardless from which material property they are derived. So for example, shift factors can be obtained by first constructing the dynamic modulus mastercurve and then those shift factors can be applied to construct the mastercurves of any other material property (Daniel 2001). However, it was learned in this research that doing so would fail to consider the part of the material's behavior that is represented through the phase angle. To overcome this problem, the shift factors in this research were obtained by constructing the storage modulus mastercurve. In that way, both the dynamic modulus and phase angle are incorporated in determining the shift factors. Figure 5.4 shows the storage modulus values, for several replicates, as a function of frequency at various testing temperatures and as a function of reduced frequency at 25°C after shifting.

Shift factors,  $a_T$ , used to shift the storage modulus,  $E'$ , versus frequency curves at -10, 5, and 35°C along the frequency axis to form a continuous master curve at 25°C, are defined as follows:

$$\text{Log}(f_R) = \log(f \times a_T) \quad (5.14)$$

where  $f_R$  = reduced frequency at the reference temperature (25°C);

$f$  = frequency at a given temperature T before shifting; and

$a_T$  = shift factor for temperature T.

Shift factors are determined by first assigning initial trial values and then using least squares technique to refine them through error minimization between actual  $E'$  values and those fitted using a log-sigmoidal function of the form shown in Equation (5.15):

$$E' = a_1 + \frac{a_2}{\left\{ a_3 + \frac{a_4}{\exp[a_5 + a_6 \log_{10}(f_R)]} \right\}} \quad (5.15)$$

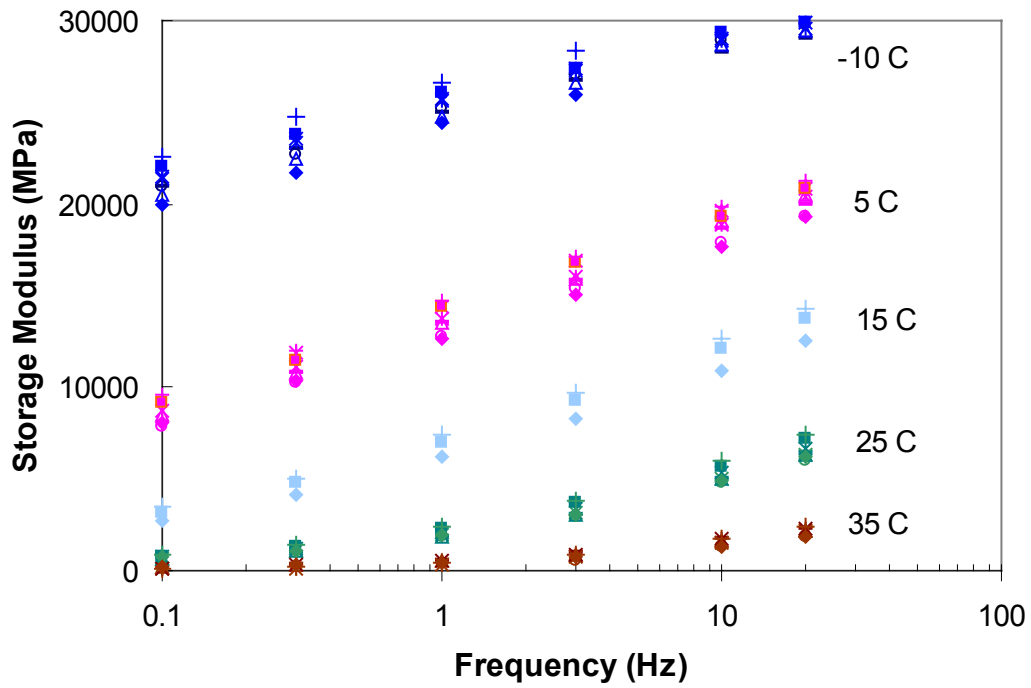
where  $f_R$  is the reduced frequency,

$a_1$  through  $a_6$  are regression coefficients, and

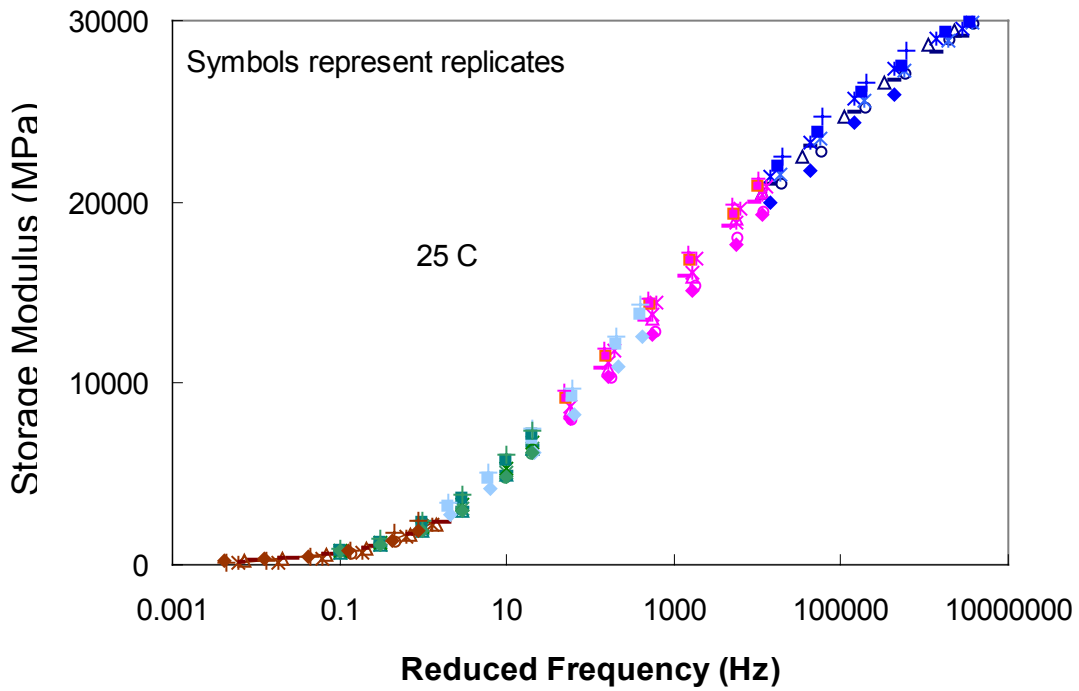
$E'$  is the storage modulus.

If shift factors for temperatures other than those incorporated in the testing program are required for the same material, they can be interpolated from the log shift factor vs. temperature plot shown in Figure 5.5. Once the shift factors are determined, they can be applied in constructing mastercurves for other material properties, such as  $|E^*|$  and  $\phi$  shown in Figures 5.6 and 5.7 respectively. As observed, the mastercurves of  $|E^*|$  and  $\phi$  obtained by shifting individual curves using shift factors obtained through  $E'$  are continuous which indicates that the shift factors are valid.

It is interesting to see from Figure 5.7 that phase angle increases with the decrease in reduced frequency which is explained by the fact that asphalt concrete exhibits more viscous behavior at lower frequencies. However, at reduced frequencies lower than 0.1 Hz, phase angle starts to decrease. This may be due to the fact that at high temperatures/slow frequencies, the asphalt concrete matrix weakens and thus individual aggregate properties start to exhibit a more significant effect on the overall asphalt concrete behavior. Since aggregates are elastic and thus exhibit no phase angle, the overall phase angle of the asphalt mix starts to drop as the reduced frequency reduces. However, non-crosslinked polymers without filler exhibit this behavior due to entanglement of the long chains; thus, there may be additional physical sources within the asphalt matrix contributing to this behavior.



(a)



(b)

Figure 5.4. Storage modulus as a function of (a) frequency and (b) reduced frequency

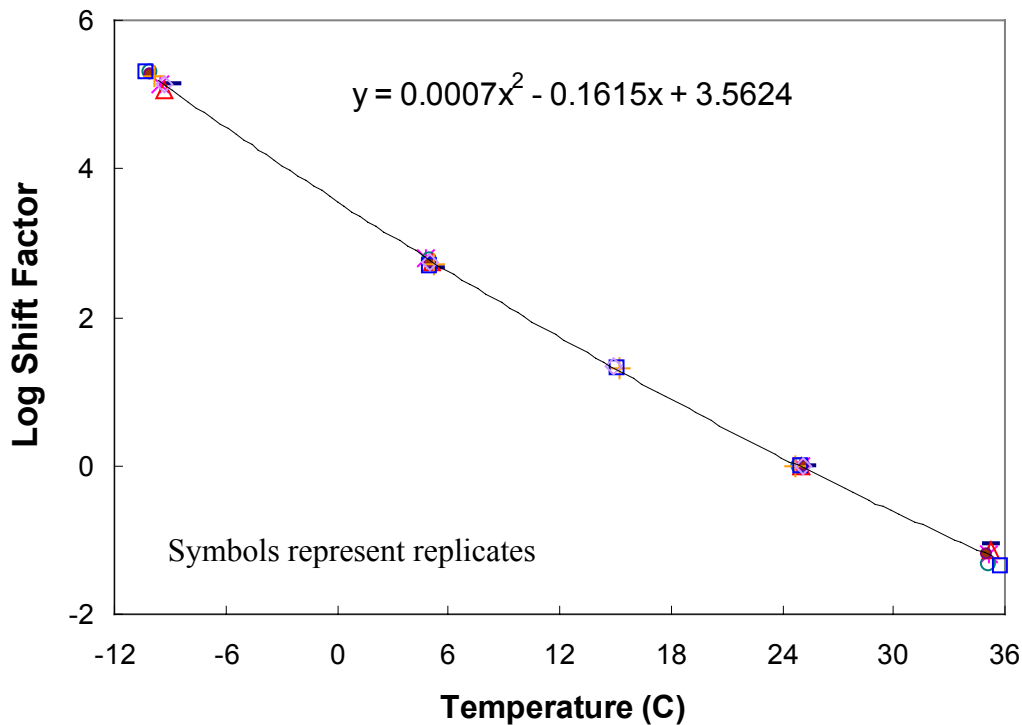
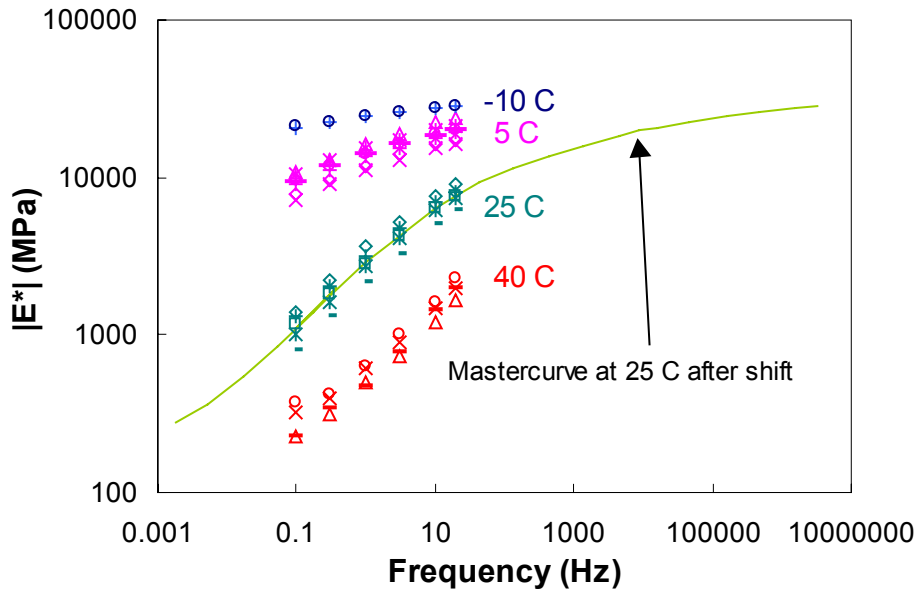
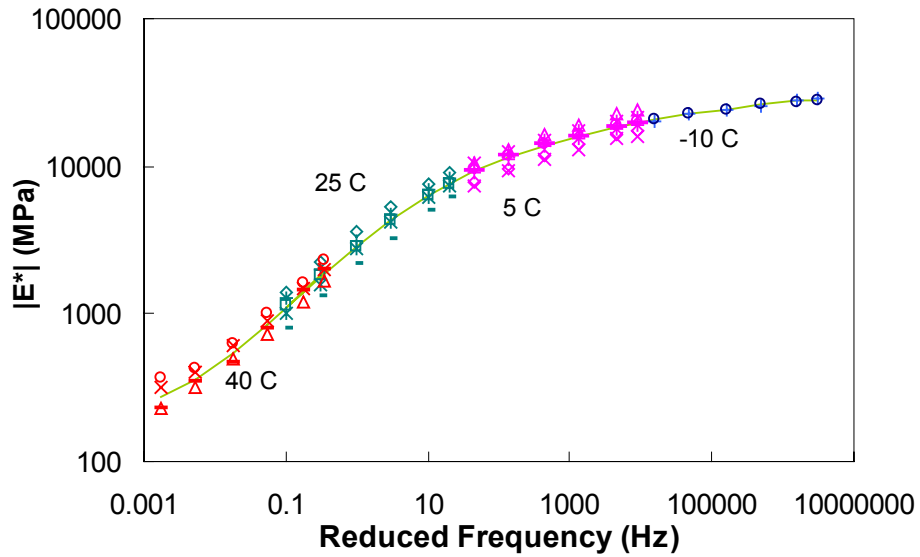


Figure 5.5. Log shift factor as a function of temperature obtained by constructing the storage modulus mastercurve at 25°C

Theoretically, the time-temperature shift factors are a material property, so they should be the same regardless of what material property they are obtained from. This was true for the case of storage modulus, phase angle, and dynamic modulus as shown previously. However, this is not an ultimate check since  $E'$  itself is obtained from  $|E^*|$  and  $\phi$ ; in addition, all properties are in the frequency domain. A better check would be to check those shift factors in constructing a creep compliance mastercurve. After each specimen was tested for frequency sweep ( $E^*$ ), a 10-second creep test was conducted in the LVE range after allowing a rest period of 5 minutes for strain recovery. Details of the creep test were presented earlier. This was done at all temperatures presented previously (-10, 5, 15, 25, 35°C).

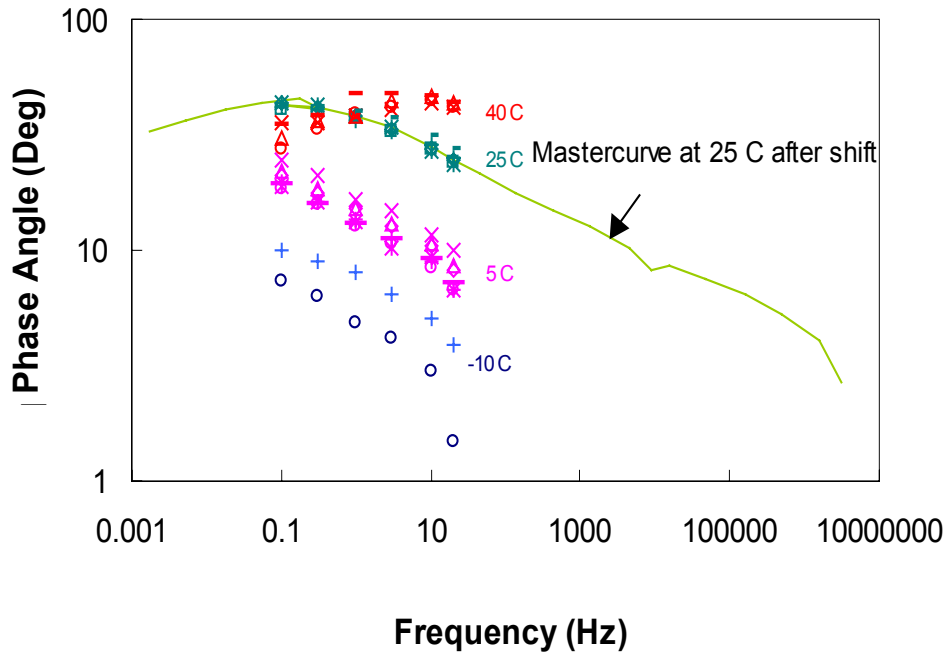


(a)

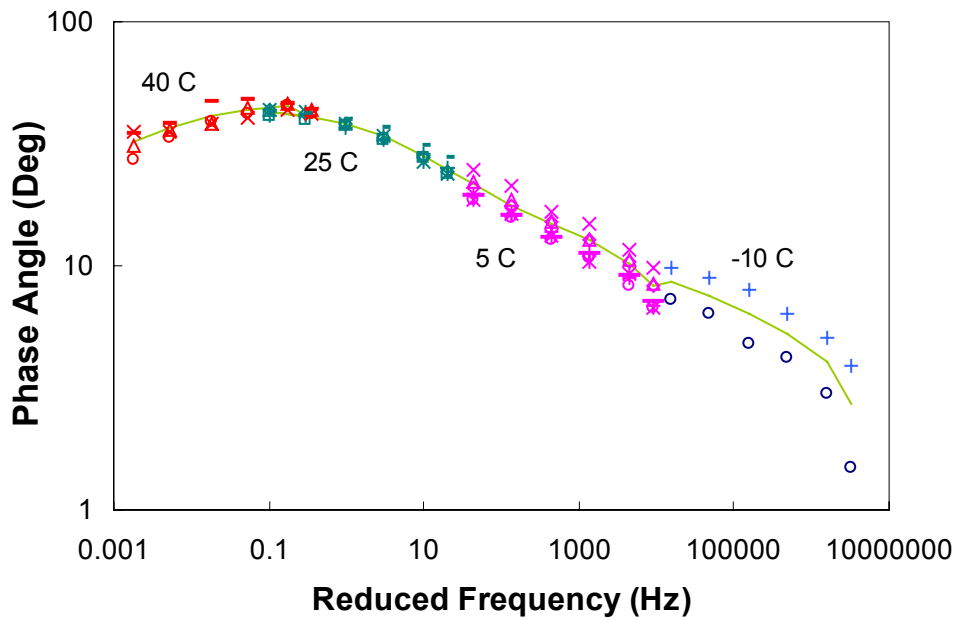


(b)

Figure 5.6.  $|E^*|$  as a function of (a) frequency before shifting and (b) reduced frequency at 25°C after shifting



(a)



(b)

Figure 5.7. Phase angle as a function of (a) frequency before shifting and (b) reduced frequency at 25°C after shifting

Figure 5.8 shows the creep curves of all specimens at all testing temperatures. Shifting the average curves of the replicates at each temperature yields the mastercurve presented in Figure 5.9. The shift factors resulting from that shift along the time axis will be referred to as the shift factors from creep curves. If the shift factors obtained previously from the storage modulus curves are applied to shift the average creep curves along the time axis, the mastercurve obtained closely matches that constructed using the shift factors from creep curves. A variation is observed at 35°C that could be attributed to the possible accumulation of damage at 35°C, at which point the specimen would have been tested for complex modulus followed by creep consecutively at 5 temperatures. The plots of log shift factor, from creep and  $E'$ , versus temperature are both plotted in Figure 5.10. As observed there is a very close match between both sets; however, they are not perfectly the same. Better collapse could be attained by doing additional investigative testing to determine the optimal testing parameters that will ensure that material behavior remain within LVE range during testing. A sample of critical testing parameters include: loading amplitude and time in creep tests, stress amplitude and rest between frequencies in  $E^*$  tests, in addition to rest period between successive  $E^*$  and creep tests at a given temperature, among others.

For the rest of this research, the time-temperature shift factors obtained by constructing the storage modulus mastercurve are used. The complex modulus test can be conducted at several frequencies and temperatures giving a wider range of frequency domain, which is wider than that obtained from short-term LVE creep tests. In addition, it is easier to ensure that specimen response in the complex modulus test is within LVE range; although more study needs to be conducted on that as stated earlier.

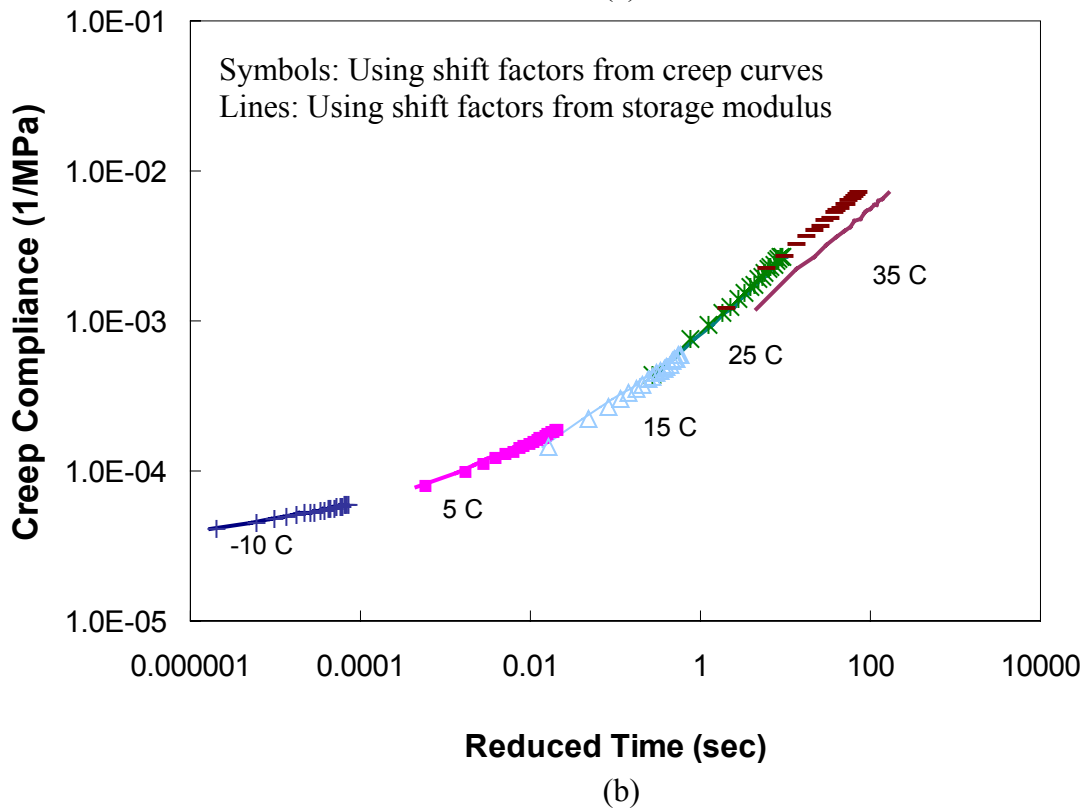
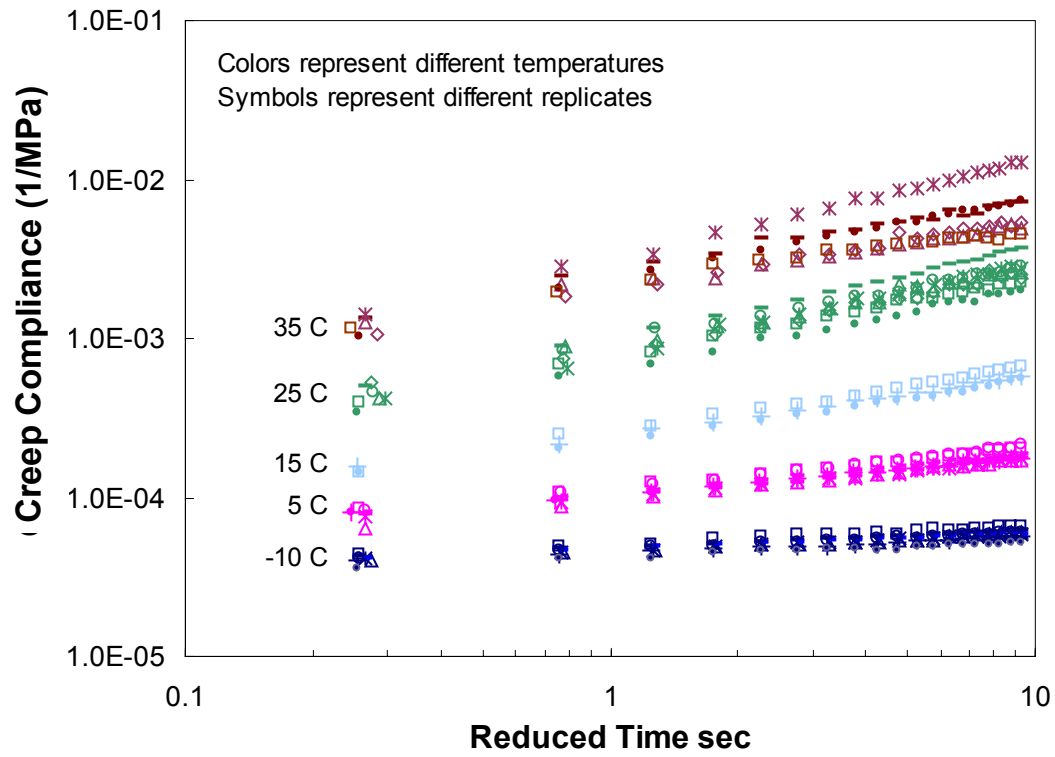


Figure 5.8. (a) Individual creep curves for different replicates and temperatures; and (b) average creep mastercurves constructed from creep and  $E'$  shift factors

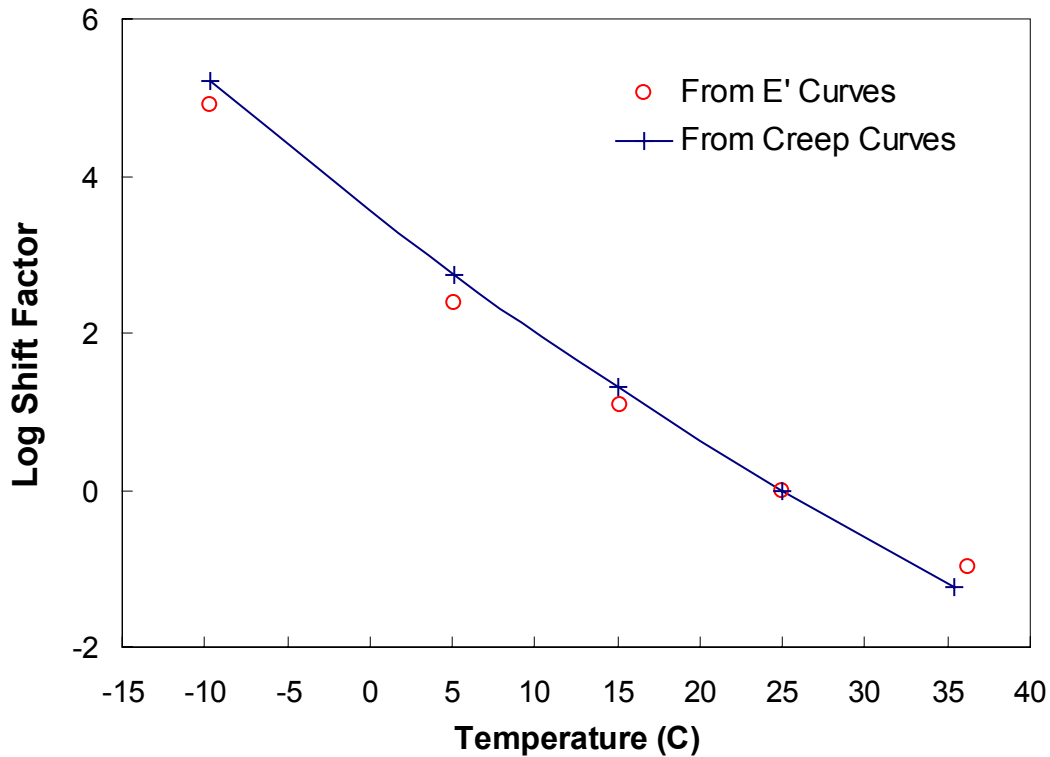


Figure 5.9. Log shift factors determined by constructing creep and E' mastercurves

#### 5.4 Interconversion among Viscoelastic Response Functions

As presented in the aforementioned section, interconversion may be required for different reasons. It is well-known that the LVE material response functions are mathematically equivalent for each mode of loading such as uniaxial or shear and thus interconversion among them is possible (Schapery et al. 1999).

Both the relaxation modulus and the creep compliance are essential for viscoelastic modeling purposes. While the relaxation modulus is necessary for the calculation of pseudostrains, the creep compliance is needed for the determination of strains beyond the viscoelastic range. In this research the complex modulus test was conducted to obtain the LVE material properties. Presented in this section are the methods used to convert from complex modulus to relaxation modulus. Since creep tests

were also performed, the obtained mastercurves were compared against those obtained through interconversion from complex modulus.

#### 5.4.1 Conversion from Complex Modulus to Relaxation Modulus

The interconversion between linear viscoelastic material functions such as frequency-domain complex modulus and time-domain relaxation modulus was illustrated by (Schapery et al. (1999) based on an approximate analytical method and on an exact mathematical formulation.

##### 5.4.1.1 Complex Modulus to Relaxation Modulus: Approximate Method

An approximate relationship between storage and relaxation moduli can be established through the following formulation:

$$E(\xi) \cong \frac{1}{\lambda'} E'(\omega) |_{\omega=(1/\xi)} \quad (5.16)$$

where  $\omega$ ,  $\xi$ ,  $E'(\omega)$ , and  $E(\xi)$  are reduced frequency, reduced time, storage modulus, a relaxation modulus at a reference temperature respectively.  $\lambda'$ , which is an adjustment function, is defined as follows:

$$\lambda' = \Gamma(1-n) \cos(n\pi/2) \quad (5.17)$$

where  $\Gamma$  is a gamma function and  $n$  is the local log-log slope of the storage modulus; that is,

$$n = \frac{d \log E'(\omega)}{d \log \omega} \quad (5.18)$$

Once relaxation modulus values are predicted along the desired time range, the data is fit to a Prony series representation (Equation (5.7)) for analysis and modeling purposes.

#### 5.4.1.2 Complex Modulus to Relaxation Modulus: Exact Method

The exact method is derived from the Wiechert model (or generalized Maxwell model), the mechanical model consisting of springs and dashpots, as shown in Figure 5.2.

For a given applied strain,  $\varepsilon$ , the stress response in the left spring,  $\sigma$ , is given by:

$$\sigma_{\infty} = E_{\infty} \varepsilon . \quad (5.19)$$

The stress,  $\sigma_m$ , in each of the Maxwell components combining a spring with a dashpot is governed by the following differential equation:

$$\frac{d\varepsilon}{dt} = \frac{1}{E_m} \frac{d\sigma_m}{dt} + \frac{\sigma_m}{\eta_m} \quad (5.20)$$

where  $\eta_m$  = coefficient of viscosity, and

$E_m$  = relaxation modulus in the term, or  $m^{\text{th}}$  Prony series coefficient.

Due to the linearity of the material components, the total stress on the Wiechert model is obtained by the summation form:

$$\sigma = \sigma_{\infty} + \sum_{m=1}^M \sigma_m \quad (5.21)$$

The Fourier transform is used in solving the above differential equation based on the elastic-viscoelastic correspondence principle, which is applied after replacing the elastic moduli by the Fourier transform of the viscoelastic properties. Thus the differential equation is transformed to an algebraic equation. Applying this technique to Equations (5.19) and (5.21), and then eliminating the stresses  $\sigma$  and  $\sigma_m$  yields the following relationship:

$$\bar{\sigma} = \left( E_{\infty} + \sum_{m=1}^M \frac{i\omega_n \rho_m E_m}{i\omega_n \rho_m + 1} \right) \bar{\varepsilon}, \quad n=1, \dots, N \quad (5.22)$$

where  $\bar{\sigma}$  and  $\bar{\varepsilon}$  are in the Fourier-transform domain, and the relaxation time of the  $m^{\text{th}}$  Maxwell element is given by:

$$\rho_m \equiv \frac{\eta_m}{E_m}. \quad (5.23)$$

Therefore, the complex modulus can be obtained from the constitutive equation shown in Equation (5.22) as follows:

$$E^* = E_{\infty} + \sum_{m=1}^M \frac{i\omega_n \rho_m E_m}{i\omega_n \rho_m + 1}, \quad n=1, \dots, N. \quad (5.24)$$

As observed from the above equation, the complex modulus is now presented in a complex form. The storage modulus is the real component of the complex modulus and hence is represented as:

$$E'(\omega_n) = E_{\infty} + \sum_{m=1}^M \frac{\omega_n^2 \rho_m^2 E_m}{\omega_n^2 \rho_m^2 + 1}, \quad n=1, \dots, N. \quad (5.25)$$

Using the storage modulus values from the testing results and through the collocation method,  $E_{\infty}$ ,  $\rho_m$ , and  $E_m$  will all be known:  $E_{\infty}$  can be found by equating it to  $E'(\omega)|_{0 < \omega < < 1}$ ; while the Prony-series coefficients,  $E_m$ 's, are obtained based on the selected relaxation times and reduced frequencies,  $\rho_m$  and  $\omega_n$ , subject to the following linear algebraic equations:

$$\{\mathbf{F}\} = [\mathbf{E}]^{-1} \{\mathbf{D}\} \quad \text{or} \quad F_m = E_{n,m}^{-1} D_n \quad (5.26)$$

where the column vectors,  $\{\mathbf{F}\}$  and  $\{\mathbf{D}\}$ , are  $E_m$  and  $E'(\omega_n) - E_{\infty}$  respectively; the superscript  $-1$  denotes an inversion; and the matrix,  $[\mathbf{E}]$ , is as follows:

$$E_{n,m} = \sum_{m=1}^M \frac{\omega_n^2 \rho_m^2}{\omega_n^2 \rho_m^2 + 1}, n=1, \dots, N. \quad (5.27)$$

However, this technique alone cannot guarantee that the coefficients of the solved  $\{\mathbf{F}\}$  column vector be positive, a condition that is not really necessary but preferable.

Obtaining positive Prony coefficients can be achieved by setting the following constraint during computation:

$$\text{MINIMIZE } [\mathbf{E}]\{\mathbf{F}\} \quad \text{SUCH THAT } \{\mathbf{F}\} > 0 \text{ AND } \{\mathbf{D}\} = [\mathbf{E}]\{\mathbf{F}\}. \quad (5.28)$$

#### 5.4.1.3 Raw vs. Adjusted Phase Angle Data

It was mentioned previously that at low reduced frequencies the phase angle starts to drop due to the larger contribution of the aggregates' elastic behavior. It remains to be seen whether adjusting this behavior by replacing the drop of the phase angle at low reduced frequencies by larger values to form an asymptote would affect the conversion to relaxation modulus. The adjusted values were obtained by fitting a log-sigmoidal function to the phase angle over the complete reduced-frequency range. This was done for both the approximate and exact interconversion techniques. Figure 5.10 shows raw phase angle mastercurves for individual specimens and the adjusted phase angle mastercurve.

To recapitulate, there are four possible variants of methods to convert complex modulus to relaxation modulus. First, the interconversion can be either based on an approximate or exact method; and secondly, raw phase angle data or adjusted data can be used in calculating the storage modulus needed for the interconversion. Table 5.1 is used to summarize the conversion methods and to designate a notation for each. As observed from Figure 5.11, which presents a comparison of the interconversion methods, the four

methods yield similar relaxation modulus mastercurves. Based on this result, it was decided that the exact method with adjusted data be used for the rest of this research study.

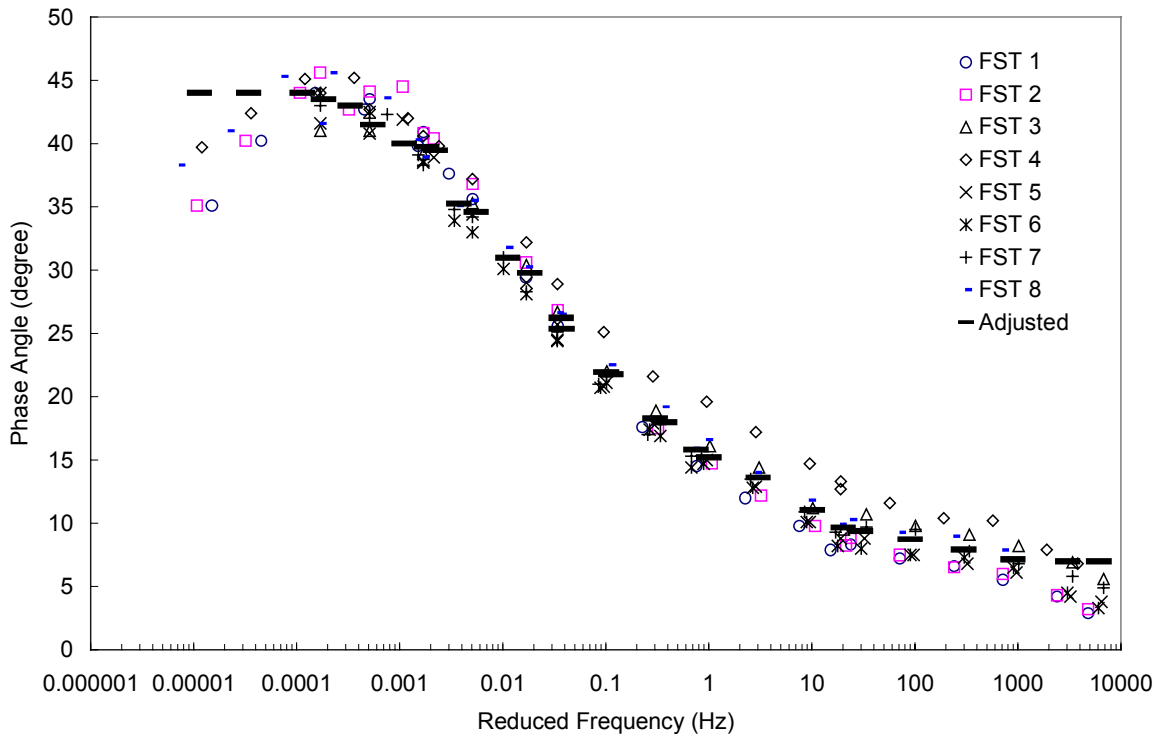


Figure 5.10. Individual phase angle mastercurves for replicate specimens along with the fitted sigmoidal mastercurve

Table 5.1 E\* to E(t) interconversion methods

Combination	Dynamic Modulus	Phase Angle	Conversion Method
AE	Raw	Adjusted	Exact
RE	Raw	Raw	Exact
AA	Raw	Adjusted	Approximate
RA	Raw	Raw	Approximate

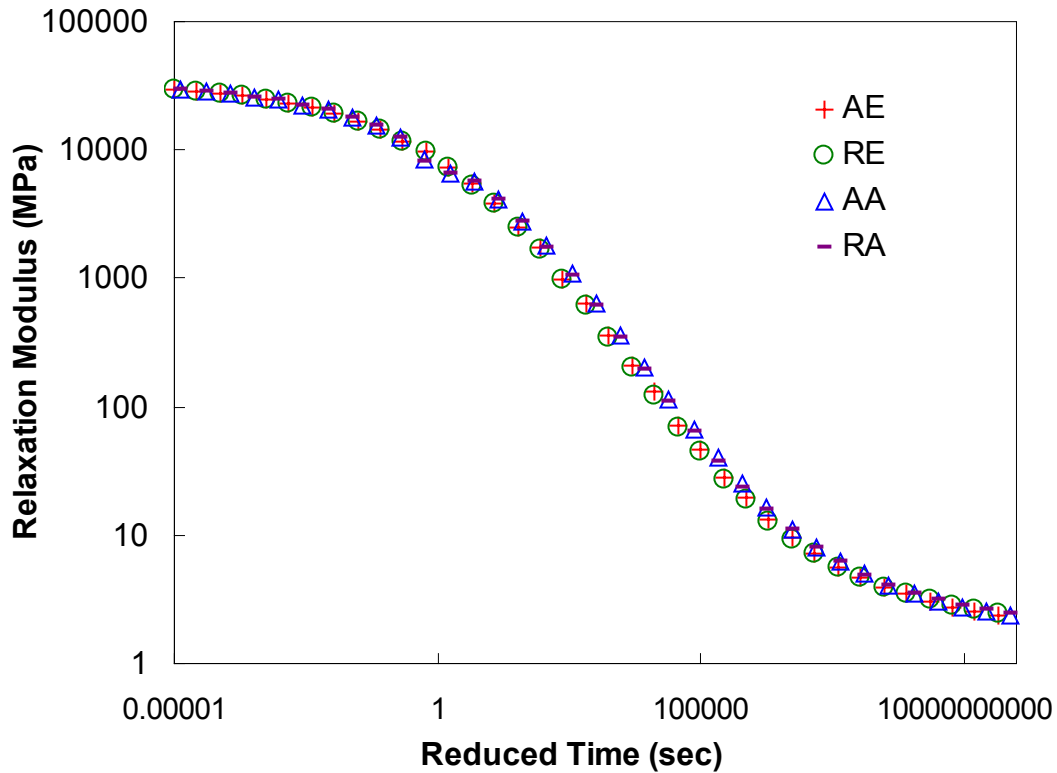


Figure 5.11. Relaxation modulus mastercurves obtained from different interconversion techniques

#### 5.4.2 Conversion from Complex Modulus to Creep Compliance

Creep tests were conducted at several temperatures and consequently creep mastercurves for individual specimens were constructed. However, as stated previously, since the LVE range is better defined for a complex modulus test and since the latter test is anyway needed as a viscoelastic fingerprint for the specimens tested, it would be advantageous to explore the methods of interconversion that enable the determination of the creep compliance from complex modulus. Values obtained from the interconversion can be compared to those obtained from testing to study the extent of accuracy or discrepancy.

Two interconversion methods will be presented. In the first one, exact mathematical formulation is used to convert directly from complex modulus to creep

compliance; while in the second method, the conversion is done via the relaxation modulus.

#### 5.4.2.1 Complex Modulus to Creep Compliance: Direct Conversion

The basis of this conversion method is based on the following exact relationship for linear viscoelastic materials:

$$D^* = \frac{1}{E^*} \quad (5.29)$$

where  $D^*$  and  $E^*$  are complex compliance and complex modulus respectively. From Equation (5.29), the storage compliance,  $D'$ , can be obtained from the following equation:

$$D' = \frac{E'}{(E')^2 + (E'')^2} \quad (5.30)$$

which further reduces to the following relationship:

$$D' = \frac{\cos \phi}{|E^*|} \quad (5.31)$$

Thus, the storage modulus of creep compliance is first obtained from the dynamic modulus and phase angle from data corresponding to all reduced frequencies tested. If

$D'$  is expressed in its prony series form, then through collocation, the Prony series coefficients for  $D'$  ( $D_n$  and  $\tau_n$ ) can be determined:

$$D' = D_0 + \sum_{n=1}^N \frac{D_n}{\omega_R^2 \tau_n^2 + 1}, \quad (5.32)$$

Then, those coefficients are used in the Prony series representation of creep compliance,

$D(\xi)$ :

$$D(\xi) = D_0 + \sum_{n=1}^N D_n (1 - e^{-\xi/\tau_n}) \quad (5.33)$$

#### 5.4.2.2 Complex Modulus to Creep Compliance: Through $E(t)$

After the complex modulus is converted to relaxation modulus, through any of the four aforementioned techniques, the obtained relaxation modulus can be converted to creep compliance through an approximate method (Daniel 2001). The approximate interconversion is based on the power law interrelationship between  $D(t)$  and  $E(t)$ . Both the creep compliance and relaxation modulus are represented in a pure power law form:

$$E(t) = E_1 t^{-n} \quad (5.34)$$

$$D(t) = D_1 t^n \quad (5.35)$$

where  $E_1$ ,  $D_1$ , and  $n$  are positive constants. From the theory of linear viscoelasticity and using Equations (5.34) and (5.35), the following relationship between  $D(t)$  and  $E(t)$  is obtained:

$$E(t)D(t) = \frac{\sin n\pi}{n\pi} \quad (5.36)$$

Since the power law cannot accurately represent either the creep compliance or the relaxation modulus over the entire range of behavior (the power law can not represent short or long time asymptotes), a local power law fit is used. In this way, the creep compliance over the entire time range of interest is represented by a series of local power law representations and the relaxation modulus in each of those ranges is calculated using Equation (5.36). From the converted data, the collocation method is used to determine the coefficients for the Prony series formulation of the creep compliance. Figure 5.12 illustrates the difference between the two interconversion methods along with a

comparison with the actual creep mastercurve obtained from testing (shift factors from storage modulus mastercurve). As observed, there is a significant difference between the three mastercurves presented. It is difficult to select a better interconversion method based on these results; however for this research, the conversion through  $E(t)$  was selected to obtain  $D(t)$  from  $E^*$ .

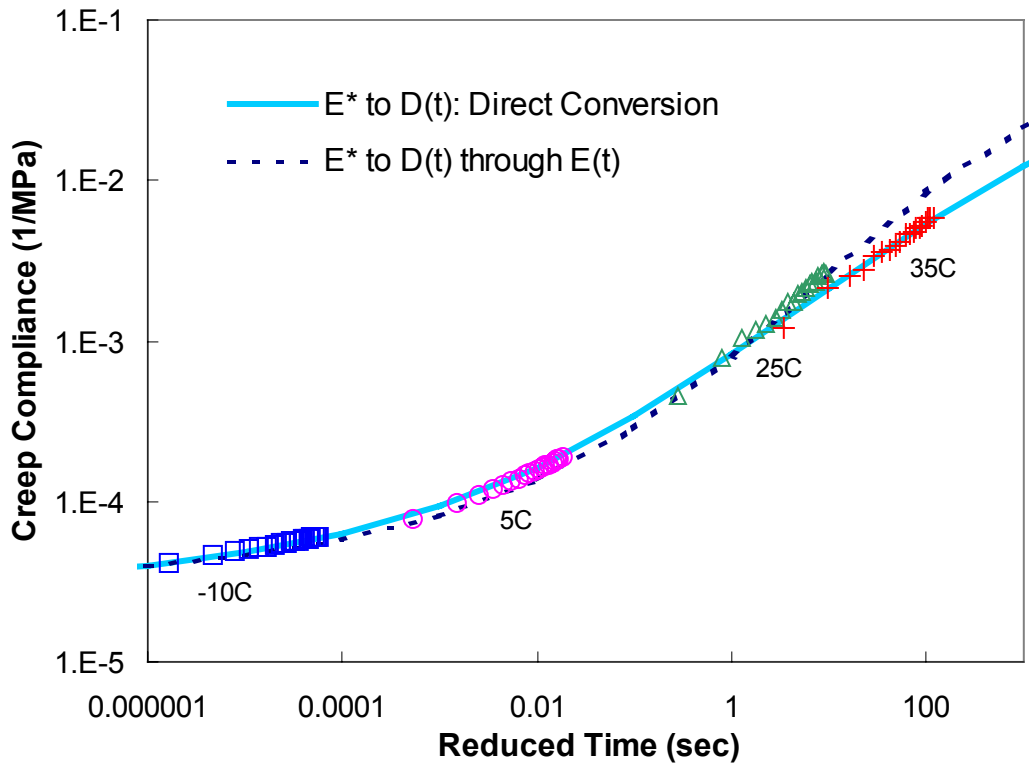


Figure 5.12. Interconversion from  $E^*$  to  $D(t)$

## **6 Validation and Application of Time-Temperature Superposition**

### **Principle in the Damaged State**

#### ***6.1 Introduction***

It has been presented earlier that asphalt concrete in its linear viscoelastic state is a thermorheologically simple material. That is, time-temperature superposition can be applied given that the material is in its undamaged state. As an application of that principle, data from complex modulus testing conducted within linear viscoelastic limits at different frequencies and temperatures should yield a single continuous mastercurve for dynamic modulus and phase angle as a function of frequency at a given reference temperature by horizontally shifting individual curves along the logarithmic frequency axis.

However, for comprehensive material modeling, laboratory testing often extends to the damaged state where micro- and macro-cracks in the asphalt concrete matrix develop and grow. It has not yet been shown that time-temperature superposition principle holds when the damage varies with time. If verified, one of the most important implications would be the reduction of the required laboratory testing program for comprehensive material characterization of asphalt mixtures.

The focus of this chapter is to determine whether asphalt concrete with time-dependent damage, including the formation of micro and macro-cracking and viscoplasticity, can still be considered a thermorheologically simple material so as to simplify the complex testing program required in this research; and more generally, to simplify characteristic and structural analysis of asphalt pavements. For that purpose, a

series of tests were conducted consisting of a linear viscoelastic complex modulus test followed by a constant crosshead rate test until failure in uniaxial tension mode at different temperatures and strain rates. The shift factors for the undamaged state were first determined by constructing the dynamic modulus mastercurve for a reference temperature; then, those shift factors were applied to the monotonic test data to construct a continuous stress versus log reduced time mastercurve for a given strain level. Theory shows (Schapery 1999) that in constant strain rate tests (for local or crosshead based strains), if mastercurves can be constructed for chosen strain levels, then the time-temperature superposition applies for asphalt concrete with growing damage.

## ***6.2 Sample Preparation and Testing Equipment***

Specimens used in this study were fabricated from 12.5-mm Maryland State Highway Administration Superpave mixtures. Information on the materials and mixture design, in addition to sample geometry were documented in a previous chapter. The testing machine used was the UTM-25. Displacements were measured using spring-loaded LVDTs; two with 75-mm gage length and two with 100-mm gage length attached to the middle section of the specimen at equal distances from the ends. As presented in an earlier chapter, using two different gage lengths enables the determination of the onset of localization since the opening of the major cracks that start to form in the asphalt matrix between the gage lengths would be numerically divided by two different gage lengths thus leading to two different strain values.

### **6.3 Testing Program**

The testing program adopted consisted of a series of complex modulus test followed by a constant crosshead-rate test in tension until failure of the specimen at several testing conditions. To check the applicability of time-temperature superposition with growing damage for a wide range of testing conditions, the number of testing conditions was increased and the number of test replicates was minimized, instead of conducting more test replicates over a narrower range of test conditions.

#### **6.3.1 Complex Modulus Test**

The complex modulus test was conducted first to obtain the linear viscoelastic properties of the specimen being tested and to determine the time-temperature shift factors for the undamaged state by constructing the storage modulus mastercurve as a function of reduced time.

#### **6.3.2 Constant Crosshead-Rate Tests**

After allowing enough time for any accumulated strain from the complex modulus testing to be recovered, each specimen was pulled at a constant crosshead rate until failure. Testing temperatures were the same as those of the complex modulus test, while crosshead strain rates varied between 0.000019 to 0.07 per second.

##### *6.3.2.1 Determination of Crosshead Strain Rates*

If the time-temperature superposition principle is applicable to asphalt concrete with growing damage, then the construction of a stress-log reduced time mastercurve for a given strain level should be feasible. To attempt that, common strain levels resulting from the various testing conditions need to exist so that the corresponding mastercurves

can be constructed. However, due to its viscoelastic nature (rate and temperature dependency), if the same loading rates are used for all the testing temperatures then it may not be possible to obtain strain levels common to all conditions. For example, for a slow loading rate at 40°C, the resulting strains will be much larger in value than the maximum strain resulting for the same strain rate at 5°C; consequently, mastercurves could only be constructed for those small strain levels common to both temperatures and smaller than the failure strain at 5°C.

To overcome that problem and obtain strains of comparable magnitudes at different testing conditions, different ranges of strain rates had to be used for different temperatures. Assuming that time-temperature superposition holds with growing damage, those rates can be determined according to the following scheme. For a given stress-log reduced time crossplot corresponding to a particular strain level, two points corresponding to temperatures  $T_1$  and  $T_2$  overlap if they have the same stresses and same log reduced times ( $\xi$ 's). Thus for a given stress,  $\log(\xi_1) = \log(\xi_2)$ . However,

$\log \xi = \log \frac{t}{a_T}$  and  $t = \frac{\varepsilon}{k'}$ , where  $\varepsilon$  is the strain and  $k'$  is the strain rate. Since the crossplot is for a constant strain level  $\varepsilon$ ,  $\log(k'_1 \times a_{T1}) = \log(k'_2 \times a_{T2})$ , or

$$\frac{k'_1}{k'_2} = \frac{a_{T2}}{a_{T1}} \quad (6.1)$$

Thus, knowing the strain rates for 25°C, Equation (6.1) can be used to determine strain rates at 5°C and 40°C that ensure overlap in the stress-log reduced time crossplot for a given strain level at the reference temperature of 25°C. The lowest rate at 5°C can be set to overlap with the second highest at 25°C and the highest at 40°C can be set to overlap with the second lowest rate at 25°C. Similarly, the above equation can be used to

determine strain rates at  $-10^{\circ}\text{C}$  that yield overlap with the  $5^{\circ}\text{C}$  data in the crossplot. Since it is proposed that time-temperature superposition is valid with growing damage in the analysis, shift factors from dynamic modulus may be used to estimate the specimen strain rates. The crosshead strain rates used in the testing program were presented in Chapter 3.

## 6.4 Experimental Results and Analysis

### 6.4.1 Complex Modulus Test

The main objective of conducting the complex modulus test is to obtain the LVE shift factors for the undamaged state. Ultimately, those shift factors will be used to check the validity of the time-temperature superposition in the damaged state. The details of the complex modulus testing and the method to obtain the LVE shift factors from the storage modulus were covered in previous chapters. Figure 6.1 shows the log shift factor variation with temperature for the specimens tested for the time-temperature validation.

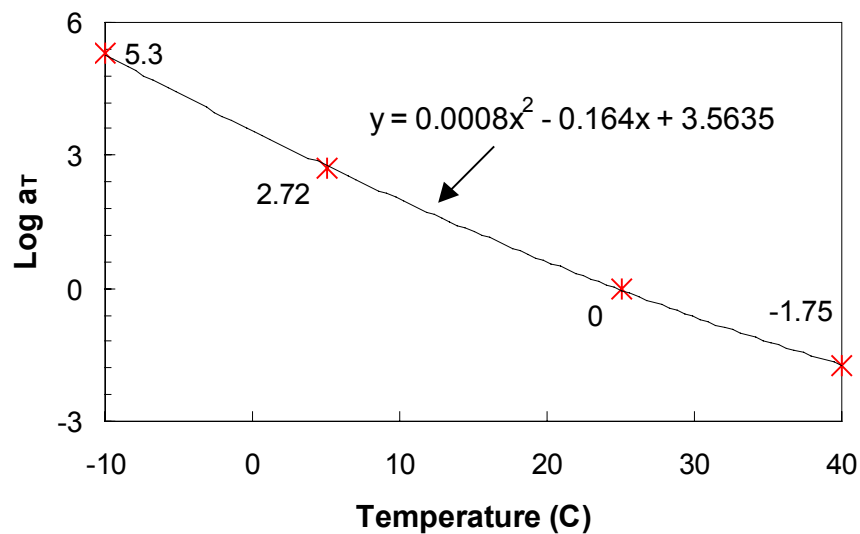


Figure 6.1. Log shift factor vs. temperature from complex modulus tests

## 6.4.2 Constant Crosshead-Rate Test

### 6.4.2.1 Stress-Strain Curves

A total of 20 tests were conducted at  $-10$ ,  $5$ ,  $25$ , and  $40^{\circ}\text{C}$ . All three tests at  $-10^{\circ}\text{C}$  failed in a brittle mode while loading; while at  $5^{\circ}\text{C}$ , only the two fastest rates failed in a brittle mode. Figures 6.2-6.5 are plots of stress-strain curves for the tests conducted at the four testing temperatures. Strains shown are those measured using 75-mm GL LVDTs mounted to the middle section of the specimen.

As observed from Figure 6.2, the stress-strain curves at  $-10^{\circ}\text{C}$  are very similar. The peak stress and its corresponding peak strain for the three tests are very comparable in value although the strain rates are very different, the fastest rate being 700 times faster than the slowest. This suggests that the rate dependence (viscoelastic behavior) is minimal at such low temperature. Figure 6.3 is a plot of stress-strain curves at  $5^{\circ}\text{C}$ . Tests at this temperature exhibit both failure modes, brittle and ductile. Tests conducted at a rate of 0.000056 exhibit a transitional failure mode; i.e., brittle fracture in the unloading stages (post-peak), where a single macro-crack develops abruptly after peak stress is reached and separates the specimen into two pieces. Figure 6.4 shows stress-strain plots of tests conducted at  $25^{\circ}\text{C}$ . There is a close match between the curves of replicates at the same rate. It is worthy of noting that for tests with failure occurring outside the gage length of the LVDTs, the strain measured using the LVDTs decreases because of strain recovery as the crack outside the LVDT grows. This can be observed for tests at strain rates of 0.0015, 0.0045, and 0.0135 per second. Comparing the stress-strain curves for all the temperatures, it is noted that strains corresponding to the peak stress are comparable for all strain rates when failure occurs in a ductile mode (Figures 6.4 and 6.5).

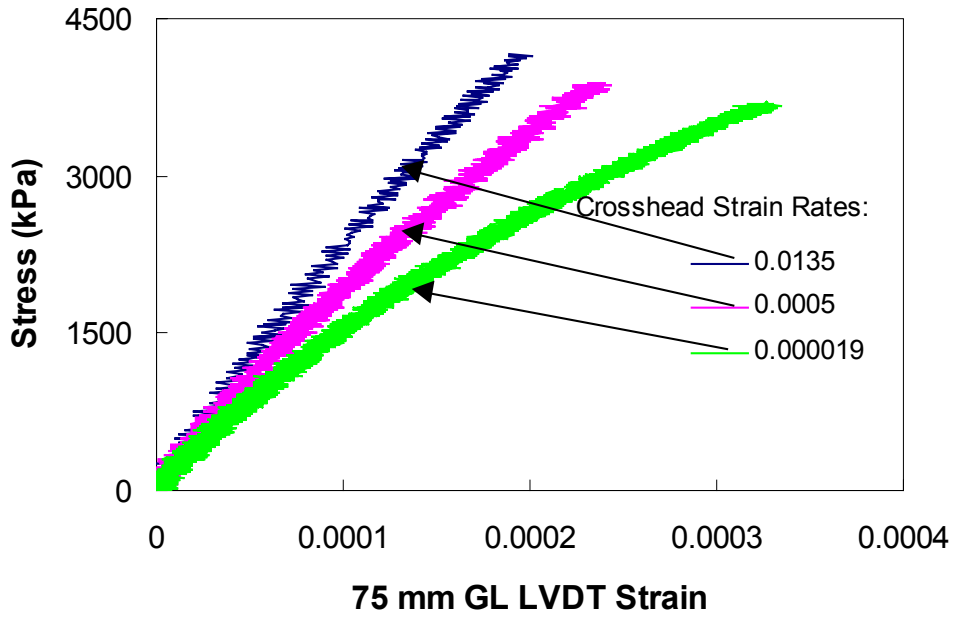


Figure 6.2. Stress-strain plot at  $-10^{\circ}\text{C}$  (1 specimen at each rate)

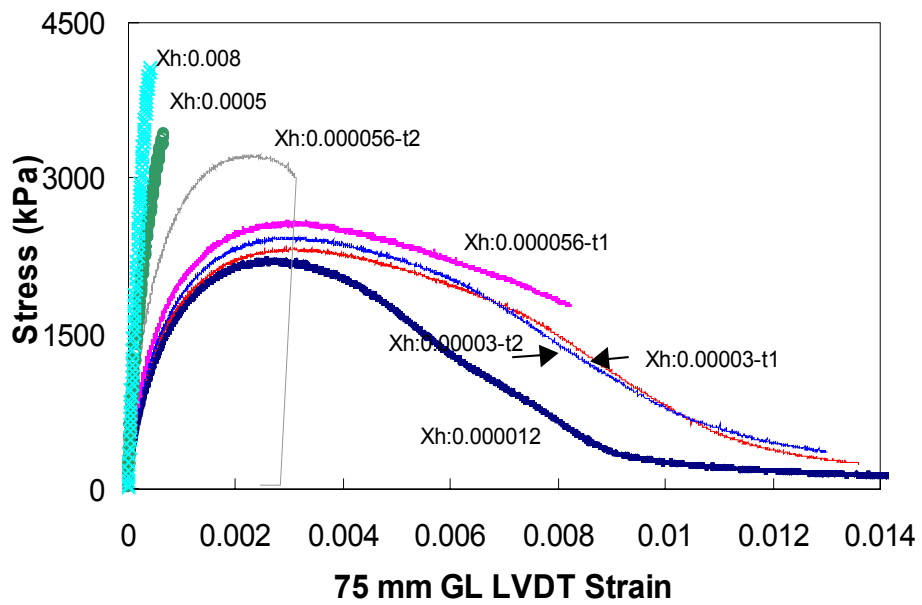


Figure 6.3. Stress-strain curves at  $5^{\circ}\text{C}$  (Crosshead strain rate and replicate number indicated next to each curve)

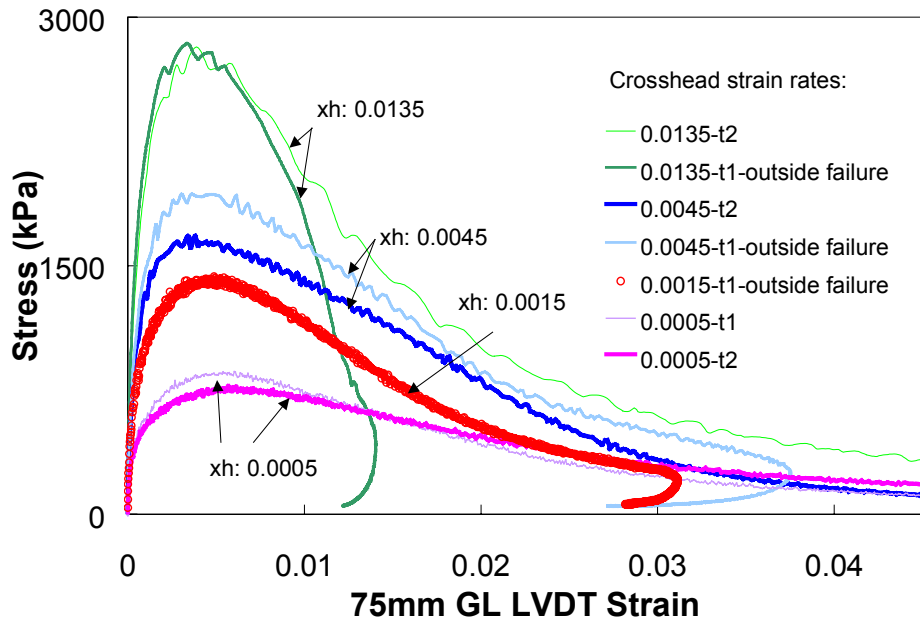


Figure 6.4. Stress-strain curves at 25°C (2 replicates at each rate except for 0.0015)

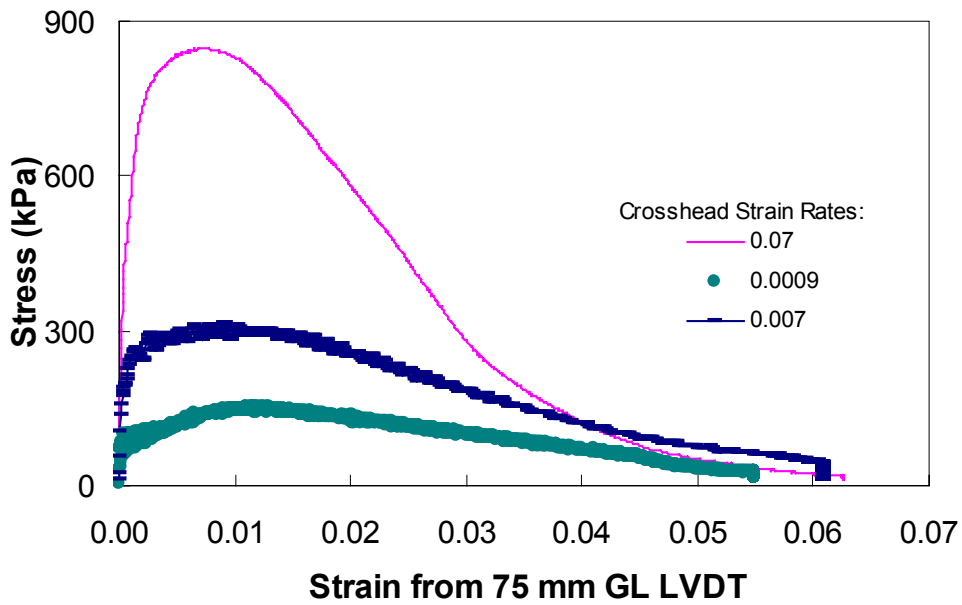


Figure 6.5. Stress-strain curves at 40°C (1 replicate per strain rate)

#### *6.4.2.2 Effect of Machine Compliance on Specimen Strains and Validity of Superposition Principle*

Because of machine compliance; i.e., deformation of certain machine components along the loading train under load, strains measured from the on-specimen and on-end plates LVDTs are smaller than those measured using the crosshead LVDT. The difference increases at low temperatures and high strain rates due to the increased stiffness of the material being tested. Also attributed to the machine compliance is the non-constant on-specimen strain rate, given that the crosshead strain rate remains constant throughout the test. For all tests, it was observed that the on-specimen LVDT strain rate followed a power law in time (up to a certain strain/time). Figure 6.6 illustrates this effect of machine compliance on specimen strain rates.

From the theoretical derivation, it is known that time-temperature superposition for damaged state can work, given that the specimen strain rate follows a pure power law, or more generally any strain that is defined by one time-scale parameter. However, for some tests a deviation from the power form occurs at the onset of strain localization if the top end plate displaces unevenly with respect to the horizontal plane. Figure 6.7 shows the onset of strain localization for a test at 5°C and strain rate of 0.00003. In this case, the onset of localization is the point where the stress-strain curves from the 75-mm GL, 100-mm GL, and plate to plate LVDTs start to deviate. After that deviation, data from those tests can not be used for superposition applications if the plate rotation occurs, and consequently the strain rate ceases to follow a pure power law. The corresponding uneven plate displacement (evident through the deviation of the two LVDT measurements, front and back) and effect on superposition is shown in Figure 6.8, while Figure 6.9 shows the

resulting deviation of strain from the power functional form. It is worthy noting that the problem of uneven plate displacement was mainly present for tests run at 5°C. This could be due to the high stiffness of the material at 5°C compared to 25° and 40°C. At -10°C, specimens failed in a brittle mode without any localization prior to failure, and thus uneven plate displacement did not occur.

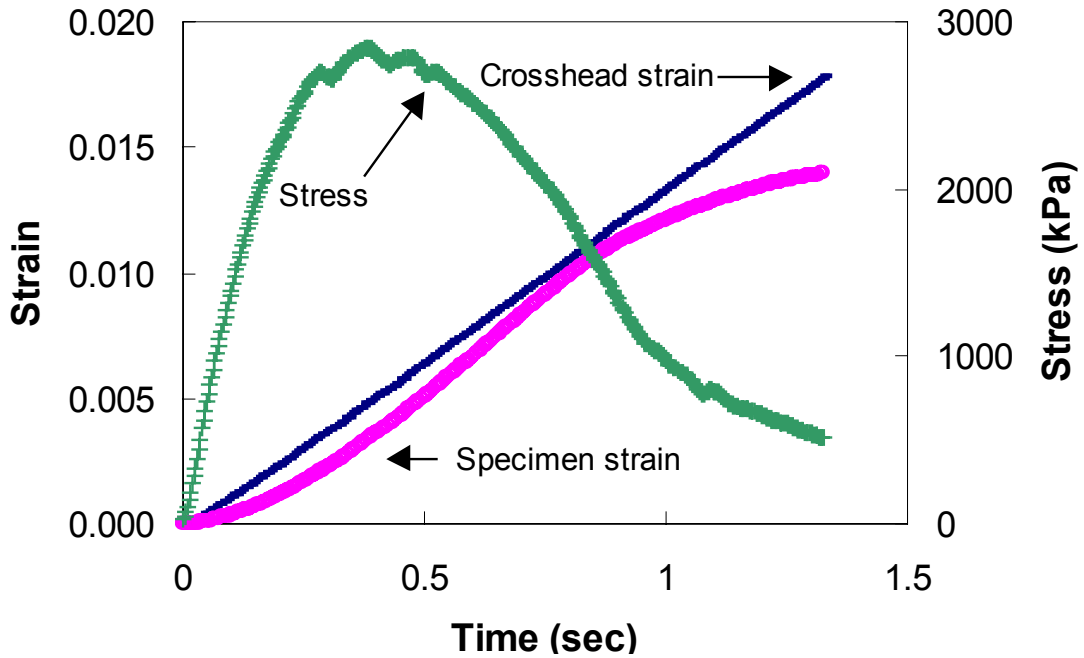


Figure 6.6. Difference between crosshead and on-specimen 75 mm GL LVDT strains for a monotonic test conducted at 25°C and 0.0135 strains/sec

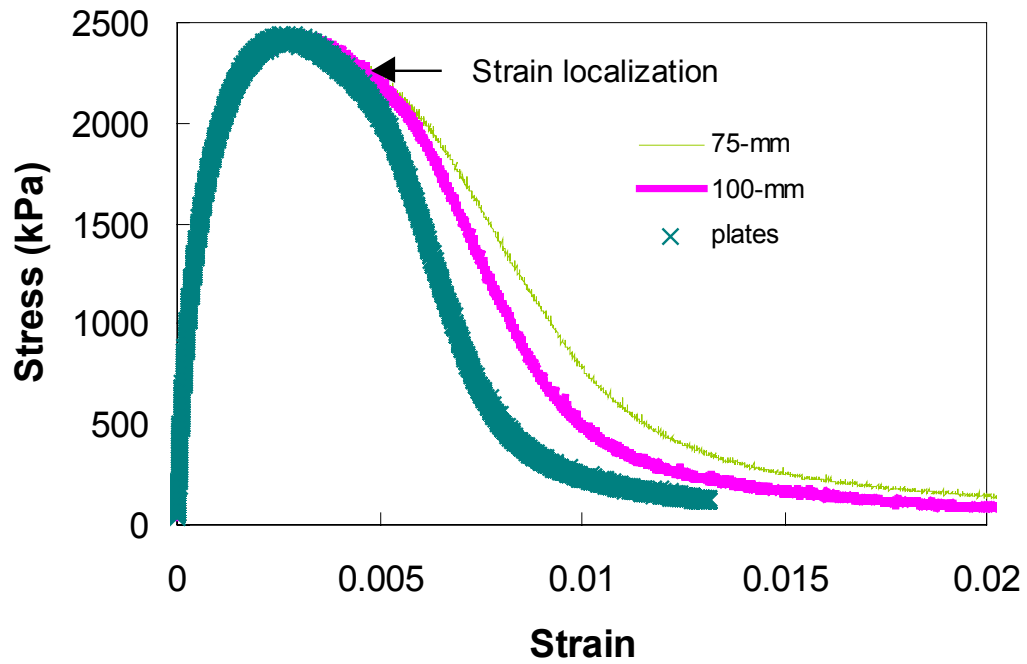


Figure 6.7. Detection of strain localization for a strain rate of 0.00003 at 5°C

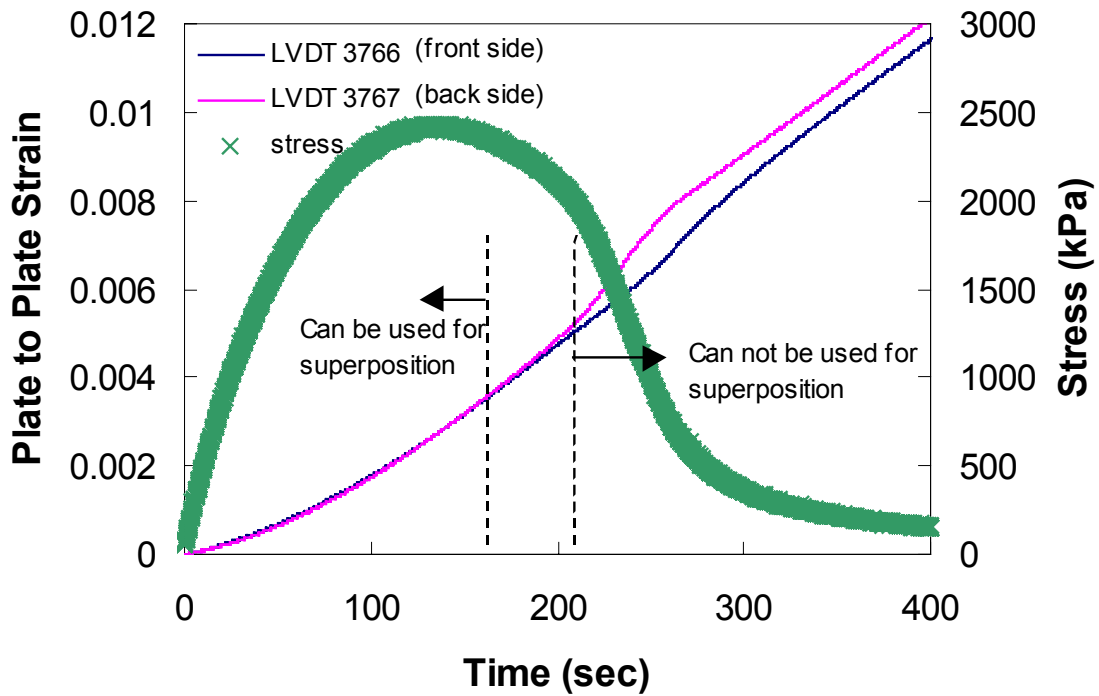


Figure 6.8. Plate uneven displacement (just after 200 seconds) and effect on superposition for a test at a strain rate of 0.00003 at 5°C

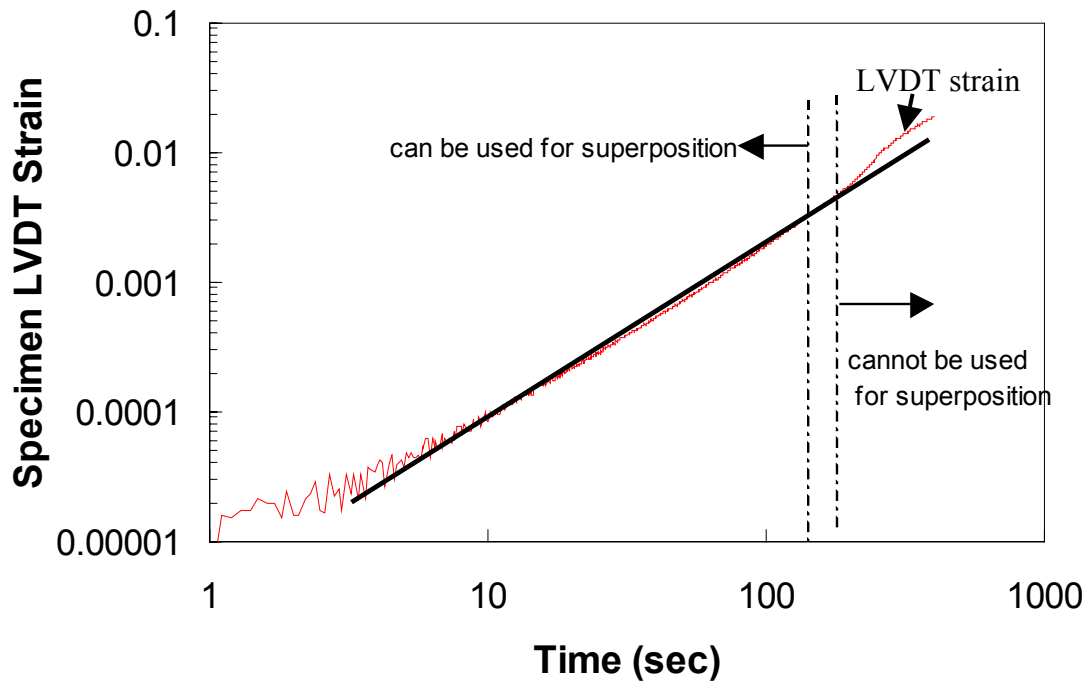


Figure 6.9. On-specimen LVDT strain deviation from pure power law (linear on log-log scales) and effect on superposition for the same test presented in Figures 6.7 and 6.8

#### 6.4.2.3 Checking for Non-Linear Viscoelasticity and Damage

When asphalt concrete is subjected to small load levels that do not induce damage such as micro-cracking or permanent deformation in the asphalt-aggregate matrix, it can be regarded as a linear viscoelastic material. For complex modulus testing, this is ensured by limiting the strains to about 70 microstrains. For constant crosshead rate tests in tension, the material exhibits linear viscoelastic behavior during initial loading and then as microcracks start to develop, a reduction in stiffness starts to occur and non-linear behavior prevails.

Upon conducting tests at different strain rates at  $-10^{\circ}\text{C}$  it was observed that stress-strain curves were very similar and almost linear. In addition, strains up to failure were very small indicating the possibility that the material does not undergo damage until

brittle fracture occurs. This may suggest that the material at  $-10^{\circ}\text{C}$  and at the range of rates tested and at  $5^{\circ}\text{C}$  for rates that caused brittle failure is linearly viscoelastic with no damage accumulating until the point of brittle fracture. If true, this finding could reduce the testing program and simplify modeling tasks. The finding is also critical for thermal cracking applications, where it is assumed that the material at freezing temperatures is linearly viscoelastic. As a byproduct of checking for the non-linearity/damage, the range of strains at which the material starts to accumulate damage can be known. It is for those strain values and higher that the time-temperature superposition for damaged states should be checked.

To check whether the non-linearity in the stress-strain curve in the constant crosshead rate tests at  $-10^{\circ}\text{C}$  and  $5^{\circ}\text{C}$  is due to rate dependency/viscoelasticity or due to stiffness reduction attributed to damage, the secant modulus from the constant crosshead rate tests is compared to the relaxation modulus obtained from the dynamic modulus. Since the complex modulus test does not damage the specimen due to the low strain amplitude (70 microstrains), the dynamic modulus characterizes the undamaged behavior of the material. If the secant modulus is related to the relaxation modulus as predicted from linear theory, then there is no damage occurring in the constant crosshead tests until the instance of immediate brittle fracture. This relationship is derived in the following formulation.

Assuming linear viscoelastic behavior, the convolution integral applies:

$$\sigma = \int_0^{\xi} E(\xi - \tau) \frac{d\varepsilon}{d\tau} d\tau \quad (6.2)$$

where  $\xi$  is reduced time,

$E(\xi)$  is the relaxation modulus at a reduced time  $\xi$ ,

$\varepsilon$  is strain,

$\sigma$  is stress, and

$\tau$  is an integration variable.

For a constant crosshead rate test:

$$\frac{d\varepsilon}{d\tau} = k \quad (6.3)$$

where  $k$  is the reduced strain rate. Equation (6.2) becomes:

$$\sigma = k \int_0^{\xi} E(\xi - \tau) d\tau \quad (6.4)$$

Representing  $E(\xi)$  in a generalized power law form, Equation (6.4) becomes:

$$\begin{aligned} \sigma &= k \int_0^{\xi} (E_0 + E_1(\xi - \tau)^{-n}) d\tau \\ \sigma &= k(E_0\xi + \frac{E_1}{1-n} \times \xi^{1-n}) \\ \sigma &= k\xi(E_0 + \frac{E_1}{1-n} \times \xi^{-n}) \end{aligned} \quad (6.5)$$

Since  $\varepsilon = k \times \xi$ , Equation (6.5) then becomes:

$$\frac{\sigma(\xi)}{\varepsilon(\xi)} = E_0 + \frac{E_1}{1-n} \times \xi^{-n} \quad (6.6)$$

where  $\frac{\sigma}{\varepsilon}$  is the secant modulus. Since  $n$  is very small at low temperatures, it can be

stated from Equation (6.6) that the secant modulus is approximately equal to the relaxation modulus for constant crosshead rate tests with no damage; i.e., linear viscoelastic conditions.

To do the comparison, the dynamic modulus mastercurve constructed as a function of reduced frequency has to be converted to relaxation modulus as a function of reduced time. For that purpose, the approximate interconversion method, presented in an earlier chapter, is used. Figure 6.10 shows the secant modulus curves obtained from all three tests conducted at  $-10^{\circ}\text{C}$  plotted with the relaxation modulus curve at a reference temperature of  $25^{\circ}\text{C}$ ; while, Figure 6.11 shows the secant modulus curves obtained from three monotonic tests at  $5^{\circ}\text{C}$ . For  $5^{\circ}\text{C}$ , only the crosshead rate test conducted at 0.008 per sec yielded brittle failure; whereas the other rates, which can be classified as medium and slow rates, yielded ductile failure conditions.

As seen, the secant modulus curves overlap well on top of the relaxation modulus mastercurve for tests at  $-10^{\circ}\text{C}$ . This suggests that at those testing conditions the material is linearly viscoelastic, and no measurable damage is accumulated as the specimen is pulled apart in tension until sudden brittle fracture occurs. On the other hand, at  $5^{\circ}\text{C}$  the 0.008 per sec test exhibits little damage just before the specimen fails; but for the other rates the secant modulus and relaxation modulus curves diverge, suggesting that damage is accumulating as the specimen is pulled apart.

It can thus be stated that for tests at  $-10^{\circ}\text{C}$ , negligible damage accumulates as the specimen is strained. Since the applicability of time-temperature superposition is to be verified for strain levels corresponding to the damaged state, strain levels higher than those resulting at  $-10^{\circ}\text{C}$  should be used for the construction of stress-log reduced time mastercurves.

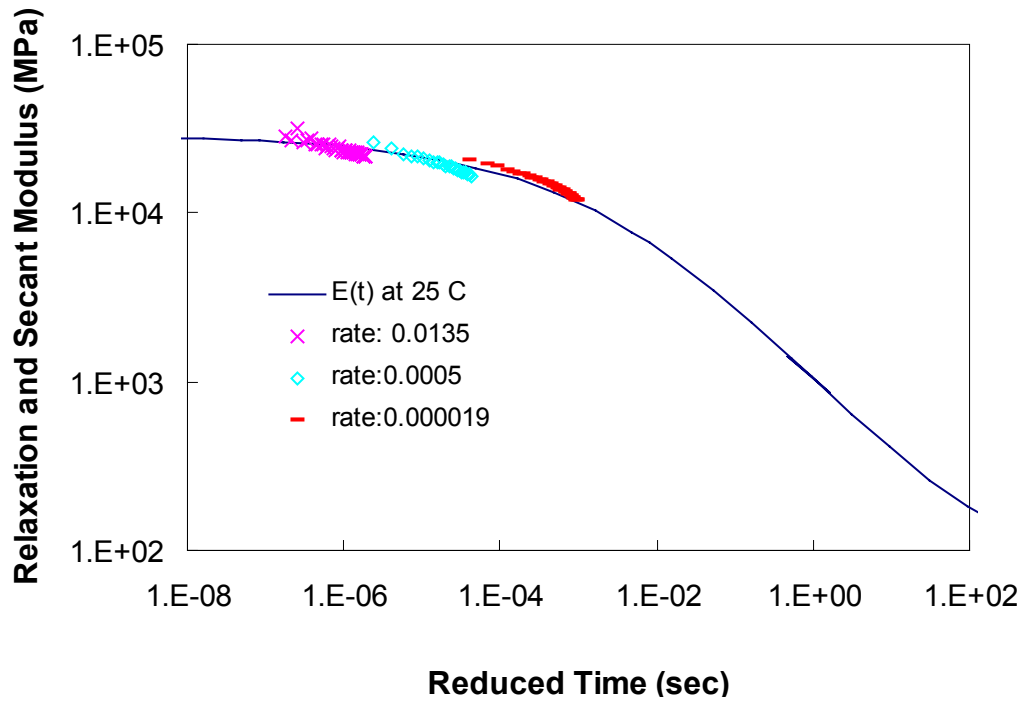


Figure 6.10. Secant modulus from constant crosshead rate tests conducted at  $-10^{\circ}\text{C}$  and relaxation modulus mastercurve at a reference temperature  $25^{\circ}\text{C}$

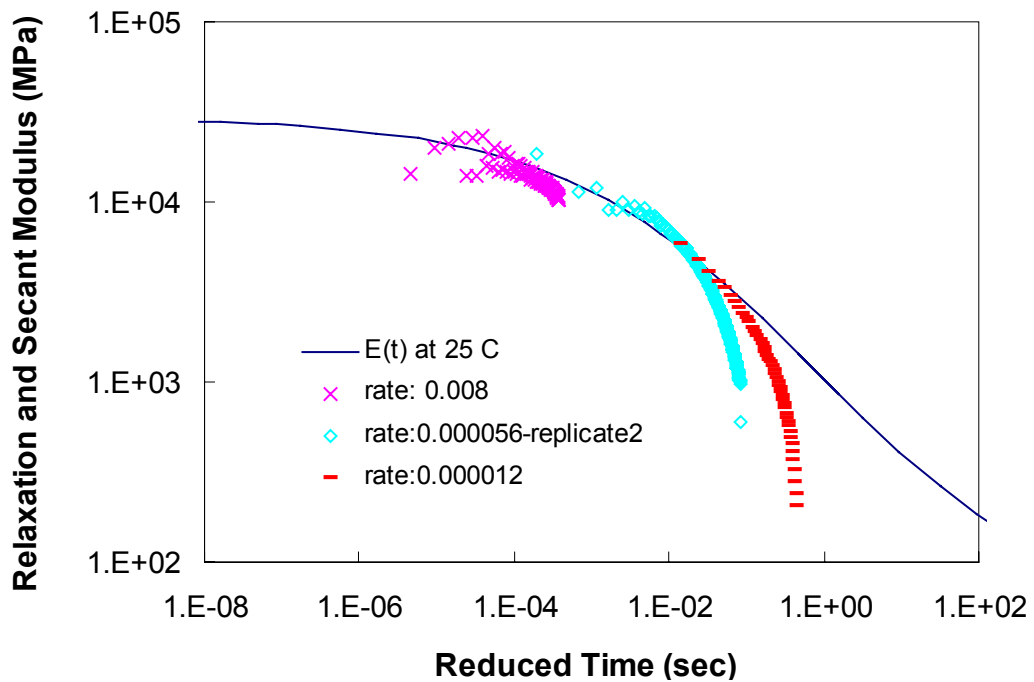


Figure 6.11. Secant modulus from constant crosshead rate tests conducted at  $5^{\circ}\text{C}$  and relaxation modulus mastercurve at a reference temperature  $25^{\circ}\text{C}$

#### *6.4.2.4 Time-Temperature Superposition with Growing Damage*

Asphalt concrete mixtures can be regarded as thermorheologically simple if, for a given strain level, a stress-log reduced time mastercurve can be constructed. Since the undamaged state is a special case of the damaged state, the shift factors determined earlier for constructing the dynamic modulus mastercurve should match those applied to construct the stress-log reduced time mastercurve. Moreover, the shift factors should only be a function of temperature and independent of strain level.

The procedure begins by selecting several strain levels for which the mastercurves are to be constructed. The strain levels should be large enough to be representative of the damaged state of the mixture, as discussed in the previous section. The strain levels presented in this research correspond to initial loading, pre-peak, peak and post-peak regions on the stress-strain curves. Even with very slow strain rates, the strain levels corresponding to the entire stress-strain curves at  $-10^{\circ}\text{C}$  were very small. Even at  $5^{\circ}\text{C}$ , the fast strain rate tests yielded low strain levels. Thus, for high strain levels there were no data from those tests that could be included for the superposition of crossplots.

For each selected strain level and testing temperature, the corresponding stress level and time from the tests conducted are obtained (Figure 6.12) and cross-plotted to form a stress versus time crossplot. This is repeated for all selected strain levels and testing temperatures. The next step is to plot the stress-time crossplot for each strain level and temperature on one graph (Figure 6.13(a)). Then, to construct the mastercurve at  $25^{\circ}\text{C}$  for a given strain level, the stress-time crossplot for that strain level and for each temperature is shifted along the logarithmic time axis using the appropriate shift factor  $a_T$  determined from the dynamic modulus testing. Figure 6.13(b) is the resulting stress-log

reduced-time crossplot schematic for an on-specimen strain of 0.005. Actual crossplots for selected strains are presented in Figures 6.14 a-l. As observed, the crossplots are smooth and continuous suggesting that superposition is valid with growing damage. For strain levels greater than 0.00019, there was no data from  $-10^{\circ}\text{C}$  tests due to early failure as discussed previously. For strains greater than 0.006, points from  $5^{\circ}\text{C}$  tests start to deviate from the reduced crossplot due to plate rotation as discussed previously. For strains larger than 0.01, only data from tests conducted at  $25^{\circ}\text{C}$  and  $40^{\circ}\text{C}$  could be incorporated. For comparison of mastercurves, three strain levels corresponding to initial, pre-peak and post-peak regions on the stress-strain curves are plotted in Figure 6.15 (a) on a single graph at reference temperature of  $25^{\circ}\text{C}$ .

#### *6.4.2.5 Time-Temperature Superposition with Growing Damage Using Crosshead Strains*

In the previous section it was shown that by using the shift factors from the undamaged state stress-log reduced time mastercurves could be constructed for the desired LVDT strains. Thus, it can be stated that using LVDT strains, asphalt concrete is thermorheologically simple with growing damage. However, it still remains to be seen whether mastercurves can be constructed using crosshead strains. As presented in Appendix C, deformations in the load cell and various connections along the loading train (machine compliance) are causing a difference between measured deformations from the crosshead and the LVDTs.

However, since it was shown that deformations due to machine compliance are elastic, then shift factors characterizing the viscoelastic (and possibly viscoplastic) component will correspond only to the material and thus should be the same as those

obtained using on-specimen LVDT strains. Using those shift factors, the same procedure used before for constructing stress-log reduced time mastercurves for LVDT strains is repeated using crosshead-based strains. Mastercurves for selected strains are presented in Figure 6.15 (b).

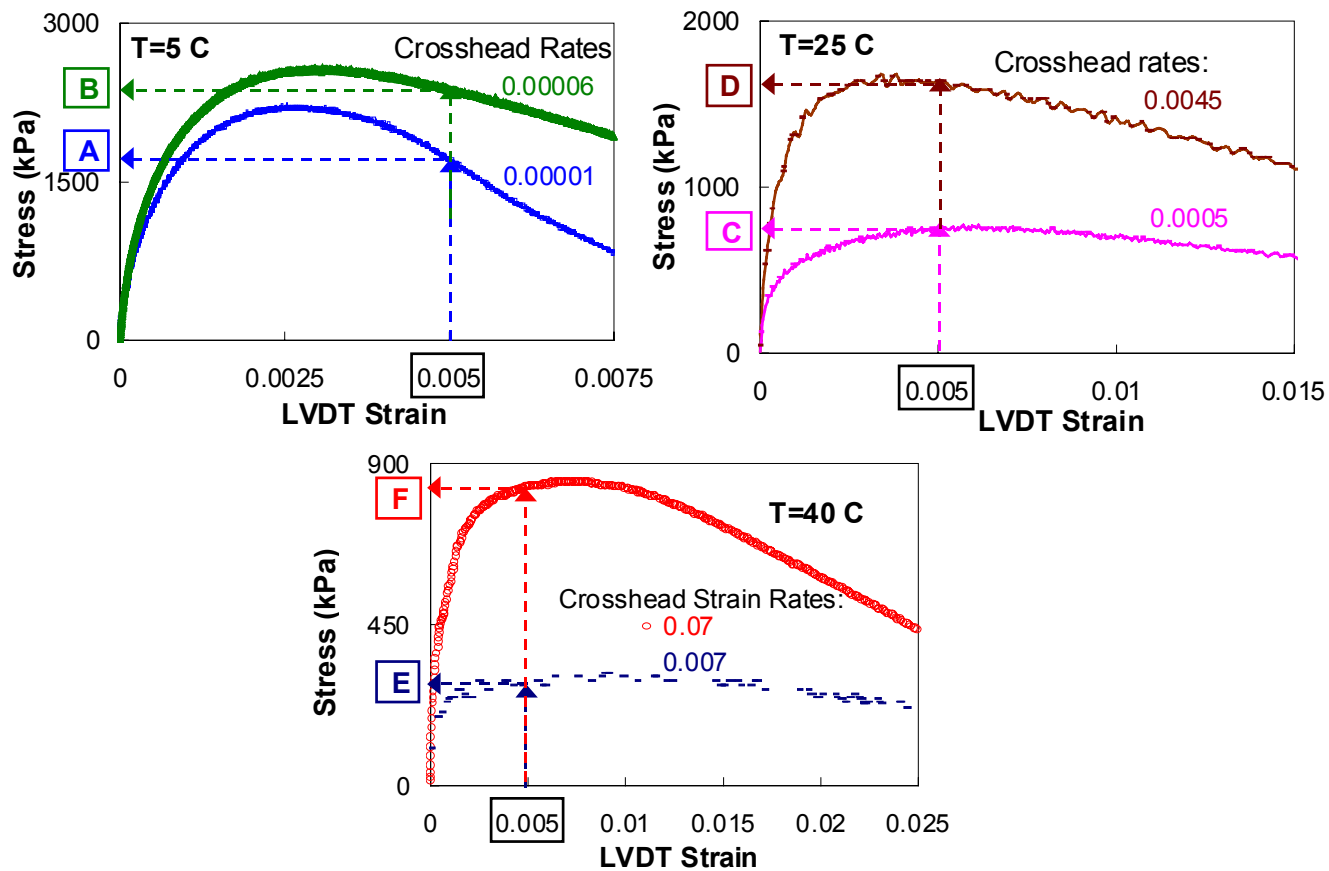
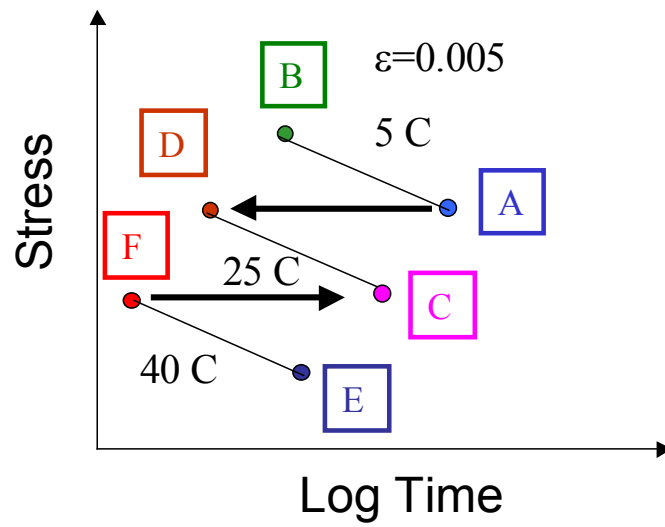
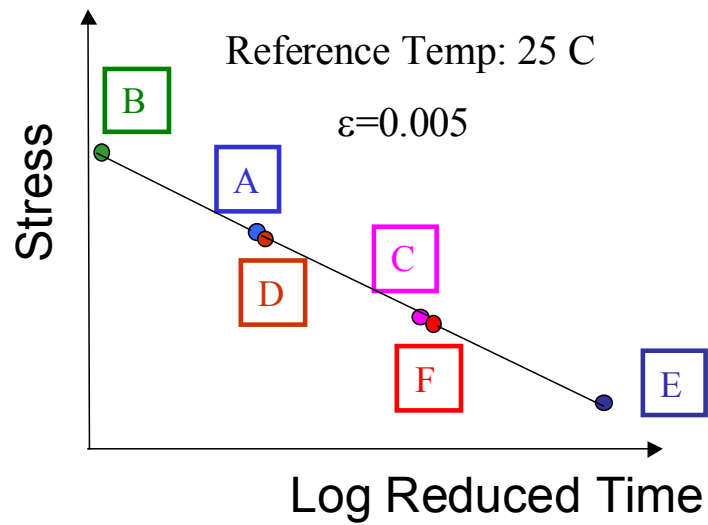


Figure 6.12. Determining stress for a strain of 0.005 for different crosshead rate tests at different temperatures



(a)



(b)

Figure 6.13. (a) Crossplot of stress and log time for a strain of 0.005; (b) crossplot of stress and log reduced time at 25°C for a strain of 0.005 after applying the LVE shift factor

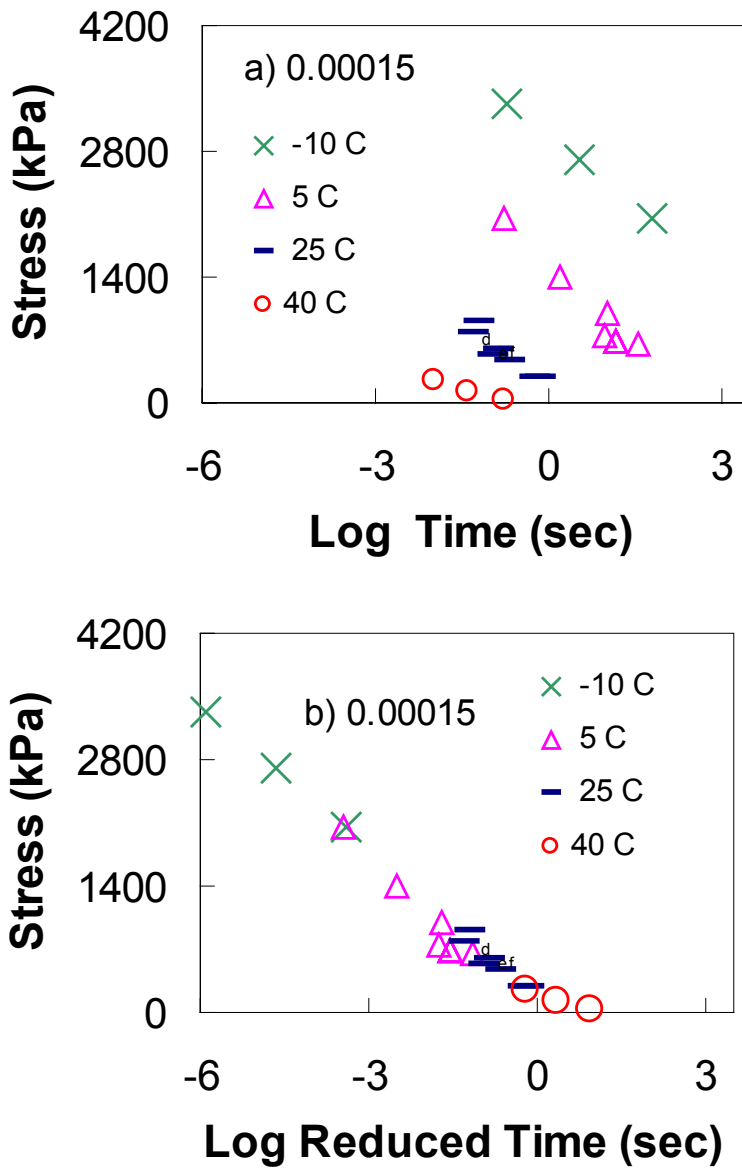


Figure 6.14. (a) and (b): Crossplots for 0.00015 LVDT strain before and after shift respectively

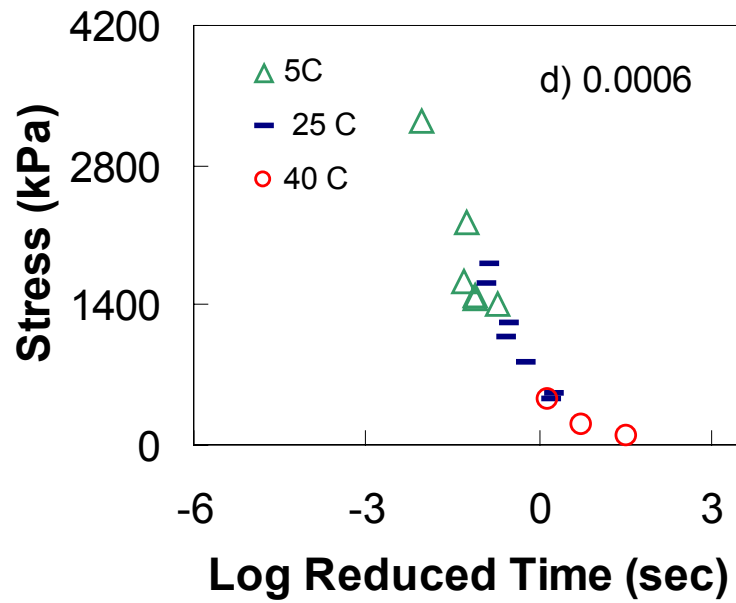
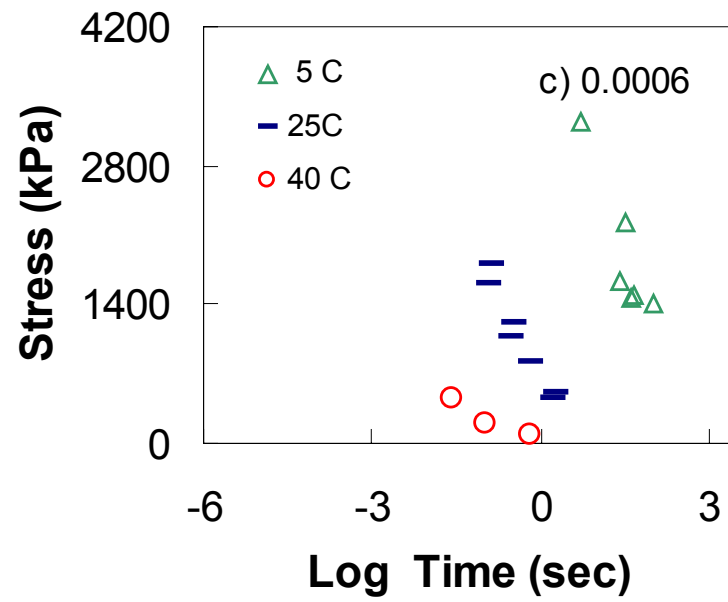


Figure 6.14. (c) and (d): Crossplots for 0.0006 LVDT strain before and after shift respectively

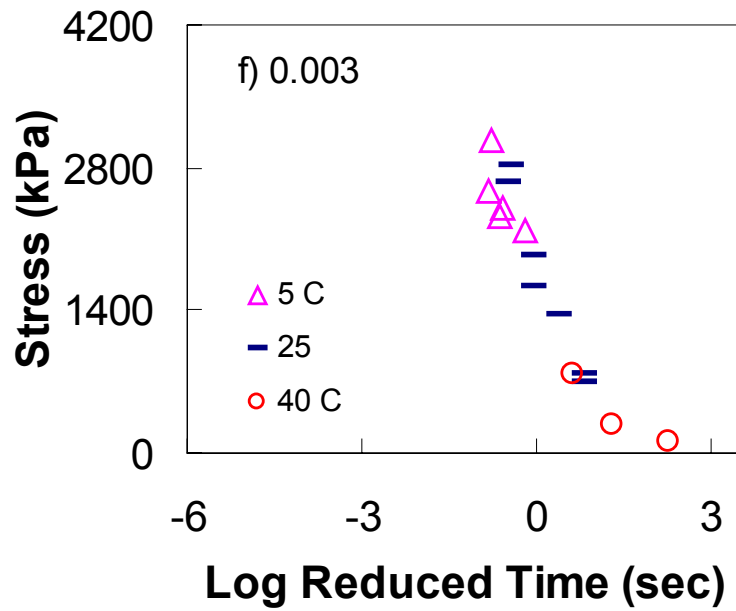
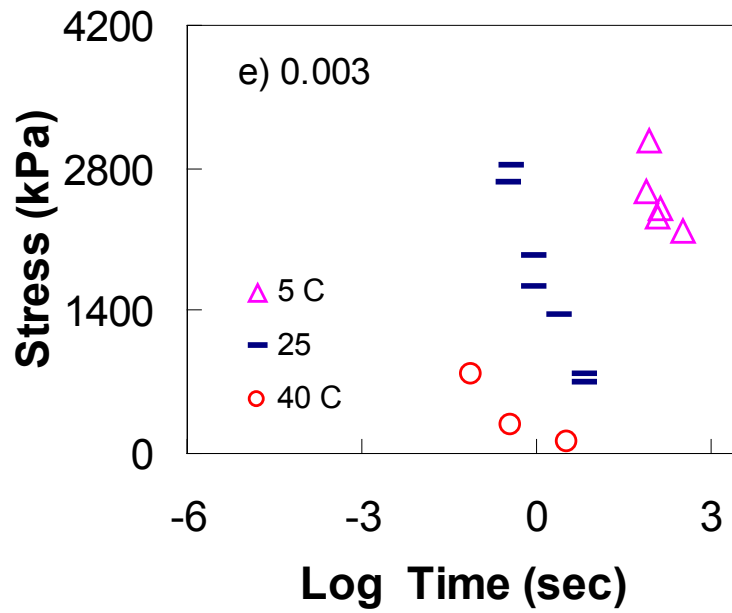


Figure 6.14. (e) and (f): Crossplots for 0.003 LVDT strain before and after shift respectively

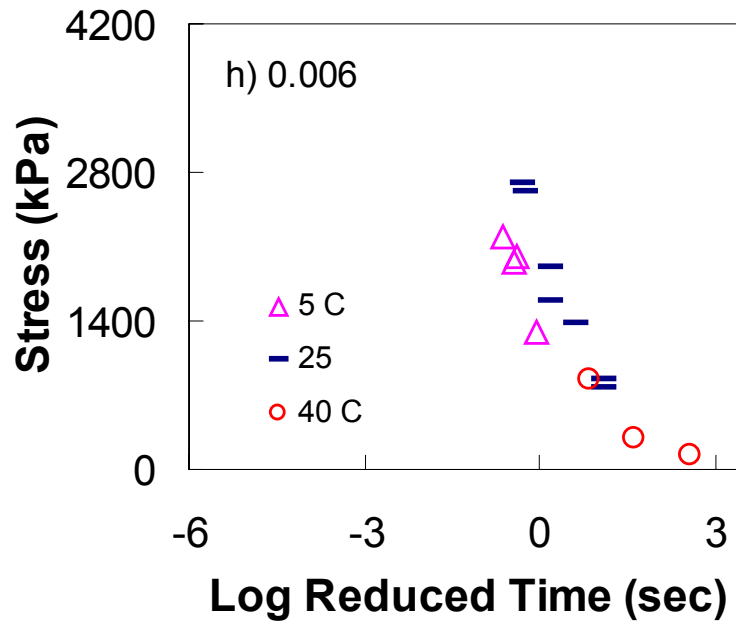
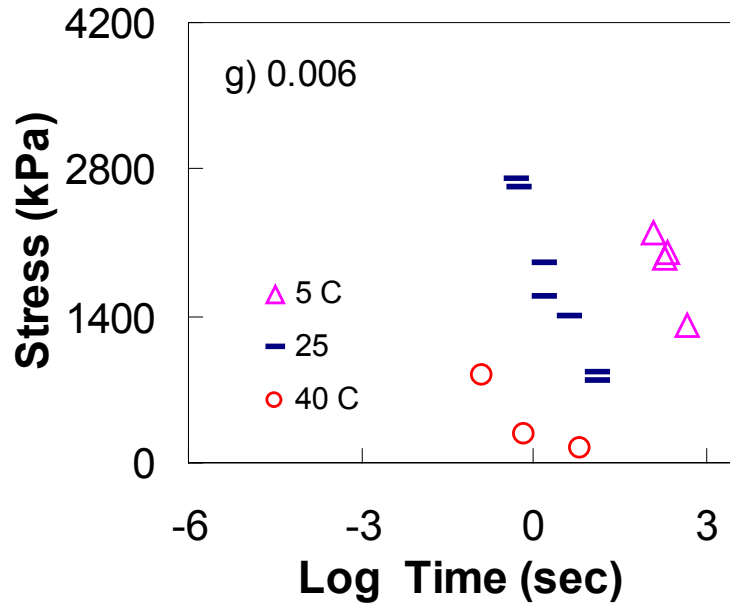


Figure 6.14. (g) and (h): Crossplots for 0.006 LVDT strain before and after shift respectively

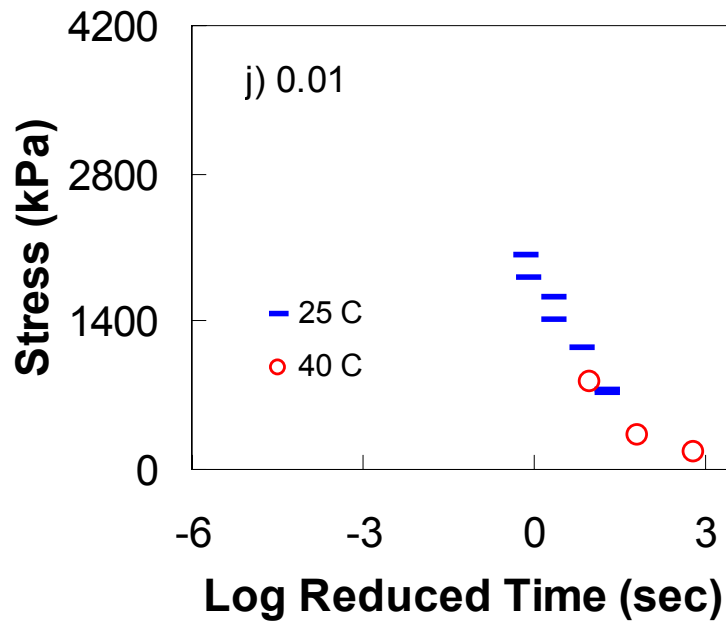
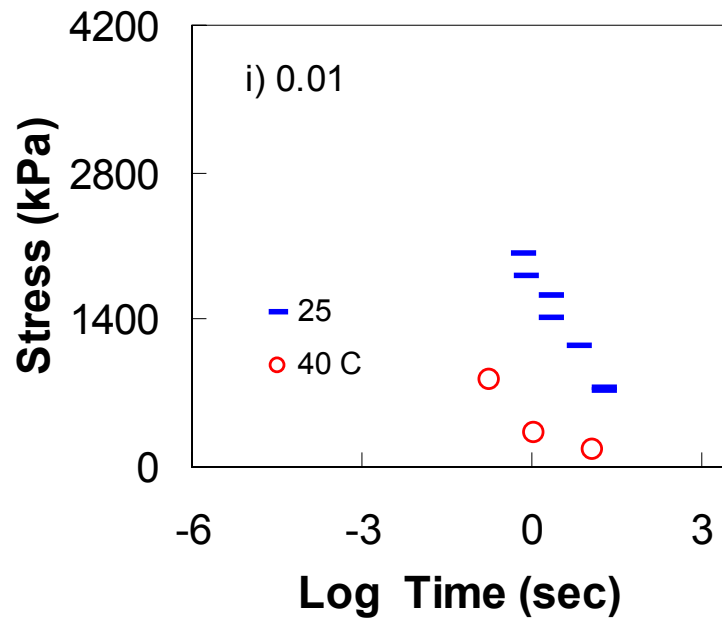


Figure 6.14. (i) and (j): Crossplots for 0.01 LVDT strain before and after shift respectively

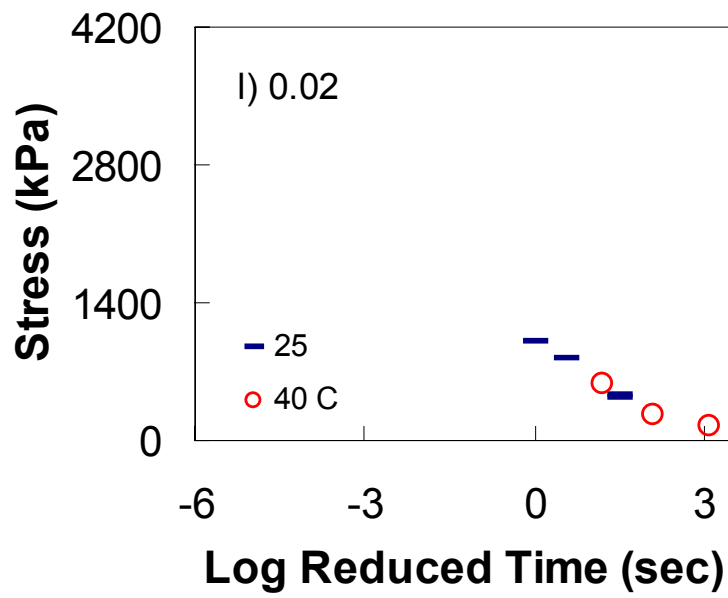
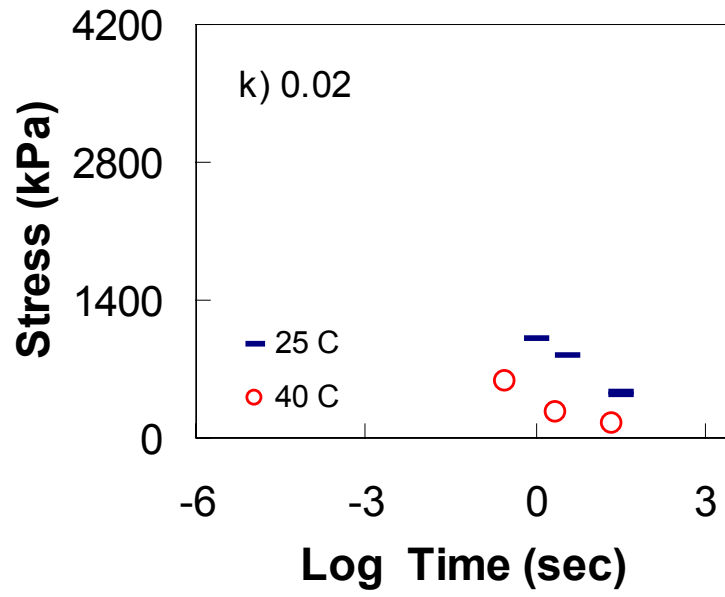
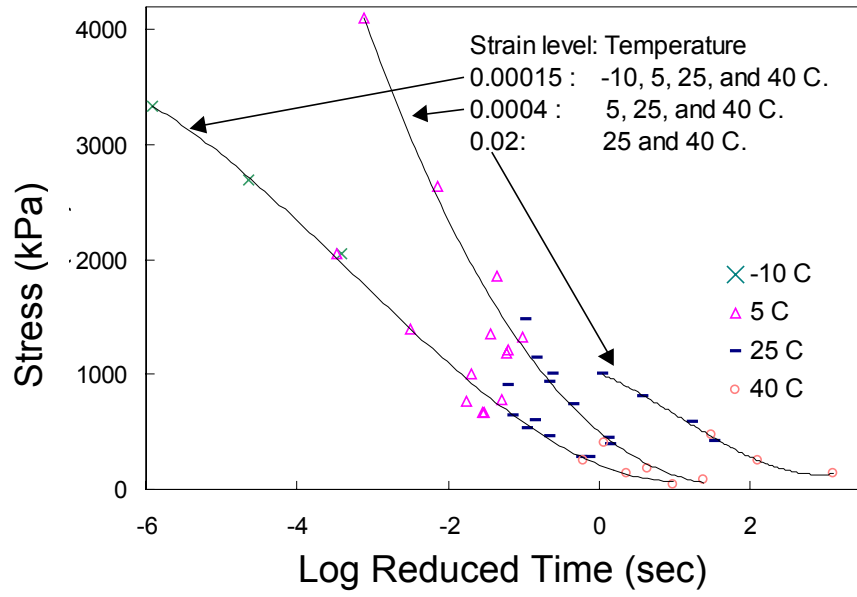
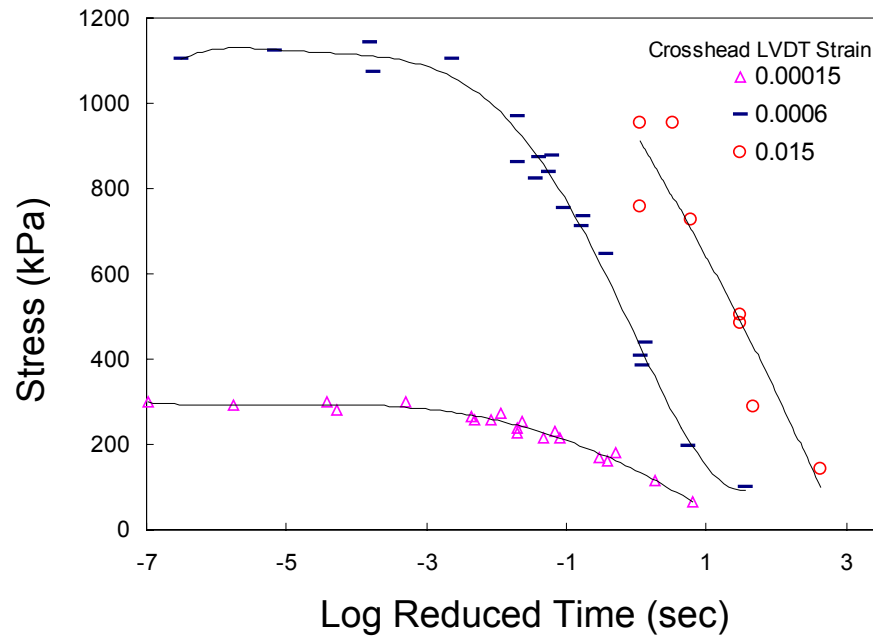


Figure 6.14. (k) and (l): Crossplots for 0.02 LVDT strain before and after shift respectively



(a)



(b)

Figure 6.15. (a) Crossplots for selected LVDT strains; (b) Crossplots for crosshead LVDT strains

## ***6.5 Applications Using Time-Temperature Superposition with Growing Damage***

A direct benefit of the validity of time-temperature superposition with growing damage is the reduction in any testing program required for modeling purposes due to the consequent reduction in the testing conditions. However, the benefit is not limited to this but extends to other applications as well. Samples of possible applications are presented in this section.

### **6.5.1 Reduction of Testing Program: Application to Repeated Creep and Recovery Test**

Since it was proven that time-temperature superposition holds even in the damaged state (microcracking and viscoplasticity), the strains for a particular test history can thus be predicted by performing a test with the same loading history and same reduced time history at another testing temperature. As an application, repetitive creep and recovery tests in uniaxial tension were conducted at 25 and 35°C with the same reduced time history and stress amplitude. The unloading and loading ramp reduced times were constant for all cycles; whereas, the loading and recovery reduced times increased by a factor of 2 from one cycle to the other until failure of the specimen. The ratio of recovery to loading time was 10 to 1. The stress amplitude was held constant for all cycles and was the same for both temperatures. Two replicates were tested at each temperature. The reduced loading times chosen are relatively short in order to replicate as much as possible realistic loading times in real pavements and to shorten the overall test duration. Once the reduced time history at 25°C was selected (Figure 6.16(a)), the LVE shift factors were used to determine the time history that needed to be applied at 35°C (Figure 6.16(b)) to yield the same reduced time history as that of the test at 25°C. The

load was chosen to yield failure in about 8 to 9 cycles. Test parameters for tests at 25 and 35°C are shown in Tables 6.1 and 6.2 respectively.

Preceding each test, a complex modulus test at 25°C was conducted to obtain the viscoelastic fingerprint of the specimen tested. Strains during creep loading and recovery were normalized using the data from the complex modulus test. The storage modulus of each specimen at each frequency was divided by that of a reference storage modulus (obtained from earlier baseline testing done on five specimens) yielding a normalizing factor for that frequency. The normalizing factors for the six frequencies: 20, 10, 3, 1, 0.3 and 0.1 Hz were then averaged to obtain a single representative normalizing factor for that specimen. Strains during creep and recovery were multiplied by that factor to obtain the normalized strains.

Figures 6.17(a) shows the normalized strain as a function of time at 25 and 35°C. Then, as the shift factors are applied to convert time at 35°C to reduced time at 25°C, the strain curves at 35°C are shifted along the reduced time axis to overlap with the strains obtained from the testing conducted at 25°C (Figure 6.17(b)). Figure 6.18, is a plot of strains as a function of time/reduced time, similar to Figure 6.17, but in log-log scale. The good overlap of the strain response when plotted against reduced time is an additional validation of the time-temperature superposition principle for asphalt concrete all the way till failure.

The significance of the observed overlap of strain histories for tests at different temperatures but with the same reduced time and loading history is the reduction of required number of testing at different temperatures. For example, instead of running

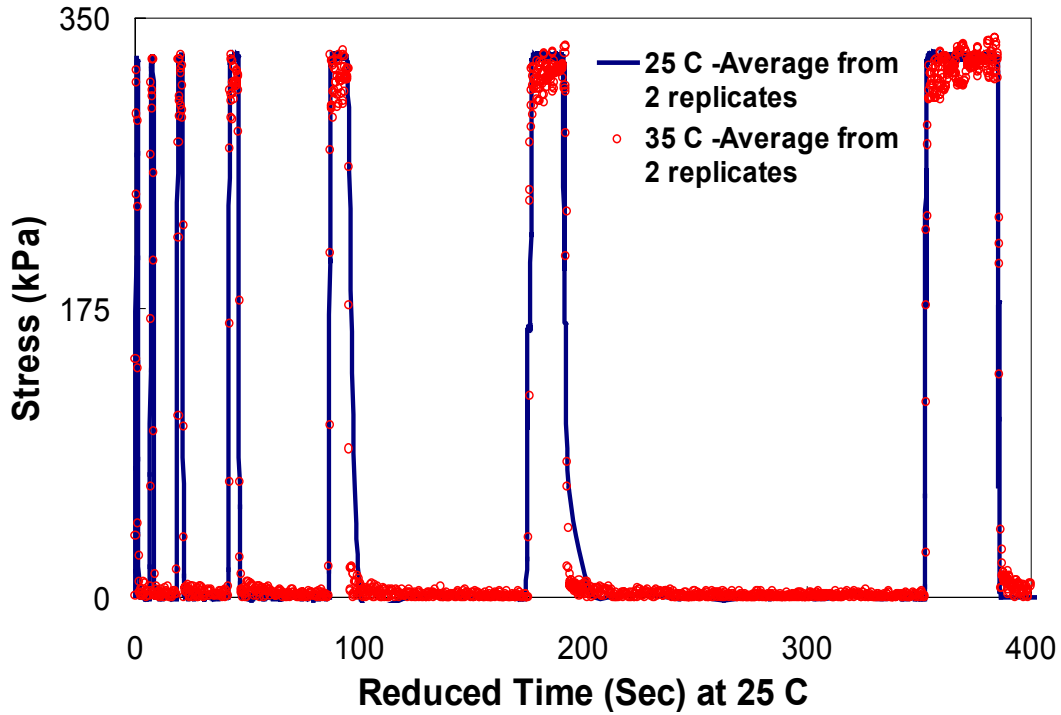
tests at various temperatures for modeling purposes, tests need to be run only at one temperature with the appropriate reduced time history.

Table 6.1. Test Parameters at 25°C

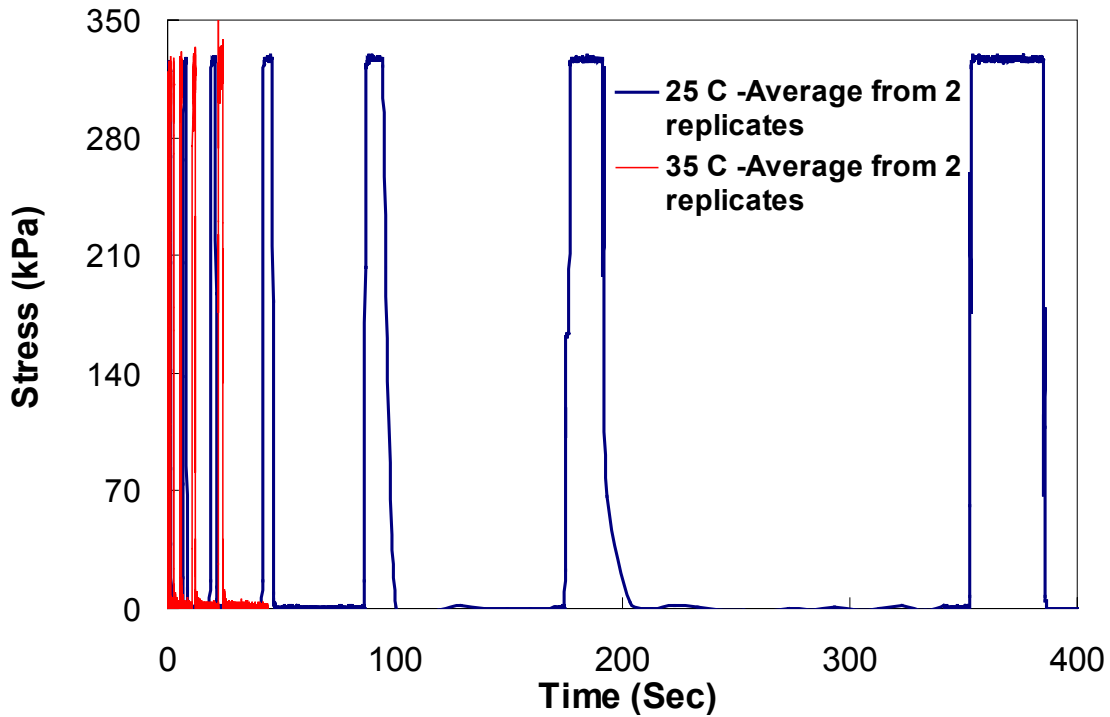
<b>25°C</b>	<b>Log <math>a_T = 0</math></b>	<b>Load: 325 kPa</b>
<b>Loading/Unloading Ramp Time (sec)</b>	<b>Loading Time (sec)</b>	<b>Recovery Time (sec)</b>
0.5	0.50	5.0
0.5	1.0	10.0
0.5	2.0	20.0
0.5	4.0	40.0
0.5	8.0	80.0
0.5	16.0	160.0
0.5	32.0	320.0
0.5	64.0	640.0
0.5	128.0	1280.0

Table 6.2. Test Parameters at 35°C

<b>35°C</b>	<b>Log <math>a_T = -1.2</math></b>	<b>Load: 325 kPa</b>
<b>Loading/Unloading Ramp Time (sec)</b>	<b>Loading Time (sec)</b>	<b>Recovery Time (sec)</b>
0.032	0.032	0.32
0.032	0.063	0.63
0.032	0.126	1.26
0.032	0.252	2.52
0.032	0.505	5.05
0.032	1.01	10.10
0.032	2.019	20.19
0.032	4.038	40.38
0.032	8.076	80.76

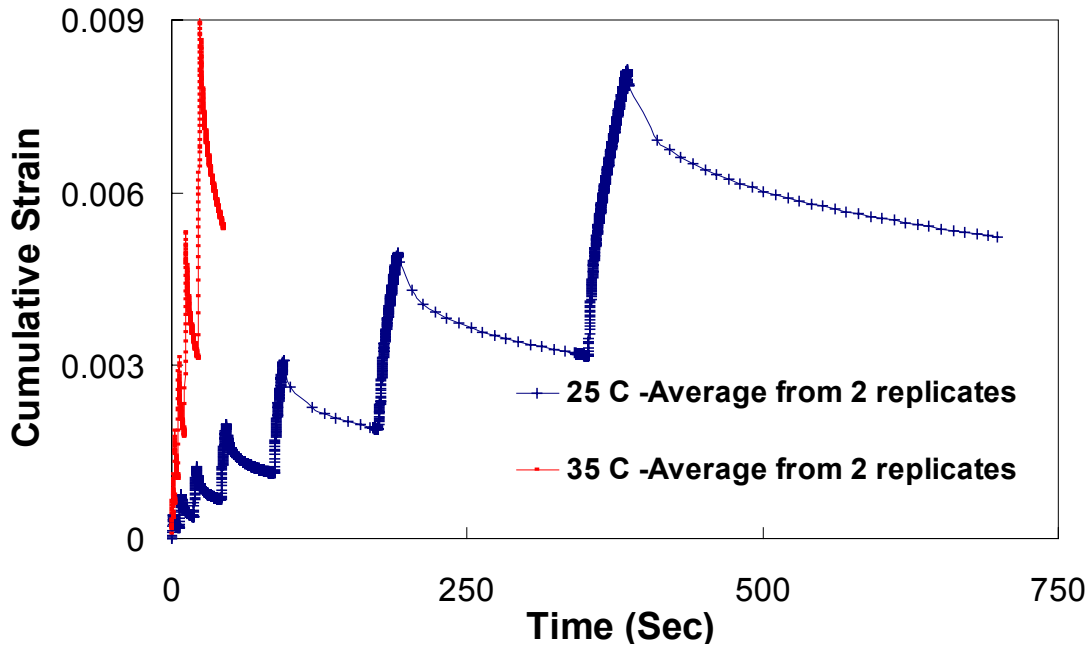


(a)

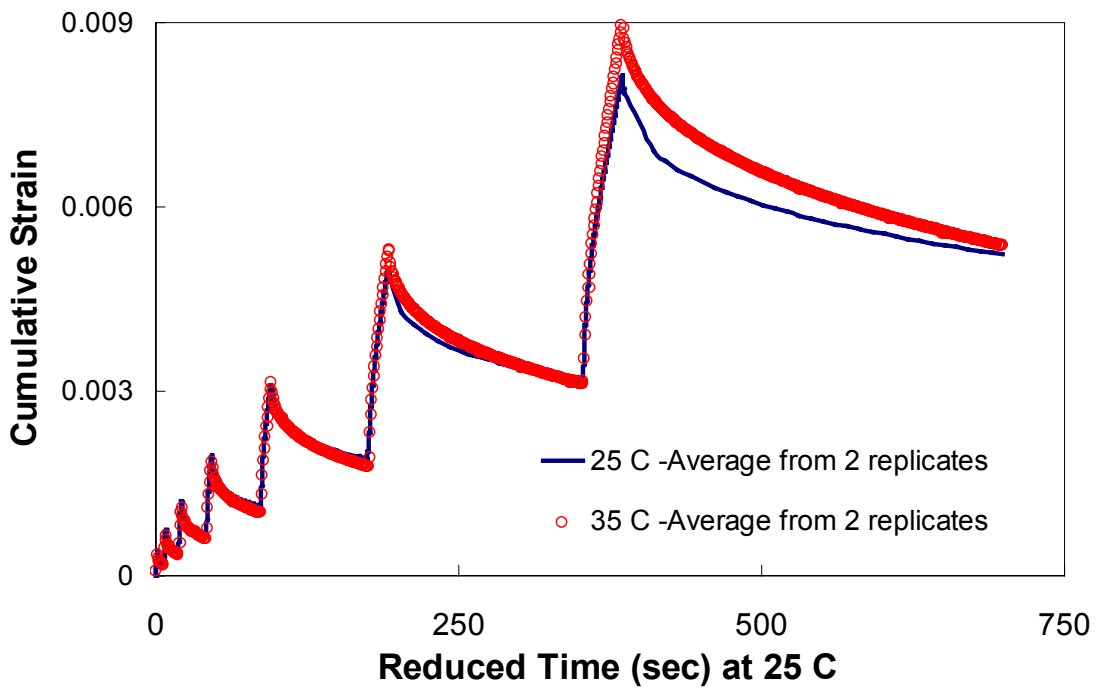


(b)

Figure 6.16. (a) Stress-reduced time history of 25 and 35°C creep and recovery tests plotted at reference temperature 25°C; (b) Corresponding stress- time history at testing temperatures 25 and 35°C

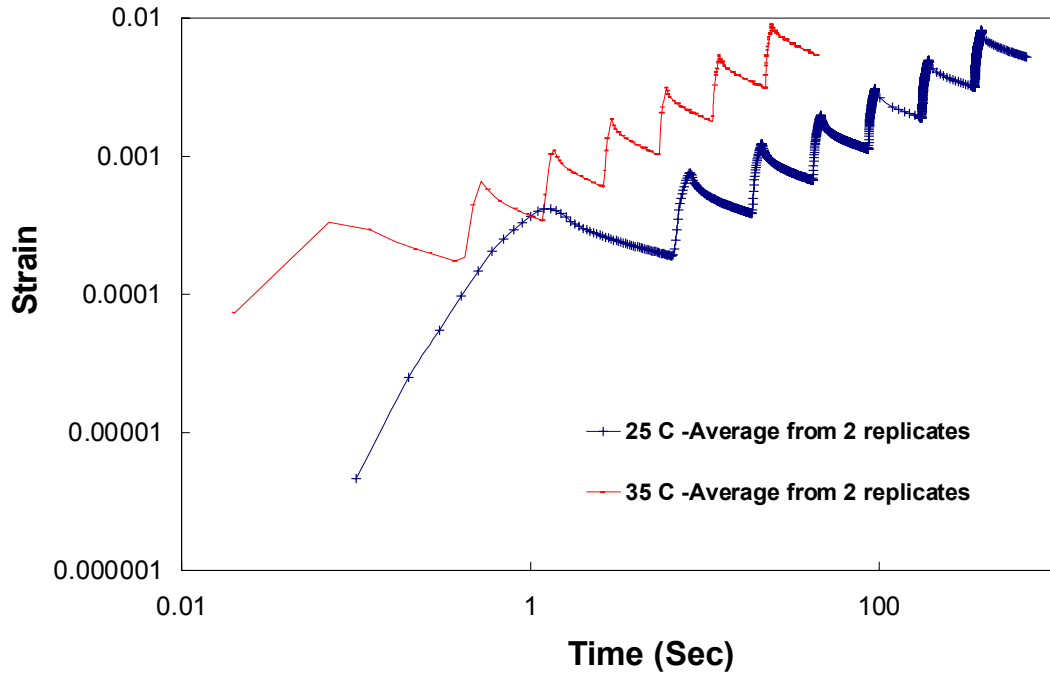


(a)

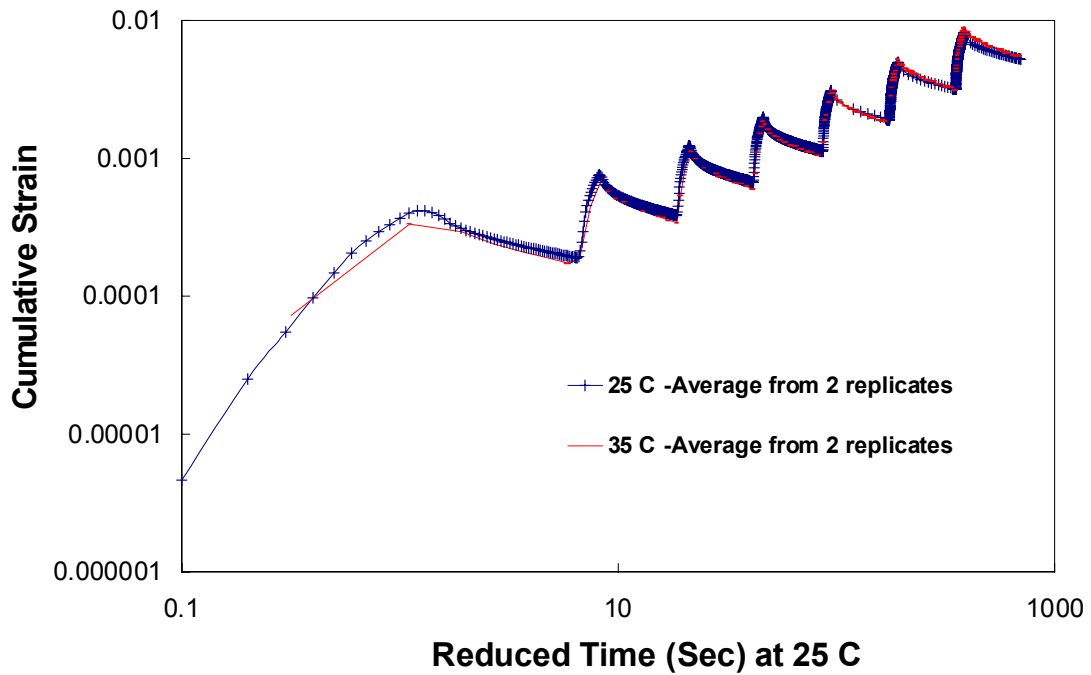


(b)

Figure 6.17. (a) Strain-reduced time history of 25 and 35°C creep and recovery tests plotted at testing temperatures; (b) Corresponding strain-reduced time history at reference temperature 25°C



(a)



(b)

Figure 6.18. (a) Strain-time history of 25 and 35°C creep and recovery tests plotted at testing temperatures (log-log scale); (b) corresponding strain-reduced time history at reference temperature 25°C (log-log scale)

## 6.5.2 Superposition of Strength and Corresponding Strain

One of the most important applications of the time-temperature superposition is the development of a mastercurve of strength as a function of reduced strain rate at a desired reference temperature (25°C). Developing such a curve enables the determination of the strength of a material at any strain rate and temperature combination. The same holds true for the strain at the peak stress.

In addition, the strength mastercurve would be of great significance for thermal cracking applications, where strength could be compared to the stress buildup due to thermal contraction to determine potential crack propagation. However, for thermal cracking applications, material properties, especially strength, need to be determined at very low temperatures. Since the lowest testing temperature investigated in this research thus far had been -10°C, additional testing was conducted at -20 and -30°C. Monotonic testing conditions and shift factors from complex modulus tests for these additional temperatures are presented in Table 6.3.

Table 6.3. Testing conditions at -20 and -30°C

Test ID	Temperature (C)	Shift factor	Crosshead rate (strains/sec)	Strength (kPa)
ttt-xh-uc-30-007	-30	$10^{8.9}$	0.007	1995
ttt-xh-uc-30-01			0.01	2100
ttt-xh-uc-20-005	-20	$10^{7.0}$	0.005	2670
ttt-xh-uc-20-01			0.01	2969
ttt-xh-uc-20-2			0.2	2770

For crosshead strains, which vary linearly with time, the strain rate is the slope of the specimen strain-time history. However, since LVDT strains do not vary linearly with time, the strain can be fit using the following power form up to the failure of the specimen;

$$\varepsilon = k' \times t^n \quad (6.7)$$

where the coefficients  $k'$  and  $n$  are regression constants. For subsequent analysis, the coefficient,  $k'$ , will be regarded as the specimen LVDT strain rate. Then, the reduced strain rates can be calculated as follows: For the crosshead strain in a linear form:

$$\varepsilon = k' \times t, \quad (6.8)$$

$$\varepsilon = k' \times a_T \times \left( \frac{t}{a_T} \right), \quad (6.9)$$

$$\varepsilon = k \times \xi, \quad (6.10)$$

where  $\varepsilon$  is strain,

$k'$  is the slope of strain vs. time at temperature T,

$a_T$  is shift factor of temperature T,

$t$  is time,

$\xi$  is reduced time at reference temperature, and

$k$  is reduced strain rate at reference temperature.

For the LVDT strain in a power form, as in the theory section (Chapter 2),

$$\varepsilon = k' \times t^n, \quad (6.11)$$

$$\varepsilon = k' \times a_T^n \times \left( \frac{t}{a_T} \right)^n, \quad (6.12)$$

$$\varepsilon = k \times (\xi)^n. \quad (6.13)$$

Therefore, for constant strain rate, the reduced strain rate is the slope multiplied by the shift factor; whereas, for strain in pure power form, the reduced strain rate is the coefficient multiplied by the shift factor raised to the power n. Referring to Figure 6.19, a linear relationship exists between the crosshead and specimen strain rates in a log-log scale, the latter being represented in either linear or power form. If the specimen strain is fitted using a power form, the reduced specimen strain rate,  $k'$ , is very comparable in value to the crosshead strain rate.

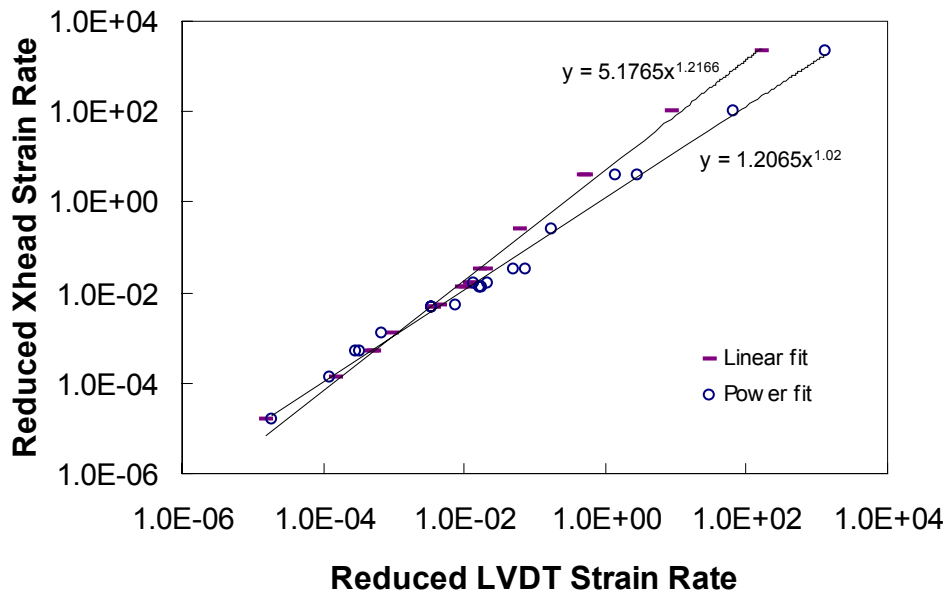


Figure 6.19. Relationship between crosshead and specimen LVDT strain rates at 25°C

Figure 6.20 shows strength mastercurves as a function of reduced strain rates at 25°C obtained using crosshead LVDT strain rates and LVDT specimen strain rates. The mastercurve plot is divided into three regions as described in Table 6.4.

Table 6.4. Failure modes

<b>Region</b>	<b>Temperature (C)</b>	<b>Loading Rate</b>	<b>Failure Mode</b>
<b>A</b>	40, 25, 5	All at 40C, 25C Slow at 5C	Ductile
<b>B</b>	5	Intermediate	Ductile, brittle failure during unloading
<b>C</b>	5, -10, -20, -30	Fast at 5C, All at -10, -20, -30C	Brittle during loading

The strength mastercurves shown in Figure 6.20 indicate the increase in strength as the strain rate increases; i.e., the rate dependence of tensile strength. However, for a certain reduced strain rate range (1 to 1000 per seconds), the failure pattern changes from ductile to brittle and the rate dependence of the strength becomes insignificant. As the reduced strain rate increases further more (greater than 10,000 per second), the strength starts to decrease. It is suggested that this is because at very low temperatures, the difference in thermal contraction coefficients of asphalt and aggregates leads to local thermal stress-induced damage, consequently leading to the weakening of the asphalt-aggregate matrix. As a result, a smaller load is required to fail the specimen. However, this damage may significantly depend on thermal history, which would cause strength to depart from thermorheologically simple behavior. There are not enough data here to critically check this behavior at fast reduced rates.

Figures 6.21 and 6.22 are plots of the mastercurve of strain at peak stress with respect to LVDT and crosshead-based strains respectively. Similarly, these mastercurves are divided into three regions according to the specimen's failure mode.

Thus, once several constant crosshead strain tests at different conditions are conducted, strength and corresponding strain mastercurves as a function of reduced strain

rate can be constructed. Those mastercurves are instrumental in determining the strength and corresponding strain at any other given temperature and strain rate condition.

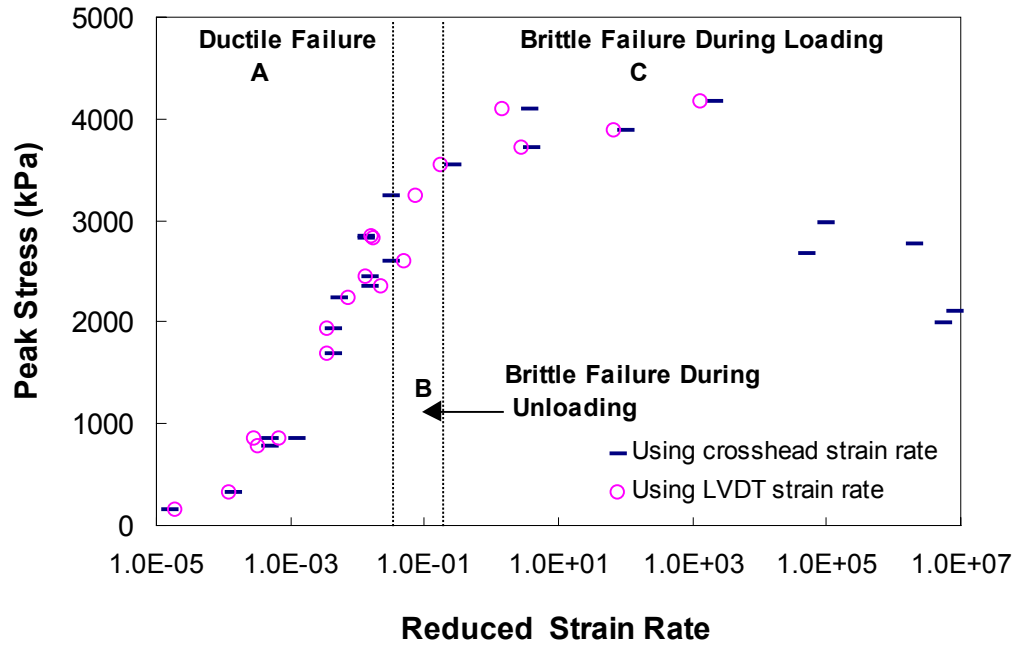


Figure 6.20. Strength mastercurve as a function of reduced strain rate (crosshead and LVDT) at 25°C

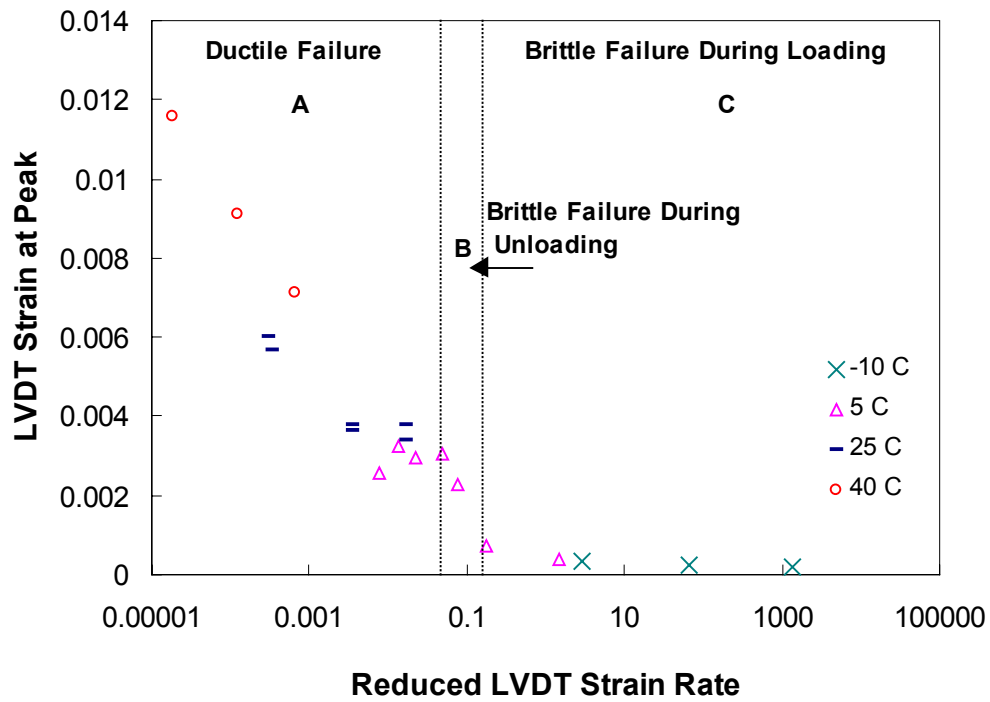


Figure 6.21. Mastercurve of specimen strain at peak stress as a function of reduced LVDT strain rate at 25°C

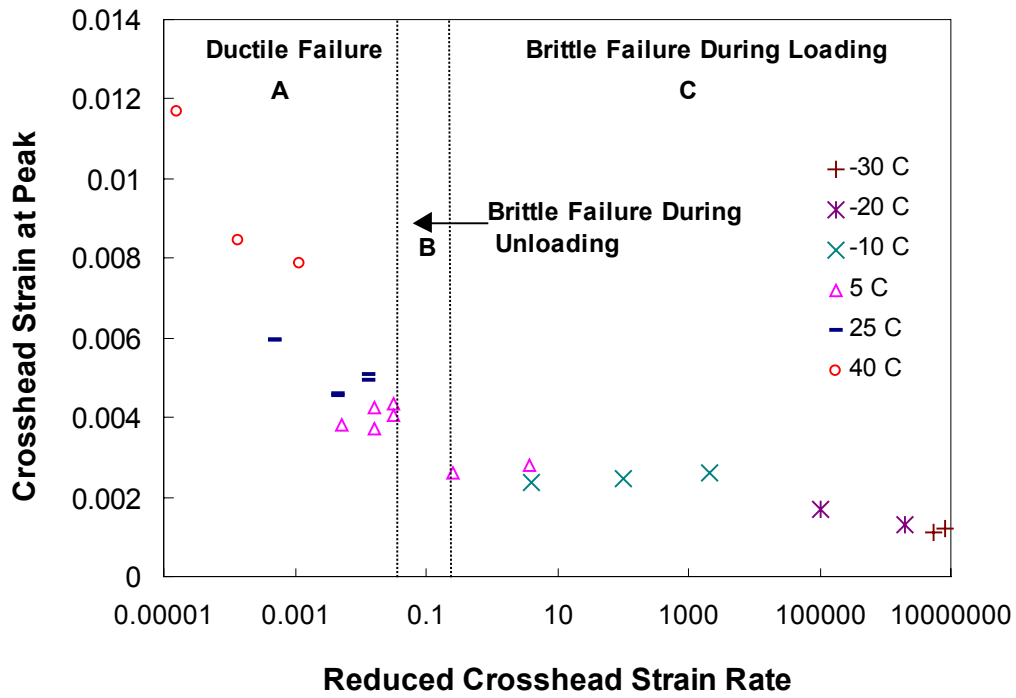


Figure 6.22. Mastercurve of crosshead strain at peak stress as a function of reduced crosshead strain rate at 25°C

### 6.5.3 Prediction of Stress-Strain Curves for Constant Crosshead Rate Tests

Having constructed the stress-reduced time crossplots for various strain levels, it is possible to predict the stresses for any given constant crosshead rate test. Those stresses can be predicted using either the crosshead strain rate or the specimen strain rate as long as it follows a pure power functional form. Stresses can only be predicted for strain levels at which stress-log reduced time crossplots exist. The following procedure was used to predict the stress-strain curve: For a given strain, the corresponding time is calculated from the strain rate in question, e.g., crosshead strain rate. Based on the temperature at which the prediction is needed, the time is divided by the appropriate shift factor to yield a reduced time at the reference temperature, 25°C. For that reduced time and using the stress-log reduced time crossplot corresponding to the selected strain, the stress is determined. For accuracy, the crossplots from which the stresses are to be determined are fitted to a polynomial function. This procedure is repeated for all strain levels for which the crossplots exist. After determining the stresses, stress-strain curves can be constructed.

In the case where the reduced strain rate yields brittle fracture, the prediction is carried out for strains less or equal to the maximum strain for that reduced strain rate. That maximum strain is obtained from the mastercurve of strain at peak as a function of reduced strain rate. Figure 6.23 outlines the prediction methodology.

The prediction procedure was applied to selected tests that were actually conducted in the testing program. In that way, predicted stress-strain curves can be compared to the actual. The on-specimen LVDT strain rate fitted to the pure power

function was used to determine the time. Crossplots used were those constructed earlier corresponding to the specimen LVDT strains.

Figure 6.24 shows the predicted and actual stress-strain curves for a test run at a crosshead strain rate of 0.0135 at 25°C. As noticed, there is an excellent match between the actual and predicted curves. Because the largest strain for which the crossplot was constructed was 0.02, stresses for strains beyond that value can not be predicted.

In Figure 6.25, the crosshead strain rate in the test was 0.000012 at 5°C. In that test, the upper plate started to displace unevenly with respect to the horizontal axis after a strain of 0.0038. As mentioned in the earlier sections, data from that instance and forward can not be used in conjunction with the time-temperature superposition principle and thus the actual stresses deviate from the predicted.

Similarly, Figure 6.26 shows actual and predicted curves for a test at -10°C with a rate of 0.0005. Since the reduced strain rates for this test is predicted to yield failure in a brittle mode (Figure 6.20), the prediction of the stress-strain curves needs to be done for strains less or equal to those corresponding to the strength.

Figure 6.27 shows both the actual and predicted stress-strain curves at 40°C for a crosshead strain rate of 0.07. The match is good in the pre-peak and post-peak regions; however, there is an over prediction of stress at peak. In general, it can be concluded that the stress prediction methodology seems to be promising. The errors in prediction are of the same order of magnitude as the difference in responses attributed to the specimen to specimen variability for the same testing condition.

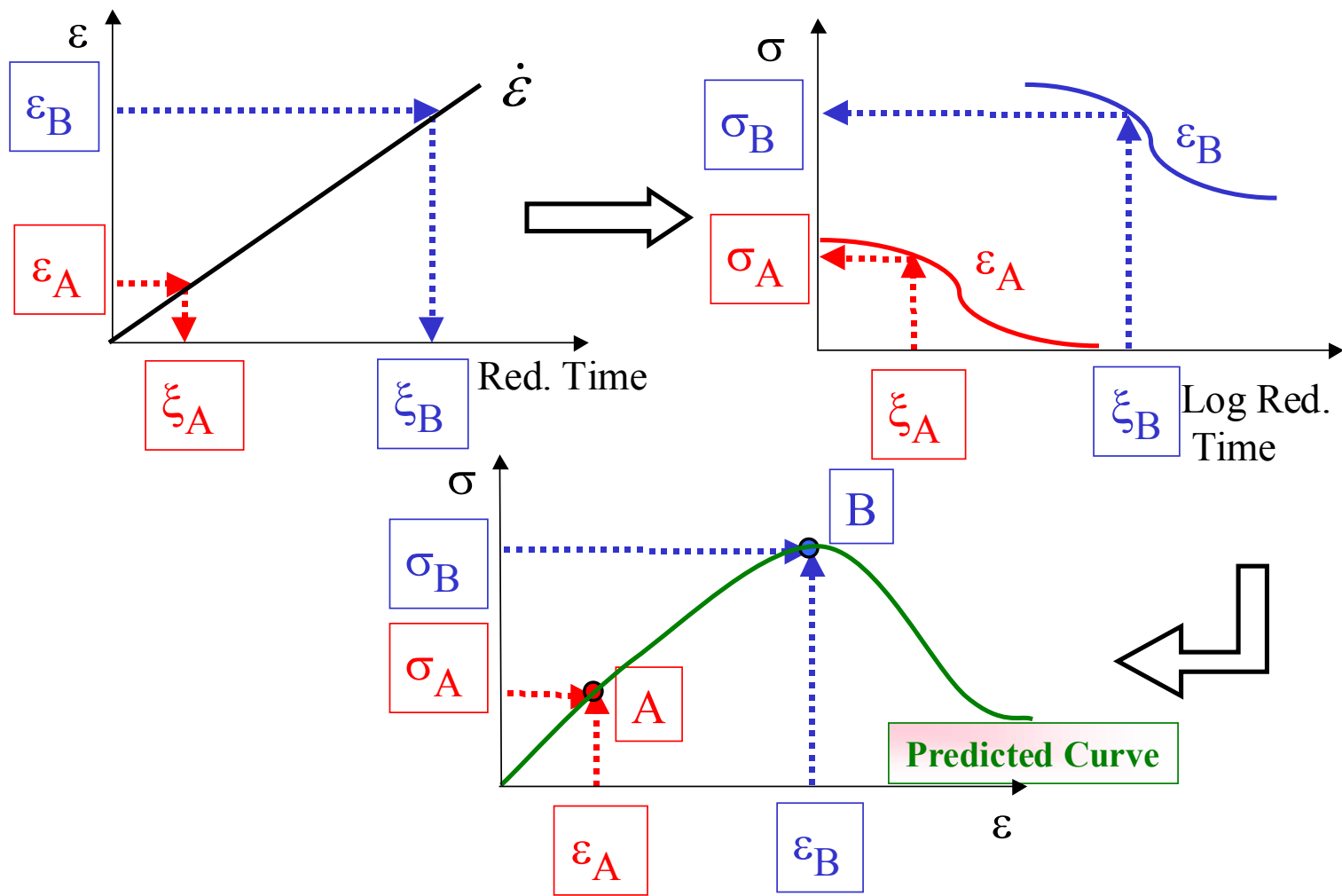


Figure 6.23. Methodology for predicting stresses for constant crosshead strain rates using stress-reduced time crossplots

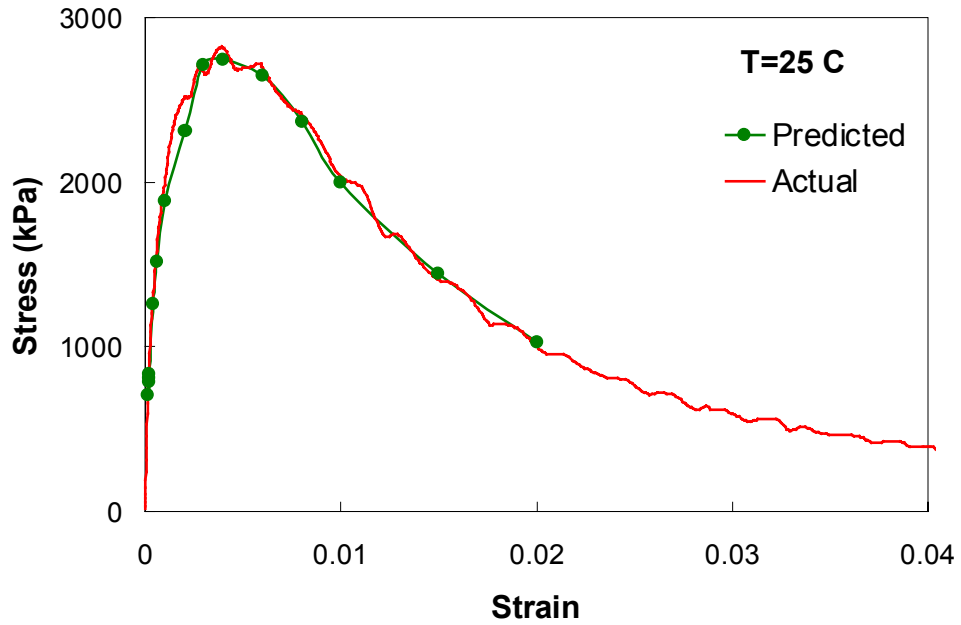


Figure 6.24. Predicted and actual stress-strain curves for a crosshead strain rate of 0.0135 at 25°C.

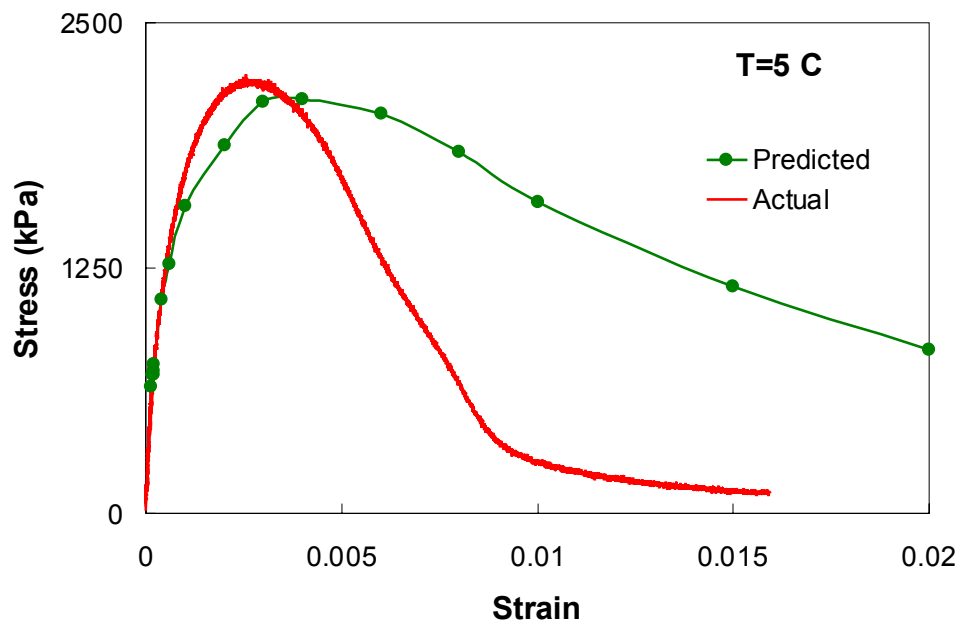


Figure 6.25. Actual and predicted stress-strain curves at 0.000012 strains/sec at 5°C

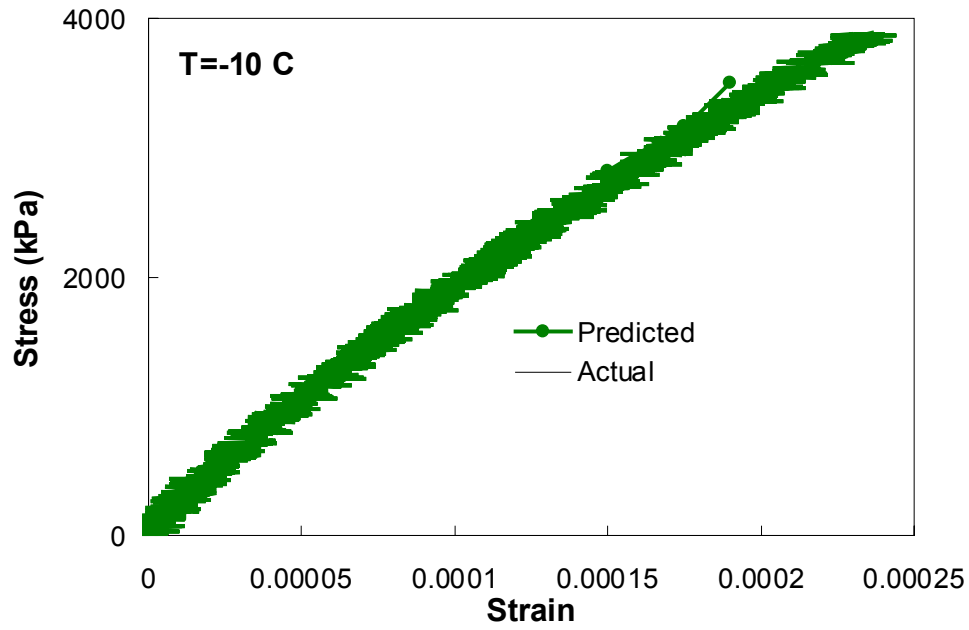


Figure 6.26. Actual and predicted stress-strain curves at 0.0005 strains/sec at  $-10^{\circ}\text{C}$

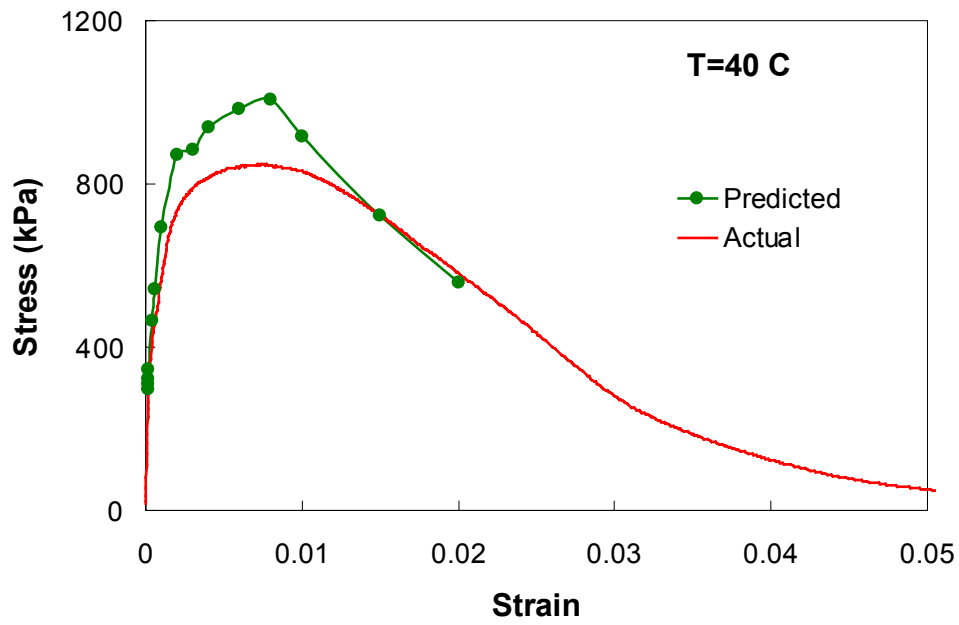


Figure 6.27. Actual and predicted stress-strain curves at 0.07 strains/sec at  $40^{\circ}\text{C}$

#### **6.5.4 Constructing Characteristic Curve at Reference Temperature**

Another important benefit which serves as an extremely valuable tool in modeling of viscoelastic behavior is the ability to collapse the characteristic  $C$  vs.  $S$  curves for tests conducted at temperatures and rates where only viscoelastic response is present. If reduced time is used instead of actual testing time in the calculation of the damage parameter  $S$ , then the characteristic curves plotted at the reference temperature should collapse. This is of great benefit because it is no longer required that tests be conducted at various temperatures and strain rates, since all of those tests will eventually yield the same characteristic curve. That, in turn, reduces amount of resources required for the additional testing.

Figures 6.28 and 6.29 show how characteristic curves at  $5^{\circ}\text{C}$  and  $25^{\circ}\text{C}$  for different rates collapse after a LVE shift factor is applied to shift the  $5^{\circ}\text{C}$  curves to a reference temperature of  $25^{\circ}\text{C}$ . It is worthy noting that at high temperatures and slow loading rates, viscoplastic strain starts to become appreciable; hence, the characteristic curves will cease to collapse with the other curves where no viscoplastic response is present.

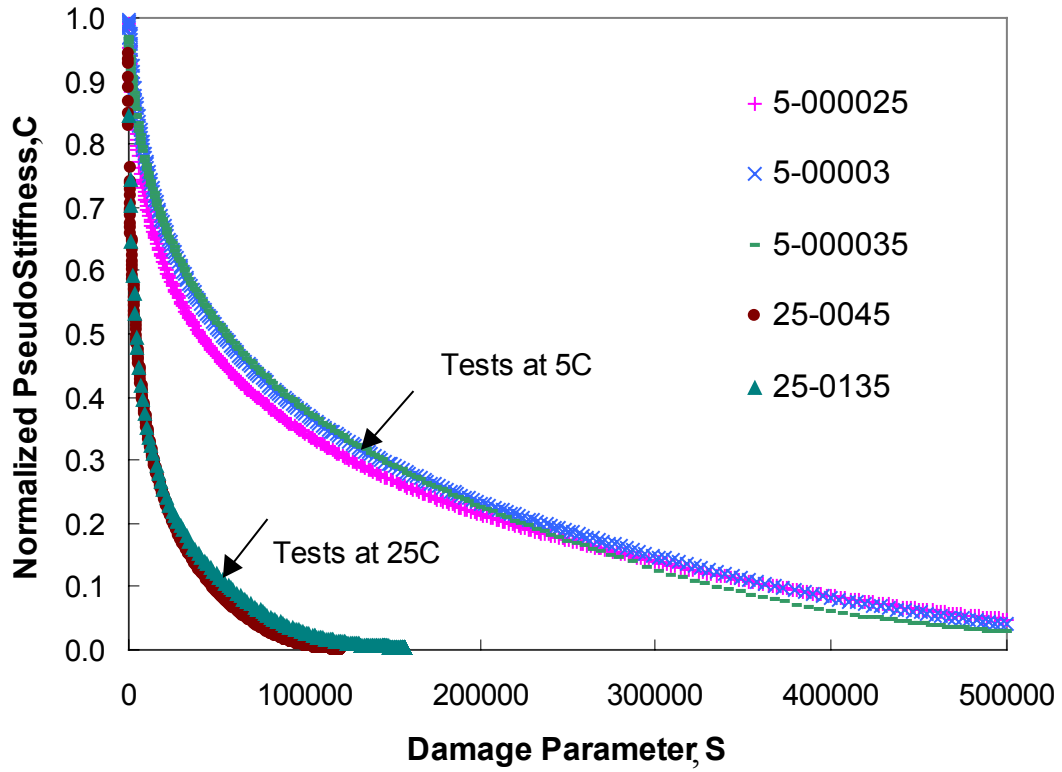


Figure 6.28. Characteristic curves at 5 and 25°C for various constant crosshead rates

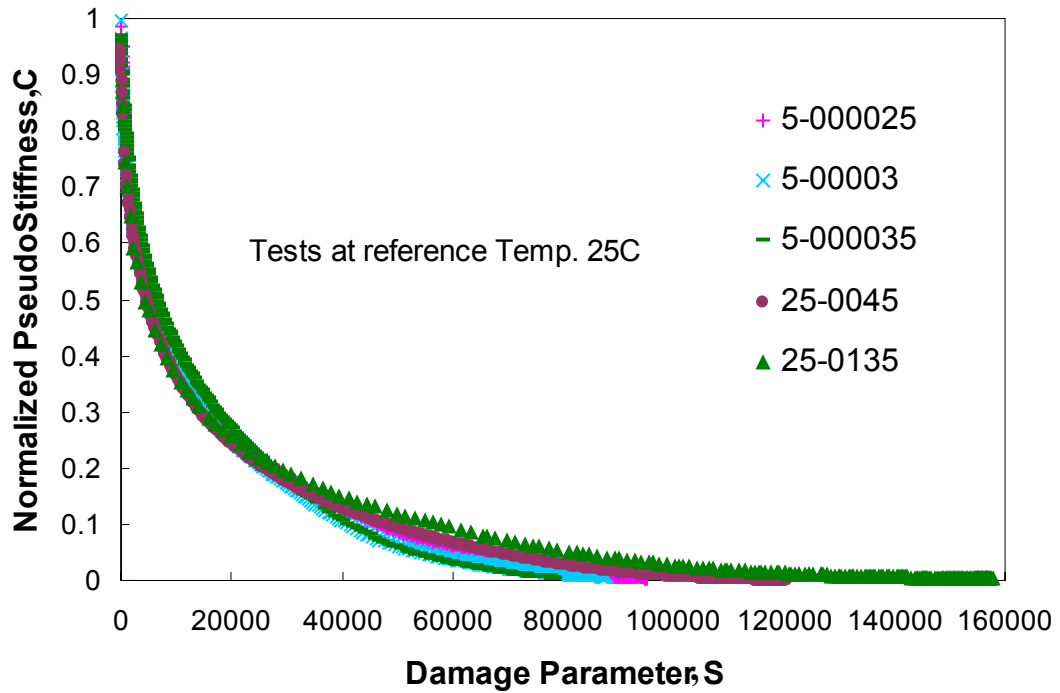


Figure 6.29. Characteristic curves for various constant crosshead rates at 5 and 25°C shifted to reference temperature of 25°C

## **7 Modeling of Viscoelastic and Viscoplastic Behavior in Tension State**

### ***7.1 Introduction***

As mentioned earlier, asphalt concrete behaves differently depending on temperature and rate of loading. Its behavior may vary from elastic and linear viscoelastic at low temperatures and/or fast loading rates to non-linear viscoelastic and viscoplastic/plastic at high temperatures or slow loading rates. Therefore any comprehensive material characterization model must include the viscoelastic, viscoplastic, and plastic behavior. The significance of including the viscoplastic and plastic components was highlighted in Chapter 2.

The modeling strategy that will be adopted in this research is to model each component behavior separately. The separation of the response into components is done best using creep and recovery tests with sufficient loading and unloading times to permit isolation of time dependence (Figure 7.1). In this research, the elastic strain is combined with the viscoelastic strain and referred to as viscoelastic strain; while plastic and viscoplastic strains are also combined together and referred to as viscoplastic strain.

#### **7.1.1 Brief Overview of Modeling Approach**

As mentioned above, the viscoelastic and viscoplastic responses will be modeled separately. For viscoelastic strains, the adopted model is based on Schapery's (1978) continuum damage-work potential theory initially developed for solid rocket propellant and later applied to asphalt concrete by Kim (1990). The model utilizes the elastic-viscoelastic correspondence principle to separate time-dependant behavior from damage due to loading, thus simplifying the modeling task. Two methods will be presented and

evaluated, the first one using ‘S’ as the damage parameter and the second one using ‘S\*’ as the damage parameter.

As for the viscoplastic response, Uzan’s strain hardening model (Uzan et al. 1985) in addition to further work by Schapery (1999) will be the basis of the viscoplastic modeling approach. Different methods for determining the model coefficients will be presented and evaluated.

In reference to the Chapter 6, it was shown that time-temperature superposition is still valid with growing damage (micro-cracking and viscoplasticity). This will reduce the required number of tests for both viscoelastic and viscoplastic modeling, since responses at a certain loading rate/temperature condition could be predicted from a test performed at another testing condition.

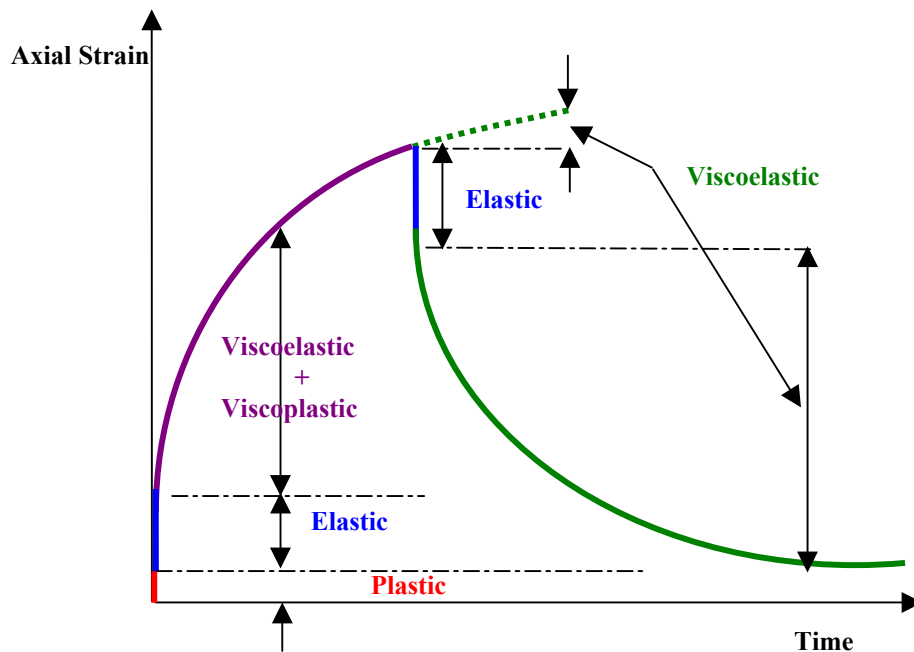


Figure 7.1. Strain decomposition from creep and recovery test

## ***7.2 Modeling of Viscoelastic Behavior***

Viscoelastic behavior will be modeled using either the C vs. S approach or the C vs. S\* approach, based on Schapery and Kim's continuum damage model. Determination of damage parameters for modeling will be obtained through conducting constant crosshead rate tests at low temperatures and fast rates where it is believed that viscoplastic strains are minimal. Five constant crosshead rate tests were conducted at different rates at 5°C. After evaluating both approaches, it was determined that the C vs. S\* approach has several advantages that make it more favorable than the C vs. S approach. However, both approaches will be presented in this section.

### **7.2.1 Testing Conducted**

Five constant crosshead rate tests in uniaxial tension mode were conducted at 5°C. It is believed that strains obtained are mostly viscoelastic with minimal presence of viscoplastic strains; thus enabling the use of the data from those tests for modeling viscoelastic behavior. New tests were conducted because earlier tests done for the time-temperature study had employed different kind of LVDTs (spring-loaded) than those that are going to be used for viscoplastic modeling (loose-core LVDTs). Stress-strain curves for those tests are presented in Figure 7.2. Complex modulus tests at different frequencies and temperatures had already been conducted using the new loose-core LVDTs to develop characteristic curves for dynamic modulus and phase angle. Relaxation modulus and creep compliance functions were then obtained. LVE shift factors were consequently obtained after constructing the storage modulus ( $E'$ ) mastercurve. Details were presented in Chapter 5.

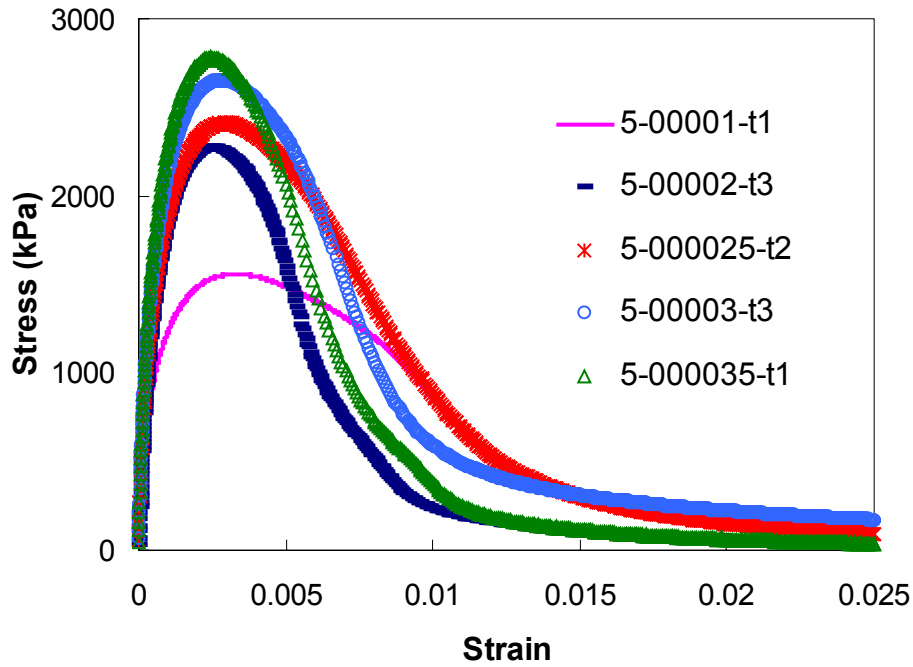


Figure 7.2. Stress-strain curves for monotonic tests at 5°C

### 7.2.2 Determination of Material Constant ‘ $\alpha$ ’

In reference to Chapter 2, the material constant  $\alpha$  was needed for the determination of the damage parameters  $S$  and  $S^*$ , where:

$$S(\xi) \cong \sum_{i=1}^N \left[ \frac{I}{2} (\varepsilon_{mi}^R)^2 (C_{i-1} - C_i) \right]^{\frac{\alpha}{1+\alpha}} (\xi_i - \xi_{i-1})^{\frac{1}{1+\alpha}}, \text{ and} \quad (7.1)$$

$$S^* \equiv \left[ \int_0^{\xi} |\varepsilon^R|^{2\alpha} d\xi \right]^{\frac{1}{2\alpha}}. \quad (7.2)$$

In many viscoelastic crack growth problems, the crack speed is governed by the  $\alpha^{\text{th}}$  power in pseudo energy release rate, in which  $\alpha$  is related to the material’s creep or relaxation properties (Schapery 1975). Depending on the characteristics of the failure zone at a crack tip,  $\alpha=(1+1/n)$  or  $\alpha=1/n$ , where  $n$  is the slope of the linear viscoelastic response function plotted as a function of time in a logarithmic scale. If the material’s

fracture energy and failure stress are constant, then  $\alpha = (1+1/n)$ . On the other hand, if the fracture process zone size and fracture energy are constant,  $\alpha = 1/n$ . This has been observed by Schapery (1975) for rubber, Lee and Kim (1998a, 1998b), and Daniel (2001) for asphalt concrete. Either form of  $\alpha$  has been used in all previous research by Kim and others as well as in the time-temperature validation study in this research.

Now that a new model is to be developed, it is worth to investigate further other possible forms for  $\alpha$ . Although the two previously used forms are derived from mechanics and sound mathematical principles, they are related to the crack tip and thus defined for a micro-scale level. The damage parameters  $S$  and  $S^*$  on the other hand are indicators of damage for the whole specimen and thus defined for a macro-scale continuum. Thus there is a possibility that the values of  $\alpha$  take a form other than the two used so far. It is postulated that the best value of  $\alpha$  is that which yields the best collapse of the  $C$  vs  $S$  and  $C$  vs  $S^*$  curves.

Various values of  $\alpha$  were applied to  $C$  vs.  $S$  and  $C$  vs.  $S^*$  curves for data from 5°C and 25°C monotonic testing. The values ranged from  $(-2+1/n)$  to  $(6+1/n)$ . The extreme values of  $\alpha$  did not yield a good collapse so only the better ones will be presented. Figures 7.3 through 7.6 show the  $C$  vs.  $S$  and  $C$  vs.  $S^*$  curves for  $\alpha$  values of  $(-1+1/n)$ ,  $(1/n)$ ,  $(1+1/n)$ , and  $(2+1/n)$ . It can be concluded that for this mixture and particular set of testing, the  $\alpha$  value of  $1/n$  yields the best collapse among the curves for both  $C$  vs.  $S$  and  $C$  vs.  $S^*$ . The deviation seen at 25°C for the slowest rate could be attributed to the presence of a small degree of viscoplasticity.

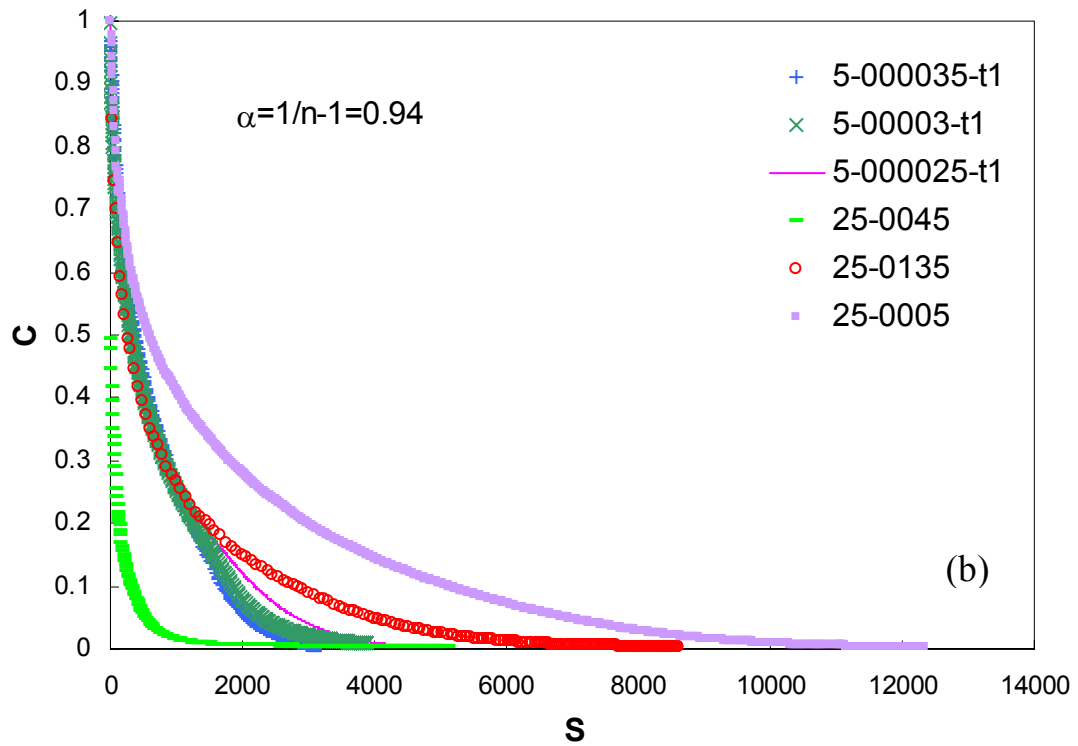
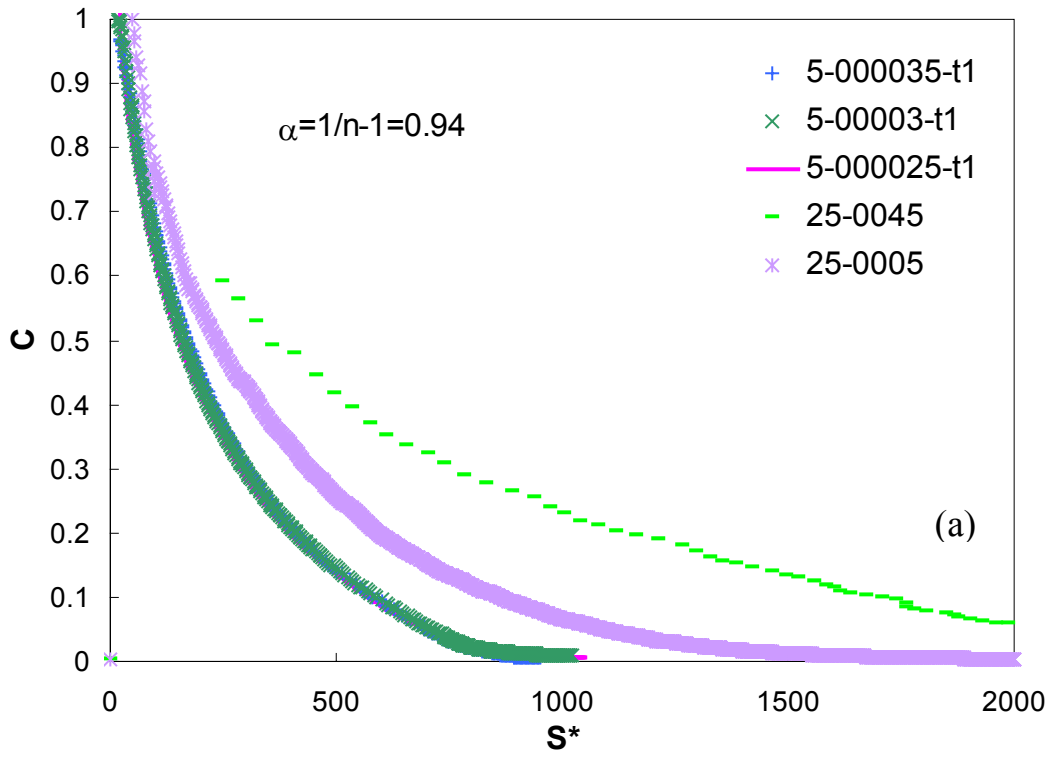


Figure 7.3. (a)  $C$  vs.  $S^*$ ; (b)  $C$  vs.  $S$  curves for  $\alpha = 1/n - 1$

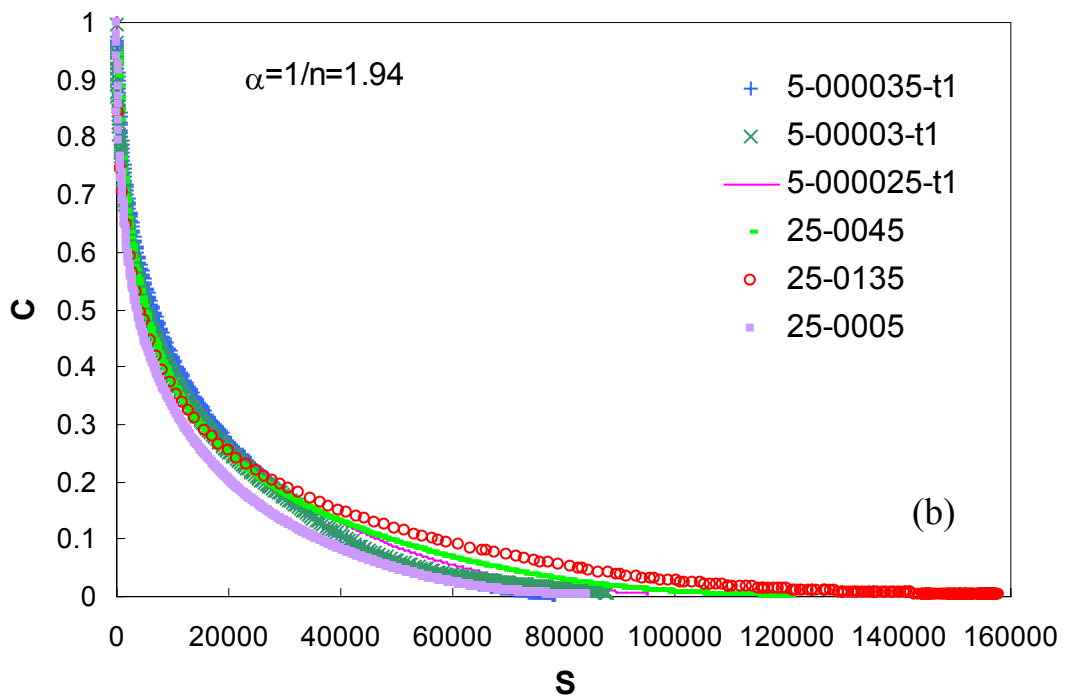
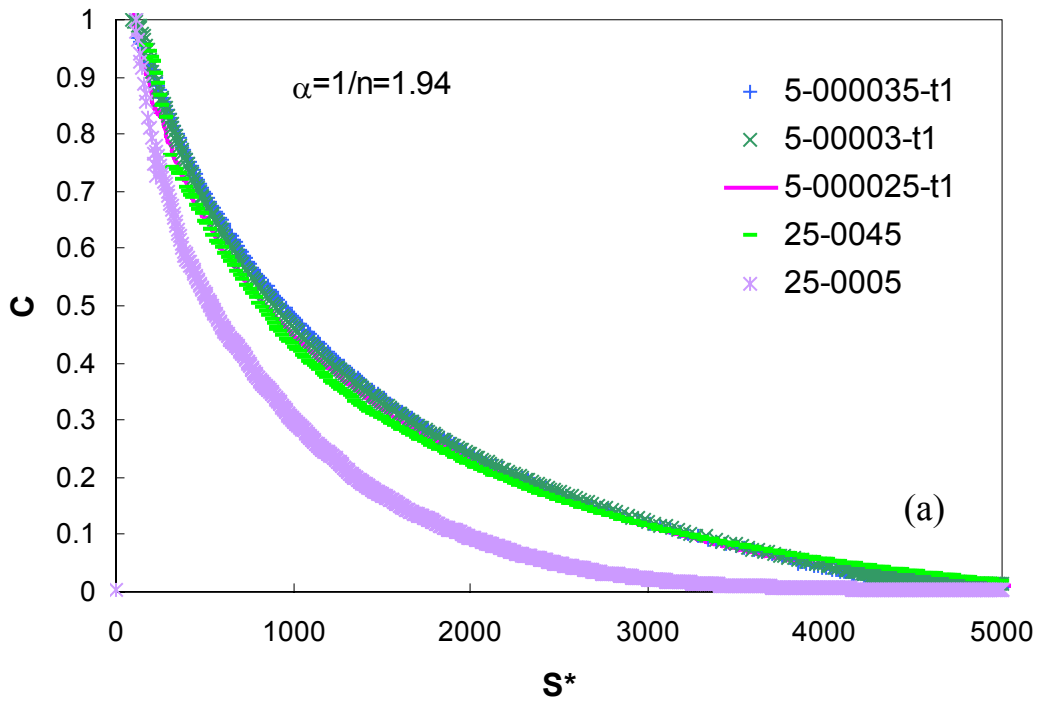


Figure 7.4. (a) C vs. S\*; (b) C vs. S curves for  $\alpha=1/n$

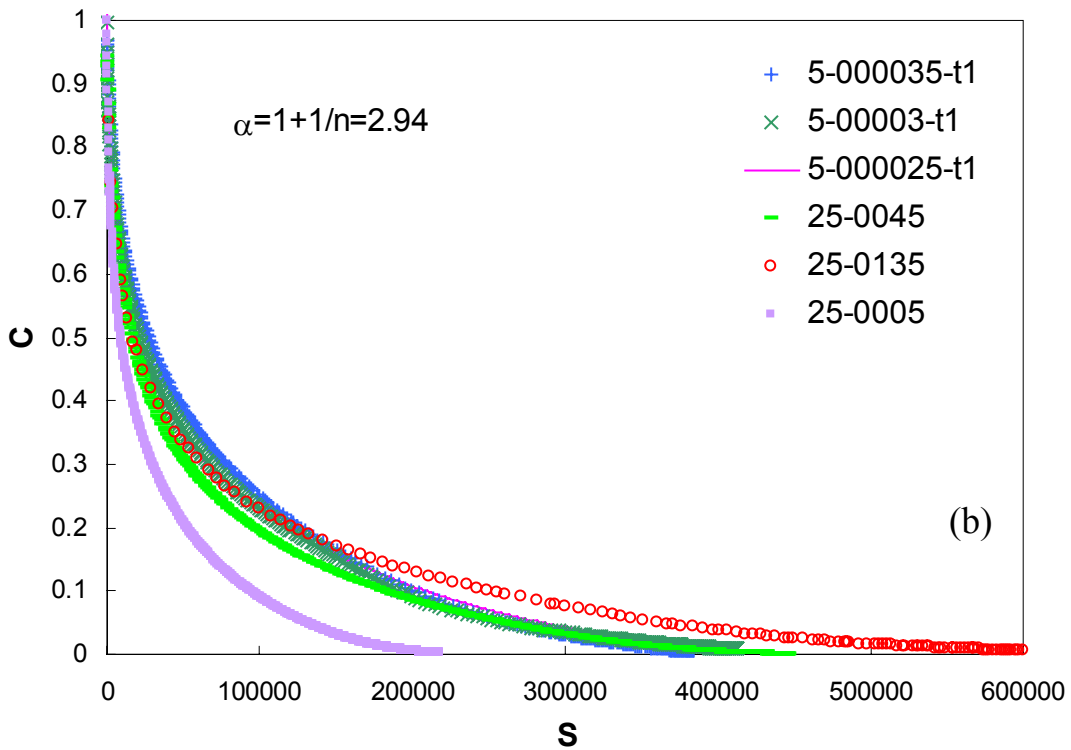
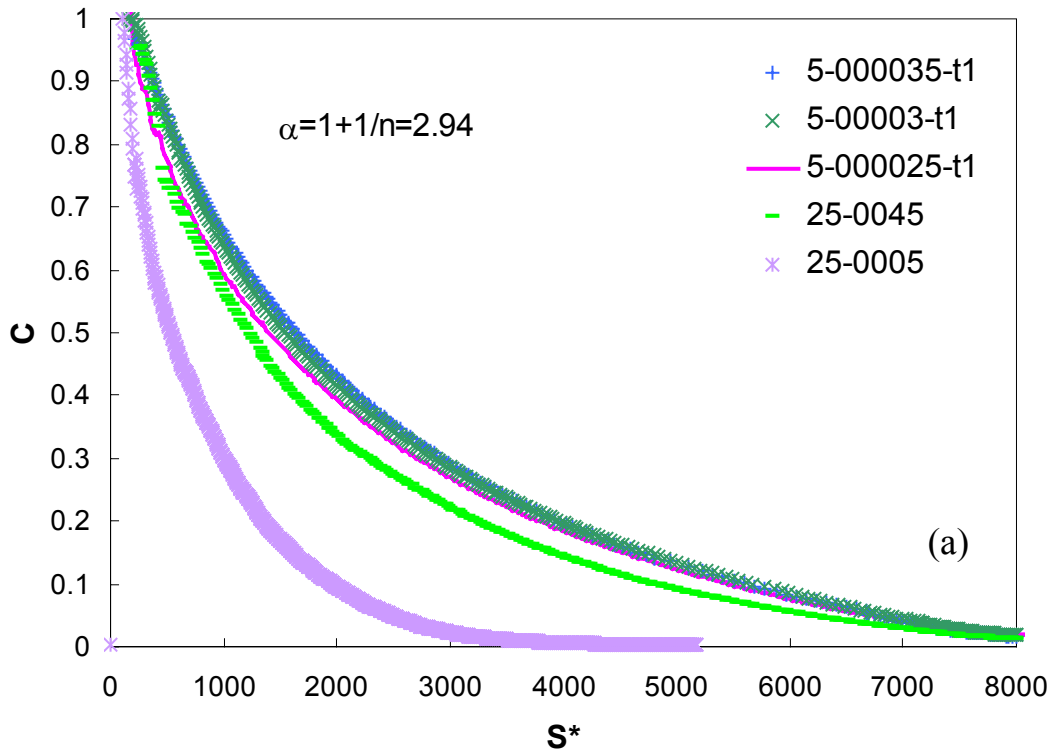


Figure 7.5. (a)  $C$  vs.  $S^*$ ; (b)  $C$  vs.  $S$  curves for  $\alpha=1+1/n$

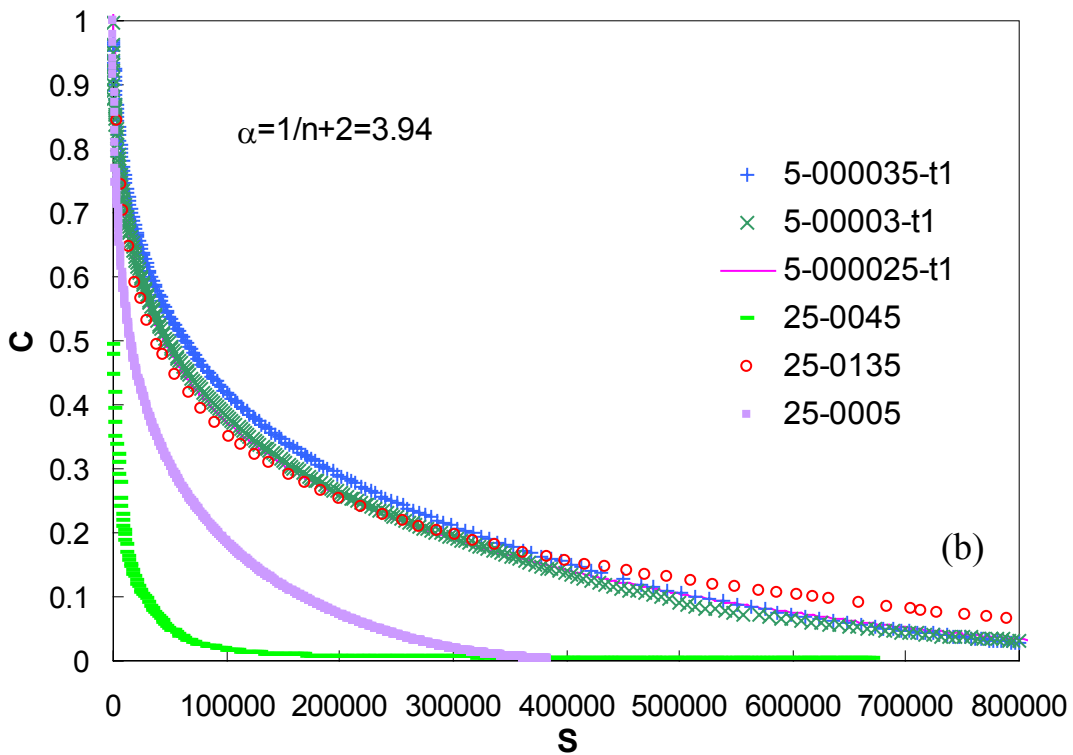
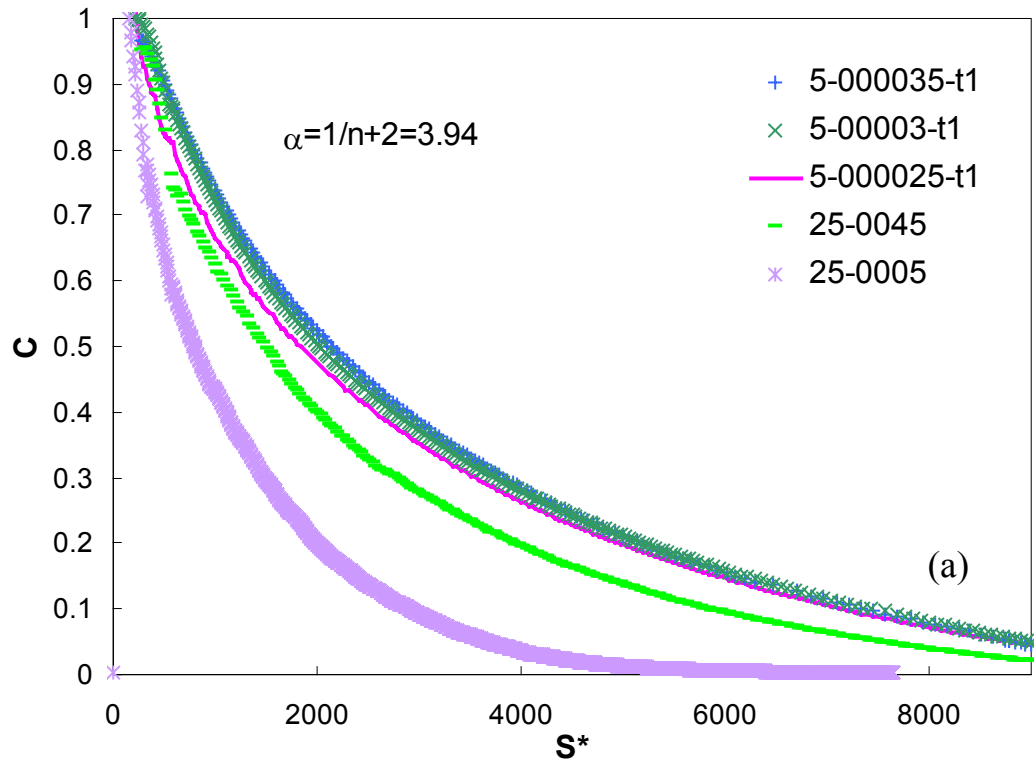


Figure 7.6. (a)  $C$  vs.  $S^*$ ; (b)  $C$  vs.  $S$  curves for  $\alpha = 2 + 1/n$

### **7.2.3 Effect of Using Time vs. Reduced Time in Calculating Pseudostrain and Damage Parameters**

In the previous chapters as well as in earlier research (Daniel 2001), actual time was used in the calculation of pseudostrain regardless of the testing temperature. On the other hand, reduced times were used to calculate the damage parameters and obtain the C vs. S and C vs. S\* curves at the reference temperature. The question that now poses itself is whether reduced time should have been used in calculating pseudostrain instead of time and whether that has any effect on the calculation of the damage parameters when shifted to the reference temperature.

To check the presence of any effect on pseudostrain and the damage parameter S, both time and reduced time were used on data from two constant-crosshead rate tests at 5°C. Monotonic tests at 5°C were chosen because testing at that temperature will be used in the development of the viscoelastic model. Figure 7.7 shows the pseudostrain vs. reduced time for the two tests, where both time and reduced time were used in calculating the pseudostrain. As observed, pseudostrain from time and reduced time are very similar up to the point of localization where they tend to deviate. This was true for both tests. As for the damage parameter S, in reference to Figure 7.8, no noticeable difference was detected even after localization between the C vs. S curves corresponding to pseudostrain from time and reduced time. Again, this observation was true for both tests at different strain rates. In spite of the latter observation, for the model development, reduced time will be used in calculating pseudostrain, primarily because it is fundamentally the better approach to follow and secondly because of the apparent deviation after localization.

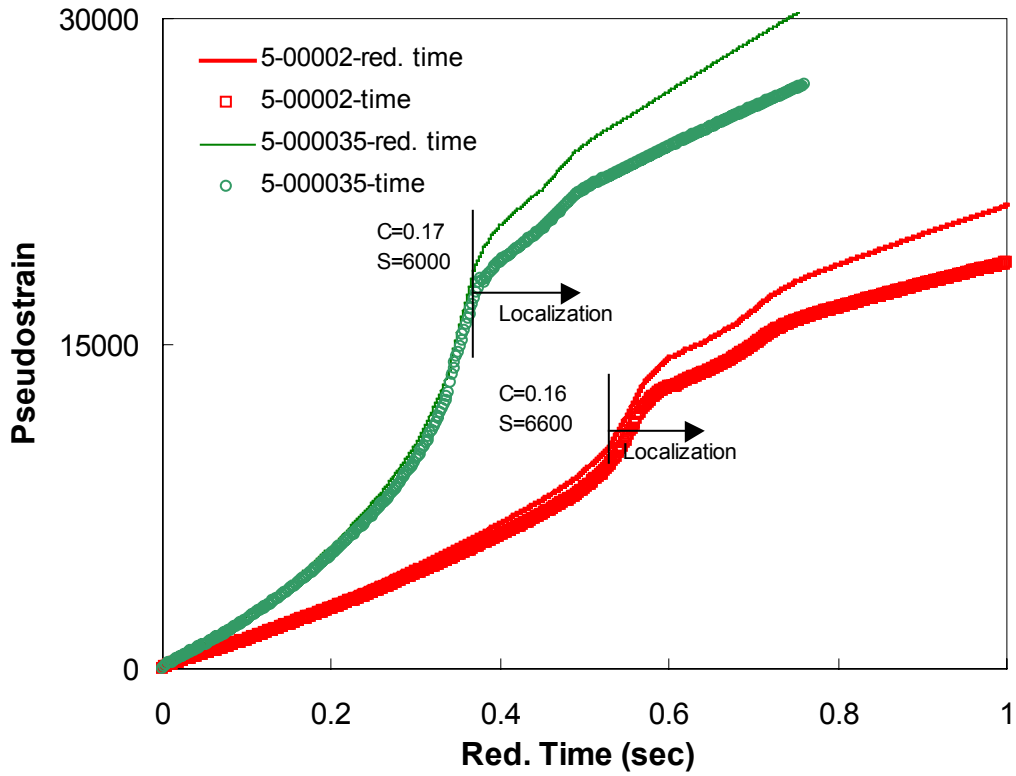


Figure 7.7. Pseudostrain for 2 monotonic tests at 5°C calculated using time and reduced time

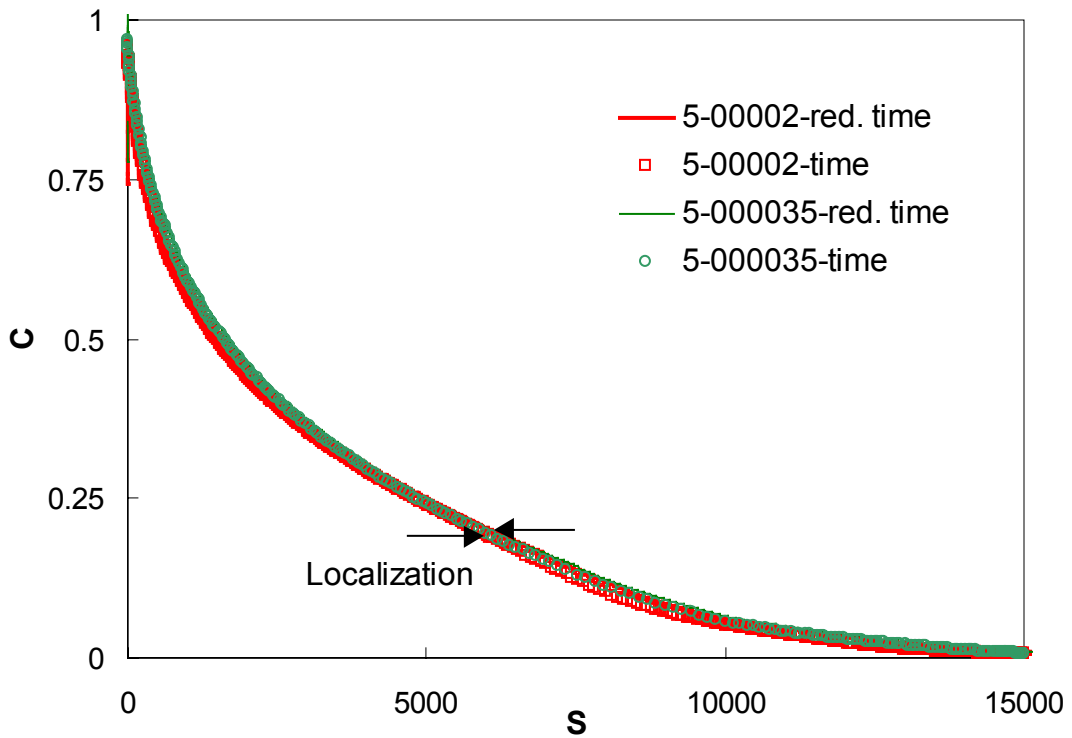


Figure 7.8. C vs. S for 2 monotonic tests at 5°C corresponding to pseudostrain calculated using time and reduced time

### 7.2.4 Validity of Using $S^*$ as a Damage Parameter

Based on the discussions in the previous chapters, the simple constitutive model for uniaxial stress-strain behavior of asphalt concrete mixtures proposed was based on  $S$  as a damage parameter used with the following constitutive equations:

$$W^R = \frac{I}{2} C(S) (\varepsilon^R)^2 \quad (7.3)$$

$$\dot{S} = \left( -\frac{\partial W^R}{\partial S} \right)^\alpha \quad (7.4)$$

where  $\dot{S}$  is the damage evolution rate,  $W^R$  is the pseudo strain energy density function, and  $\alpha$  is a material constant. For a uniaxial loading problem, the material characterization may be simplified by changing the damage parameter from  $S$  to  $S^*$  upon substituting Equation (7.3) into Equation (7.4) and integrating the resulting equation to obtain an implicit one-to-one functional relationship between the two damage parameters (Park and Kim, 1996):

$$S^* = \left[ \int_0^S \frac{dS}{(-0.5dC/dS)^\alpha} \right]^{1/2\alpha} \quad (7.5)$$

where  $S^*$  is a Lebesgue norm of the pseudostrain:

$$S^* \equiv \left[ \int_0^\xi |\varepsilon^R|^{2\alpha} d\xi \right]^{1/2\alpha} \quad (7.6)$$

Kim and Little (1990) demonstrated that the uniaxial behavior can be characterized using  $S^*$  as a damage parameter for a moderate extent of damage but it was later shown by Park and Kim (1996) that it could be applied to damage up to failure.

In this subsection, it will again be investigated whether  $S^*$  could in fact be used as a damage parameter for the present testing data. If  $S^*$  values calculated using Equations 7.5 and 7.6 for the constant crosshead rate tests data are the same, then it can be stated that  $S^*$  can be used to characterize the viscoelastic behavior of asphalt concrete. Figure 7.9 shows plots of  $S^*$  obtained via both equations along with the line of equality. As observed, the values are approximately the same up to peak stress where the values start to deviate with the difference becoming greater as damage grows reaching a value of 15% at the point of localization. The difference at localization could be considered appreciable; however, since the comparison is good up to peak stress and since it had been shown in earlier research (Kim 1990, Lee 1998a) that the  $C$  vs.  $S^*$  and  $C$  vs  $S$  approaches are comparable in characterizing asphalt mixtures, it will be used as a candidate approach in developing the viscoelastic characterization model.

Figure 7.10 shows the direct relationship between  $S$  and  $S^*$ , where  $S^*$  is obtained from both Equations (7.5) and (7.6). The relationship could be classified as following a power form in the beginning and then changing to a linear relationship. Figure 7.11, on the other hand, shows the  $C$  vs.  $S$ , and  $C$  vs.  $S^*$  (from both equations) for a constant crosshead rate test at 25°C. Again, the curves almost overlap up to peak stress, after which they start to deviate.

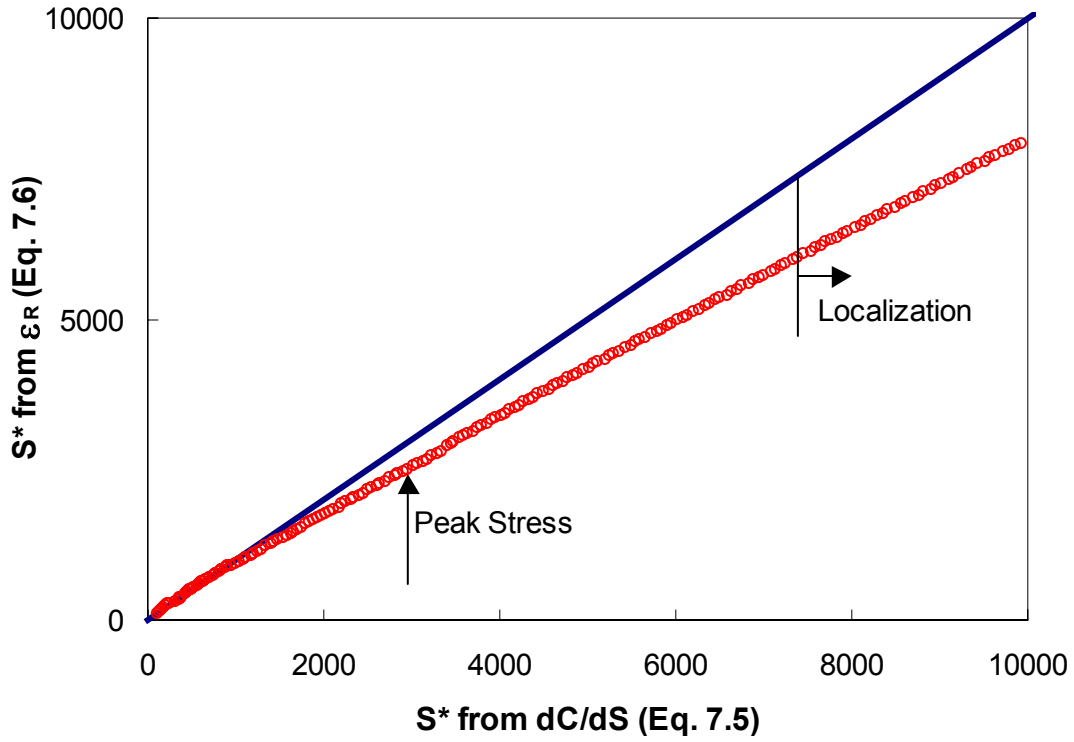


Figure 7.9. Comparison of  $S^*$  as calculated from Equations (7.5) and (7.6)

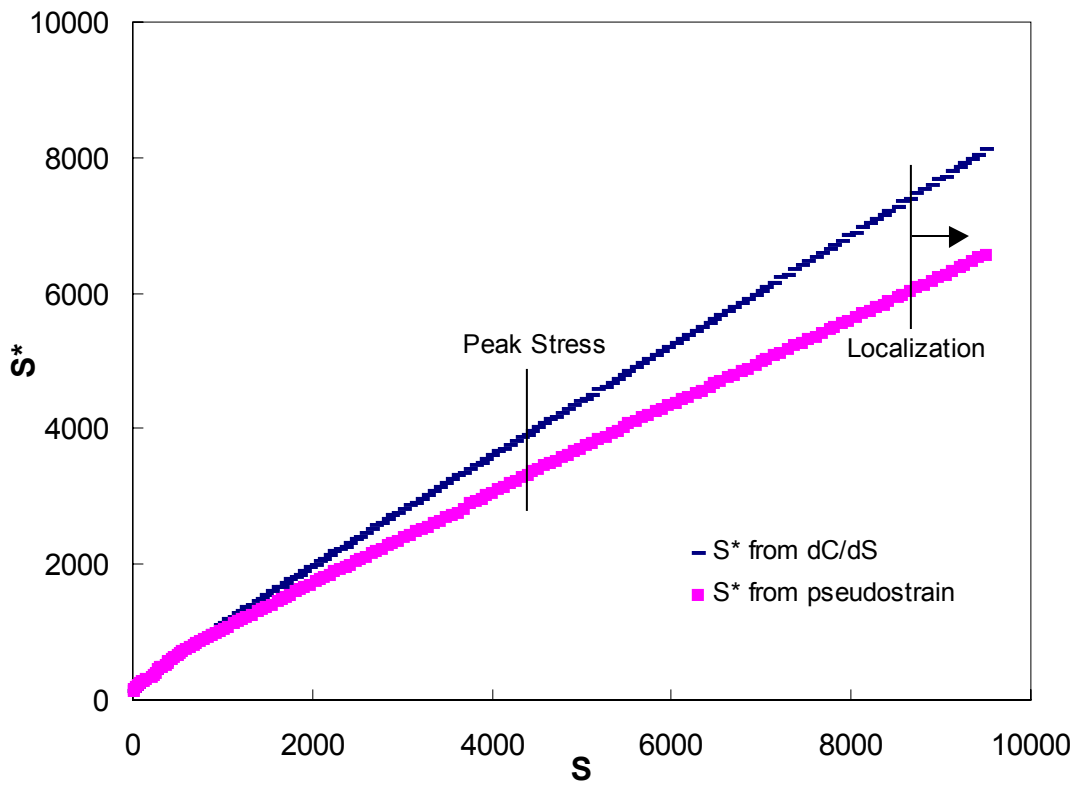


Figure 7.10. Relationship between  $S$  and  $S^*$  using monotonic test data at  $25^{\circ}\text{C}$

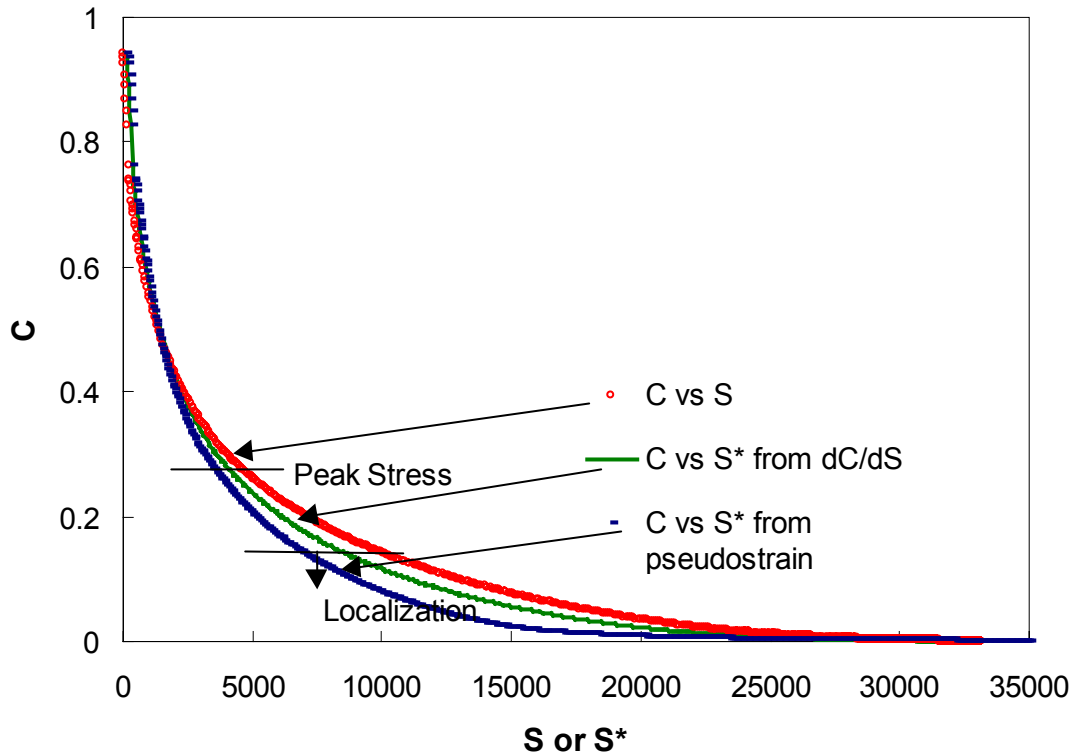


Figure 7.11.  $C$  vs.  $S$  and  $C$  vs.  $S^*$  for a monotonic test at  $25^{\circ}\text{C}$

### 7.3 Viscoelastic Model: $C$ vs. $S$ Approach

As mentioned in the introductory section of this chapter, two candidate approaches to model the viscoelastic behavior of asphalt concrete mixtures will be presented. The approaches are very similar, the difference being in the selection of the damage parameter used:  $S$  vs.  $S^*$ . The relationship between those parameters was discussed in the previous section. The  $C$  vs.  $S$  approach will be first discussed, where the theoretical formulation, determination of model parameters, and the associated problems will be presented. In the next section, the same will be presented for the  $C$  vs.  $S^*$  approach.

### 7.3.1 Theoretical Formulation

It was shown that the C vs. S curves for the constant crosshead rate tests conducted at 5°C collapse, which suggests that there is no significant viscoplastic response. Therefore, the 5°C data can be used for the development of the viscoelastic model. For viscoelastic behavior, Equation (7.7) holds true:

$$\sigma = C(S)\varepsilon^R \quad (7.7)$$

where  $\sigma$  is stress,  $\varepsilon^R$  is pseudostrain, C is the material damage function, and S is an internal state variable (damage parameter). The form of Equation (7.7) requires a prior knowledge of the viscoelastic strain ( $\varepsilon_{ve}$ ) because S is expressed as a function of  $\varepsilon_{ve}$  as shown in Equation (7.6). However, in actual experiments the total strain and stress are measured. It is therefore convenient to describe the damage parameter S in terms of stress. The following section illustrates the derivation of the relationship between S and stress.

The crack growth rate law suggests the following:

$$\frac{dS}{d\xi} = A(\varepsilon^R)^q \quad (7.8)$$

where  $\xi$  is reduced time,  $q = 2\alpha$ , and A is a regression coefficient that yields best overlap among different rates. From Equations (7.7) and (7.8),

$$\frac{dS}{d\xi} = A\left[\frac{\sigma}{C(S)}\right]^q \quad (7.9)$$

Rearranging and integrating both sides yields:

$$\int_0^S C^q(S) dS = A \int_0^\xi \sigma^q d\xi \quad (\text{say, equal to } F(S)) \quad (7.10)$$

Define  $f(S)$  as follows:

$$f(S) = F(S)^{\frac{1}{q}} = A^{\frac{1}{q}} \left[ \int_0^{\xi} \sigma^q d\xi \right]^{\frac{1}{q}} \quad (7.11)$$

From the constant crosshead rate tests, the function  $C(S)$  can be obtained. Therefore,  $F(S)$  can be known by determining  $\int_0^S C^q(S) dS$ . By taking the Lebesgue norm (i.e., raising  $1/q^{\text{th}}$  power) of  $F(S)$  to get  $f(S)$  and plotting  $f$  vs.  $S$  from the constant crosshead rate test results,  $S$  can be expressed in terms of  $f$ . That is,

$$S = G(f) = M(\text{Lebesgue Norm of } \sigma) \quad (7.12)$$

Hence,  $S$  becomes a function of the Lebesgue norm of stress. From the definition of

pseudostrain,  $\varepsilon^R = \frac{1}{E_R} \int_0^{\xi} E(\xi - \tau) \frac{d\varepsilon}{d\tau} d\tau$ , and Equation (7.7), the following equation is

obtained and used for the prediction of viscoelastic strains for any stress history:

$$\varepsilon_{ve} = E_R \int_0^{\xi} D(\xi - \xi') \frac{d\left(\frac{\sigma}{C(S)}\right)}{d\xi'} d\xi \quad (7.13)$$

where  $E_R$  is a reference modulus,  $\xi'$  is an integration variable and  $D()$  is the creep compliance.

Therefore Equation (7.13) is the viscoelastic model to be used to predict strains if stresses and corresponding times at a particular temperature (reduced times) are known.

To be able to solve for the strains,  $C(S)$  corresponding to every stress and time needs to

be known, so that  $\frac{\sigma}{C(S)}$  can be known. This can be achieved by firstly determining the

characteristic relationship between  $C$  and  $S$  for that material, such as from the constant

crosshead rate tests where viscoplasticity is absent (Equation (7.7)), and secondly by

determining a relationship between  $S$  and stress, Equation (7.12). Then, a relationship

between  $C$  and  $\sigma$  can consequently be obtained, and the integral in Equation (7.13) is numerically solved to determine viscoelastic strain. The creep compliance,  $D(\xi)$ , is determined through interconversion from storage modulus as described in Chapter 5.

### 7.3.2 Determination of Relationships for Model Development

As noted in the previous section, viscoelastic characterization requires that relationships between the damage parameter  $S$  and stress in addition to the relationship between normalized pseudostiffness  $C$  and  $S$  be determined.

#### 7.3.2.1 $C$ vs. $S$ Relationship

The  $C$  vs.  $S$  characteristic relationship can be obtained from the five constant crosshead rate tests conducted at 5°C, the stress-strain curves of which were presented in Figure 7.2. As observed from Figure 7.12, the curves plotted at a reference temperature of 25°C overlap well; with the best fit from non-linear regression, based on a 3-term exponential series, being:

$$C = 1 - 0.06 S^{0.46} + 0.01 S^{0.45} + 0.03 S^{0.5} \quad (7.14)$$

#### 7.3.2.2 Relationship between Damage Parameter $S$ and Lebesgue Norm of Stress

As concluded in Equation (7.12), the relationship between  $S$  and stress is through the Lebesgue norm of stress. Thus,

$$S = M(A^q [\int_0^{\xi} \sigma^q d\xi]^{\frac{1}{q}}) \quad (7.15)$$

where  $q=2\alpha$ .  $A$  is a regression coefficient yielding the best overlap among the 5°C monotonic tests. Note that in this section  $\alpha=1/n$  is to be used; thus,  $q=2/n$ . Consequently,

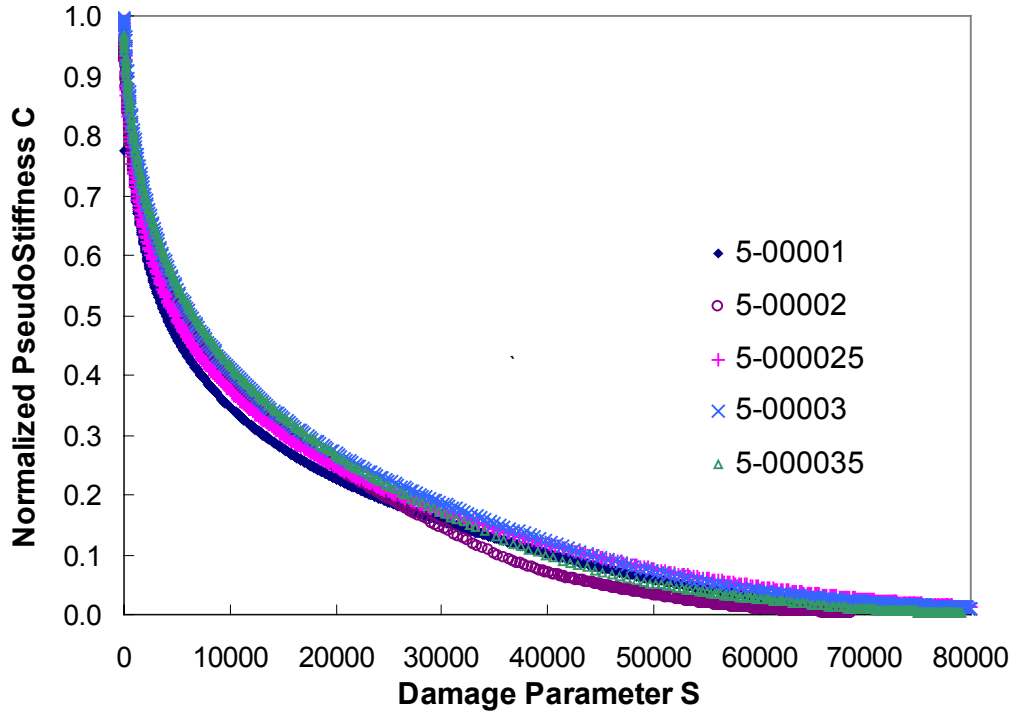


Figure 7.12. Characteristic C vs. S curves from monotonic testing at 5°C shifted to a reference temperature of 25°C

for an n value of 0.52, q is equal to 3.85. For that q value, knowing  $\xi$ ,  $\epsilon_R$ , and S for each monotonic test, the regression coefficient A can be determined using Equation (7.8).

The differential  $\frac{dS}{d\xi}$  can be determined via two approaches. In the first approach a functional relationship (power form) between S and  $\xi$  is determined and later the first derivative of that relationship is determined to evaluate  $\frac{dS}{d\xi}$  values corresponding to the reduced times. As for the other approach, the values are determined through numerical differentiation; i.e., using the localized slope method  $\left(\frac{\Delta S}{\Delta \xi}\right)$ . Then, regression is run to determine values of A for each test. Unfortunately, after the analysis was carried out, two problems surfaced, the first one being that depending on which approach is used to

calculate  $\frac{dS}{d\xi}$ , different values of A are obtained. The other problem was that no value of A could be obtained if the value of q is set as  $2\alpha$ . The value of q was found to be test dependent and had to be set as a variable to be determined through regression. And even when that was done, values of A and q for the different tests varied significantly from each other. Figure 7.13 is a plot of the variation of  $\frac{dS}{d\xi}$  as a function of pseudostrain.

Table 7.1 summarizes the values of A and q obtained through regression on the data from the 5°C monotonic testing data.

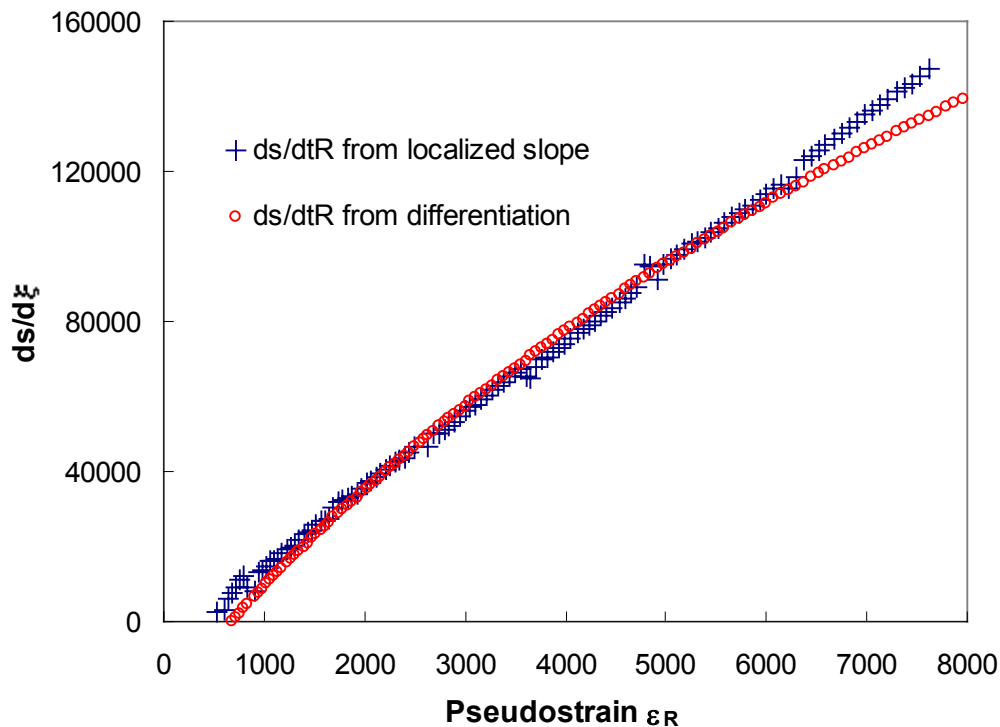


Figure 7.13.  $dS/d\xi$ , from the localized slope method and from direct differentiation, as a function of  $\varepsilon_R$  for a test at 5°C and a constant crosshead rate of 0.00002

### 7.3.3 Problems Associated with the C vs. S Approach

As denoted earlier and presented in Table 7.1, there are two main problems that obstruct the use of S as a damage parameter in developing the viscoelastic model. The

first problem lies in the fact that A values obtained from the two aforementioned valid approaches are different. In addition, the variation in the values of A and q from one test to the other prevents developing a unique relationship relating the damage parameter to S. Last but not least, the fact that the q value obtained from the best fit is close to 1, whereas theory states that it should be equal to  $2\alpha$  which is equal to around 4 raises a great concern about the validity of the steps involved in this approach. Consequently, this approach will, for the time being, be dropped as a candidate for the development of a viscoelastic model until further research is done in the future.

Table 7.1. A and q values for 5°C monotonic tests obtained through different techniques

Test ID	$dS/d\xi$	A	q
5-00001	Local Derivative	127.9	0.62
	Direct Differentiation	129.2	0.62
	<b>Average</b>	<b>128.55</b>	<b>0.62</b>
5-00002	Local Derivative	9.67	1.03
	Derivative of Power fit	20.4	0.94
	<b>Average</b>	<b>15.035</b>	<b>0.985</b>
5-000025	Local Derivative	34	0.89
	Derivative of Power fit	52.5	0.84
	<b>Average</b>	<b>43.25</b>	<b>0.865</b>
5-00003	Local Derivative	34.7	0.91
	Derivative of Power fit	50.1	0.87
	<b>Average</b>	<b>42.4</b>	<b>0.89</b>
5-000035	Local Derivative	9.86	1.08
	Derivative of Power fit		
	<b>Average</b>	<b>9.86</b>	<b>1.08</b>

#### 7.4 Viscoelastic Model: $C$ vs. $S^*$ Approach

This approach is similar to the previous approach with the difference being in the damage parameter and model relationships used for the prediction of viscoelastic strains.

##### 7.4.1 Theoretical Formulation

Similar to the previous approach, Equation (7.16) is used to characterize the viscoelastic behavior.

$$\sigma = C(S^*)\varepsilon^R \quad (7.16)$$

where  $\sigma$  is the stress,  $\varepsilon^R$  is the pseudostrain,  $C$  is the pseudostiffness, and  $S^*$  is the damage parameter.  $C$  can be viewed as the material's structural integrity and ranges from 0 (complete failure) to 1 (virgin material).  $S^*$ , which is the Lebesgue norm of pseudostrain, can be viewed as a global damage parameter and mathematically represented by Equation (7.17):

$$S^* \equiv \left[ \int_0^{\xi} |\varepsilon^R|^{2\alpha} d\xi \right]^{1/2\alpha} \quad (7.17)$$

It has been shown earlier by Park and Schapery (1996) that  $S^*$  can be represented as a function of the Lebesgue norm of stress. In mathematical form:

$$S^* = f \left[ \int_0^{\xi} \sigma^{2\alpha} d\xi \right]^{1/2\alpha} \quad (7.18)$$

where  $\xi$  is reduced time at a reference temperature, in this research 25°C, and  $\alpha$  is a constant. The viscoelastic strain is given by the inverse of the convolution integral, Equation (7.18):

$$\varepsilon_{ve} = E_R \int_0^{\xi} D(\xi - \xi') \frac{d\left(\frac{\sigma}{C(S^*)}\right)}{d\xi'} d\xi' \quad (7.19)$$

where  $\varepsilon_{ve}$  is viscoelastic uniaxial strain,  $E_R$  is reference modulus set as an arbitrary constant (set to 1 in this research),  $D(\xi)$  is uniaxial creep compliance,  $\xi$  is the reduced time of interest at a reference temperature (25°C), and  $\xi'$  is an integration variable. Creep compliance is already known through conversion from complex modulus.

Similarly, just like in the previous approach, relationships relating  $C$  to  $S^*$  and  $S^*$  to stress should be determined to predict the viscoelastic strain. Once determined, then for a given stress at a given reduced time (time at a given temperature) the viscoelastic strain can be determined after performing the numerical integration.

## 7.4.2 Determination of Relationships for Model Development

### 7.4.2.1 $C$ and $S^*$ Relationship

Knowing time, stress, and strain for every constant crosshead rate test performed at 5°C, a relationship between  $C$  and  $S^*$  can be determined. Since minimal viscoplastic strains are expected at 5°C, a single relationship between  $C$  and  $S^*$  should hold for all the tests according to Equation (7.16). As mentioned previously, an  $\alpha$  value of  $1/n$  gave the best collapse between the  $C$  vs.  $S^*$  curves (Figure 7.14). Only the slowest rate at 5°C exhibited slight deviation at low  $C$  values. The relationship between  $C$  and  $S^*$  (Equation (7.20)) is obtained by fitting a 6-term power series using non-linear optimization to the  $C$  vs.  $S^*$  data from all the tests.

$$C = 1 - 13 S^{* (-0.1)} + 32 S^{* (-0.4)} + 21 S^{* (-0.3)} + 32 S^{* (-0.6)} - 27 S^{* (-0.6)} - 13 S^{* (-0.5)} \quad (7.20)$$

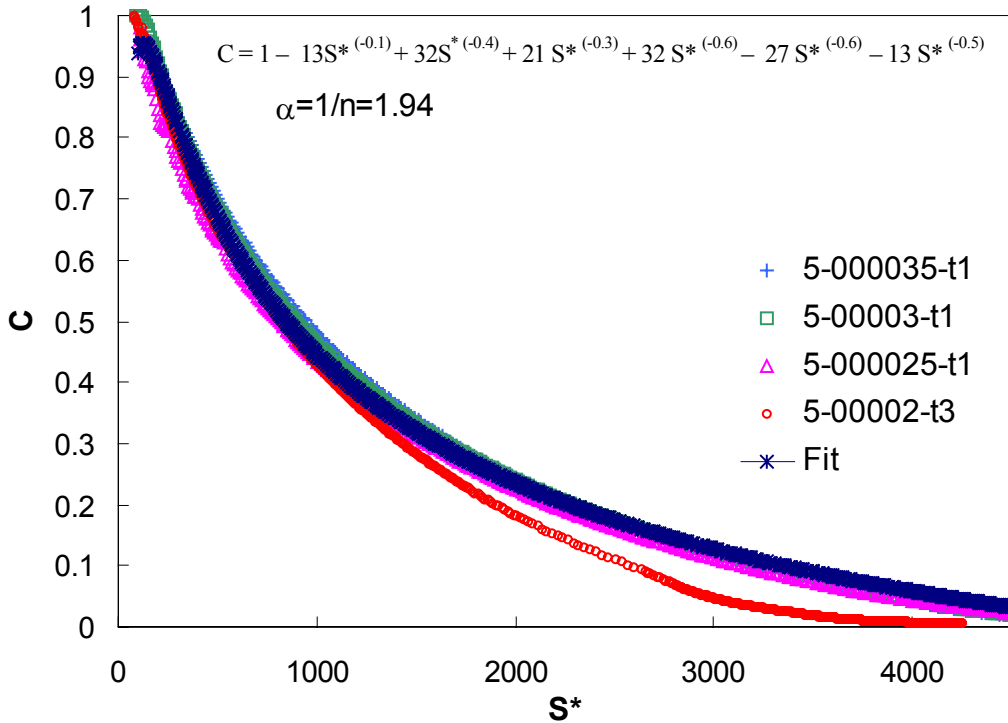


Figure 7.14. C vs. S\* for tests at 5°C plotted at a reference temperature 25°C

#### 7.4.2.2 Relationship between Damage Parameter S\* and Lebesgue Norm of Stress

Knowing the C vs. S\* relationship, the next step is to relate S\* to stress.

Again, from the data obtained from the monotonic tests conducted at 5°C, a single relationship could be obtained that relates S\* to the Lebesgue norm of stress. However, as seen in Figure 7.15, that relationship holds true up to the point where the S\* value is about 2500 and the Lebesgue norm value is about 1750. After that, as stress increases, S\* increases dramatically implying a very rapid failure rate. In fact, that inflection point corresponds to the point of localization as observed from the stress-strain and the strain-time curves for those tests. Such a behavior is expected because at that temperature after localization and development of macrocracks, the failure of the specimen occurs very

rapidly. The relationship up to localization (Equation (7.21)) is obtained using non-linear regression by fitting a 5-term exponential series to the individual test data. The constraint in this approach is that predictions for strains corresponding to  $S^*$  and Lebesgue norm values beyond 2500 and 1750 respectively will be erroneous.

$$S^* = 2800 e^{-1.6Leb} + 5 e^{0.004Leb} - 32 e^{0.002Leb} - 1200 e^{-0.0002Leb} + 1200 e^{0.0005Leb} \quad (7.21)$$

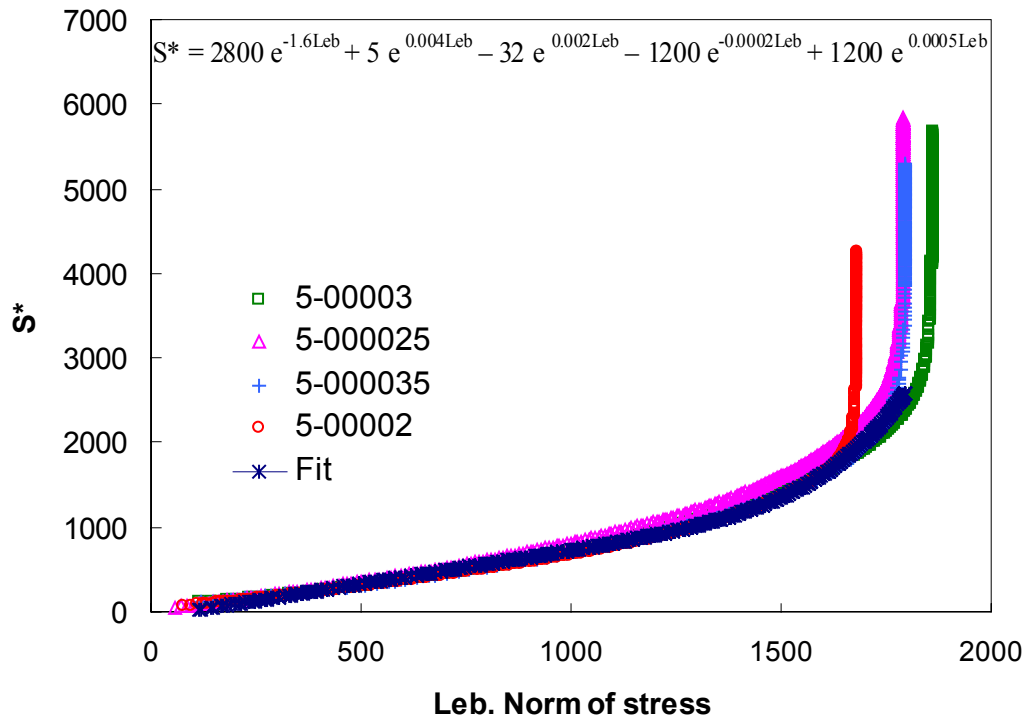


Figure 7.15.  $S^*$  vs. Lebesgue norm for tests at  $5^{\circ}\text{C}$  plotted at a reference temperature  $25^{\circ}\text{C}$

#### 7.4.2.3 Summary of the Viscoelastic Model

Having determined the relationship between  $S^*$  and stress and the relationship between  $C$  and  $S^*$ , Equation (7.19) can now be used to predict the viscoelastic strains by performing the numerical integration. A step by step procedure to develop the model is as follows:

1. Conduct complex modulus testing at several temperatures and frequencies to obtain the material response functions (storage modulus, relaxation modulus, and creep compliance). From the storage modulus mastercurve, determine the LVE shift factors and  $n$  for the calculation of  $\alpha$ .
2. Conduct constant crosshead rate tests at low temperatures and fast strain rates. From stress and reduced time, calculate pseudostrains, normalized pseudostiffness ( $C$ ), and  $S^*$ .
3. Plot the  $C$  vs.  $S^*$  curves and develop the  $C$  vs.  $S^*$  characteristic relationship.
4. Calculate the Lebesgue norm of stress and determine the characteristic relationship between  $S^*$  and stress.
5. Knowing  $S^*$  vs. stress and  $C$  vs.  $S^*$  relationship, predict for given stress and reduced time the viscoelastic strain using Equation (7.19).

#### **7.4.3 Validation of the Viscoelastic Strain Model**

Now that a viscoelastic model has been developed, it is important to check whether the predictions match the actual viscoelastic response. For the validation check, the strains for constant crosshead rate tests will be predicted, the tests being both those used to develop the model and other tests that were not used. Tests used for the verification of the time-temperature superposition study at  $-10^{\circ}\text{C}$  and  $5^{\circ}\text{C}$  will be a good set to use. However, any test that is to be used has to have been conducted at a fast strain rate so that the presence of any viscoplastic strain, which can not be handled by the viscoelastic model, be minimal. Figures 7.16 through 7.18 show predicted vs. actual strain from constant crosshead strain tests at  $-10^{\circ}\text{C}$  and  $5^{\circ}\text{C}$ . As observed, there is an

excellent match between the predicted viscoelastic and actual strains for the test at  $-10^{\circ}\text{C}$  and for 0.008 rate test at  $5^{\circ}\text{C}$ . For the slower rate at  $5^{\circ}\text{C}$ , the prediction is not as close because at that test condition viscoplastic strains are more significant. Unlike the previous two tests which failed in brittle mode, the slow rate test at  $5^{\circ}\text{C}$  failed in a ductile mode. As observed for that test (Figure 7.18), the prediction starts to become less accurate after localization due to the erroneous  $S^*$ -Lebesgue norm of stress relationship after that point. Figure 7.19 shows the actual vs. measured strains for a test at  $40^{\circ}\text{C}$  and rate of 0.00009. The prediction is inaccurate in this condition mainly due to the dominance of viscoplastic strain at that testing condition.

Therefore, it can be concluded that:

1. The viscoelastic model yields accurate predictions for tests that do not yield significant viscoplastic behavior, and
2. Predictions can be made up to the point of failure when the specimen fails in a brittle mode.
3. For ductile failure, the prediction is valid up to localization.

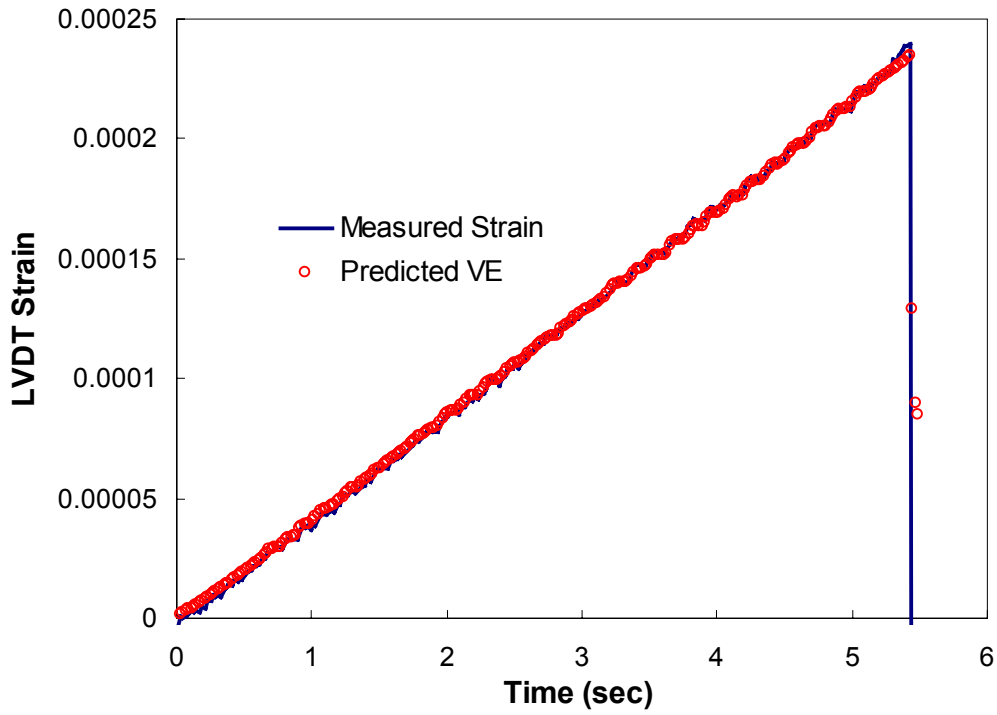


Figure 7.16. Predicted viscoelastic strain vs. actual strain at  $-10^{\circ}\text{C}$  and a rate of 0.0005

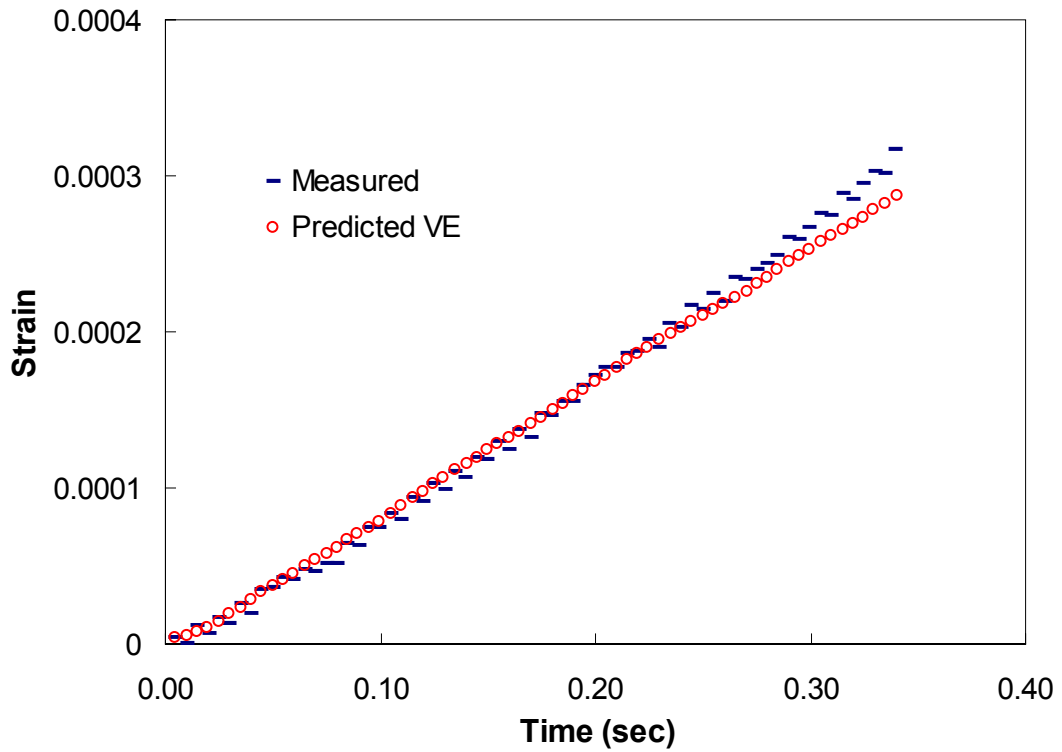


Figure 7.17. Predicted viscoelastic strain vs. actual strain at  $5^{\circ}\text{C}$  and a rate of 0.008

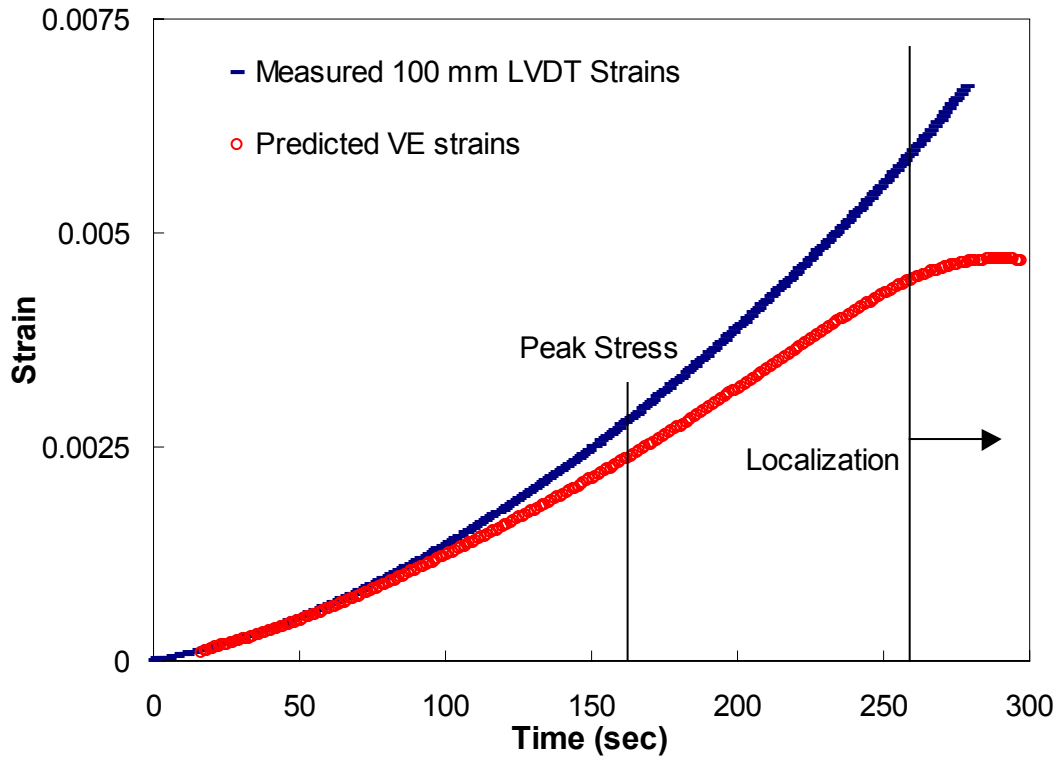


Figure 7.18. Predicted viscoelastic strain vs. actual strain at 5°C and a rate of 0.000025

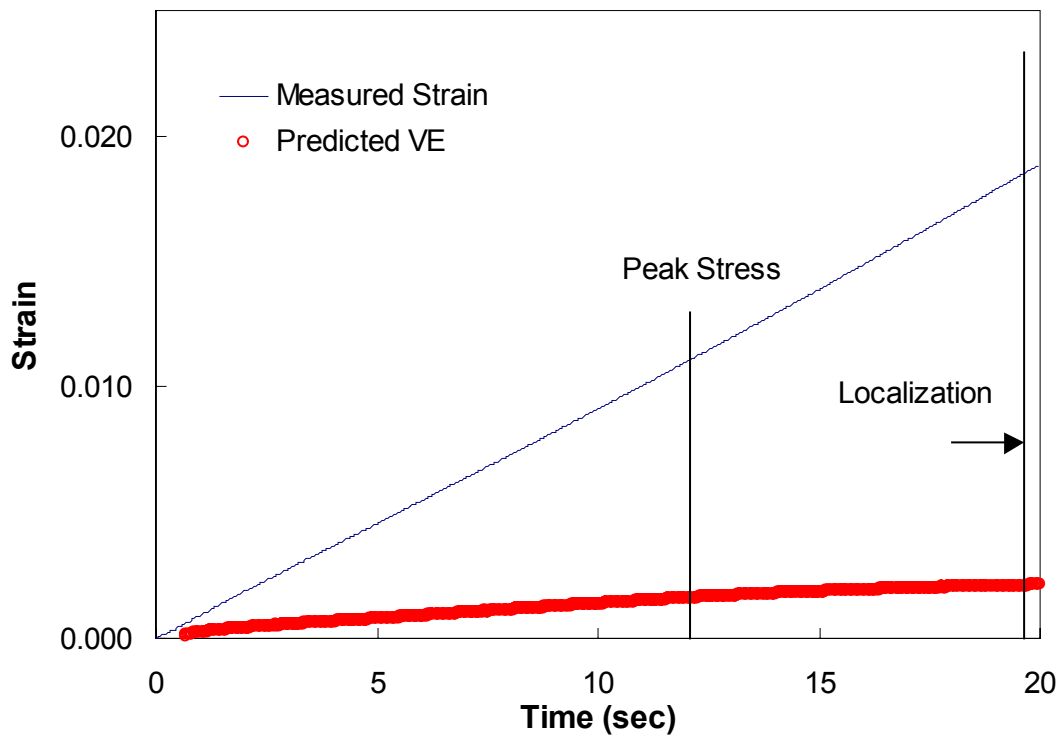


Figure 7.19. Predicted viscoelastic strain vs. actual strain at 40°C and a rate of 0.00009

### 7.5 Modeling of Viscoplastic Behavior

The first step involved in modeling viscoplastic behavior is to separate, for a particular loading history, the resulting viscoplastic from the viscoelastic response. Separation becomes easier when the load is applied as a step function (creep and recovery tests). Two approaches for the determination of viscoplastic strain in creep and recovery tests are presented in the subsequent sections. The objective is to determine the viscoplastic strain at the end of the recovery period of each cycle:  $\epsilon_{vp1}$ ,  $\epsilon_{vp2}$ , and  $\epsilon_{vp3}$  at  $\xi_2$ ,  $\xi_4$ , and  $\xi_6$  respectively, and so on for the rest of the cycles until failure (Figure 7.20).

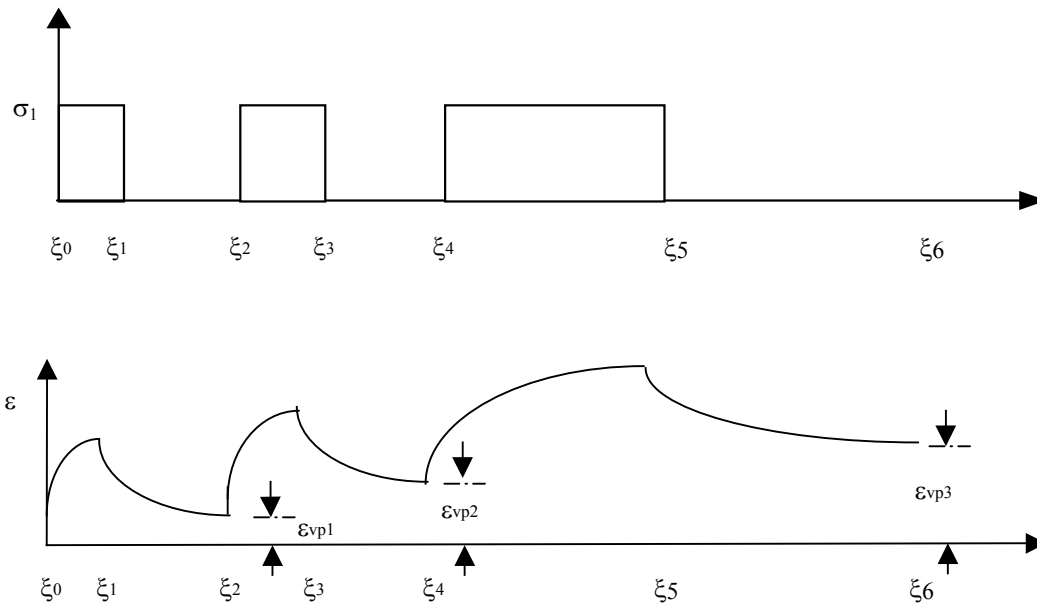


Figure 7.20. Typical stress and strain histories for creep and recovery tests

Once an approach for determining viscoplastic strains is selected, an experimental program consisting of two series of creep and recovery tests, S4 and S5, are performed to model the viscoplastic behavior. It is worth noting that since the time-temperature superposition holds for viscoplastic behavior, the tests need be conducted at only one

temperature using reduced times given that viscoplastic strains are present in the response. The three proposed approaches to determine viscoplastic strain are presented in the following section.

### **7.5.1 Determining Viscoplastic Strains at the End of Creep and Recovery Cycles**

When a creep and recovery cycle test is conducted, viscoelastic and viscoplastic strains are accumulated during the loading stage and then during recovery the viscoelastic strains recover. If enough recovery period is allowed, both viscoelastic strain recovery and micro-crack healing mechanisms will occur, thus leaving viscoplastic strain as the only permanent strain left. Since no viscoplastic strain is accumulated during recovery, the strain at the end of recovery of a given cycle will be equivalent to the cumulative viscoplastic strain measured at the end of that cycle minus measured cumulative viscoplastic strain at the end of the recovery period of the previous cycle. Thus, viscoplastic strains for individual cycles can be obtained if the cumulative viscoplastic strain at the end of each cycle is known; that is:

$$\varepsilon_{vp(n)} = \varepsilon_{cvp(n)} - \varepsilon_{cvp(n-1)} \quad (7.22)$$

where  $\varepsilon_{vp(n)}$  is the viscoplastic strain accumulated during the  $n^{\text{th}}$  cycle, and  $\varepsilon_{cvp(n)}$  is the cumulative viscoplastic strain at the end of the recovery period of the  $n^{\text{th}}$  cycle.

#### *7.5.1.1 Direct Measurement of Strain at the End of Recovery Periods*

Viscoplastic strains can be determined directly by measuring the strains at the end of the recovery periods of the creep and recovery cycles (Figure 7.20). This is the simplest method to obtain the viscoplastic strain; however, preliminary tests done show that the recovery period that is required for the full recovery of viscoelastic strains is too

long. For a 10-second loading, allowing a 6000-sec recovery was still not enough for the full recovery of viscoelastic strain. Therefore, if the strain at the end of the recovery period is measured and assumed to be equal to the viscoplastic strain, an over-prediction of viscoplastic strain will occur. The longer the period allowed for recovery the smaller the error; but a very long recovery period will yield a very long overall testing duration which could deem to be impractical. Therefore, this approach, as presented, could not be used for the determination of the viscoplastic strains from the repetitive creep and recovery tests.

#### *7.5.1.2 Direct Measurement with Prediction of Viscoelastic Strains at the End of Recovery Periods*

As stated previously, if the recovery period is not long enough, the strains at the end of the period will be composed of viscoelastic strain, which would not yet have fully recovered, in addition to viscoplastic strain. If the viscoelastic strain can be accurately predicted at the end of the recovery period, then the viscoplastic strain would be the difference between the measured strain and the predicted viscoelastic strain.

The viscoelastic model developed earlier was used to predict the viscoelastic strains for the repetitive creep and recovery test history. However, due to specimen-to-specimen variation, there was inconsistency in the resulting viscoplastic strains. This was the first shortcoming of the approach. Secondly, if this approach is followed, then any inaccuracies and limitations of the viscoelastic model, such as validity of prediction up to the point of localization only, will transfer to the viscoplastic model and hence yield to errors in the viscoplastic model itself. Keeping the development of both models independent is a better strategy and hence this approach was dropped.

### 7.5.1.3 Fitting Recovery Strains Using Log-Sigmoidal Function

As stated in the section discussing the first approach, very long recovery periods are needed for the viscoelastic strains to fully recover. It would then take days to conduct a single repetitive creep and recovery test required for modeling. A solution would be to allow for a recovery period long enough to make fitting the following log-sigmoidal function to the recovery strains possible:

$$\varepsilon_r = a_1 + \frac{a_2}{\left\{ a_3 + \frac{a_4}{\exp[a_5 + a_6 \log_{10}(t)]} \right\}} \quad (7.23)$$

where  $t$  is the time,  $a_1$  through  $a_6$  are regression coefficients, and  $\varepsilon_r$  is the recovery strain.

As known, when the log-sigmoidal fit is plotted on a log-log plot, it yields a lower and upper asymptote. The value corresponding to the lower asymptote, at which no more viscoelastic recovery is assumed to take place, is the value of the viscoplastic strain.

Figure 7.20 shows the strain history for a typical repetitive creep and recovery test in tension until failure of the specimen. As seen, the time of recovery is not enough to allow for full viscoelastic strain recovery as evidenced by continuing decrease in strain and absence of an asymptote, especially for the last cycles. For example, even a 12,000-second recovery period was not enough for full viscoelastic strain recovery as seen in Figure 7.21. In that figure, the recovery strain for each cycle is plotted as a function of time on a log-log scale with the start time for each recovery period being zero and not actual time from start of testing. The sigmoidal function fits the recovery strain for each cycle well, and an asymptote can be seen if the time range is extended.

This approach will be selected for incorporation in the model development, in which the value of the strain obtained from the asymptote will be considered as the cumulative viscoplastic strain accumulated at the end of that cycle.

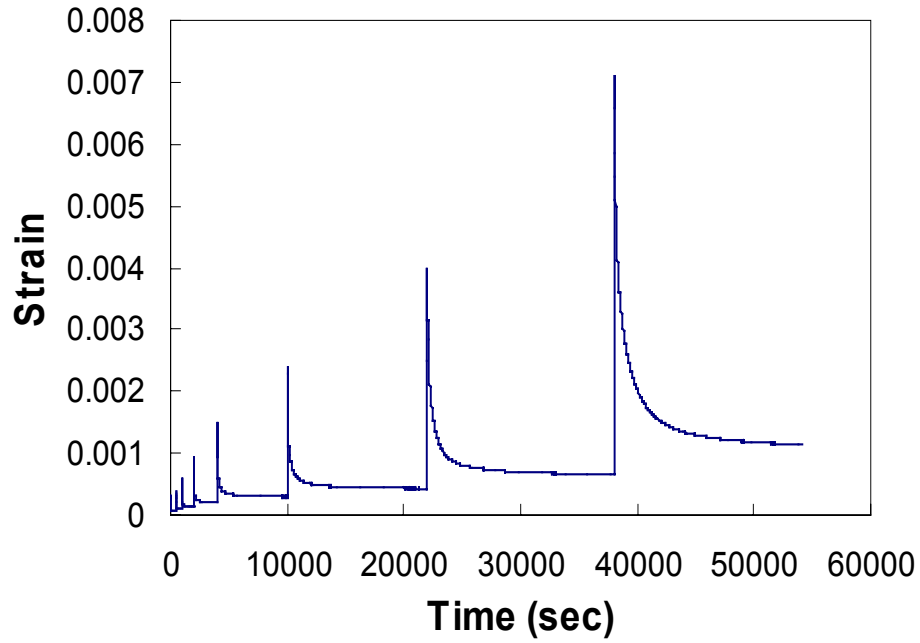


Figure 7.20. Typical strain response from a repetitive creep and recovery test till failure

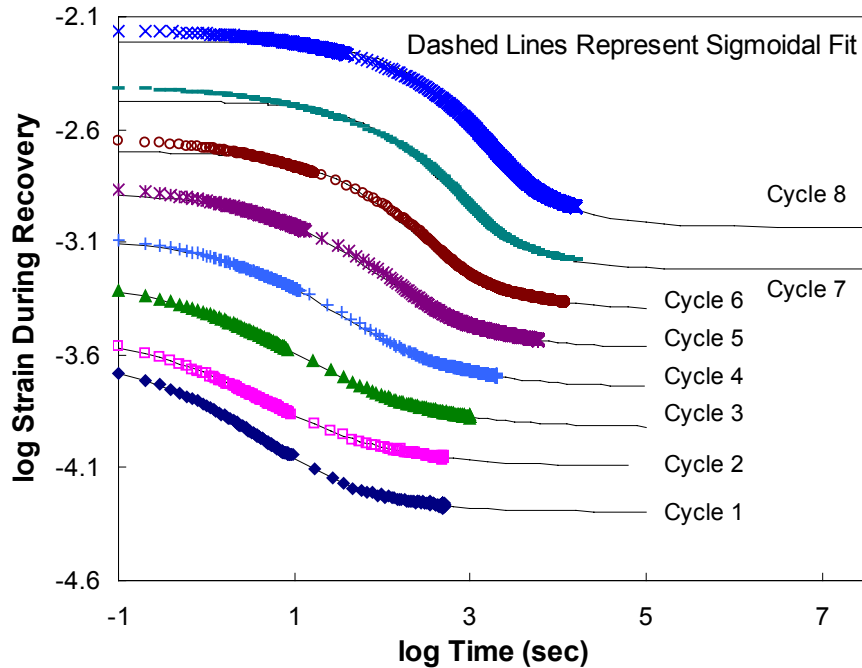


Figure 7.21. Recovery strains for cycles of a repetitive creep and recovery test (corresponds to strain history shown in the previous figure, plotted on a log-log scale where start time of each recovery period is set to zero)

## 7.5.2 Theoretical Formulation and Testing Program

After presenting in the previous section the approaches that can be adopted to determine the viscoplastic strain and selecting the most suitable one, the theory which will serve as the foundation of the viscoplastic model in addition to the required experimental tests are presented next.

### 7.5.2.1 Theoretical Formulation

Viscoplastic strain is assumed to follow a strain-hardening model of the form (Uzan et al 1985.):

$$\dot{\epsilon}_{VP} = \frac{g(\sigma)}{\eta_{VP}} \quad (7.24)$$

where  $\dot{\varepsilon}_{vp}$  is the viscoplastic strain rate, and

$\eta_{vp}$  is the material's coefficient of viscosity.

Assuming that  $\eta$  is a power law in strain (Uzan et al. 1985), Equation (7.24) becomes:

$$\dot{\varepsilon}_{vp} = \frac{g(\sigma)}{A\varepsilon_{vp}^p} \quad (7.25)$$

where A and p are model coefficients. Rearranging and then integrating both sides yields:

$$d\varepsilon_{vp} \times \varepsilon_{vp}^p = \frac{g(\sigma) \times dt}{A} \quad (7.26)$$

$$\varepsilon_{vp}^{p+1} = \frac{p+1}{A} \int_0^t g(\sigma) dt \quad (7.27)$$

Raising both sides of Equation (7.27) to the (1/p+1) power yields:

$$\varepsilon_{vp} = \left( \frac{p+1}{A} \right)^{1/p+1} \left( \int_0^t g(\sigma) dt \right)^{1/p+1} \quad (7.28)$$

For a **creep** test, stress is constant; thus Equation (7.28) becomes:

$$\varepsilon_{vp} = \left( \frac{p+1}{A} \right)^{1/p+1} g(\sigma)^{1/p+1} t^{1/p+1} \quad (7.29)$$

Assuming  $g(\sigma) = B\sigma_1^q$ , Equation (7.29) becomes:

$$\varepsilon_{vp} = \left( \frac{p+1}{A} \right)^{1/p+1} \times (B\sigma_1^q)^{1/p+1} \times (t)^{1/p+1} \quad (7.30)$$

Coupling coefficients A and B into coefficient D, Equation (7.30) becomes:

$$\varepsilon_{vp} = \left( \frac{p+1}{D} \right)^{1/p+1} \times (\sigma_1^q)^{1/p+1} \times (t)^{1/p+1} \quad (7.31)$$

Substituting time in Equation (7.31) by reduced time yields:

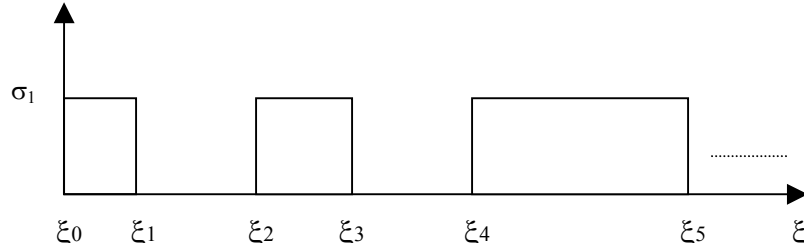


Figure 7.22. Schematic of a stress history of an S4 test

$$\varepsilon_{vp} = \left( \frac{p+1}{D} \right)^{1/p+1} \times (\sigma_1^q)^{1/p+1} \times (\xi)^{1/p+1} \quad (7.32)$$

To determine the viscoplastic strain coefficients (D, p, and q), two series of repetitive creep and recovery tests in tension until failure of the specimen are proposed: S4 (change in time of loading) and S5 (change in stress).

#### 7.5.2.2 Testing Program

Tests required for determining the model coefficients at different temperatures need only to be run at one temperature, in this case 25°C. Once those coefficients are determined, they apply to any other temperature, by simply substituting time with reduced time using the LVE shift factor for that temperature.

#### S4 Series Testing

Test S4 consists of repeated creep and recovery cycles at constant tensile stress amplitude and increasing loading and recovery times up to failure. The purpose of this test is to determine the time coefficient “p” in Equation (7.32).

The stress level, loading and recovery times in addition to the ratio of loading times of subsequent cycles were selected so that failure occurs within 7 to 8 cycles. The recovery period was designed to increase with the increase in loading time. The duration

selected had to enable the fitting of a log-sigmoidal function to the recovery strains when plotted against time on a log-log scale. Figure 7.22 shows the stress history of an S4 test, whereas Table 7.2 shows the test parameters.

Table 7.2. S4 testing parameters

Cycle	Stress (kPa)	Loading Time (sec)	Recovery Time (sec)
1	400	0.5	500
2	400	0.5	500
3	400	1	1000
4	400	2	2000
5	400	4	6000
6	400	8	12000
7	400	16	16000
8	400	32	16000

For the first cycle:

$$\varepsilon_{vp1} = \left( \frac{p+1}{D} \right)^{1/p+1} \times (\sigma_1)^{q/p+1} \times (\xi_1 - \xi_0)^{1/p+1} \quad (7.33)$$

where  $\varepsilon_{vp1}$  is the viscoplastic strain accumulated at the end of the first cycle. During rest periods, there is no viscoplastic strain accumulation since the stress is zero. Thus, at the end of the second cycle, the cumulative viscoplastic strain,  $\varepsilon_{vp2}$ , is given by:

$$\varepsilon_{vp2} = \varepsilon_{vp1} + \left( \frac{p+1}{D} \right)^{1/p+1} \times (\sigma_1)^{q/p+1} \times (\xi_1 - \xi_0)^{1/p+1} \quad (7.34)$$

$$\varepsilon_{vp2} - \varepsilon_{vp1} = \left( \frac{p+1}{D} \right)^{1/p+1} \times (\sigma_1)^{q/p+1} \times (\xi_3 - \xi_2)^{1/p+1} \quad (7.35)$$

Dividing Equation (7.35) by Equation (7.33) yields:

$$\frac{\varepsilon_{vp2} - \varepsilon_{vp1}}{\varepsilon_{vp1}} = \left( \frac{\xi_3 - \xi_2}{\xi_1 - \xi_0} \right)^{1/p+1} \quad (7.36)$$

Knowing the viscoplastic strains for the first and second cycles would thus enable the determination of “p”. The same can be done for the second and third cycle and so on, each time obtaining a new value of “p”. The values could be different due to variabilities attributed to testing; therefore, an average or refined “p” value would then need to be calculated.

### S5 Series Testing

Test S5 consists of repeated creep and recovery cycles with constant loading and recovery times but increasing stress amplitudes in tension up to failure. The purpose of this test is to determine the stress coefficient “q” in Equation (8.32). Similar to S4, the loading amplitudes and times are selected to yield failure in 7 to 8 cycles while recovery times are related to the ability of fitting a log sigmoidal function to the recovery strains thus enabling the determination of viscoplastic strains. . Figure 7.23 shows the stress history of an S4 test; whereas Table 7.3 shows the test parameters.

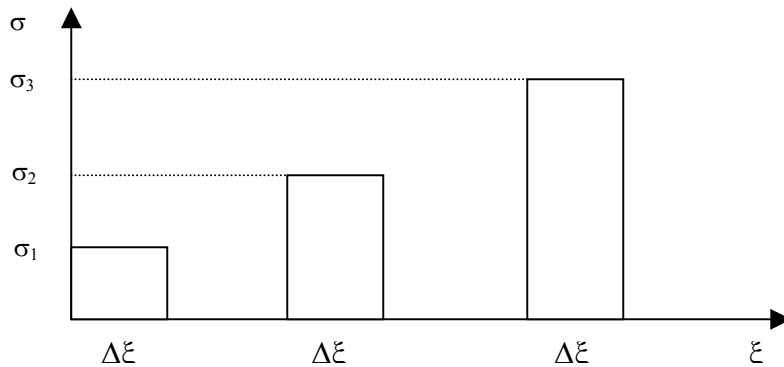


Figure 7.23. Schematic of a stress history of an S5 test

Table 7.3. S5 testing parameters

Cycle	Stress (kPa)	Loading Time (sec)	Recovery Time (sec)
1	20	10	500
2	20	10	500
3	40	10	500
4	80	10	2000
5	160	10	2000
6	320	10	10000
7	640	10	12000

For the first cycle:

$$\varepsilon_{vp1} = \left( \frac{p+1}{D} \right)^{1/p+1} \times (\Delta\xi)^{1/p+1} \times (\sigma_1)^{q/p+1} \quad (7.37)$$

For the second cycle:

$$\varepsilon_{vp2} - \varepsilon_{vp1} = \left( \frac{p+1}{D} \right)^{1/p+1} \times (\Delta\xi)^{1/p+1} \times (\sigma_2)^{q/p+1} \quad (7.38)$$

Dividing Equation (7.38) by Equation (7.37) yields:

$$\frac{\varepsilon_{vp2} - \varepsilon_{vp1}}{\varepsilon_{vp1}} = \left( \frac{\sigma_2}{\sigma_1} \right)^{q/p+1} \quad (7.39)$$

Knowing the viscoplastic strains and the value of “p” from S4, the value of “q” can then be determined. The same can be done for the second and third cycles and so on, each time obtaining the value of “q”. Again, the values could be different due to experimental reasons. An average “q” value would then be determined. Once “q” is determined, Equation (7.33) or (7.37) can be used to determine the coefficient “D”.

### *7.5.2.3 Alternative Methods to Obtain Model Coefficients from S4 and S5 Tests*

The value of coefficient D was highly dependent on whether it was calculated from Equation (7.33) or Equation (7.37). In addition, it varied depending on which cycles the equations were applied. This led to the exploration of alternative methods to obtain D and, if needed, other ways to get p or q.

Three approaches to determine the model coefficients using the test data were investigated. In the first approach, the time exponent coefficient 'p' was first determined from the S4 test data, while the stress exponent coefficient 'q' was determined from S5 test data. The coefficient 'D' was then calculated either using the S4 or the S5 data. In the second approach, 'p' was determined from the S4 data and then 'q' and 'D' were determined by non-linear regression using data from both S4 and S5 tests. As for the third approach, p, q, and D were determined using non-linear regression on test data from all S4 and S5 tests. The second approach yielded the best correlation between predicted and measured viscoplastic strains and hence was used for determining the model coefficients.

### **7.5.3 Testing Results**

There was a significant specimen-to-specimen variation in S4 and S5 testing; for that reason, a large number of replicates had to be conducted to get representative results adequate enough to be used for determining the model coefficients. Although more tests were conducted, only results from four representative S4 tests and three S5 tests were used in determining the coefficients and will be presented here. Figures 7.24 and 7.25 are stress and strain histories respectively of an S4 test conducted at 25°C in tension, while Figures 7.26 and 7.27 are those for S5.

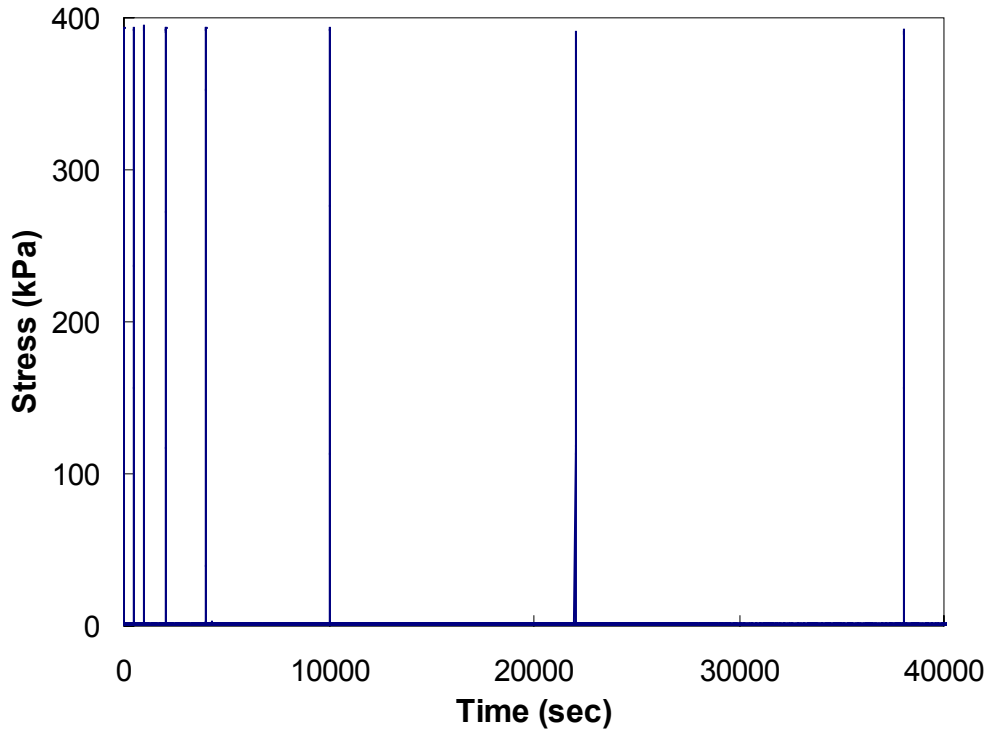


Figure 7.24. Stress history of an S4 test conducted at 25°C

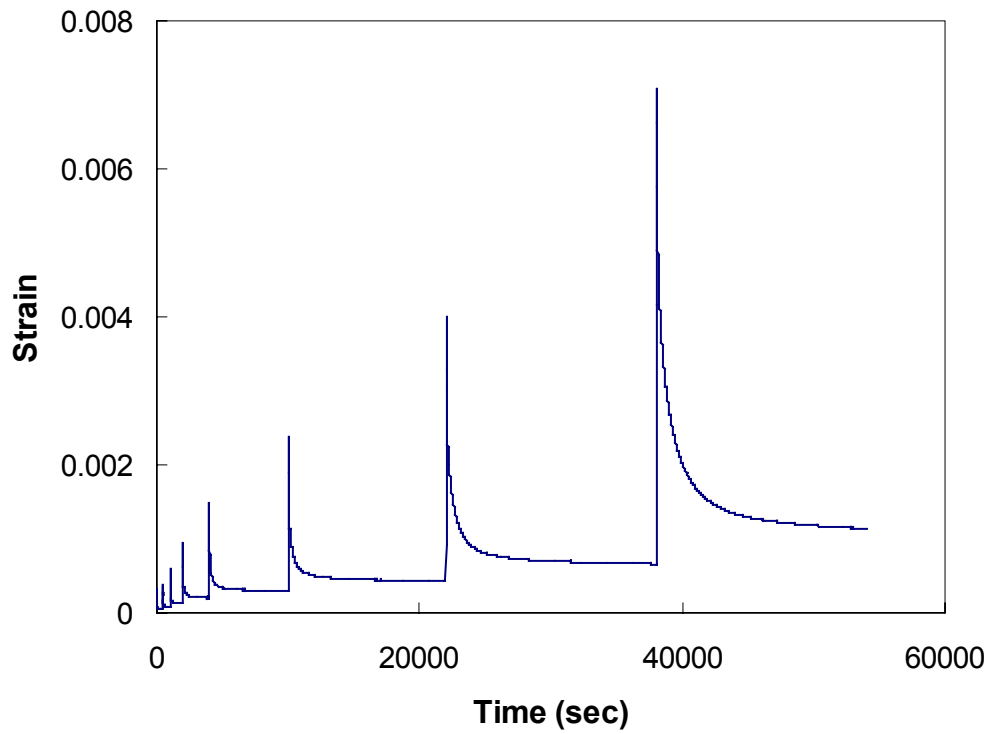


Figure 7.25. Strain history of an S4 test conducted at 25°C

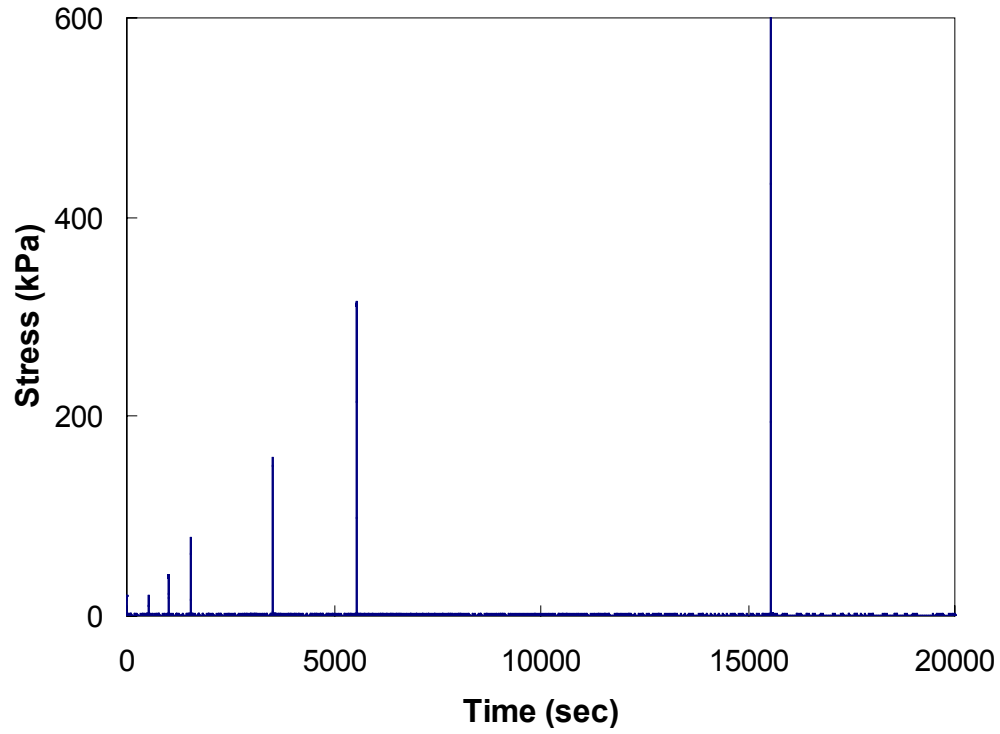


Figure 7.26. Stress history of an S5 test conducted at 25°C

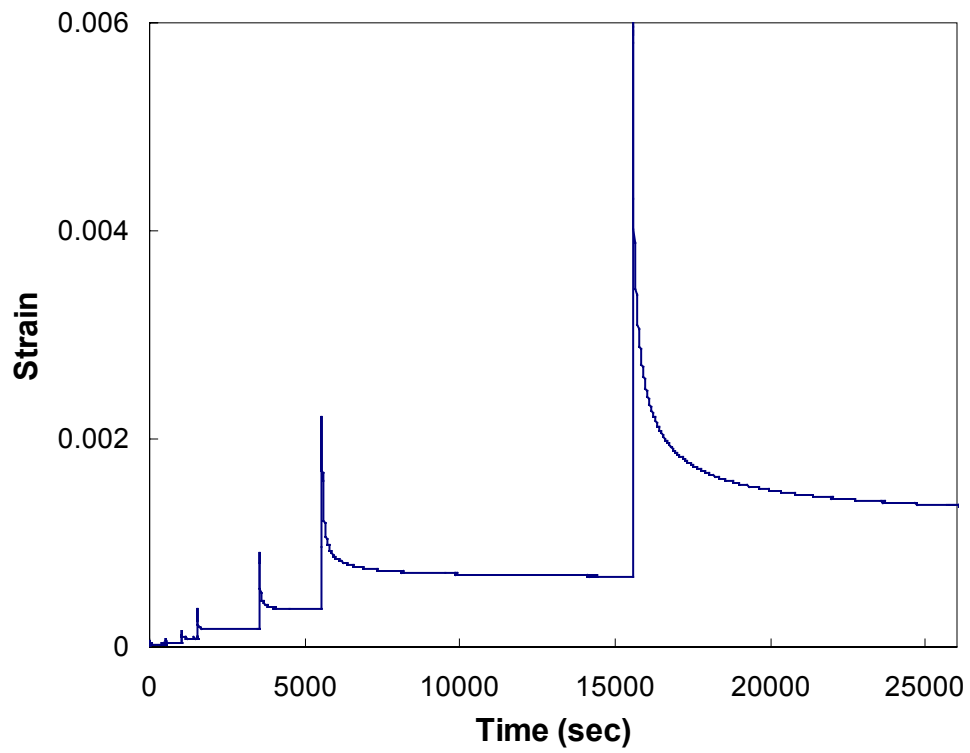


Figure 7.27. Strain history of an S5 test conducted at 25°C

Figure 7.28 is a log-log plot of cumulative strain measured at the end of each cycle as a function of that cycle's loading time for the S4 test, where the loading time from one cycle to the next cycle increases by a factor of two. Among the four replicates the plots are similar and more or less linear on log-log-scale, but there is a noticeable variability in the strain values of each. Figure 7.29 on the other hand, is a log-log plot of cumulative strain measured at the end of each cycle as a function of that cycle's stress amplitude for the S5 test, where the amplitude increases from one cycle to the next by a factor of two. There is a better match in the form and values of the plots among the three replicates presented. From the S4 and S5 test data the values of the coefficients  $p$ ,  $q$ , and  $D$  were 0.6, 1.45, and  $9e^{10}$  respectively.

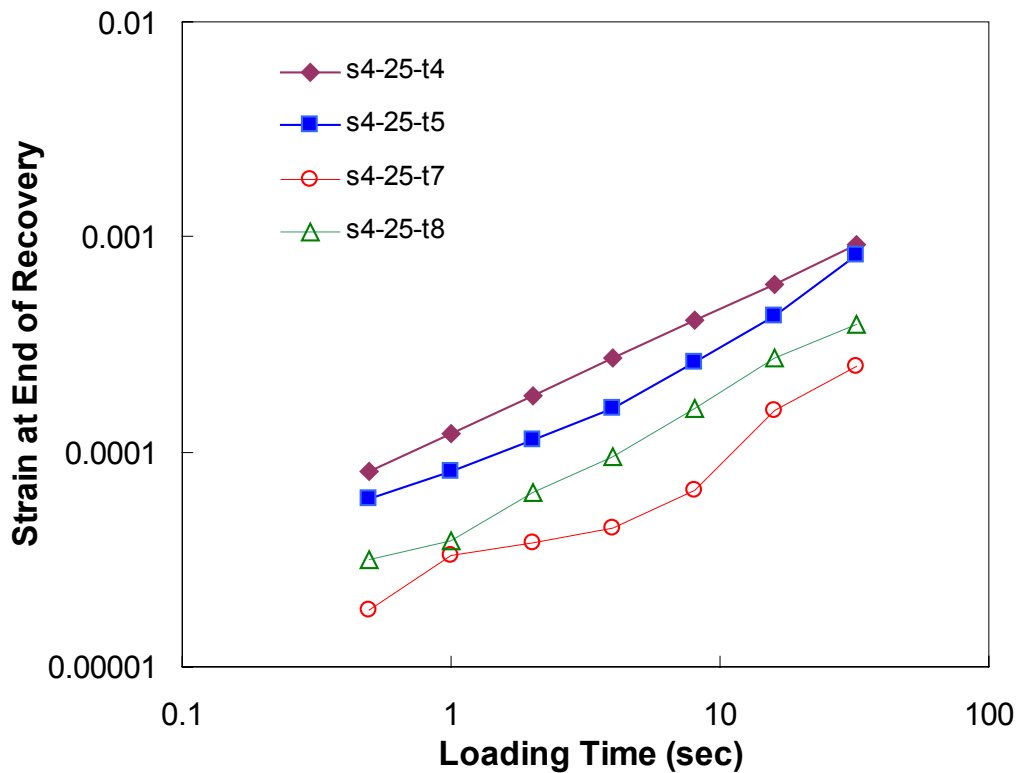


Figure 7.28. Plot of cumulative strain as a function of loading time for S4 tests

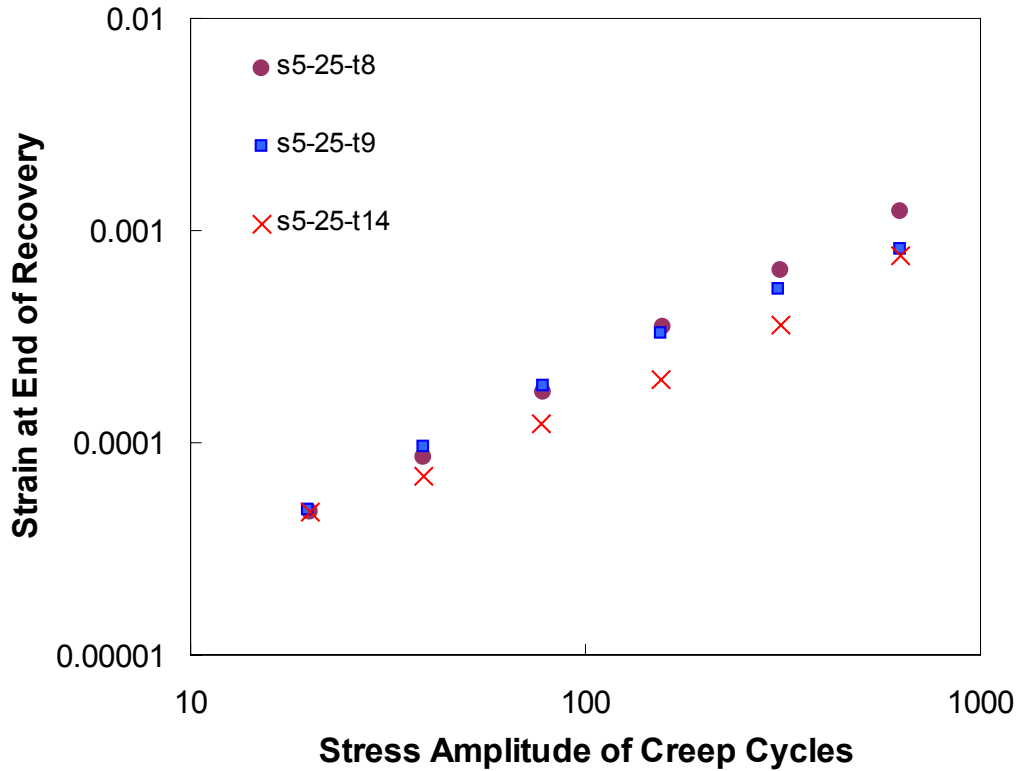


Figure 7.29. Plot of cumulative strain as a function of stress for S5 tests

Figures 7.30 and 7.31 show the incremental viscoplastic strain; i.e., the viscoplastic strain accumulated during a particular cycle as a function of the loading period of that cycle for S4 tests, on normal and log-log scales respectively. Similarly, Figures 7.32 and 7.33 show the incremental viscoplastic strain as a function of loading period on normal and log-log scales respectively. In all these four figures, the predicted strains are also plotted using the model coefficients determined.

As apparent from the figures, the model over-predicts viscoplastic strains for the S4 tests while the viscoplastic strains for the S5 tests are under-predicted. For the measured data available, it was not possible to obtain better fits for each type of testing since data from both the S4 and S5 tests were used together in the non-linear regression. If more tests had been conducted, a better fit could have been obtained. If the predicted

and measured viscoplastic strains for both S4 and S5 tests are plotted on the same graph, the data lies along the line of equality (Figure 7.34), suggesting that the model does a good job in predicting the viscoplastic strains. The best fit for the data yields an  $R^2$  value of 0.86, which is deemed acceptable. The final check on the validity of the model and its coefficients is left to the next section.

#### **7.5.4 Validation of the Viscoplastic Model**

Based on theory, the C vs. S curves for constant crosshead rate tests collapse except when viscoplastic response becomes a significant constituent of the asphalt mixture behavior. A procedure for checking the accuracy of the viscoplastic model is: (1) to predict the viscoplastic response using Equation (7.2) and the determined model coefficients; (2) to subtract the VP strain from the actual measured strain; (3) to calculate C and S\* using the estimated VE strain; and (4) to check the collapse of C vs. S\* curves at varying temperatures and loading rates.

This check will be performed on constant crosshead strain tests at 5, 25 and 40°C. As seen in Figure 7.35, the C vs. S curves for tests at 5 and 25°C at fast strain rates (0.135 and 0.0045) collapse when plotted at a reference temperature of 25°C because of the dominance of the viscoelastic strain and absence of any significant viscoplastic strain. However, the curves for the tests at 25°C with slow strain rate (0.0005) and at 40°C do not collapse on top of each other nor with the other curves (25°C with fast rates and 5°C). This is attributed to the significant presence of viscoplastic strain relative to the viscoelastic strain. Figure (8.36) depicts the C vs. S\* data calculated from the VE strains estimated by subtracting the VP strains from the measured total strains. The C vs. S curves collapse quite well in this figure. This success shows that the proposed

viscoplastic model does indeed successfully predict viscoplastic behavior, especially that it was checked on a type of test that is different than that from which it was developed; i.e., constant crosshead rate vs. repetitive creep and recovery.

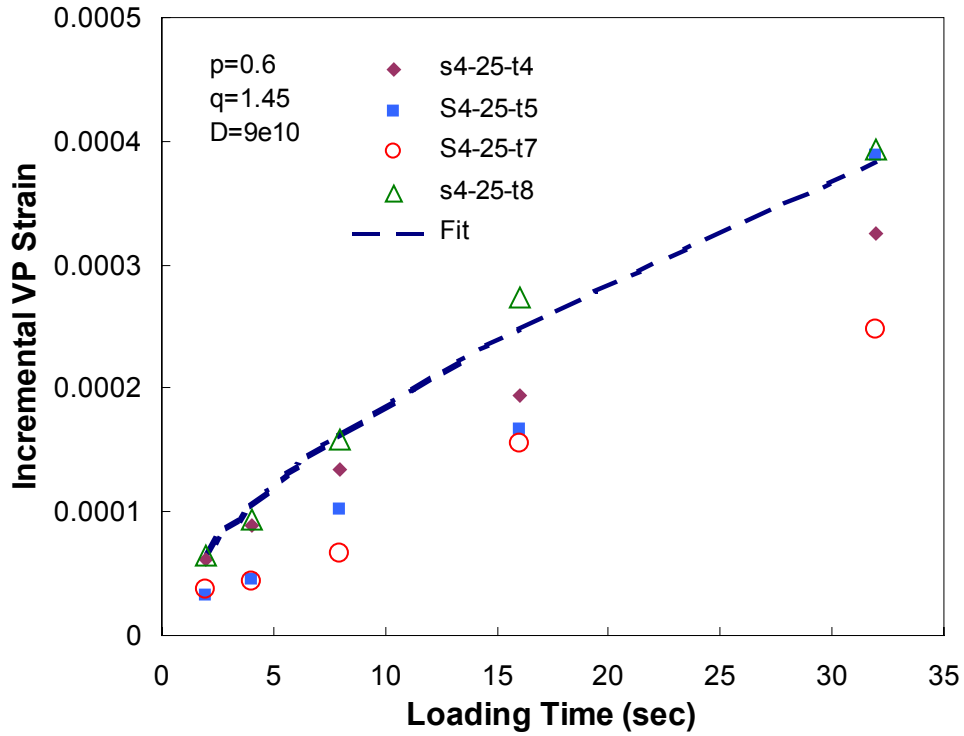


Figure 7.30. Incremental viscoplastic strain as a function of loading time for S4 tests

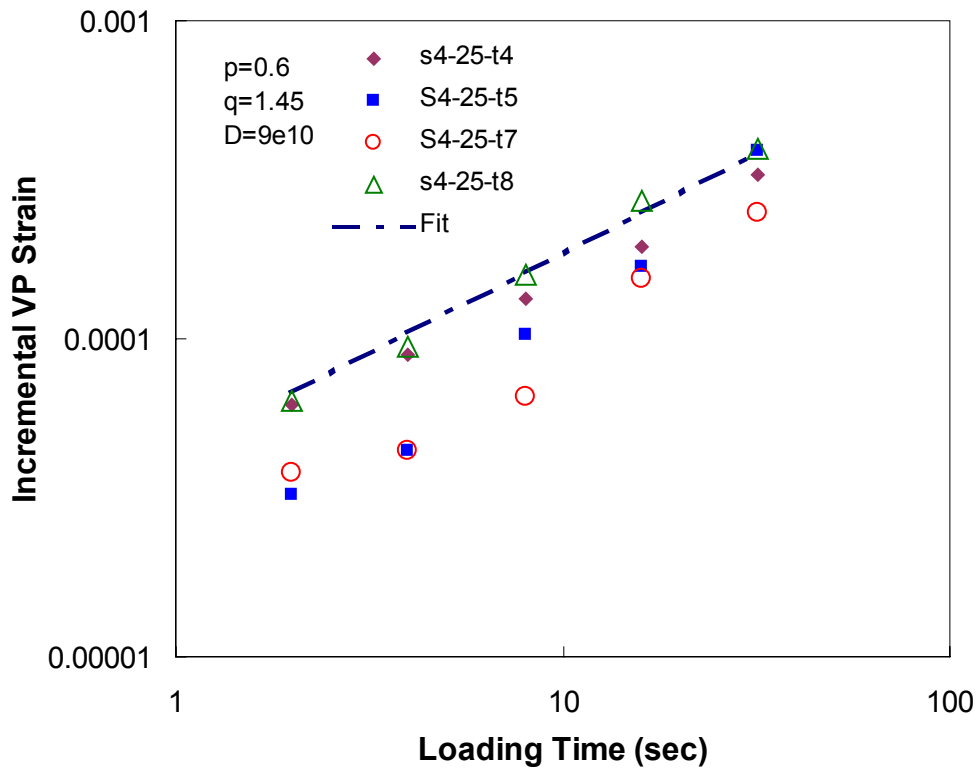


Figure 7.31. Incremental viscoplastic strain as a function of loading time for S4 tests (log-log scale)

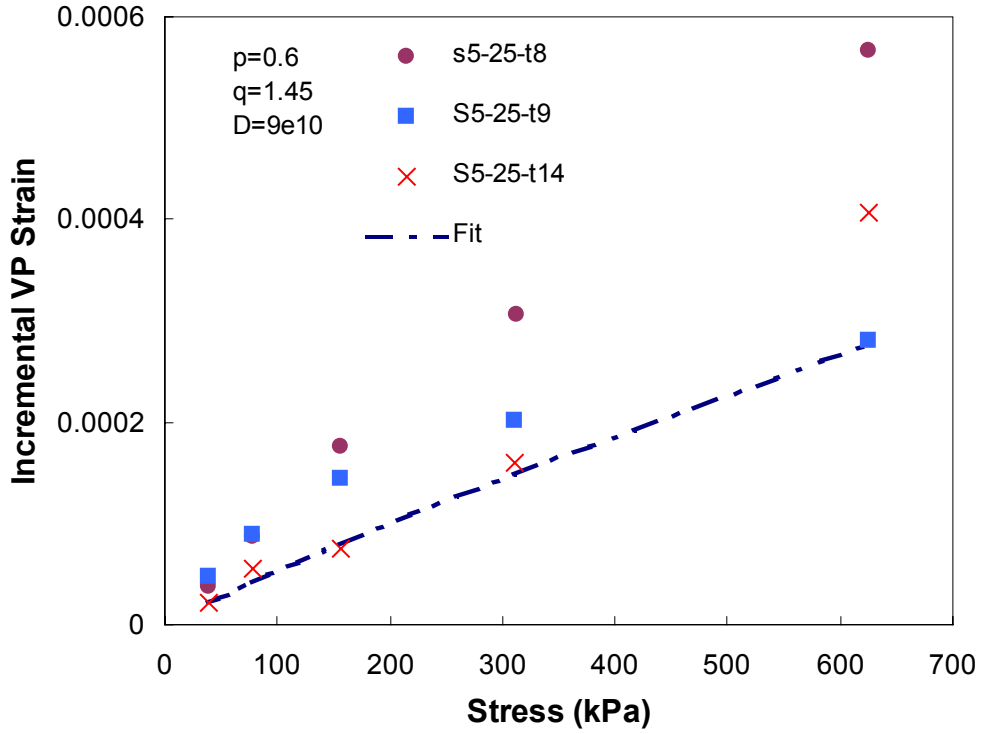


Figure 7.32. Incremental viscoplastic strain as a function of stress for S5 tests

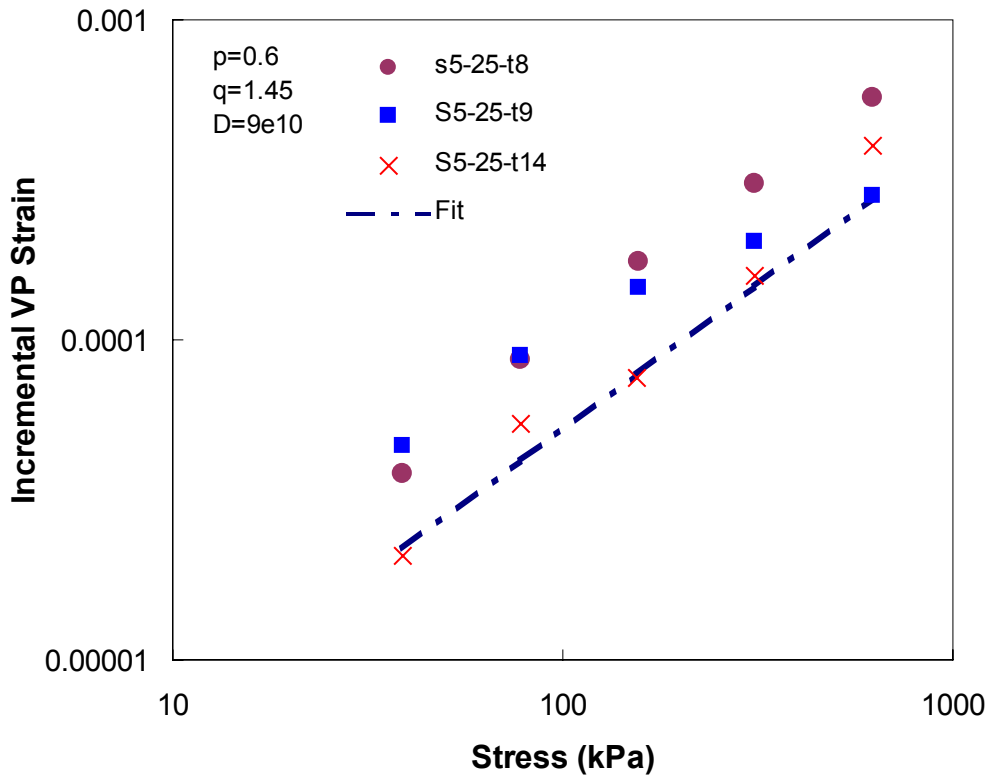


Figure 7.33. Incremental viscoplastic strain as a function of stress for S5 tests (log-log scale)

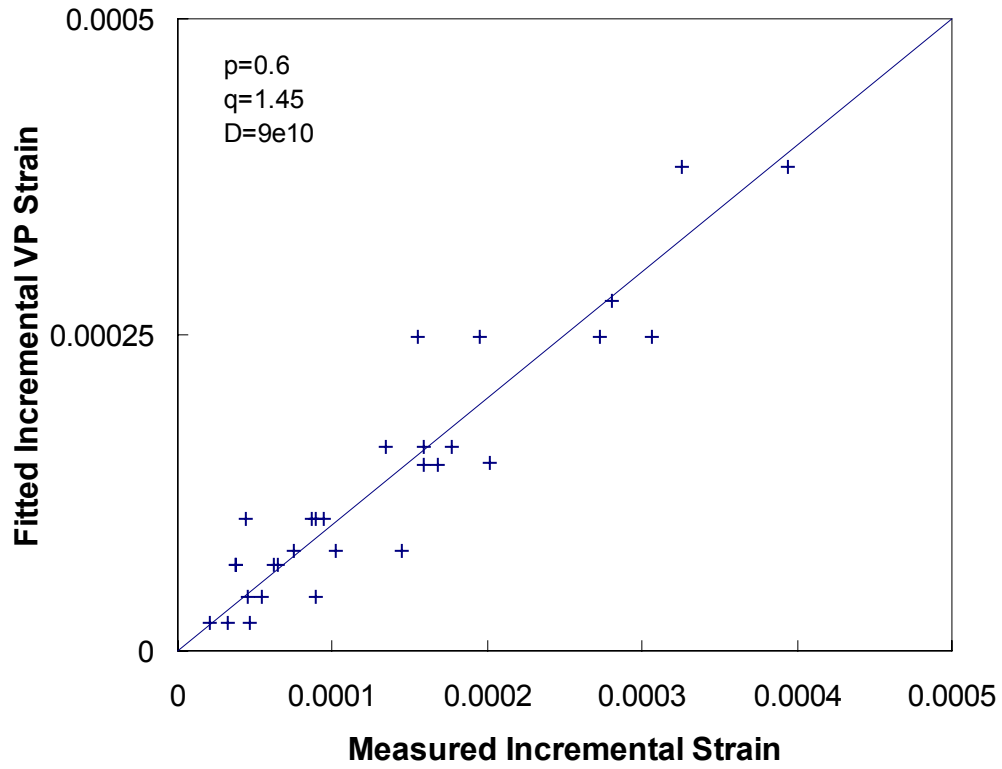


Figure 7.34. Predicted vs. measured incremental strains for data from S4 and S5 tests

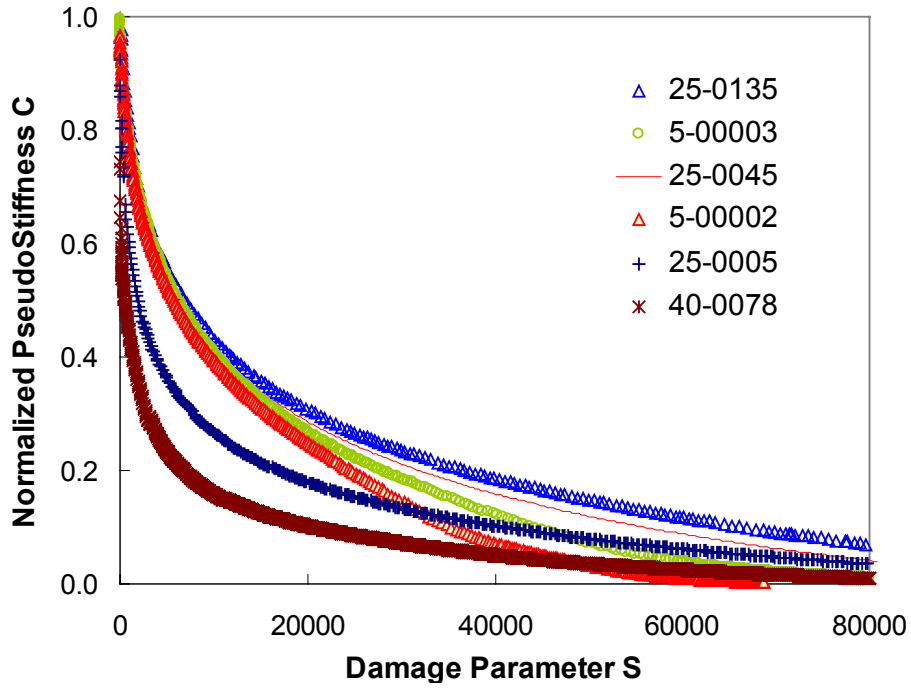


Figure 7.35. C vs. S curves for constant crosshead rate tests based on total measured strains at a reference temperature of 25°C

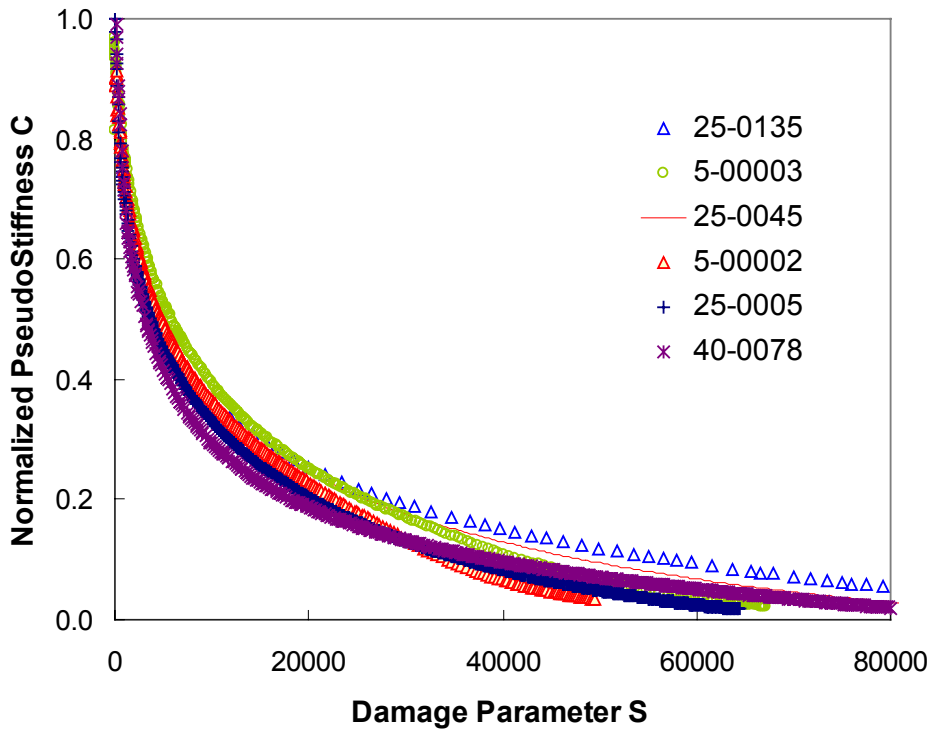


Figure 7.36. C vs. S curves for constant crosshead rate tests based on total measured strains – predicted VP strains at a reference temperature of 25°C

## 7.6 Formulation and Validation of the ViscoElastoPlastic Model

In the previous sections, the viscoelastic and viscoplastic models were developed and validated independently. Those models can now be integrated together, where the viscoelastic and viscoplastic responses predicted from their respective models can be added to obtain the total response for a given stress history. This integrated model is referred to as the ViscoElastoPlastic model.

Equation (7.19) is used to predict the viscoelastic behavior, while the viscoplastic behavior for a general loading history can be derived from Equation (7.28). By assuming  $g(\sigma) = B\sigma_1^q$  and coupling coefficients A and B into coefficient C, then Equation (7.28) becomes:

$$\varepsilon_{vp} = \left( \frac{p+1}{C} \right)^{1/p+1} \left( \int_0^t \sigma^q dt \right)^{1/p+1} \quad (7.40)$$

Combining Equations (7.19) and (7.40) and replacing time with reduced time, the resulting equation predicts the total strain history for a general loading history:

$$\varepsilon = \varepsilon_{ve} + \varepsilon_{vp} = E_R \int_0^\xi D(\xi - \xi') \frac{d\left(\frac{\sigma}{C(S^*)}\right)}{d\xi'} d\xi' + \left( \frac{p+1}{C} \right)^{1/p+1} \left( \int_0^\xi \sigma^q d\xi \right)^{1/p+1} \quad (7.41)$$

To check the validity and accuracy of the model, the model is applied to the constant crosshead rate tests that were conducted for both the verification of the time-temperature superposition principle study and the modeling of viscoelastic behavior. For all those tests, the stress, strain, time, and temperature (reduced time) are known; thus, it is possible to predict the viscoelastic and viscoplastic strains from the stress and reduced time and compare their sum to the measured (actual) strain response.

The tests selected were those conducted at  $-10$ ,  $5$ ,  $25$ , and  $40^{\circ}\text{C}$  at several strain rates. It is expected that the tests at  $40^{\circ}\text{C}$  yield predominantly viscoplastic strains while those at  $-10^{\circ}\text{C}$  yield predominantly viscoelastic strains. As for tests at  $25^{\circ}\text{C}$ , the relative magnitude of the strain components will probably be a function of the strain rate, more specifically a slower rate yielding a greater viscoplastic response.

Figures 7.37 through 7.43 show the viscoplastic strain, viscoelastic strain, and their sum (total predicted strain) for tests at  $-10$ ,  $5$ ,  $25$ , and  $40^{\circ}\text{C}$  for different strain rates. Those figures are intended to show the relative magnitude of each strain component compared to total strain. As observed, with the increase in temperature and the decrease of strain rate, the ratio of viscoplastic strain to viscoelastic strain increases, which is in line with theory of viscous behavior. Strains are plotted only up to localization, because the estimated model coefficients are not valid after the localization.

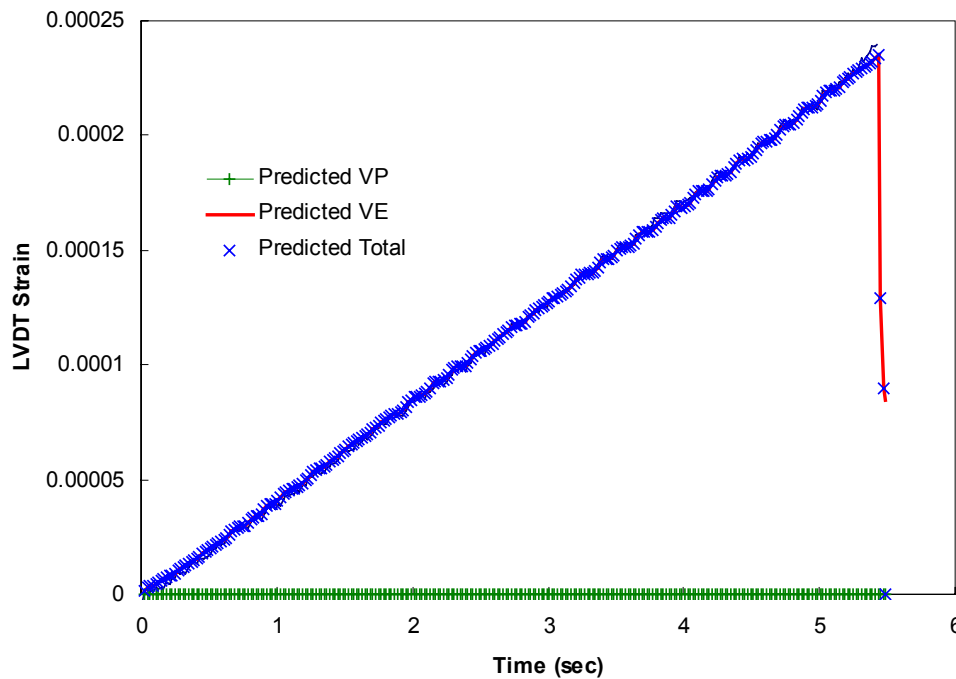


Figure 7.37. Predicted viscoplastic, viscoelastic, and total strain at  $-10^{\circ}\text{C}$  and  $\dot{\epsilon}$  rate of  $0.0005$

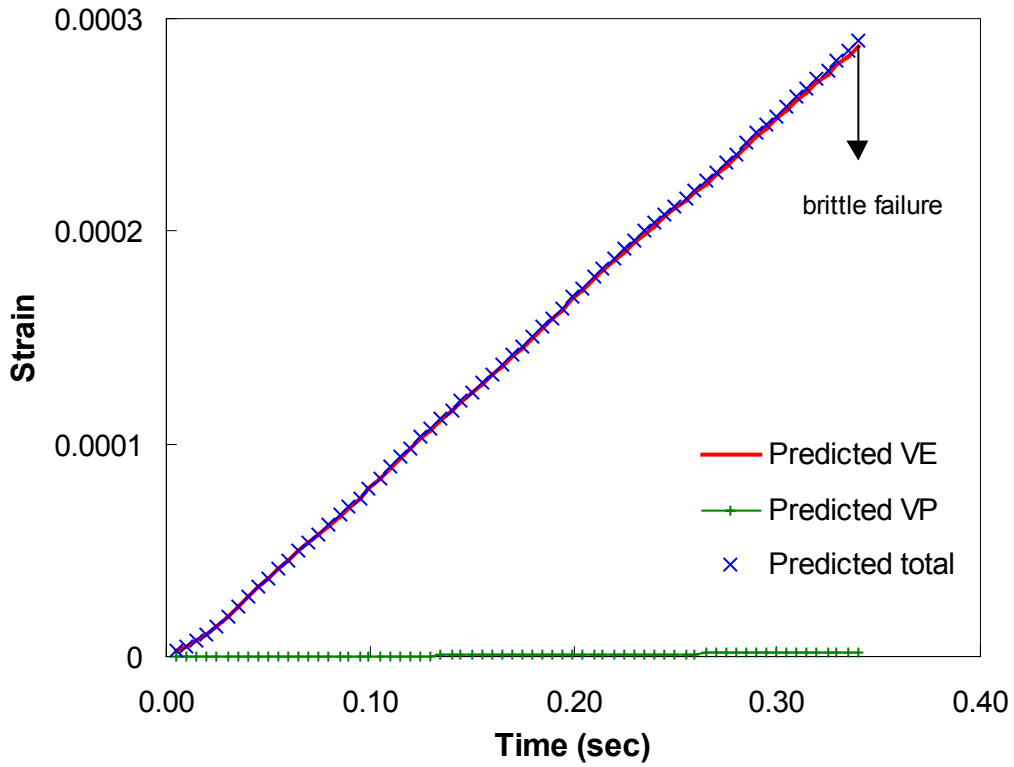


Figure 7.38. Predicted viscoplastic, viscoelastic, and total strain at 5°C and  $\dot{\epsilon}$  rate of 0.008

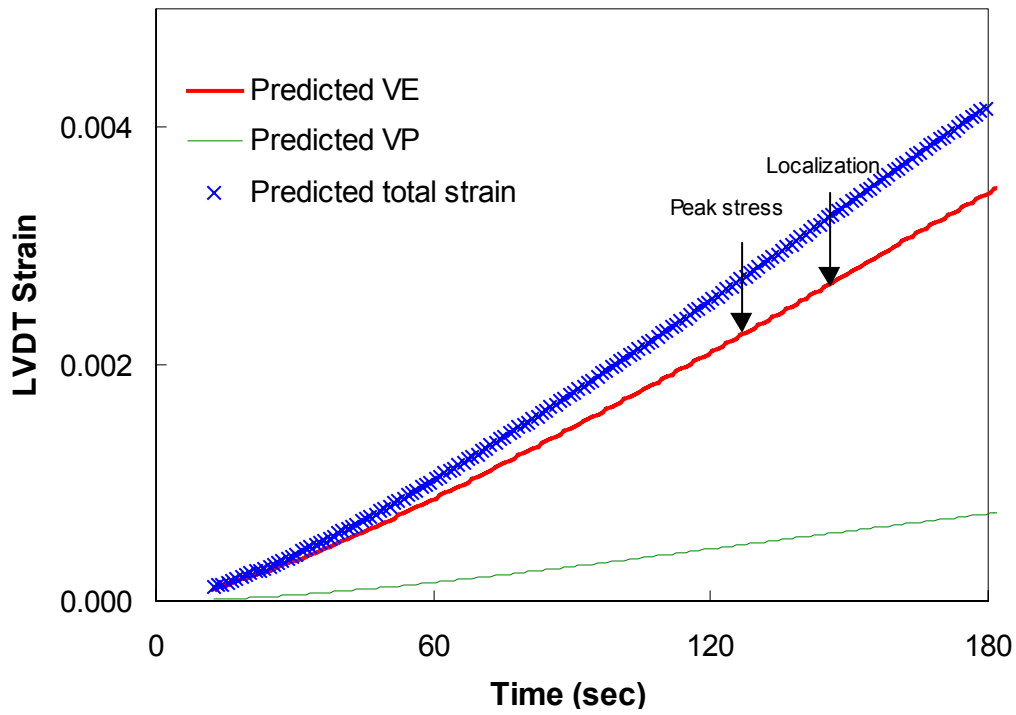


Figure 7.39. Predicted viscoplastic, viscoelastic, and total strain at 5°C and  $\dot{\epsilon}$  rate of 0.00003

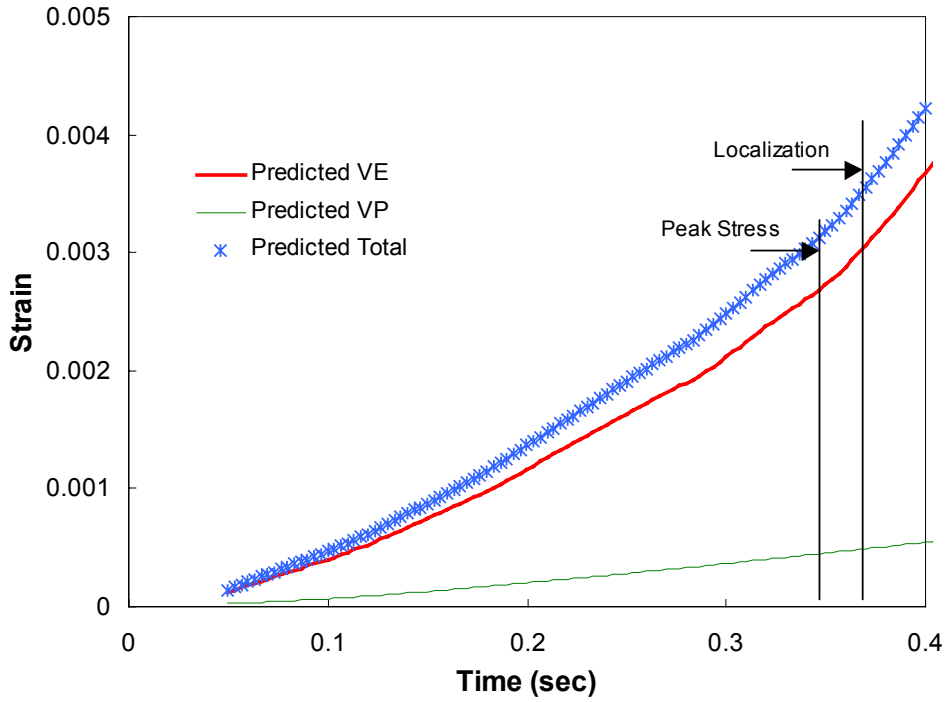


Figure 7.40. Predicted viscoplastic, viscoelastic, and total strain at 25°C and  $\epsilon$  rate of 0.0135

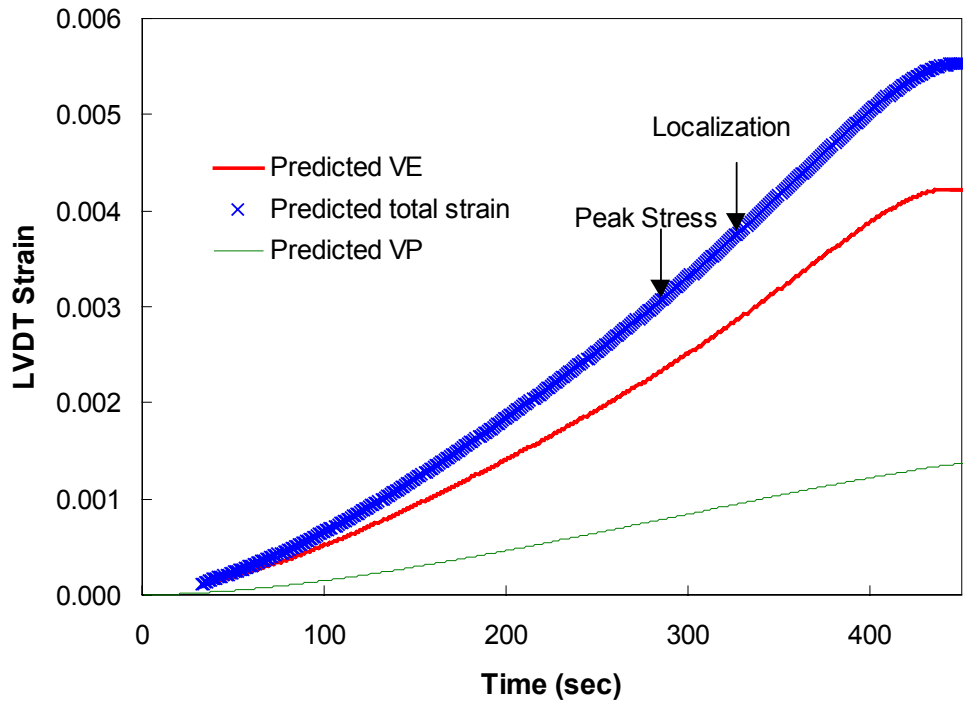


Figure 7.41. Predicted viscoplastic, viscoelastic, and total strain at 5°C and  $\epsilon$  rate of 0.000012

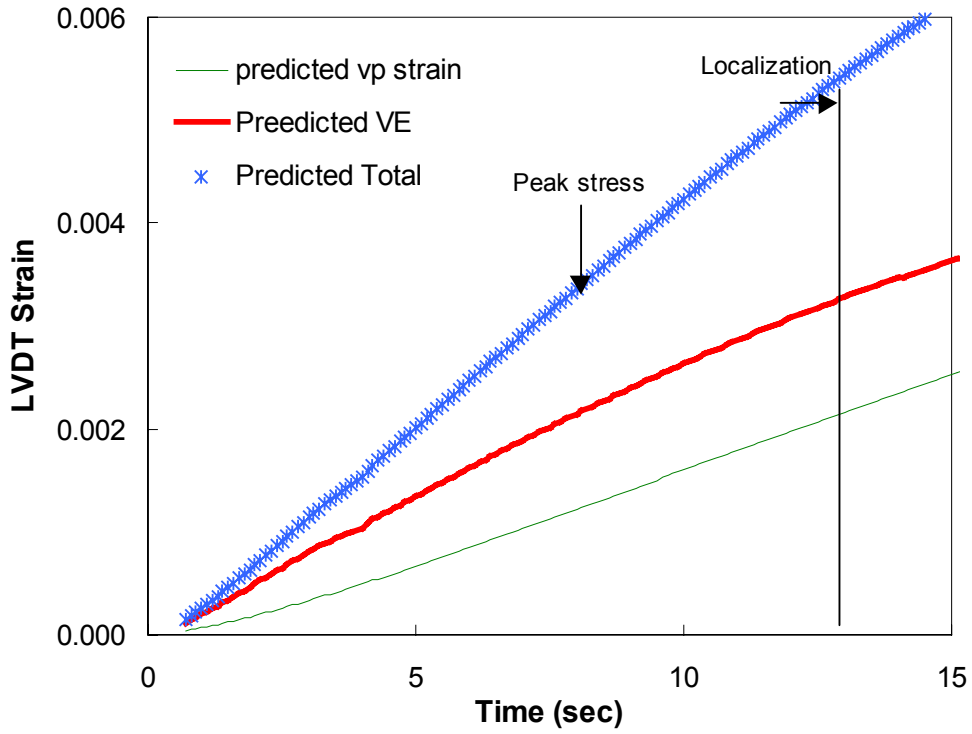


Figure 7.42. Predicted viscoplastic, viscoelastic, and total strain at 25°C and  $\dot{\epsilon}$  rate of 0.0005

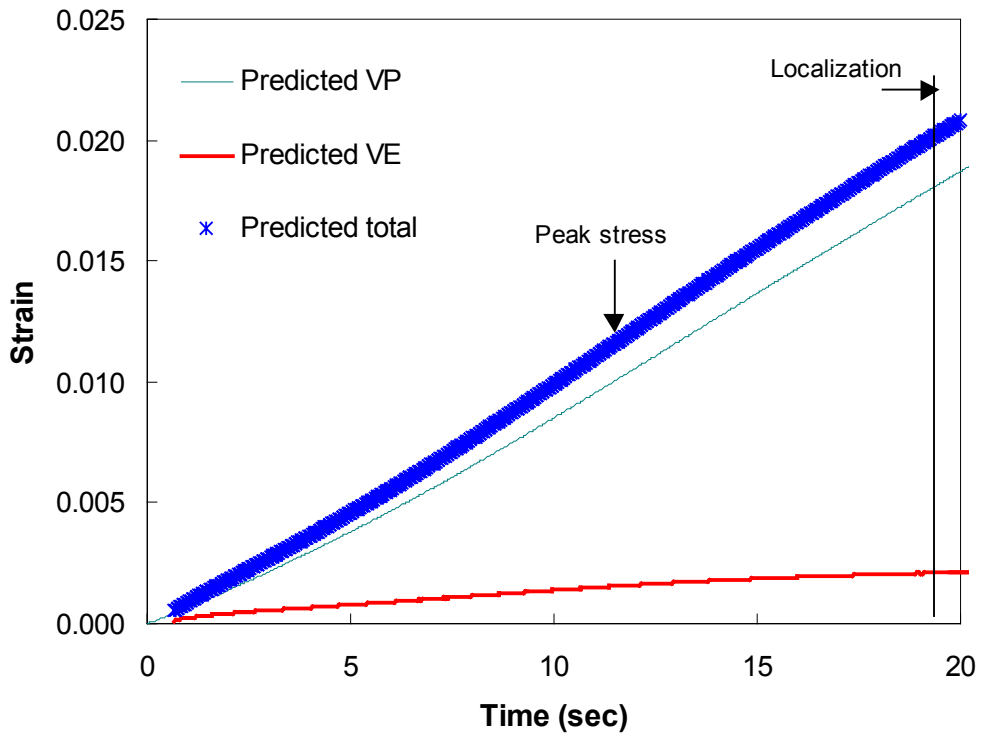


Figure 7.43. Predicted viscoplastic, viscoelastic, and total strain at 40°C and  $\dot{\epsilon}$  rate of 0.0009

Table 7.3 presents the percentage of viscoplastic (including plastic) and viscoelastic (including elastic) strains for various constant crosshead rates conducted at various temperatures and strain rates. The data is listed in the decreasing order of reduced strain rate. Figure 7.44 is a bar chart showing the percentage of the viscoelastic and viscoplastic strains for the various reduced strain rates presented; while Figure 7.45 shows the variation of viscoelastic and viscoplastic strain as a function of reduced strain rate.

Table 7.3. Percent viscoelastic and viscoplastic strain as a function of temperature and strain rate

<b>Temperature (°C)</b>	<b>Crosshead Rate (<math>\epsilon</math>/sec)</b>	<b>Reduced Crosshead Rate (<math>\epsilon</math>/sec)</b>	<b>% VE Strain at Peak Stress</b>	<b>% VP Strain at Peak Stress</b>
-10	0.0135	2700	100	0
-10	0.0005	100	100	0
5	0.008	5.0	100	0
-10	0.000019	3.8	100	0
5	0.000056	0.35	93	7
5	0.00003	0.019	94	6
25	0.0135	0.0135	95	5
5	0.000012	0.008	90	10
25	0.0045	0.0045	84	16
25	0.0005	0.0005	71	29
40	0.0078	0.00017	57	43
40	0.0009	2e-5	39	61

Figure 7.45 provides an excellent illustrative view on how the proportion of component strains varies as a function of reduced strain rate. As observed, after a reduced crosshead rate of 4  $\epsilon$ /sec (Region C), the total strain is composed solely of the

viscoelastic strain. In region B, where the crosshead reduced strain rate ranges from 0.01 to 4  $\epsilon$ /sec, the viscoelastic strain averages about 95% of total strain. As for region A, the viscoelastic and viscoplastic strains are both present with their proportion being equal at a reduced crosshead strain rate of 0.0001  $\epsilon$ /sec. The values of the aforementioned reduced strain rates are converted to the strain rates at individual temperatures and presented in Table 7.4.

For modeling of viscoelastic behavior, it will be most accurate if crosshead strain rates within region C are used. However, because of brittle failure and small corresponding values of damage parameters S and S\*, their benefit will be very limited in developing the viscoelastic model. Instead, it is seen that if reduced crosshead strain rates within region B are used, then failure will be ductile, and viscoelastic modeling will be possible. There will be an error however, because the strains used for developing the model will not be solely viscoelastic but instead include on average 5% viscoplastic strains. All the tests used for developing the viscoelastic model fall within region B. It is worthy noting that the divisions of the reduced strain rate values into regions in addition to the transformation of the reduced rates to corresponding strain rates at actual temperatures are both mixture dependent.

Table 7.4. Strain rates corresponding to reduced strain rates in Figure 7.45

<b>Crosshead Reduced Rate at 25°C</b>	<b>Significance</b>	<b>Corresponding Crosshead Rate</b>			
		<b>Temperature (°C)</b>			
		<b>-10</b>	<b>5</b>	<b>25</b>	<b>40</b>
<b>0.0001</b>	VE = VP	5e-10	1.8e-7	0.0001	.0065
<b>0.01</b>	VE = 95%	5e-8	1.8e-5	0.01	0.65
<b>4</b>	VE = 100 %	2e-5	0.008	4	260

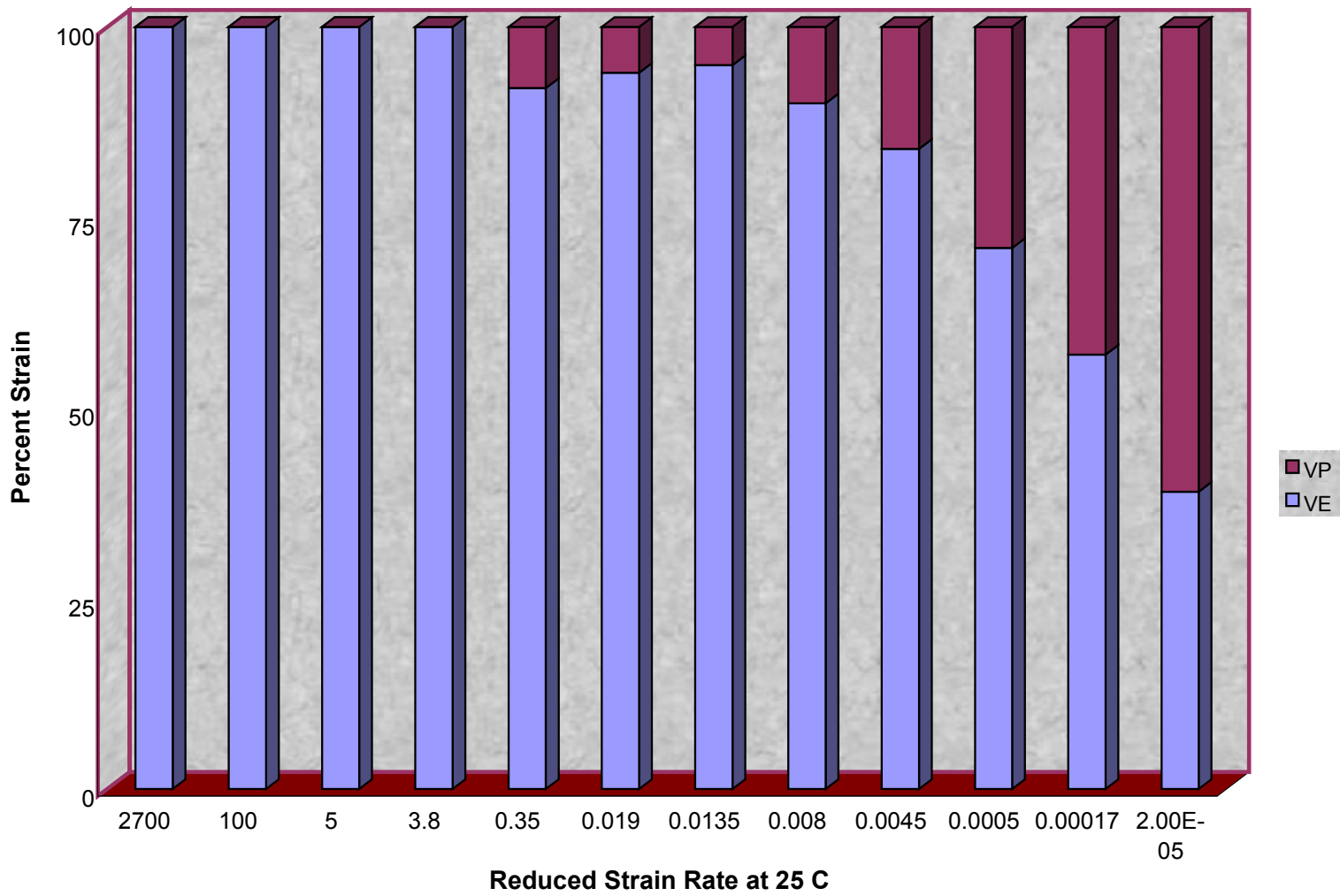


Figure 7.44. Percent viscoelastic and viscoplastic strains for different reduced strain rates at 25°C

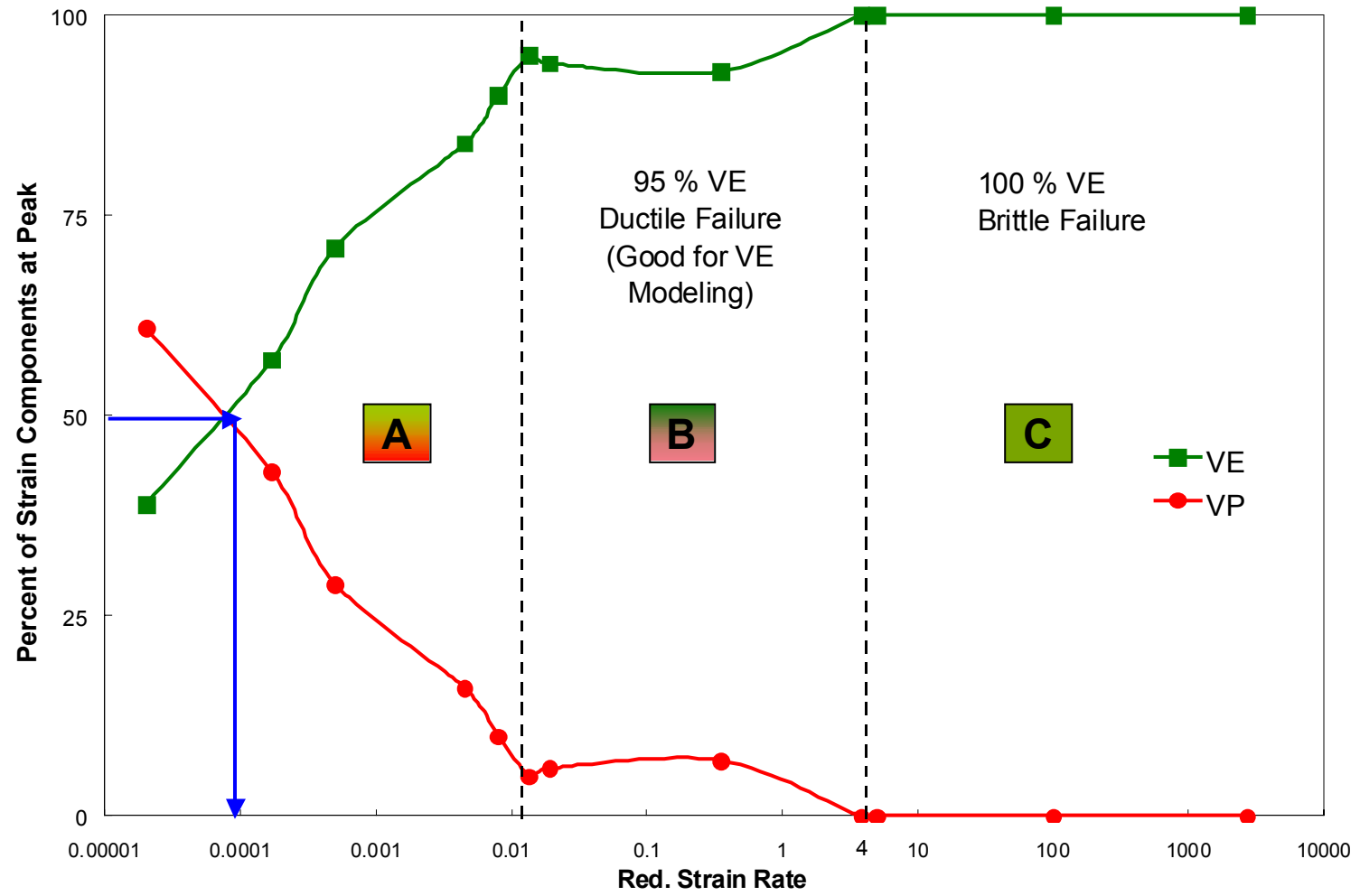


Figure 7.45. Percent viscoelastic and viscoplastic strains as a function of reduced strain rate at 25°C

The final and most important check is to compare the total predicted strains with the actual on-specimen strains measured from constant crosshead rate tests, some of which were used for modeling but the majority was not. Figures 7.46 through 7.63 show the stress-strain curves for the predicted and measured strains for various temperatures and strain rates. For some of the figures, the on-specimen strains measured using two gage lengths allow for the visualization of the point of localization, which is the instance where the stress-strain curves for the two gage lengths start diverging. It is worthy noting that the predicted strains were calculated based on data from 100-mm gage length; consequently, the predicted strains should be compared with strains measured using 100-mm gage length LVDTs.

As observed from the figures, there is an excellent match between the measured and predicted strains for all temperatures and strain rates. Predictions for replicates are almost identical, demonstrating the accuracy of the viscoelastoplastic model developed. The only shortfall remaining is its inability to predict behavior at and after localization. For complete behavior prediction, the strains after localization must be obtained via a technique that measures the strains at local levels since LVDTs are not a valid method of measuring representative strains over a wide area (corresponding to the gage length) when micro and macro-cracks start to develop. In this research, the Digital Image Correlation (DIC) technique was adopted. This issue will be discussed in the following section.

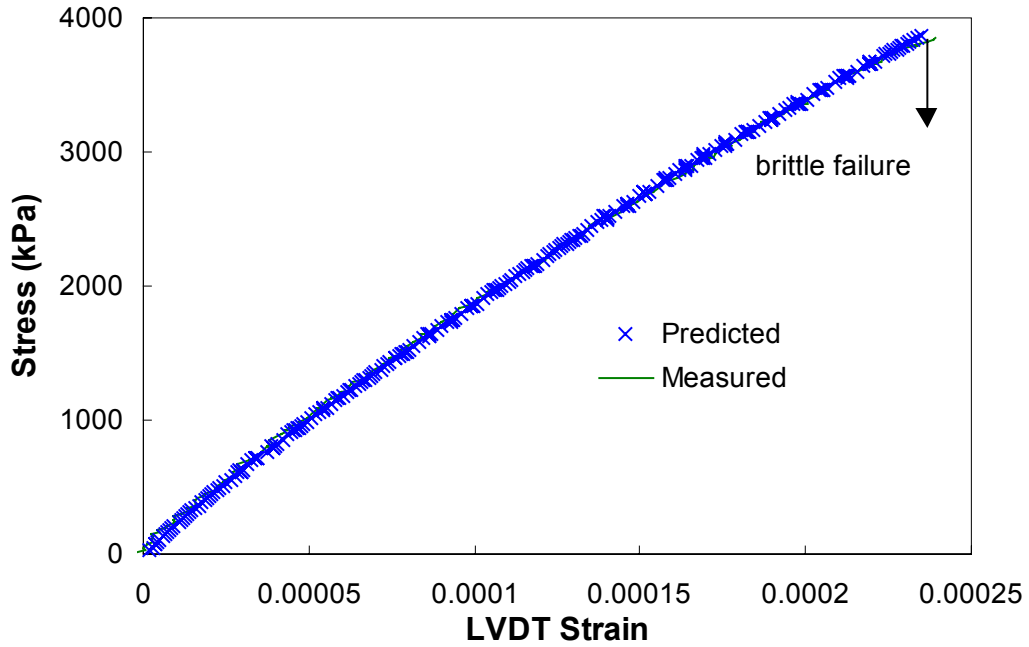


Figure 7.46. Actual and predicted stress-strain curves at  $-10^{\circ}\text{C}$  and  $0.0005 \text{ } \epsilon/\text{sec}$

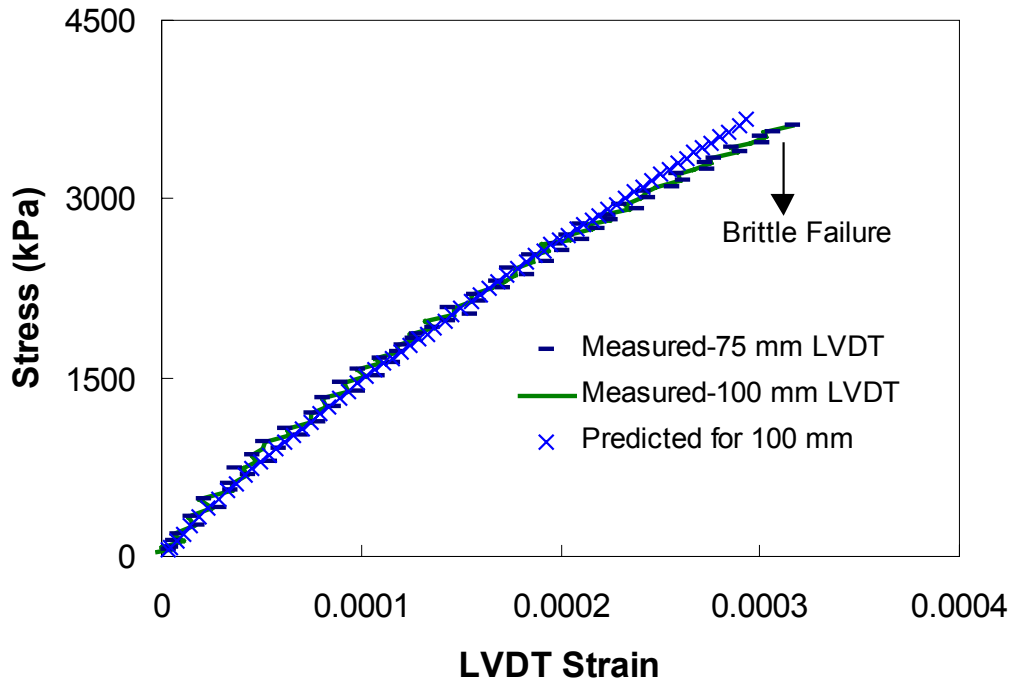


Figure 7.47. Actual and predicted stress-strain curves at  $5^{\circ}\text{C}$  and  $0.008 \text{ } \epsilon/\text{sec}$

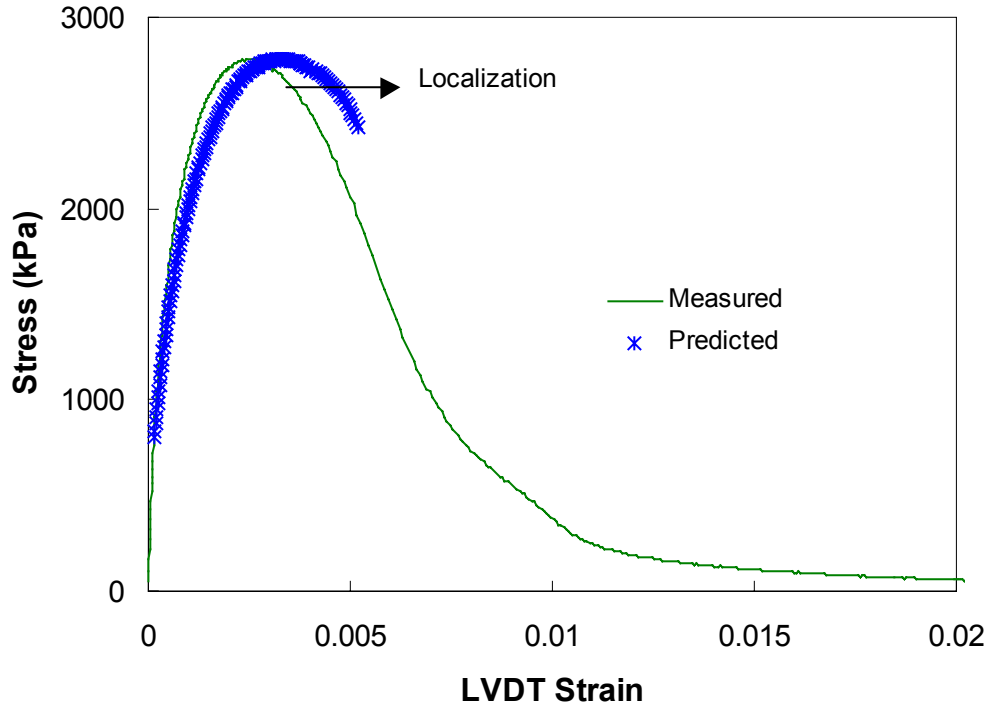


Figure 7.48. Actual and predicted stress-strain curves at 5°C and 0.000035  $\epsilon$ /sec

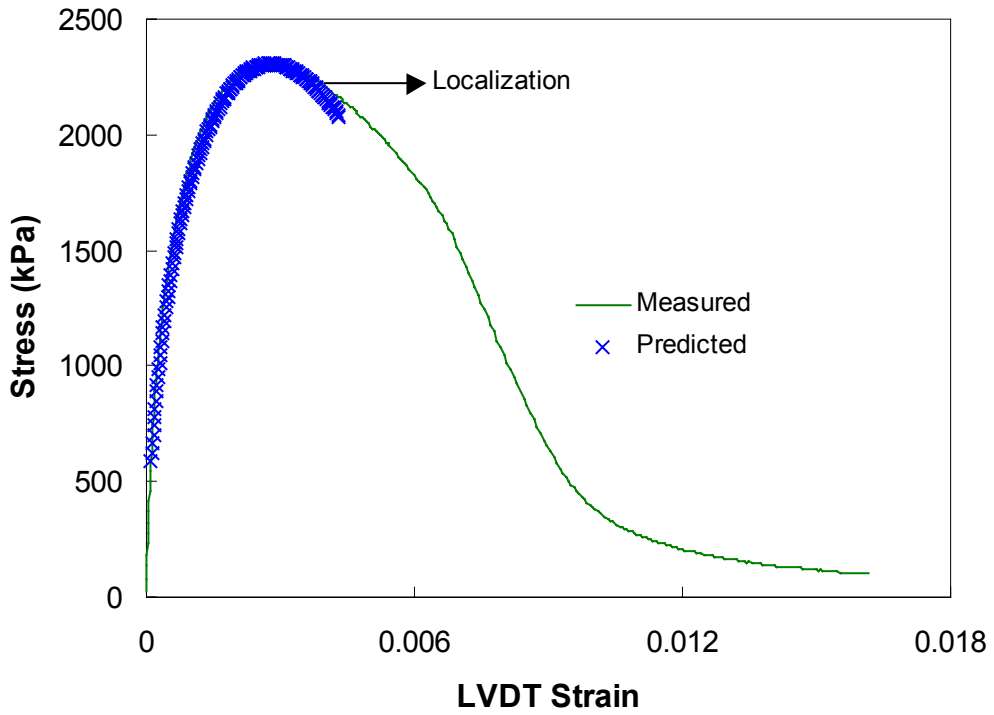


Figure 7.49. Actual and predicted stress-strain curves at 5°C and 0.00003  $\epsilon$ /sec (Replicate 1)

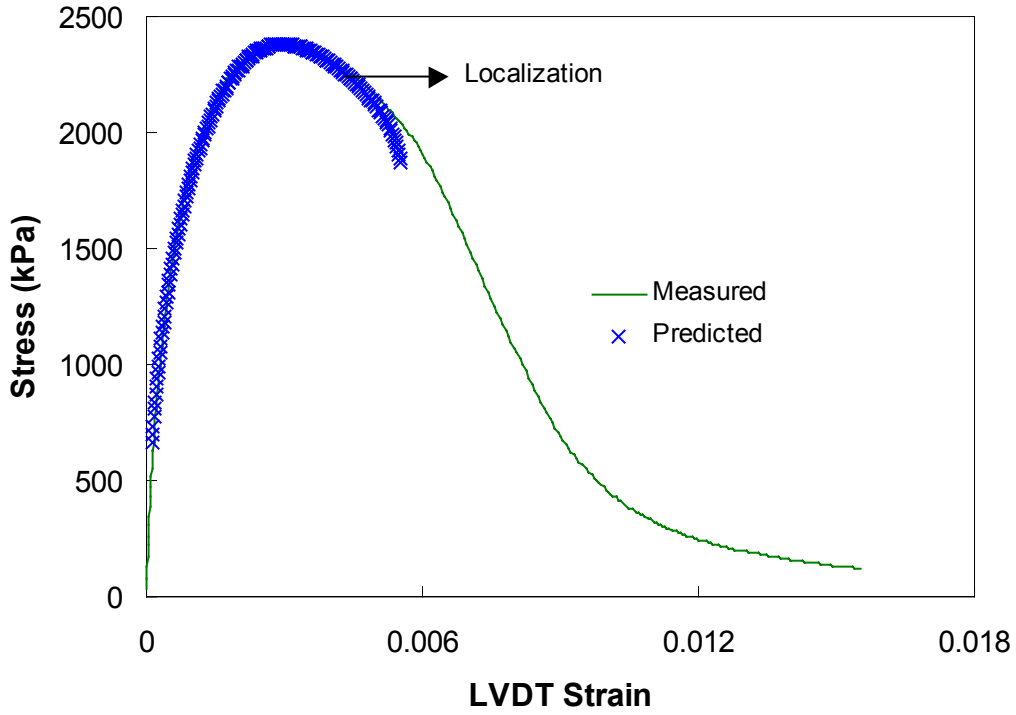


Figure 7.50. Actual and predicted stress-strain curves at 5°C and 0.00003  $\epsilon$ /sec (Replicate 2)

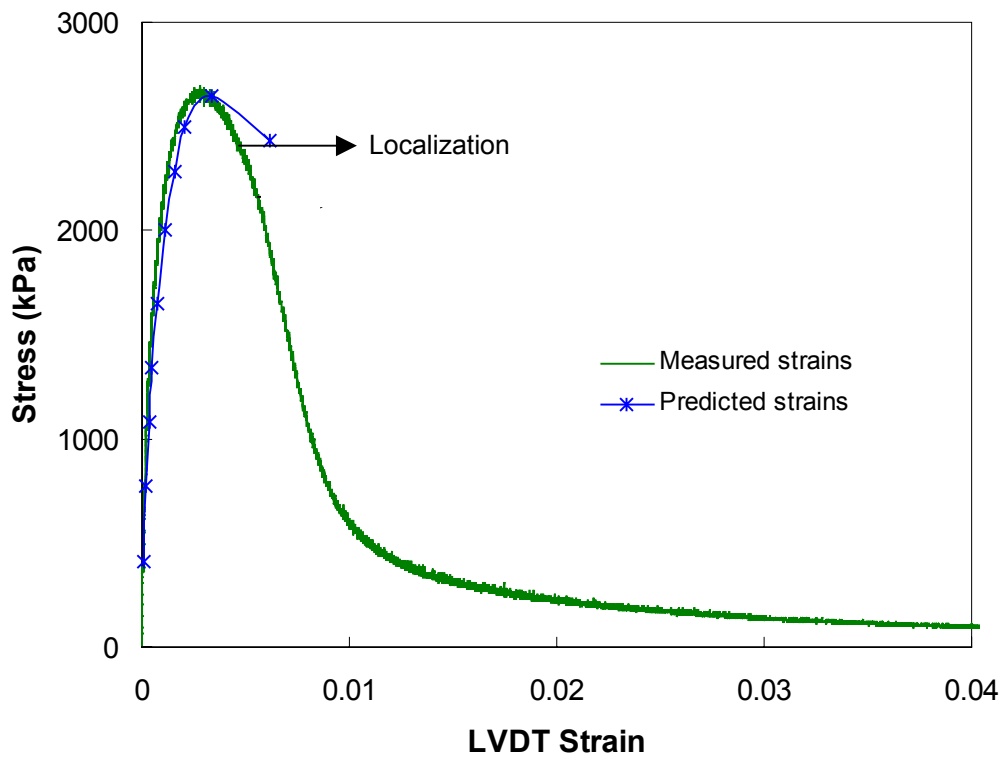


Figure 7.51. Actual and predicted stress-strain curves at 5°C and 0.00003  $\epsilon$ /sec (Replicate 3)

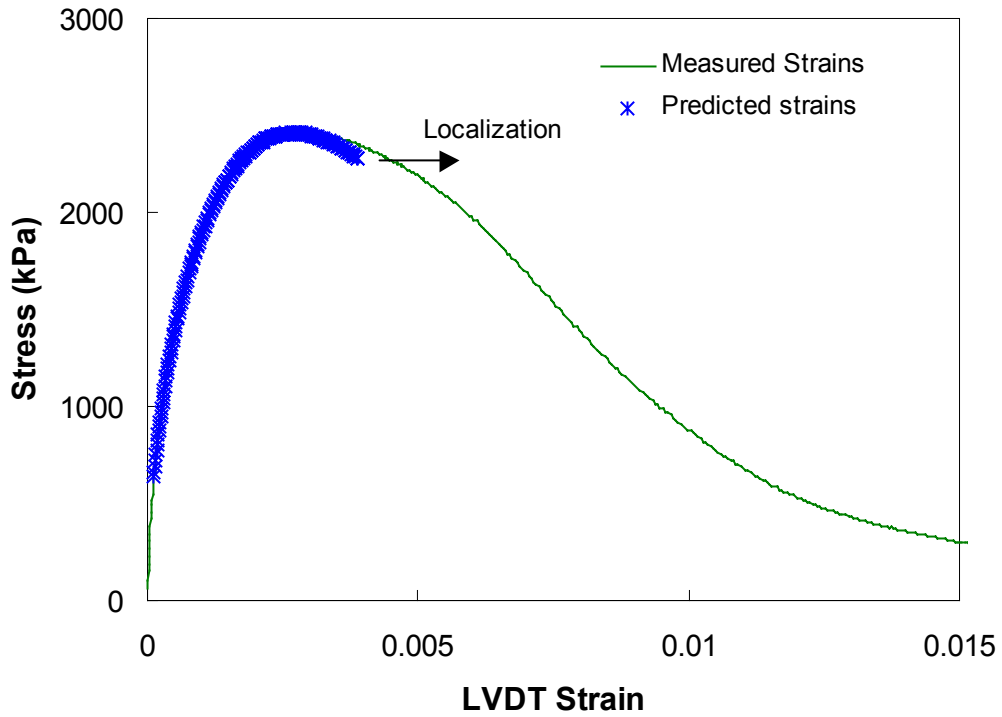


Figure 7.52. Actual and predicted stress-strain curves at 5°C and 0.000025  $\epsilon$ /sec

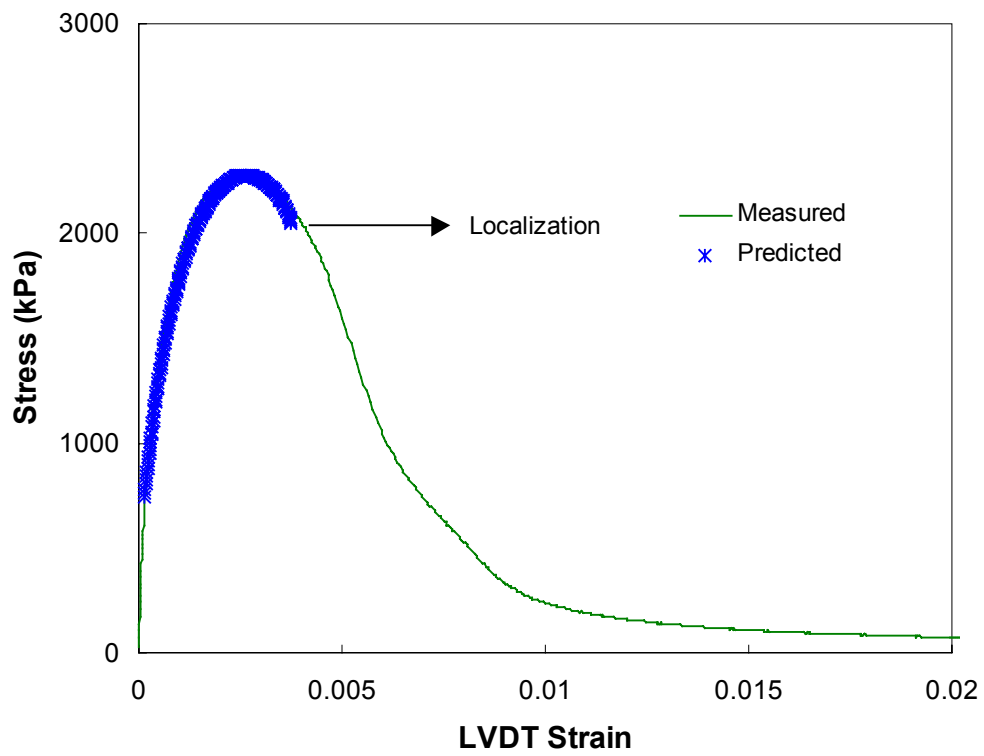


Figure 7.53. Actual and predicted stress-strain curves at 5°C and 0.00002  $\epsilon$ /sec

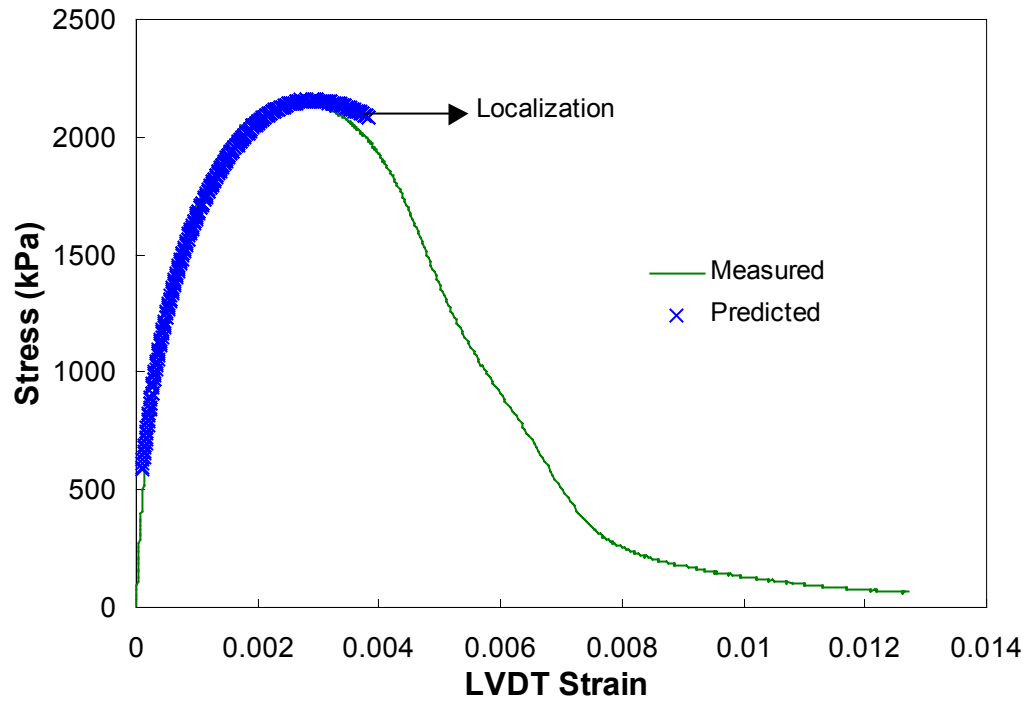


Figure 7.54. Actual and predicted stress-strain curves at 5°C and 0.000012  $\epsilon$ /sec

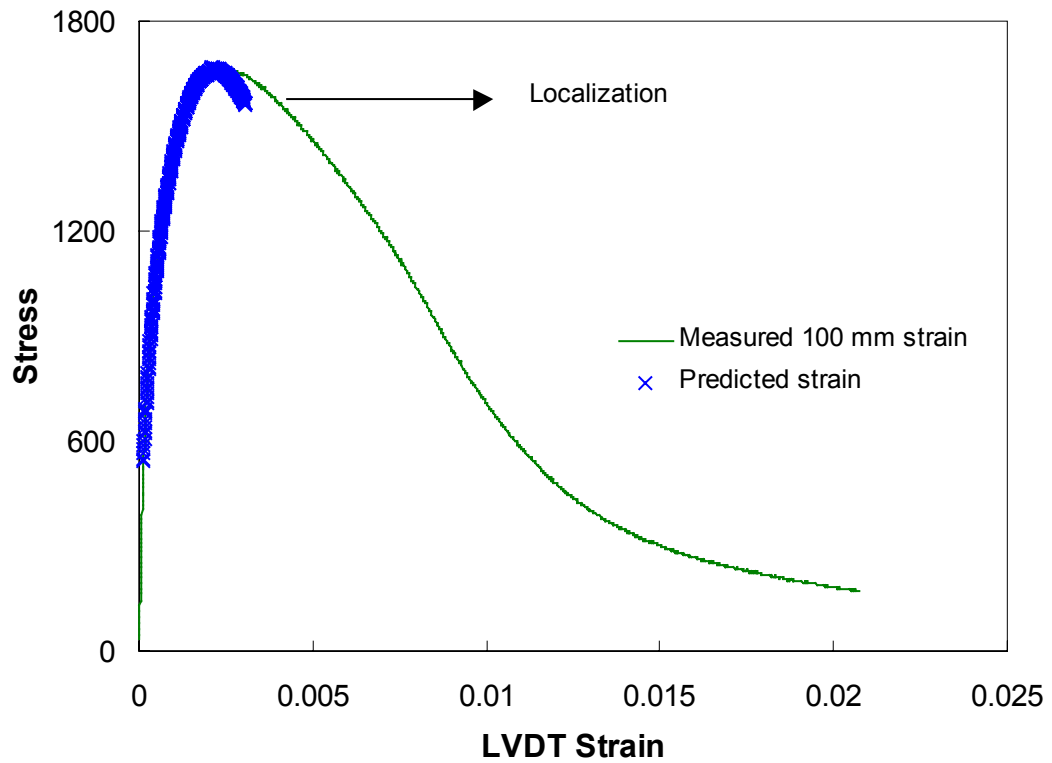


Figure 7.55. Actual and predicted stress-strain curves at 5°C and 0.00001  $\epsilon$ /sec

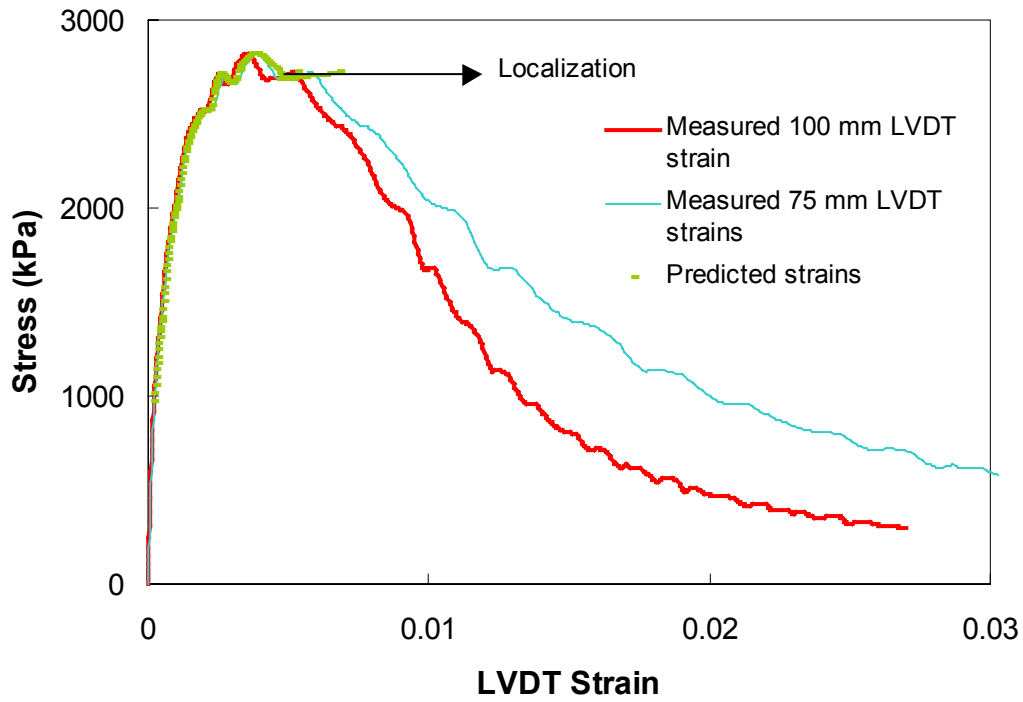


Figure 7.56. Actual and predicted stress-strain curves at 25°C and 0.0135  $\epsilon$ /sec

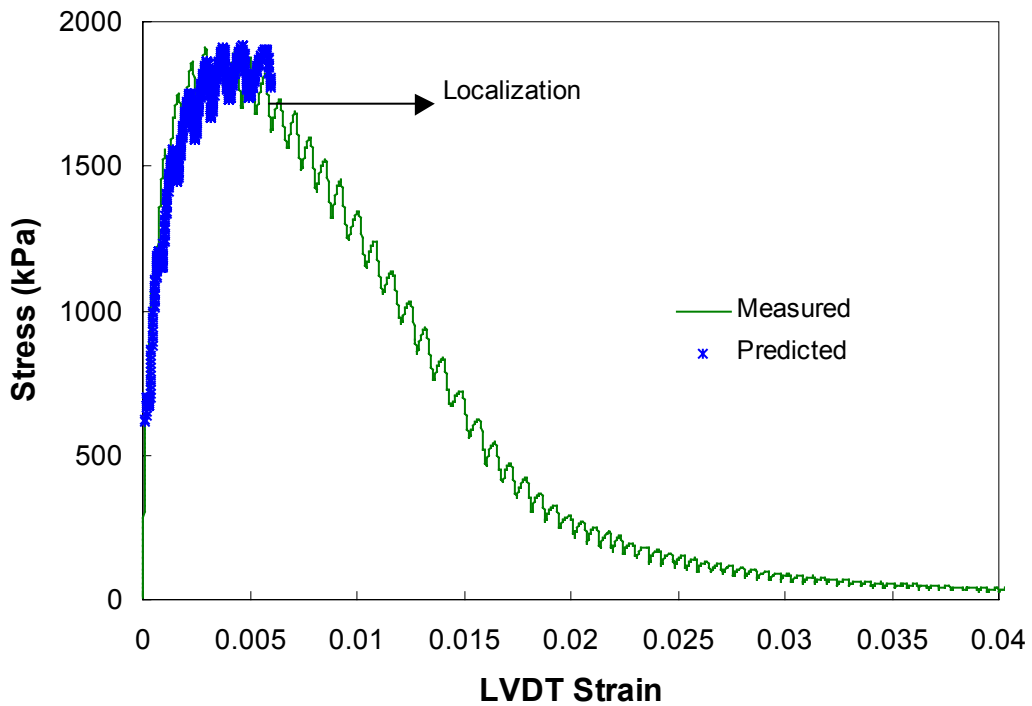


Figure 7.57. Actual and predicted stress-strain curves at 25°C and 0.0045  $\epsilon$ /sec

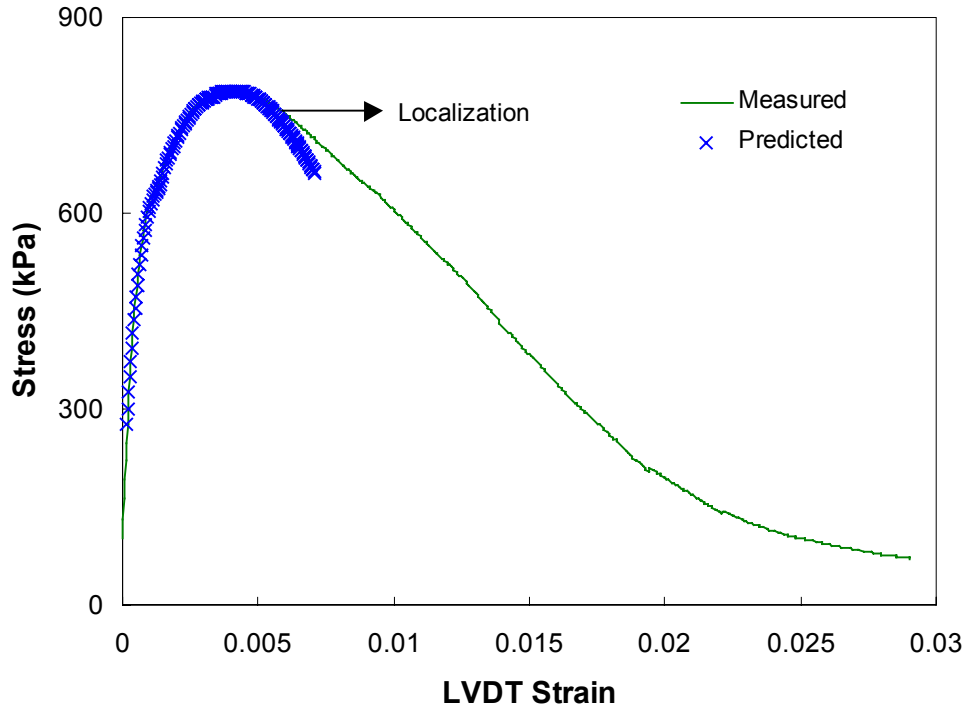


Figure 7.58. Actual and predicted stress-strain curves at 25°C and 0.0005  $\epsilon$ /sec (Replicate 1)

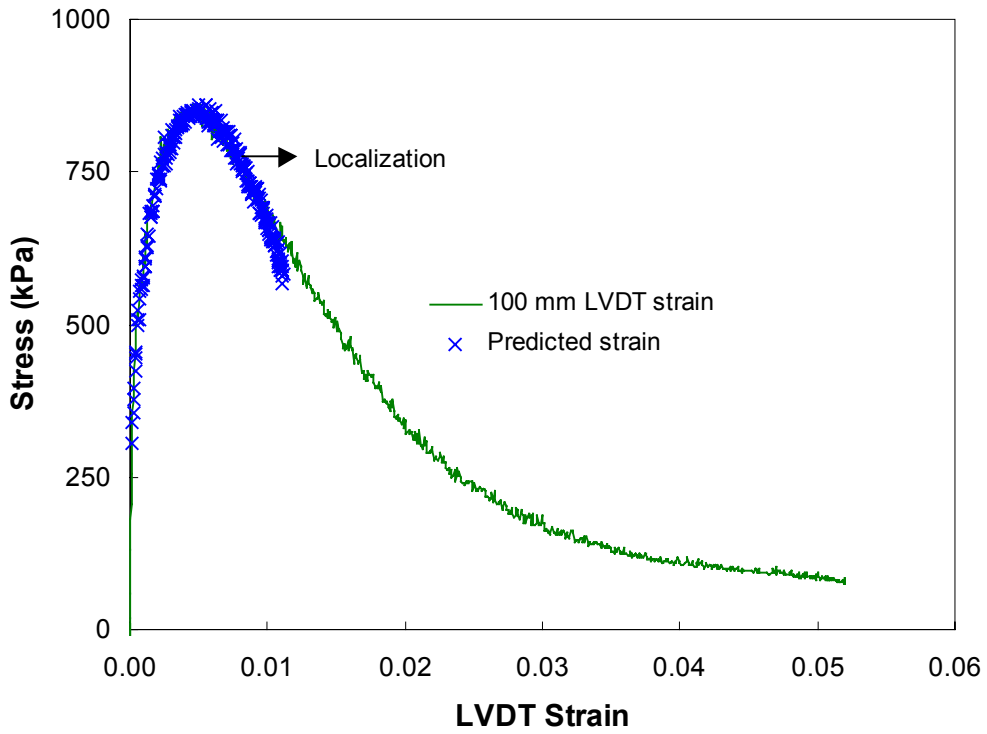


Figure 7.59. Actual and predicted stress-strain curves at 25°C and 0.0005  $\epsilon$ /sec (Replicate 2)

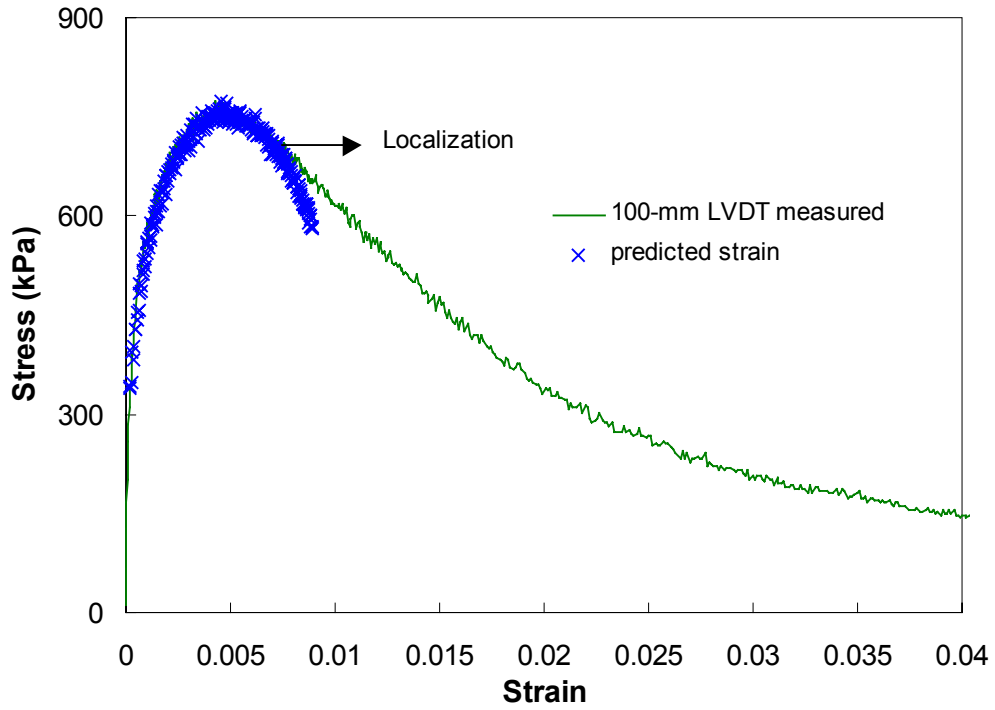


Figure 7.60. Actual and predicted stress-strain curves at 25°C and 0.0005  $\epsilon$ /sec (Replicate 3)

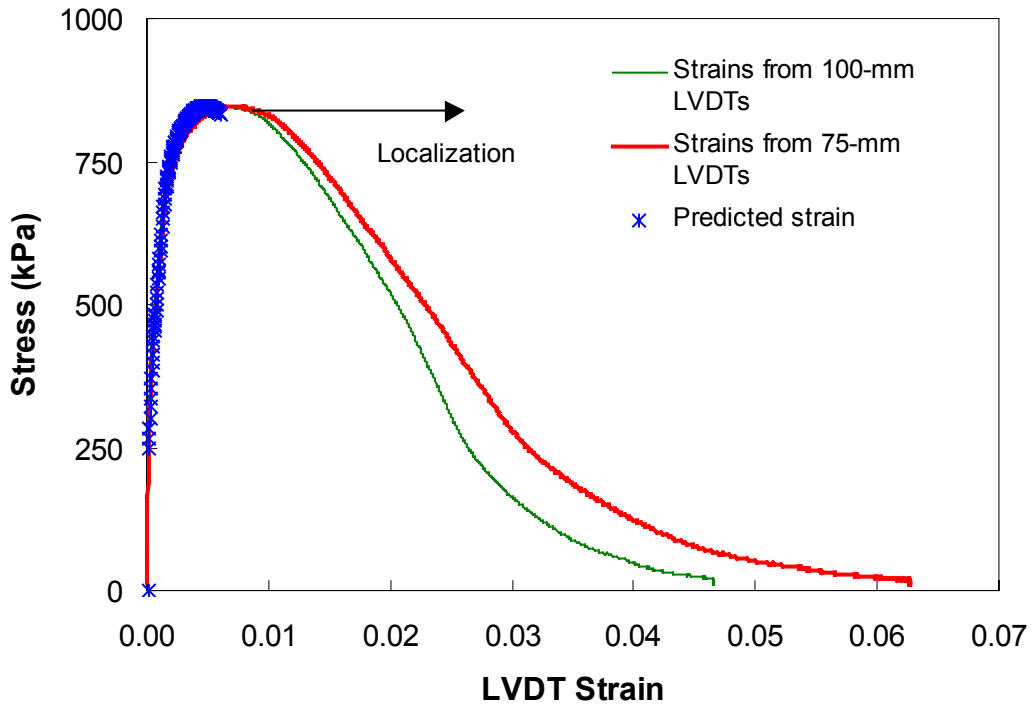


Figure 7.61. Actual and predicted stress-strain curves at 40°C and 0.07  $\epsilon$ /sec

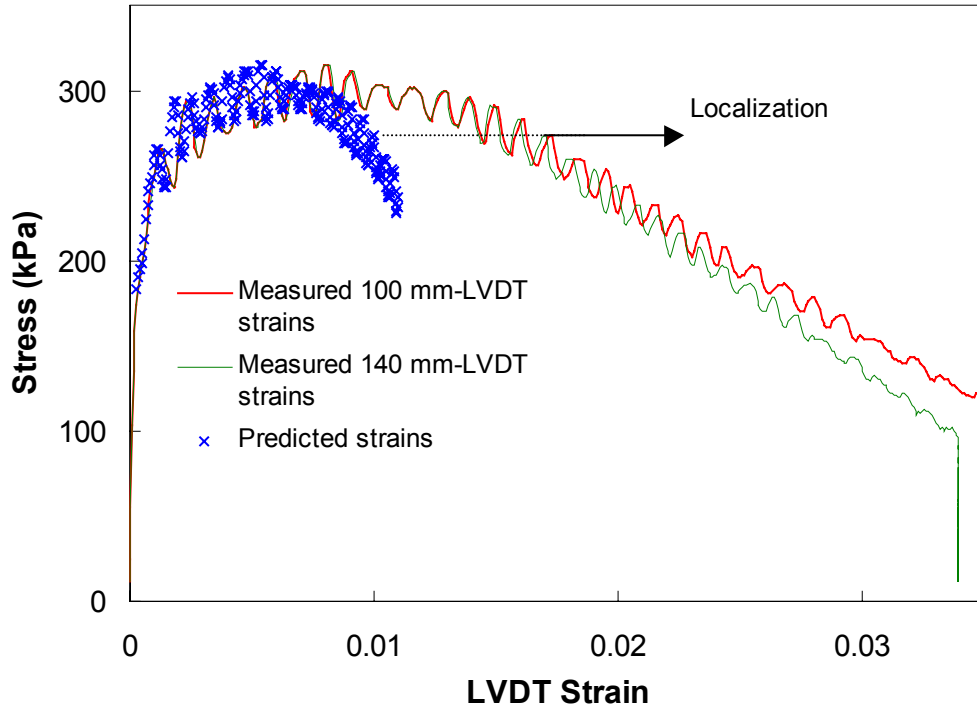


Figure 7.62. Actual and predicted stress-strain curves at 40°C and 0.0078  $\epsilon$ /sec

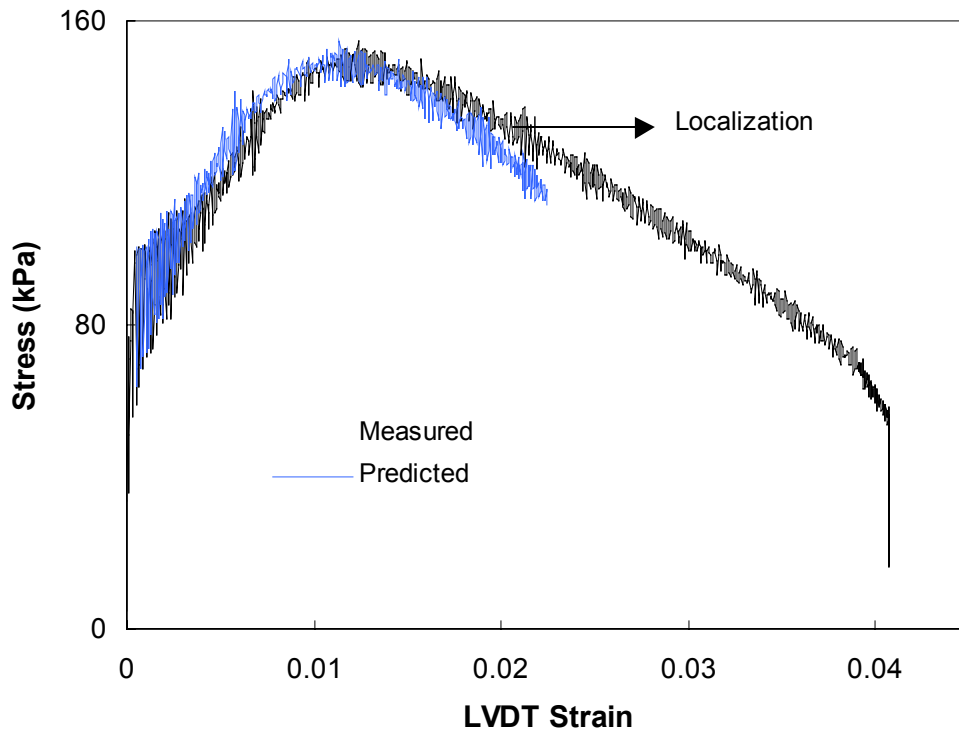


Figure 7.63. Actual and predicted stress-strain curves at 40°C and 0.0009  $\epsilon$ /sec

## ***7.7 Extension of the ViscoElastoPlastic Model beyond Localization***

### **7.7.1 LVDT vs. DIC Strains**

As mentioned in the previous section, the proposed model ceases to characterize asphalt concrete accurately after localization. The inaccuracy in characterization roots to the fact that after localization the microcracks that have developed as the specimen was strained start to coalesce and join to form several dispersed macrocracks. At that stage, strains become localized near the cracks and hence are not distributed uniformly over the gage length of the LVDTs. Consequently, the measured average strain from the LVDT ceases to be representative of the specimen as a whole and the resulting developed relationships between the applied stress and measured/predicted strains become erroneous. As the macrocracks develop, one or several macrocracks grow in the fracture process zone (FPZ) and ultimately split the specimen.

For accurate characterization after localization strains need to be measures in the fracture process zone. Since it is impractical to attach LVDTs with very small gage length to cover the fracture process zone which is about 4 to 5 mm in width (Seo 2002), alternative methods have to be devised for the strain measurement in that area. DIC, digital image correlation, is a promising technique used to capture the displacements and strains off surfaces of the specimen. Seo had shown that there is an excellent correspondence between 100-mm gage length LVDT strains and those measured using DIC before localization on prismatic specimens.

Although the DIC system is a 2-dimensional system, Seo was able to use it on cylindrical specimens by measuring strains from a 50-mm wide strip in the front, thus minimizing the error caused by the curvature of the cylindrical specimen.

Figure 7.64 is an illustration of a cylindrical specimen with two 100-mm gage length LVDTs attached and a 50 mm wide, 100 mm tall DIC image showing vertical strains. Strains from LVDTs and DIC have a good correspondence between each other up to peak stress then diverge significantly after localization (Figure 7.65 and Figure 7.66), where LVDT strains are smaller than DIC strains measured from a 5-mm FPZ strip. The main reason behind that phenomenon is because strains in areas other than the FPZ relax as microcracks develop and the LVDT strains are calculated from the entire gage length even though displacements occur mainly within the FPZ.

The major drawback of the DIC system is its limited data acquisition rate, thus making it less favorable to be used for monotonic tests that have a fast loading rate and cyclic tests. Since LVDT and DIC strains are similar prior to peak stress, LVDT strains will be used for pre-peak characterization and DIC strains for post-peak characterization. Figure 7.67(a) is a DIC image of the vertical strain of a 75x140 mm specimen during the pre-peak stage, while Figure 7.67(b) is an image corresponding to the instance of localization. In the first figure (pre-peak) the uniformity in strain within the gage length of the LVDT yields to similar DIC and LVDT strains. On the other hand, at localization the concentration of strains within the FPZ causes a difference in strain between the DIC and the 100-mm gage length LVDT.

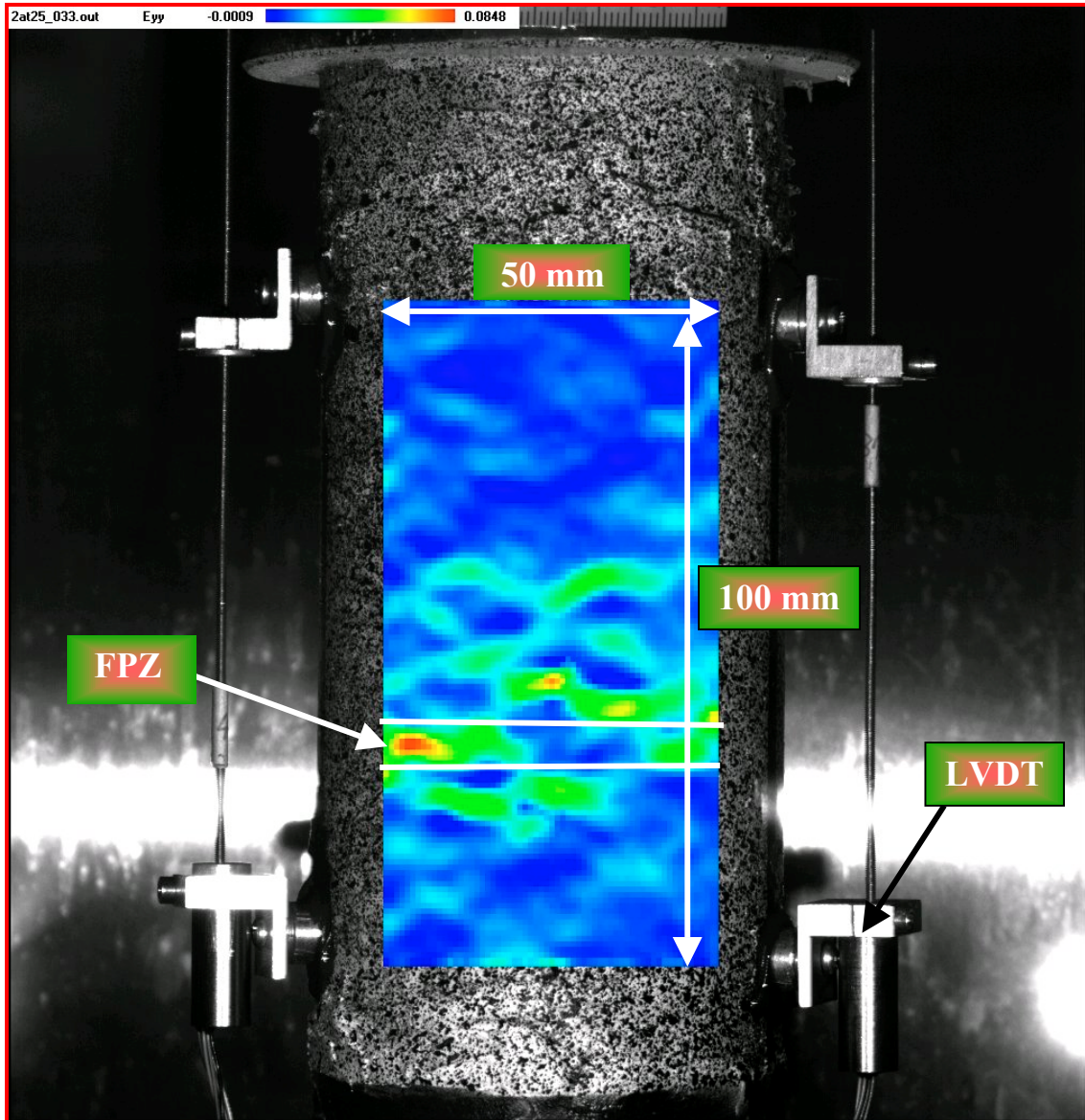


Figure 7.64. 75x140 mm specimen with 100 mm GL LVDTs with 50x100 mm DIC superposed image showing FPZ

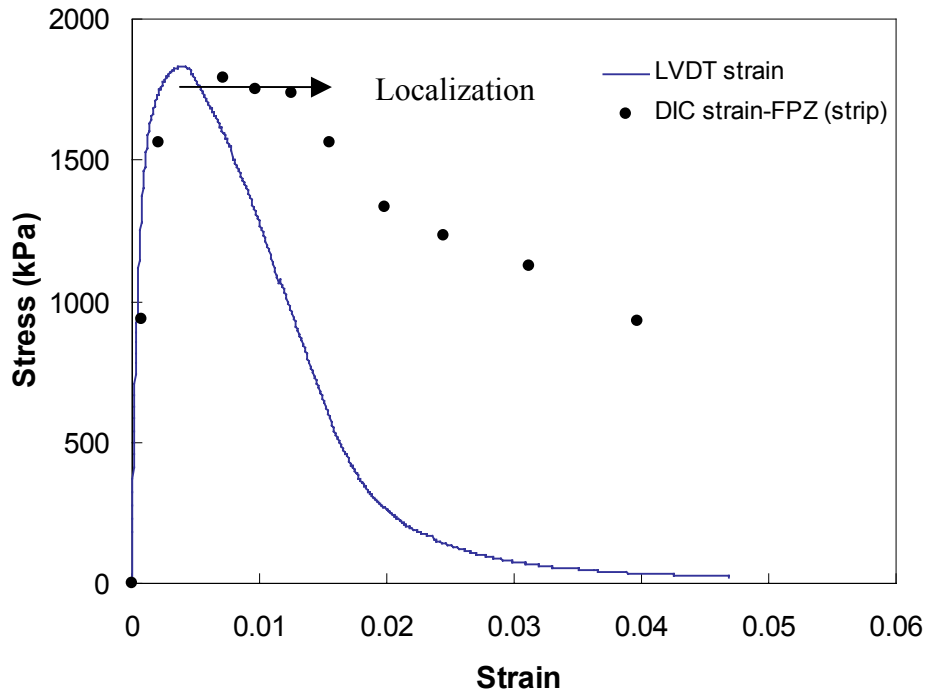


Figure 7.65. Comparison between DIC and LVDT strains for a monotonic test at 25°C and 0.0005  $\epsilon$ /sec (Courtesy of Seo)

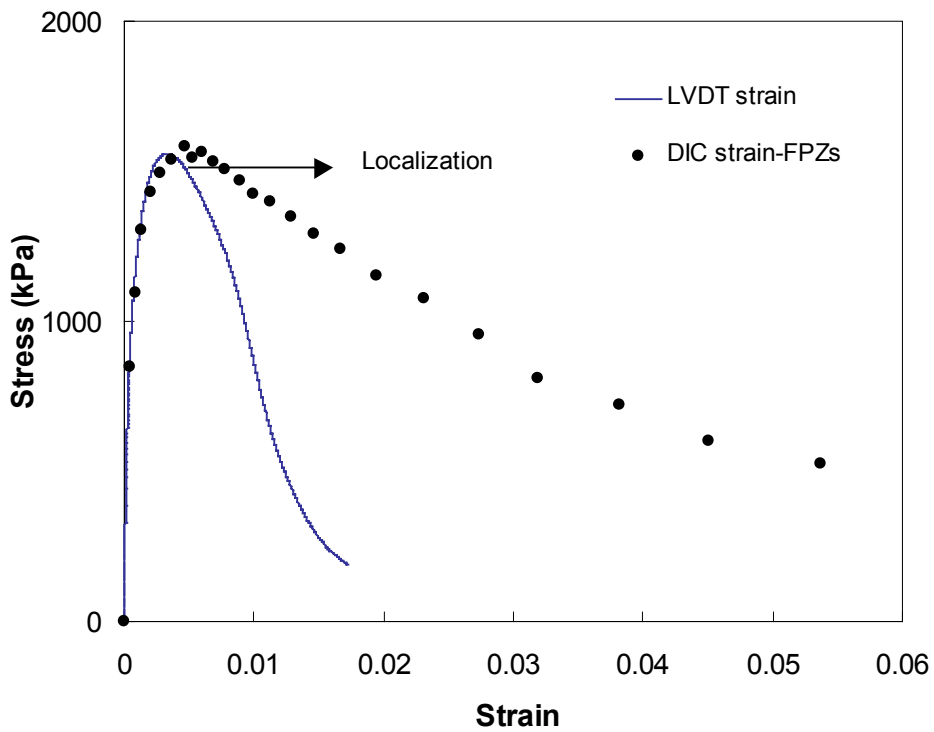


Figure 7.66. Comparison between DIC and LVDT strains for a monotonic test at 5°C and 0.00003  $\epsilon$ /sec (Courtesy of Seo)

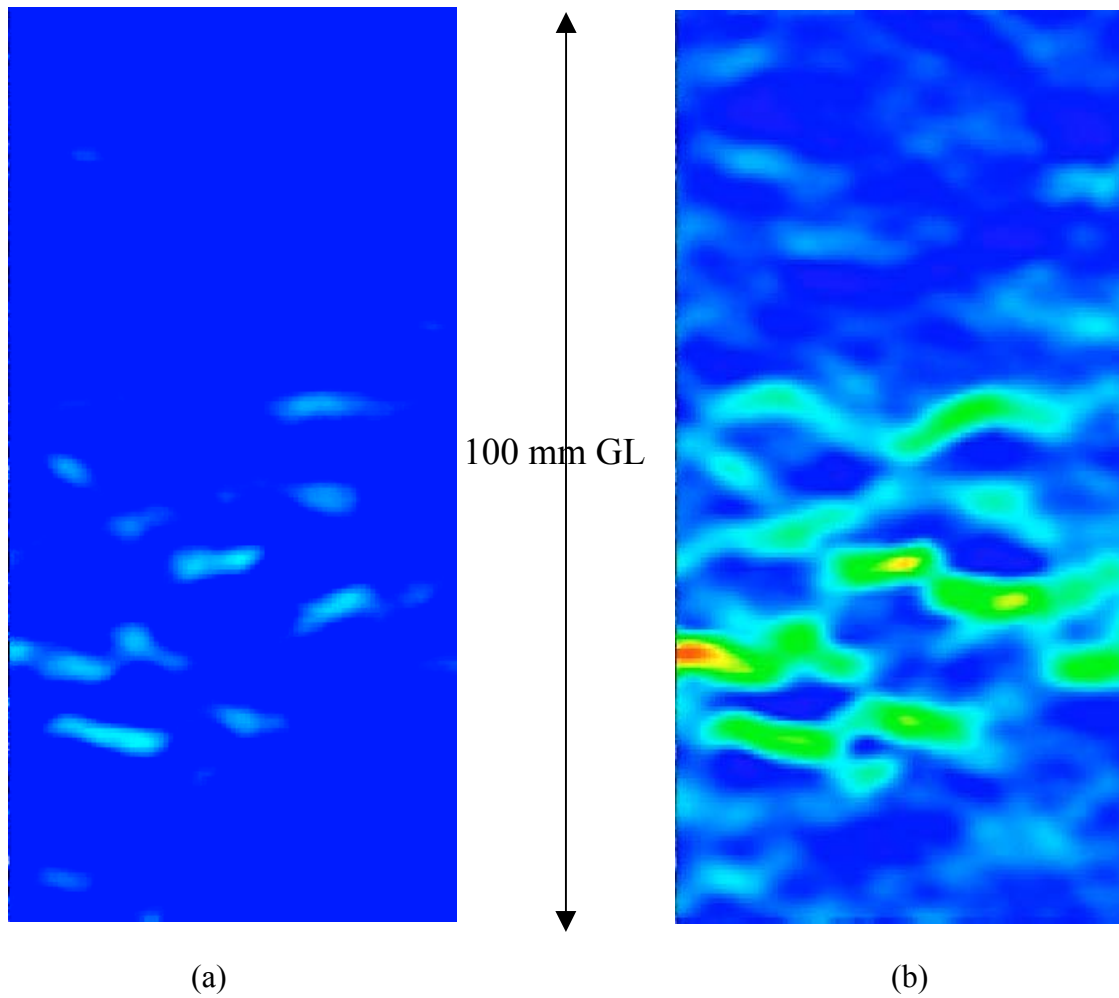


Figure 7.67. DIC 50x100 mm DIC image showing strain distribution during: (a) pre-peak and (b) localization  
(As colors change from blue to green to red, the value of vertical strain increases)  
(Courtesy of Seo)

### 7.7.2 Model Development Using DIC

The same steps followed in the development of the viscoelastoplastic model using LVDT strains will be used in this section, except the DIC strains are used after localization. Since strains from LVDTs and DIC are similar up to peak stress, LVDT strains will be used prior to peak. The LVDT strains are preferred because only a few points are available from DIC due to the slow data acquisition rate of DIC relative to that of the NI board acquiring data from the LVDTs. After peak, DIC strains are used because LVDT strains are not valid as localization starts to develop. So, as such, there is a switch in the strain data just before peak (Figure 7.69) that consequently leads to a switch in the normalized pseudostiffness  $C$  and damage parameter  $S^*$ . As a result, new characteristic relationships between  $C$  and  $S^*$  and between  $S^*$  and Lebesgue norm of stress are developed and plotted in Figures 8.69 and 8.70. It is worthy noting that in these figures a smooth transition occurs between the LVDT and DIC data in the characteristic  $C$  vs.  $S^*$  and  $S^*$  vs. Lebesgue norm curves.

Figure 7.71 could without doubt be regarded as the fruit of this research. Using the viscoelastoplastic model developed using 100-mm gage length LVDTs, strains are predicted given stress and time for a constant crosshead rate test at  $5^\circ\text{C}$  and  $0.0003 \text{ } \varepsilon/\text{sec}$ . For that same test, the model based on LVDT strains for pre-peak data and FPZ DIC strains for post-peak data is used for strain prediction. The following important observations can be drawn:

- In the pre-peak regions, the strains measured from LVDTs as well as DIC, and those predicted from the LVDT based model and the combined LVDT-DIC model almost perfectly match.

- In the post-peak region the measured DIC strains are larger than those measured using LVDTs, especially after localization.
- The LVDT-based model predicts strains accurately up to localization.
- The LVDT-DIC based model accurately predicts strains accurately even beyond localization up to the instance of macrocrack development. Beyond that instance, fracture mechanics may have to be used to model the crack growth.

It is important to note that the LVDT-DIC based model has not been applied extensively yet. It needs to be verified under a wider range of testing conditions. In addition, more work needs to be done to refine the model especially in developing a procedure for determining the optimal FPZ width and in exploring the potential possibility of extrapolating the prediction methodology to post-fracture regions; i.e., after development of macrocracks.

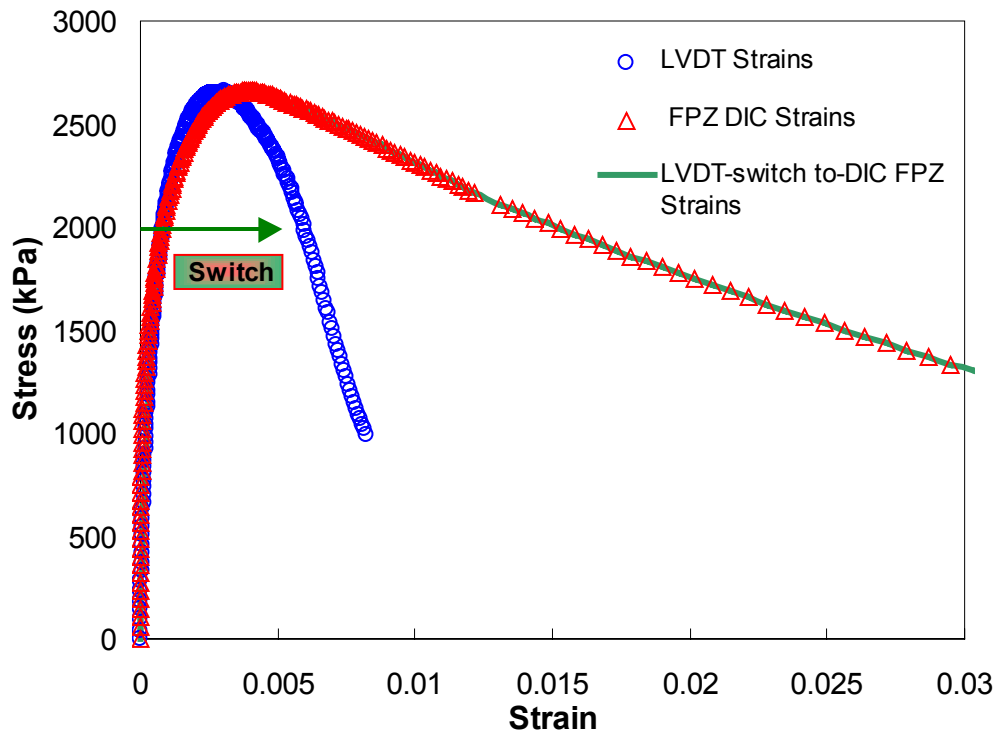


Figure 7.68. LVDT and DIC strains for a test at 5°C and 0.00003  $\epsilon/\text{sec}$

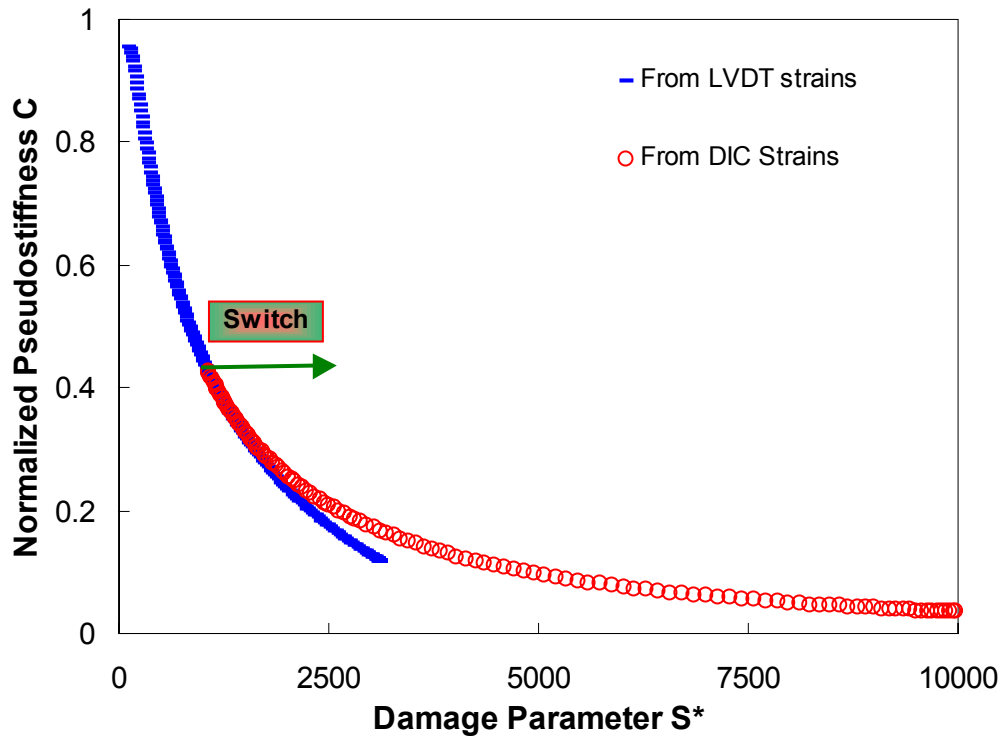


Figure 7.69.  $C$  vs.  $S^*$  curve using LVDT and DIC strains

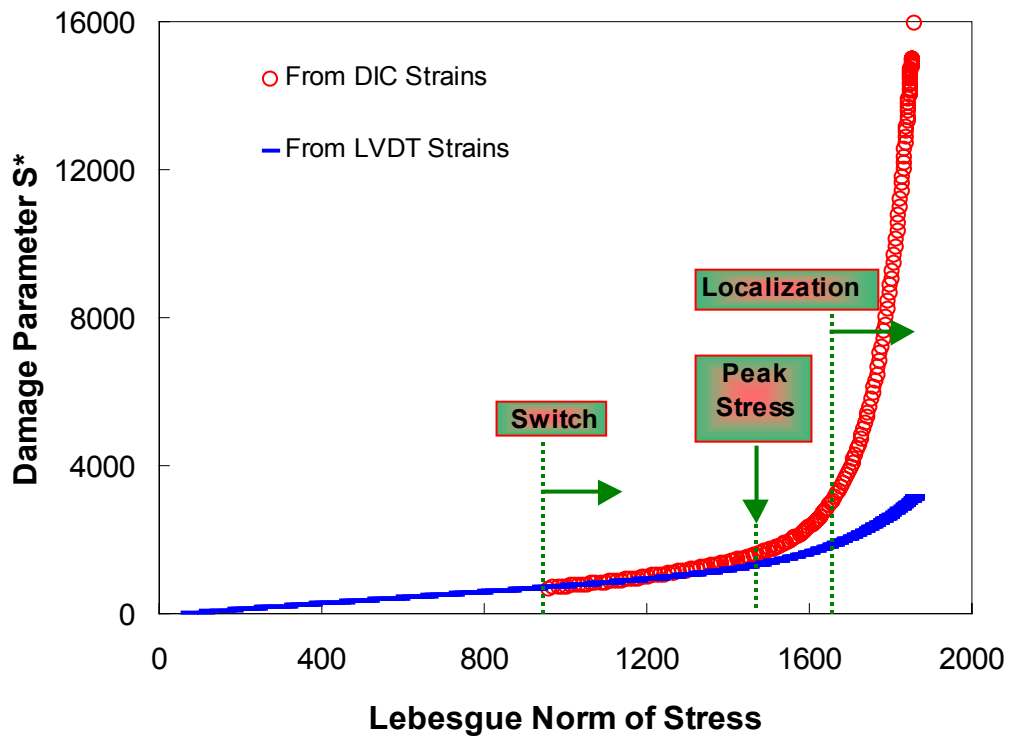


Figure 7.70.  $S^*$  vs. Lebesgue norm of stress using LVDT and DIC strains

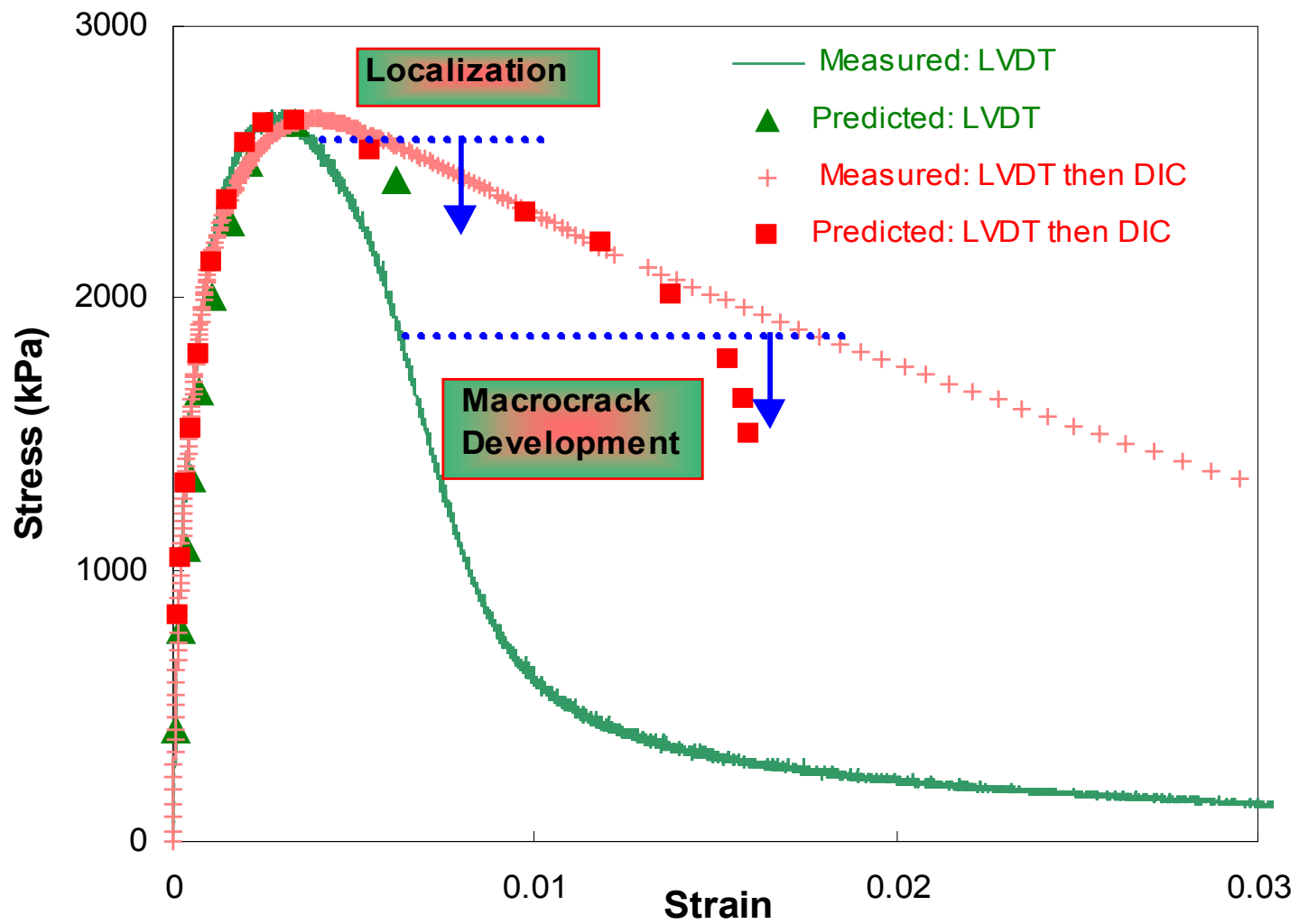


Figure 7.71. Measured and predicted  $\sigma$ - $\epsilon$  curves using LVDT strains and LVDT with a switch to DIC strains

## **8 Conclusions and Future Work**

### ***8.1 Conclusions***

To characterize asphalt concrete, the approach adopted in this research divides the characterization problem into two components: characterizing viscoelastic response and characterizing viscoplastic response. While the continuum damage model consisting of constitutive equations and damage evolution equations has been presented for the characterization of the viscoelastic behavior of asphalt concrete, different approaches have been presented for characterizing the viscoplastic response. The test protocols involved consist of uniaxial constant crosshead tests until failure at low temperatures and a series of uniaxial repetitive creep and recovery tests at high temperatures.

The developed ViscoElastoPlastic model performs very well in predicting material responses up to localization based on strains measured from on-specimen LVDTs. Since the viscoelastic part of the model is based on continuum damage mechanics and the concept of internal state variables, modeling responses after localization and the development of microcracks requires strain measurement near the fracture process zone. However, as the microcracks grow, coalesce and evolve to form major macrocracks, the theory of fracture mechanics has to be used for predicting the response.

## **8.2 Future Work**

### **8.2.1 Post-Fracture Characterization**

Future work should focus on integrating the research results obtained from fracture mechanics testing (Seo 2002) with the current model to extend the prediction beyond the stage of macrocrack development. In addition, more effort needs to be placed on the existing model to try and extrapolate the existing model to predict responses in post-fracture regions.

### **8.2.2 Confining Pressure Effect**

To truly consider the developed model as a comprehensive characterization model, the effect of confining pressure needs to be explored. It is proposed that the same testing protocols be repeated at different confining pressures to study the validity of the model. This includes the re-evaluation of the validity of the time-temperature superposition for growing damage under confinement.

### **8.2.3 Evaluation Testing**

If this model is an accurate characterization model, then the prediction of responses should be valid for any type of input. To evaluate the model, it should accurately predict responses over the widest and most robust set of evaluation tests, such as shear frequency sweep, fatigue beam tests, or any random loading tests. All the tests should be performed on the same reference mix that was initially used for model development. Based on the evaluation results, any modification, enhancement, further evaluation or acceptance and implementation would be recommended.

### **8.2.4 Sensitivity Analysis**

There are three primary objectives of the sensitivity study:

1. To confirm that the model parameters are in fact sensitive to changes in mixture properties. This is referred to as the “engineering reasonableness” of the material model and parameters.
2. To determine the sensitivity of the model parameters to testing protocols such as temperatures, loading rates and amplitudes, and even types of tests. This will aid in reducing the testing protocols for model development to the simplest and minimum required.
3. To try and develop relationships between material properties and model parameters. This will aid in predicting model parameters and hence performance from mix properties before actually conducting the testing protocols for developing the model.

## References

Alavi, S., T. Merport, T. Wilson, J. Groeger, A. Lopez. (1997) "LTPP Materials Characterization Program: Resilient Modulus of Unbound Materials (LTPP Protocol P46) Laboratory Startup and Quality Control Procedure". *Report FHWA-RD-96-176*. FHWA, U.S. Department of Transportation.

American Association of State Highway And Transportation Officials, 1998, *June 1998 Interim Edition – AASHTO Provisional Standards*.

Asphalt Institute, 1996, *Superpave Mix Design*, Superpave Series N0 2 (SP-2), Asphalt Institute, Lexington, Kentucky.

American Society for Testing and Materials (1985) "Standard Test Method for Dynamic Modulus of Asphalt Mixtures", D 3497-79 (1985), Annual Book of ASTM Standards, Vol. 04.03.

Chehab, G., E.N. O'Quinn, and Y.R. Kim. (2000) "Specimen Geometry Study for Direct Tension Test Based on Mechanical Tests and Air Void Variation in Asphalt Concrete Specimens Compacted by Superpave Gyratory Compactor". *Transportation Research Record 1723*, TRB, National Research Council, Washington, D.C., pp.125-132.

Chehab, G.R., Y.R. Kim, R.A. Schapery, M. Witzack, R. Bonaquist (2002) "Time-Temperature Superposition Principle for Asphalt Concrete Mixtures with Growing Damage in Tension State" *Asphalt Paving Technology*, AAPT, In Print

CITGO Asphalt Refining Company (1998) "Superpave Binder Evaluation Lot 4," Tested April 13, 1998

Daniel, J.S., Y.R. Kim, and H.J. Lee (1998). "Effects of Aging on Viscoelastic Properties of Asphalt-Aggregate Mixtures." *Transportation Research Record*, TRB, No. 1630, pp.21-27.

Daniel, J.S. (2001). "Development of a Simplified Fatigue Test and Analysis Procedure Using a Viscoelastic, Continuum Damage Model and its Implementation to WesTrack Mixtures", Ph.D. Dissertation, North Carolina State University, Raleigh, NC.

Harvey, J., Mills, T., Scheffy, C., Sousa, J., and Monismith, C. L. (1994) "An Evaluation of Several Techniques for Measuring Air-Void Content in Asphalt Concrete Specimens," *Journal of Testing and Evaluation*, JTEVA, Vol.22, No. 5, September 1994, pp. 424-430.

Kim, Y.R., Y.C. Lee, and H.J. Lee (1995). "Correspondence Principle for Characterization of Asphalt Concrete." *Journal of Materials in Civil Engineering*, ASCE, Vol. 7, No.1, pp. 59-68.

Kim, Y.R. and J.S. Daniel (1997). "Development of a Mechanistic Fatigue Prediction Model for Aging Asphalt-Aggregate Mixtures." Final Report submitted to Western Research Institute.

Kim, Y.R. and Y.C. Lee (1995). "Interrelationships Among Stiffnesses of Asphalt-Aggregate Mixtures." *Journal of the Association of Asphalt Paving Technologists*, Vol. 64, pp.575-606.

Kim, Y.R. and D.N. Little (1990). "One-Dimensional Constitutive Modeling of Asphalt Concrete." *ASCE Journal of Engineering Mechanics*, Vol. 116, No. 4, pp. 751-772.

Lee, H.J. (1996). "Uniaxial Constitutive Modeling of Asphalt Concrete Using Viscoelasticity and Continuum Damage Theory." Ph.D. Dissertation, North Carolina State University, Raleigh, NC.

Lee, H.J. and Y.R. Kim (1998a). "A Uniaxial Viscoelastic Constitutive Model for Asphalt Concrete under Cyclic Loading." *ASCE Journal of Engineering Mechanics*, Vol. 124, No. 11, pp. 1224-1232.

Lee, H.J. and Y.R. Kim (1998b). "A Viscoelastic Continuum Damage Model of Asphalt Concrete with Healing," *ASCE Journal of Engineering Mechanics*, Vol. 124, No. 11, pp. 1-9.

McGennis, R. and Mack, P. (1999) "Improved Superpave Standards: Summary of Proposed Changes to Superpave Mix Design," *South Central Superpave Center News*, Vol. 1, No. 2, 1999.

McGraw, E.O. (2000). "Quality Control in Fabricating and Testing Laboratory Asphalt Concrete Specimens." M.S. Thesis, North Carolina State University, Raleigh, NC.

Park, S.W. Y.R. Kim, and R.A. Schapery (1996). "A Viscoelastic Continuum Damage Model and Its Application to Uniaxial Behavior of Asphalt Concrete." *Mechanics of Materials*, Vol. 24, No. 4, pp. 241-255.

Park S.W., and R.A. Schapery, (1997) "A Viscoelastic Constitutive Model for Particulate Composites with Growing Damage", *International Journal of Solids and Structures*, Vol. 34, 931-947, (March 1997).

Park, S.W. and Y.R. Kim (1999). "Interconversion between Relaxation Modulus and Creep Compliance for Viscoelastic Solids," *ASCE Journal of Materials in Civil Engineering*, Vol. 11, No. 1, pp. 76-82.

Schapery R. A., (1978)“Fracture Mechanics of Solid Propellants”, Fracture Mechanics, Edited by N.Perrone, H. Liebowity, D. Mulville, W. Pilkey; University Press of Virginia, Charlottesville, 387-398.

Schapery, R.A. (1981). “On Viscoelastic Deformation and Failure Behavior of Composite Materials with Distributed Flaws.” *Advances in Aerospace Structures and Materials*, AD-01, ASME, New York, pp. 5-20.

Schapery, R.A. (1984). “Correspondence principles and a generalized J-integral for large deformation and fracture analysis of viscoelastic media.” *Int. J. Fract.*, Vol. 25, pp.195-223.

Schapery, R.A. (1990). “A Theory of Mechanical Behavior of Elastic Media with Growing Damage and Other Changes in Structure.” *J. Mech. Phys. Solids*, 38, pp.215-253.

Schapery R. A. (1999).“Nonlinear Viscoelastic and Viscoplastic Constitutive Equations with Growing Damage”, *Int. Journal of Fracture*, Vol. 97, 33-66.

Schapery, R.A. and S.W. Park (1999). “Methods of interconversion between linear viscoelastic material functions. Part II- an approximate analytical method.” *International Journal of Solids and Structures*, Vol. 36, pp. 1677-1699.

Schapery, R.A. “Non-linear Viscoelastic and Viscoplastic Constitutive Equations Based on Thermodynamics”, *Mechanics of Time Dependent Materials*, Vol. 1, 1997, pp. 209-240.

Seo Y., Y. R. Kim, M.W. Witzak, and R. Bonaquist, (2002). “Application of the Digital Image Correlation Method to Mechanical Testing of Asphalt-Aggregate Mixtures”, *Journal of the Transportation Research Board*.

Superpave Models Team “Advanced Material Characterization Models Framework and Laboratory Test Plan-Final Report”, (September 1999), Department of Civil engineering, Arizona State University.

Superpave Models Team “Volumetric Design of Standard Mixtures Used by the University of Maryland Models Team”, (September 1999 (b)), Department of Civil engineering, Arizona State University.

Uzan, J. “Asphalt Concrete Characterization for Pavement Performance Prediction”, *Asphalt Paving Technology*, AAPT, Vol. 65, 1996, pp. 573-607

Uzan, J. Perl, M., and Sides, A. (1985) “ Viscoelastoplastic Model for Predicting Performance of Asphalt Mixtures”, *Transportation Research Record* 1043, pp. 78-79.

Williams M.L., R.F. Landal, and J.D. Ferry (1955) “The Temperature Dependence of Relaxation Mechanisms in Amorphous Polymers and Other Glass Forming Liquid”, *The Journal Of The American Chemical Society*, Vol. 77.

Witczak, M. (2000) “Simple Performance Test: Test Results and Recommendations”. *Interim Task C Report*, NCHRP 9-19.

## **Appendices**

## **Appendix A: Specimen Preparation**

### ***A.1 Mixture Information***

The first section of this appendix presents additional data about the 12.5 mm MD Superpave mix components and design in Tables A.1 through A.5 and in Figure A.1.

Table A.1. Maryland Mixture Stockpile and Aggregate Data

Test	Method	#10	Washed #10	#8	#7	#6	#57	#4
<b>Gradation</b>	AASHTO T27							
<b>50.0 mm</b>								100
<b>37.5 mm</b>						100		84.6
<b>25.0 mm</b>						90.0	100	37.2
<b>19.0 mm</b>					100	55.0	92.7	4.3
<b>12.5 mm</b>				100	90.4	6.0	44.1	1.2
<b>9.5 mm</b>		100	100	93.7	63.7	0.5	18.1	0.4
<b>4.75 mm</b>		93.3	92.2	18.6	12.5		3	
<b>2.36 mm</b>		62.9	59.1	3.2	2.7		1.1	
<b>1.18 mm</b>		39.1	31.7	1.3				
<b>0.600 mm</b>		26.7	17.4					
<b>0.300 mm</b>		19.4	9.5					
<b>0.150 mm</b>		15.2	5.2					
<b>0.075 mm</b>		12.4	3.7	1.2	1.1	0.5	0.8	0.4
<b>Specific Gravity</b>	AASHTO T84/T85							
<b>Bulk</b>		2.594	2.664	2.698	2.706	2.709	2.712	2.710
<b>SSD</b>		2.646	2.687	2.712	2.717	2.718	2.722	2.717
<b>Apparent</b>		2.735	2.729	2.736	2.736	2.729	2.740	2.729
<b>Absorption, %</b>		2.0	0.9	0.5	0.4	0.3	0.4	0.3
<b>LA Abrasion, %</b>	AASHTO T96			26	26		26	
<b>Sodium Sulfate Soundness,</b>	AASHTO T104	1.2	1.2	0.1	0.1		0.1	
<b>Fine Aggregate Angularity</b>	AASHTO T304	45.5	45.6					
<b>Sand Equivalent</b>	AASHTO T176	89	92					
<b>Fractured Faces, %</b>	PTM 621	100	100	100	100	100	100	100
<b>Flat and Elongated, %</b>	ASTM D4791							
<b>5:1</b>				10.4	7.5		4.5	
<b>3:1</b>				20.2	20.8		17.5	

Table A.2. AASHTO MP1 grading for 12.5-mm MD mix binder

<b>Condition</b>	<b>Test</b>	<b>Method</b>	<b>Result</b>
<b>Unaged Asphalt</b>			
	Specific Gravity at 25°C	AASHTO T228	1.021
	Flash Point	AASHTO T48	294°C
	Viscosity at 135°C	ASTM D4402	0.420 Pa.s
	Viscosity at 165°C	ASTM D4402	0.114 Pa.s
	$G^*/\sin\delta$ at 10 rad/sec, 64°C	AASHTO TP5	1.260 kPa
<b>RTFO Aged Residue</b>			
	Mass Change	AASHTO T240	0.14 %
	$G^*/\sin\delta$ , at 10 rad/sec, 64°C	AASHTO TP5	2.516 kPa
<b>PAV Aged Residue</b>			
	$G^*/\sin\delta$ , at 10 rad/sec, 25°C	AASHTO TP5	4154 kPa
	Creep Stiffness, at 60 sec, -12°C	AASHTO TP1	209.0 MPa
	m-value at 60 sec, -12°C	AASHTO TP1	0.342

Table A.3. Mixing and compaction temperatures

<b>Condition</b>	<b>Temperature, °C</b>	
	<b>Maximum</b>	<b>Minimum</b>
<b>Mixing</b>	159	153
<b>Compaction</b>	147	142

Table A.4. 12.5 mm mixture verification results

Property	Trial 1 Actual	Estimated Optimum	Final
Asphalt Content	5.0	5.29	5.2
Air Voids	4.7	4.0	4.0
G <sub>mm</sub>	2.501	2.493	2.488
VMA	15.3	15.2	15.5
VFA	69.2	74	74
Filler/Effective Asphalt Ratio	1.22	1.26	1.26

Table A.5. Final 12.5 mm MD mixture design

Property	Design	Superpave Criteria
<b>Gradation</b>		
19.0 mm	100	
12.5 mm	97	
9.5 mm	87	
4.75 mm	58	
2.36 mm	35	
1.18 mm	21	
0.600 mm	13	
0.300 mm	9	
0.150 mm	8	
0.075 mm	6.1	
Asphalt Content, %	5.2	
G <sub>mm</sub>	2.492	
G <sub>sb</sub>	2.674	
Air Voids, %	4.0	4.0
VMA, %	15.5	>14.0
VFA, %	74	65-75
Filler/Effective Asphalt Ratio	1.26	0.6 – 1.2
% G <sub>mm</sub> at N <sub>initial</sub>	84.8	> 89.0
% G <sub>mm</sub> at N <sub>maximum</sub>	97.6	< 98
Coarse Aggregate Angularity	100/100	95/90
Fine Aggregate Angularity	46	> 45
Flat and Elongated	8.3	< 10
Sand Equivalent	91	> 45

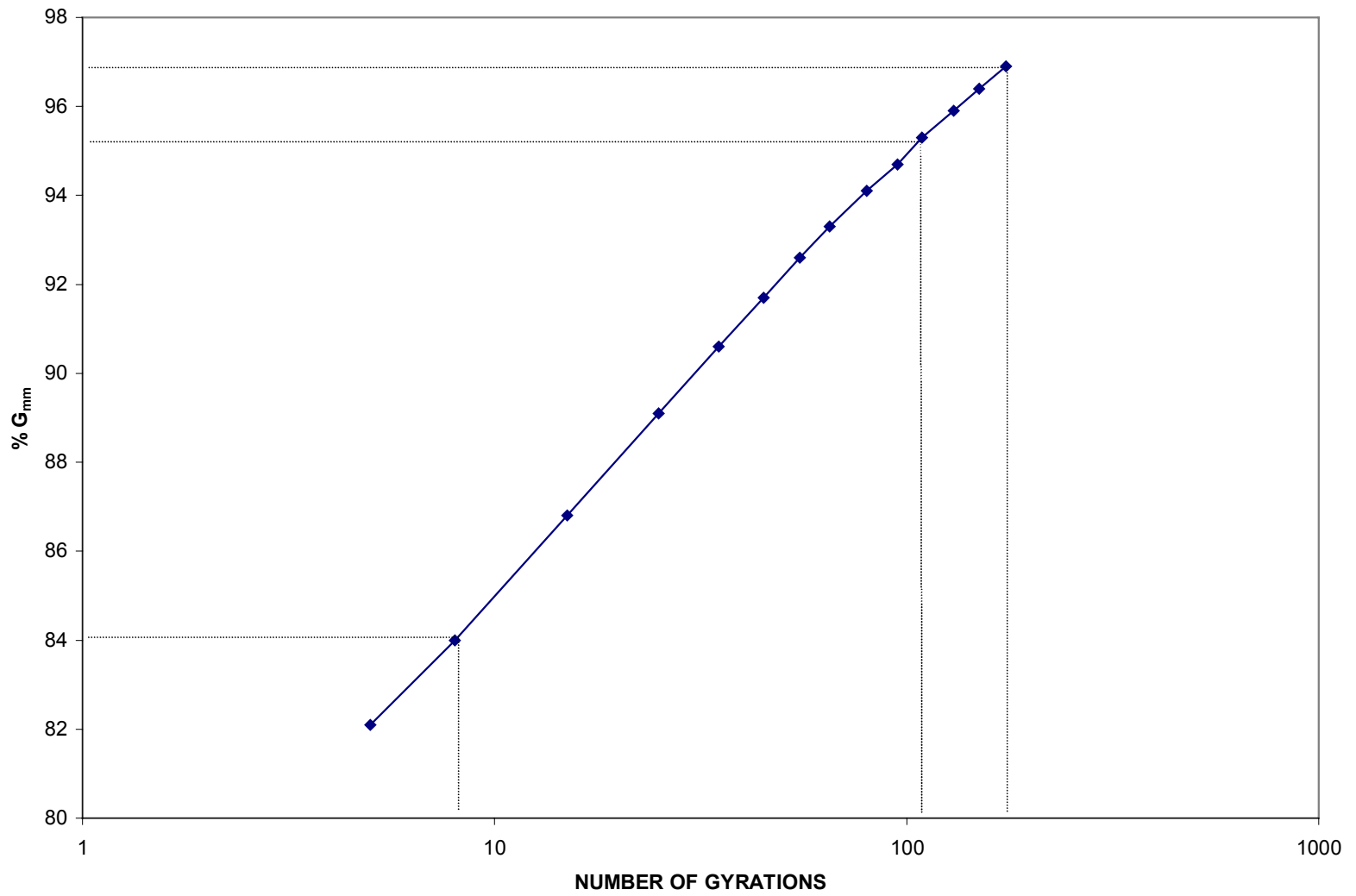


Figure A.1. 12.5 mm MD mixture trial compaction data

## ***A.2 Specimen Preparation Protocols***

The following procedures are for specimens taller than 150 mm.

For specimens of lesser height, the same procedures could be followed except that only one batch is needed for each specimen.

### **A.2.1 Batching**

Prepare 2 batches for each specimen. Mass of each batch should be half the total mass of aggregates needed for the specimen.

#### *A.2.1.1 Equipment Needed:*

1. Scoop
2. Flat-bottom pans
3. Balance: Sensitivity of 1 gram
4. Aluminum foil

#### *A.2.1.2 Procedure:*

1. Place an empty pan on the balance and zero it.
2. For each aggregate size, scoop from the bucket the quantity needed.
  - Look at the # on the side of the bucket to find the size of aggregate.
  - Start piling the aggregates on one side of the pan moving to the other side in cases you put more than required. Then you can easily extract out the excess without taking out any other aggregate sizes.
3. Re-zero the balance after all the aggregate sizes for each aggregate category are

added.

4. Repeat steps 2 and 3 for other categories (sand, bag fines, etc.).
5. Spread the larger aggregates over the fine aggregates and sand so that fine particles are not lost when subjected to draft of air.
6. Cover the pan with aluminum foil or with another pan (if no aluminum foil is available) and label the foil/pan with the specimen number and mass of the batch.

## **A.2.2 Mixing**

### *A.2.2.1 Equipment Needed:*

1. Oven
2. Mixer with timer
3. Flat-bottom metal pans
4. Thermometers
5. Balance: Sensitivity of 0.1 gram
6. Mixing spoon, bowl, and whip
7. Spatula
8. Gloves
9. Torch
10. Paper towels
11. Safety glasses

### *A.2.2.2 Procedure:*

1. Place pans containing aggregate in the oven at 20°C higher than mixing temperature

- (166 C) for 4 hours, preferably over night.
2. Heat mixing bowl, spoon, spatula, and whip at mixing temperature for about 2 hours.
  3. Heat the asphalt binder in the oven 20°C higher than mixing temperature for 2 hours.
    - Make sure the lid is off the asphalt can.
  4. Remove the asphalt binder from the oven and place it on the hot plate set at 4°C higher than mixing temperature.
  5. Once this temperature is met, you can start mixing.
  6. Remove the mixing bowl, spoon, spatula, and whip from the oven.
    - Set up the whip in the mixing machine and place the rest on the table.
  7. Remove the aggregates from the oven and pour them into the mixing bowl.
  8. Mix the aggregates in the bowl with the spoon and form a crater in the middle of the blended aggregates.
  9. Place the mixing bowl on the scale beside the hot plates and zero it.
  10. Pour the required amount of asphalt into the crater in the bowl.
    - Use paper towels to extract the excess amount of asphalt.
    - TOTAL mass of asphalt = (mass aggregate / % mass aggregate) \* % mass asphalt
  11. Mix quickly with the spoon to blend the aggregate with the asphalt and pile the mix up on the side opposite to the notch that connects the mixing machine with the mixing bowl.
  12. Attach the bowl to the mixing machine and pull up the lever on the mechanical mixer to rise up the bowl. You may need to rotate the whip or move the aggregates to raise the bowl because the whip will get in the way.

13. Set the mechanical mixer to a minimum speed of one minute.
  - Make sure you wear safety glasses during the mixing procedure.
  - When machine is on, push the bowl up with your hand to ensure that the aggregates on the bottom will also be mixed.
  - After half a minute stop the mechanical mixer and scrape the bowl with the spatula to get the fine aggregates mixed in.
  - Continue the mixing for the other half a minute and this time heat the bottom with a torch.
14. When all the aggregates are coated with asphalt, remove the bowl from the mixer.
15. Record the mixing temperature.
16. Remove the whip from the mechanical mixer and wipe off all fine aggregates into the bowl.
17. With the spatula, scrape the fine particles on the inside the bowl and distribute them evenly throughout the mix.
18. Pour the mix into a round-bottom pan and with the spoon scrape the mixing bowl to get all the fine aggregates and put them evenly throughout the mix.
19. Put the mix back in the oven for aging or until compaction.
  - Set oven to 3 or 4 degrees higher than compaction temperature.
20. Put bowl, whip, spatula, and spoon back in the oven until you are ready to prepare the next batch.

Repeat the procedure for the other batches, but note that:

  - If the same mixing bowl and whip is to be used again, they should be free from fine particles (as much as you can).

- Reheat the mixing bowl, spoon, spatula, and mixer whip at mixing temperature for about 10 minutes.

#### *A.2.2.3 AGING*

If the mix is to be aged, then the mix should be put in flat pans instead of round pans and spread the asphalt at an even thickness. For each mix, place the pans in the oven at 135°C for 4 hours.

### **A.2.3 Compaction**

2 batches are needed for the preparation of each specimen.

#### *A.2.3.1 Equipment needed:*

1. Superpave Gyrotory Compactor
  - Ram Pressure: 600kPa
  - Gyration Angle: 1.25 Deg
  - Gyration Speed: 30 gyr./min
2. Mold: 150 mm
3. Metal Plate: 150 mm diameter (for ServoPac)
4. Paper Disks: 150 mm diameter
5. Thermometer
6. Spoon and Spatula

#### *A.2.3.2 Procedure:*

1. While mix is in short-termed aging, turn the compactor on. The power switch is

located on the backside of the machine.

- Follow the Pre-Compaction Procedure located on the wall by the air pressure machine.
  - Turn on the air pressure, making sure you check for water first.
  - Unlock and turn on the wing nut located behind the Superpave Gyrotory Compactor.
2. Set the compaction pressure, angle, and gyration speed to the proper value. For ServoPac, set  $N_{\max}$  to 500. Set the height to the appropriate value (178mm).
  3. One hour prior to compaction, place the mold, plates, spoon, and spatula in the oven at compaction temperature.
  4. After 4 hours of short-term aging use the thermometer to take the temperature of the mix:
    - If compaction temperature is lower than 135°C, heat the mix in the oven at 12°C higher than compaction temperature for no more than 30 minutes. Remove the mix when it reaches a temperature higher than compaction temperature by 3 or 4 degrees.
    - If compaction temperature is higher than 135°C, place the mix at room temperature till it reaches a temperature 3 or 4 degrees higher than compaction temperature.
  5. Remove the mold, plates, spoon, and spatula from the oven.
  6. Place the base plate in the mold and place a paper disk on top of it.
  7. Measure out the appropriate amount of aggregate to be added from each batch.

- Put a round-bottom pan on the scale and zero it. Then add the appropriate mass of mix. Throw out the excess mix.
- 8. Put both the measured mixes back into the oven and use the thermometer to measure the temperature of the mix inside the oven.
- 9. Once the mix has reached the compaction temperature pour half the mix (from the first pan) into the mold and push the mix down with a spatula so that it settles and creates more room for the second half (mix two). Make sure the asphalt penetrates to the bottom of the mold.
- 10. Weigh the appropriate amount of mass from the second batch and pour it into the mold. Using the spatula penetrate it down to the bottom to settle the mix. Also, push on the top with the spatula to further settle the mix.
- 11. Place a paper disk on top of the mix, and the metal plate on top.
- 12. Center the mold inside the compactor.
- 13. Push the “lower mold” button, the “lock mold” button, and then the “start” button.
- 14. After compaction is complete, remove the mold from the compactor wait five minutes for the specimen to cool. (You can use the air gun to cool the mold).
- 15. Align the mold to be prepared for extruding. Press the extrude button and hold down the top collar while the specimen is being extruded.
- 16. Allow five minutes for the specimen to cool. (You can use the air gun).
- 17. Remove the paper disks and mark the specimen with its ID name, top, and bottom.
- 18. Flip the specimen onto a pan and place the specimen in front of the fan for further cooling.
- 19. Place the mold, plates, and spatula back in the oven for fabrication of other

specimens.

## **A.2.4 Coring**

### *A.2.4.1 Equipment Needed:*

1. Coring machine
2. Drain
3. Hose
4. Coring bit (75mm or 100mm)
5. Pan
6. Rags

### *A.2.4.2 Procedure:*

1. Move coring machine near drain so the excess water and fine aggregates will flow down the drain.
2. Attach the correct size coring bit.
3. Put the specimen bottom first into the clamps located below the coring bit. Make sure the top is facing up and the specimen is centered.
  - Push the bit downward onto the specimen to get the specimen centered in place.
  - Tighten both clamps at the same time to secure the specimen in the center.
4. Connect the water hose to the machine and make sure it is twisted on tight.
5. Put a pan and some rags under the specimen so when it drops the specimen will not crack or deform.
6. Stand behind the machine and turn the water on by pulling the lever slowly until there

is no dripping and little splash. (Constant flow of water).

7. Put on earplugs and turn the power switch on located on top of the coring machine.
8. Slowly rotate the lever arm. Do not force the lever arm. The whole process should take at least ten minutes.
9. When you get close to the end of the specimen rotate the arm very slowly so no chipping occurs at the bottom of the specimen.
10. Use the water mop to force all the water down the drain.

### **A.2.5 Sawing**

#### *A.2.5.1 Equipment:*

1. Sawing machine
2. Plug
3. Hose

#### *A.2.5.2 Procedure:*

1. For tall specimens set up the wide V-securing jig, and for short specimens set up the thin V-securing jig.
  - Use the wrench to loosen the jig and move it to the appropriate spot on the side of the saw.
2. Measure how much you want to cut from the specimen.
  - Make sure to measure starting from the inside of the saw.
  - Cut more from the top of the specimen than from the bottom because more air voids are located at the top of specimens. (e.g., from top 20 mm and bottom 18

- mm)
3. Make sure the table top-wheels are aligned, the nuts are tight, and the jig is secure in place.
  4. Put the plug at the bottom of the saw machine and fill up the bottom with water from the hose located on the wall.
  5. Hook the sawing machine up to the electricity and flip up the electricity lever beside the hoses on the wall.
  6. Connect the electricity plug on the sawing machine to the pump plug on the sawing machine.
  7. Roll the V-jig under the saw and flip on the power switch to turn the saw and water pump on.
  8. Gently and slowly pull down the lever arm to cut the specimen.
    - Go slow when you get to the bottom of the specimen so it does not chip.
  9. Mark the top of the specimen.
  10. Move the V-jig to the other side of the saw to cut the bottom side of the specimen.
  11. Repeat steps 2-9 for the bottom of the specimen.

## **A.2.6 Air Voids Measurement**

### *A.2.6.1 SSD (Saturated Surface Dry) Method*

Measure the amount of air voids in a specimen.

1. Dry the specimen very well by using an air pressure gun or by using the vacuuming procedure in Corelok. You have to make sure there is no water coming out of the pores. Do not rely on the surface looking dry.

2. Zero the scale and weigh the specimen.
  - Record all your data on the fabrication data sheet.
3. Soak the specimen in a bucket of water for around four minutes.
4. Weigh the specimen submerged in water by putting it in the basket inside the Gilson tank. Wait until the water level stabilizes and then take your measurement.
5. Make sure the water is clean from dirt and that its temperature is 20-25 C; i.e., room temperature.
6. After recording the submerged weight, dry the surface of the specimen by dabbing it with a dry rag until excess water on the surface is removed; i.e., SSD state. Weigh it on the scale to get the SSD weight.
7. Use the air void spreadsheet or the equation in your notebook to find the % air voids.
  - Pre-core-and-cut should have air voids of around 6% and post-core-and-cut specimens should have  $4 \pm 0.5\%$  air voids.

#### *A.2.6.2 Corelok Vacuum Sealing Method*

Unlike the SSD method, the Corelok method for measuring air voids does not account for the surface holes of a specimen as air voids; consequently, resulting in a lower and more accurate measurement of the total air voids in the specimen.

#### Equipment:

1. Scale
2. Green foam for the submerged basket
3. Foam cushion
4. Foam cushion with supporting bars

## 5. Yellow Corelok bag

### Procedure:

1. Place the foam cushion on the scale and re-zero the scale.
2. Make sure the basket in the water scale has a green cushion over the metal wires so that the wires will not rip the bag.
3. Tear off one of the yellow bags and make sure there are no holes or tears in the bag!
  - When you put the rest of the bags back make sure the side with the open end of the bags is face down.
4. Weigh the bag.
  - Record all data on the CoreLok bulk specific gravity data collection table
5. Weigh the dry specimen before sealing.
6. Put the three Corelok white plates in the machine for small specimens and one or two for larger specimens.
  - More plates will decrease the time needed for vacuuming.
7. Place the black cushion with bars facing up on top of the white plates to hold the specimen in place.
8. Put the specimen inside the yellow bag and place the specimen and bag on top of the black cushion in the CoreLok.
9. Slide the black cushion to center the specimen in the CoreLok and get the bag to exceed the sealing bars.
  - Do not pull on the bag to move the specimen because you risk ripping the bag.
  - Make sure there is plenty of bag exceeding the sealing bars to ensure a tight seal.

10. Lock the machine and set the vacuum dial to ten (the max vacuum) and the seal dial to 4.5.
11. Press start and hold down the top of the machine ensure that no air escapes the CoreLok.
12. When the procedure ends, check the bag by tugging on it and looking at the edges to see if the specimen was sealed correctly.
13. Weigh the sealed specimen.
14. Weigh the sealed specimen in the water.
  - Fold the bag around the specimen as you put it into the water so the bag will not tear on the metal.
  - Once the sealed specimen is submerged, shake the bag to release any trapped air bubbles from the folds of the bag.
15. Cut the bag open with scissors and reweigh the specimen dry.
  - This will make sure the specimen was sealed correctly.
16. Use the CoreLok spreadsheet to find the bulk specific gravity.
17. Calculate the percent air voids from:  $1 - (\text{Bulk S.G.} / \text{Max S.G.}) * 100$

### **A.2.7 Gluing Specimens**

#### *A.2.7.1 Equipment:*

1. Devcon Plastic Steel Putty (A), No. 10110-1 lb. Container
2. Acetone/rubbing alcohol
3. 3 Popsicle sticks
4. Rubber gloves

5. Gluing jig

6. Balance

*A.2.7.2 Procedure:*

1. Clean the end plates and the ends of the specimen with degreaser solvent, such as rubbing alcohol or acetone.
  - Lay the specimen on its side so no dirt will get on the ends of the specimen and allow the surface of the specimen and end plates to dry.
2. Add hardener to resin in the ratio of 1:9 by weight or 1:2.5 by volume at room temperature.
  - For 75 mm diameter end plates with circular concentric grooves, about 4:36 g is enough.
3. Using a Popsicle stick for the resin (black), the hardener (white), and then one for mixing weigh out the appropriate amount of each on a scrap square of cardboard.
4. Mix thoroughly with a putty knife until a gray streak-free mix is achieved.
5. Apply the mix firmly to surfaces, filling the grooves of the end plate and air void pockets present on the specimen surface. A 1 mm layer should be eventually present between the end plate surface and the specimen surface.
  - Working time for the epoxy is 45 minutes.
6. After one end of the specimen is glued (bottom), screw the bottom glued end plate into the jig and align the specimen vertically in the gluing jig.
  - Repeat the gluing procedure for the other end (top) and tighten the jig to center and align the specimen.

- Use the Popsicle stick to spread excess glue around the specimen and plate to fill air voids. Remove excess glue.

7. Keep specimen in the gluing gig for at least 4 hours (curing time) and full cure is achieved after 24 hours.

### **A.2.8 Removing Adhesive**

1. After testing place the end plates with the remaining attached part of the specimen into the oven and heat at 170 C or higher (185 C) for an hour or longer.
2. With a sharp tool such as a putty knife or screwdriver, peel off the epoxy and any remaining asphalt concrete from the end plate surface.

### **A.2.9 Cleaning End Plates**

After specimens are tested, you must remove the end plates so they can be used again.

#### *A.2.9.1 Equipment:*

1. Oven
2. Flat-bottom pan
3. Putty knife
4. Safety goggles
5. Freezer
6. Drill
7. Flat-head screwdriver
8. Acetone
9. Paper towels

*A.2.9.2 Procedure:*

1. Put endplates that are glued to the specimens in the oven for about two hours at 185C.
  - Do not leave the endplates in the oven for more than two hour because the glue will become harder to get off.
2. Take one endplate out at a time and put it in the flat-bottomed pan.
3. Use the putty knife to remove the glue and asphalt.
  - Wear safety goggles and push the putty knife away from your body so particles do not fly up and hit you.
4. Repeat steps 2 and 3 for all remaining endplates.
5. Throw glue and remaining specimen away.
6. Use the power drill with a wired brush to extract the remaining glue particles.
  - It is easiest if you put the endplate in the vice and then clean.
7. Use a small flat-head screwdriver to help you get the glue that the drill was not able to remove between the grooves off the endplate.
8. Put the endplates in the freezer until they are cooled to room temperature.
9. Once at room temperature, use acetone to clean the endplates.
10. After you pour acetone onto the paper towel, be sure to close the cap on the acetone because acetone evaporates quickly.
11. Minimize the inhalation of acetone; wear latex gloves and keep area ventilated.
12. Clean with the acetone until no more dirt appears on the paper towel.

## Appendix B: Photographs

### *B.1 Specimen Fabrication*



Figure B.1. Compactor mold and extension collar



Figure B.2. ServoPac gyratory compactor

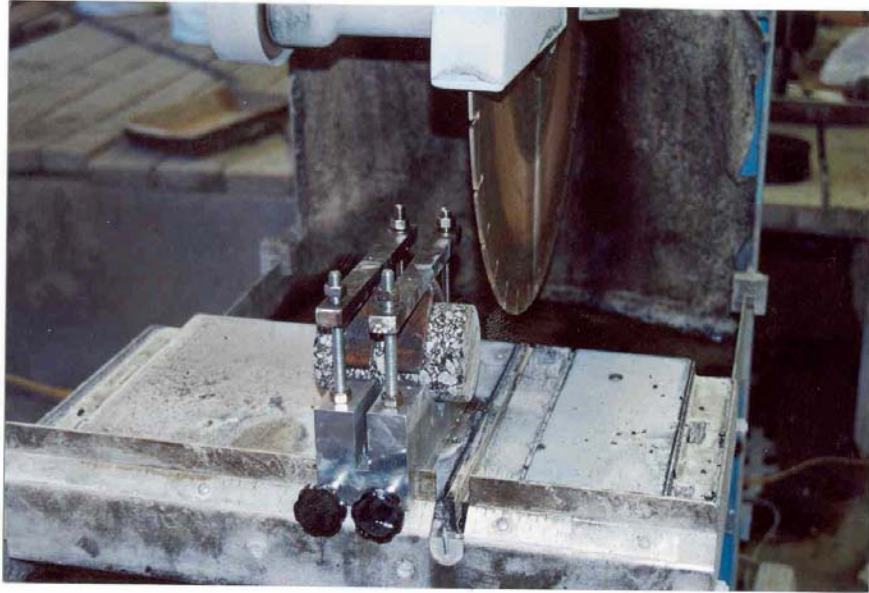


Figure B.3. Coring and sawing machines

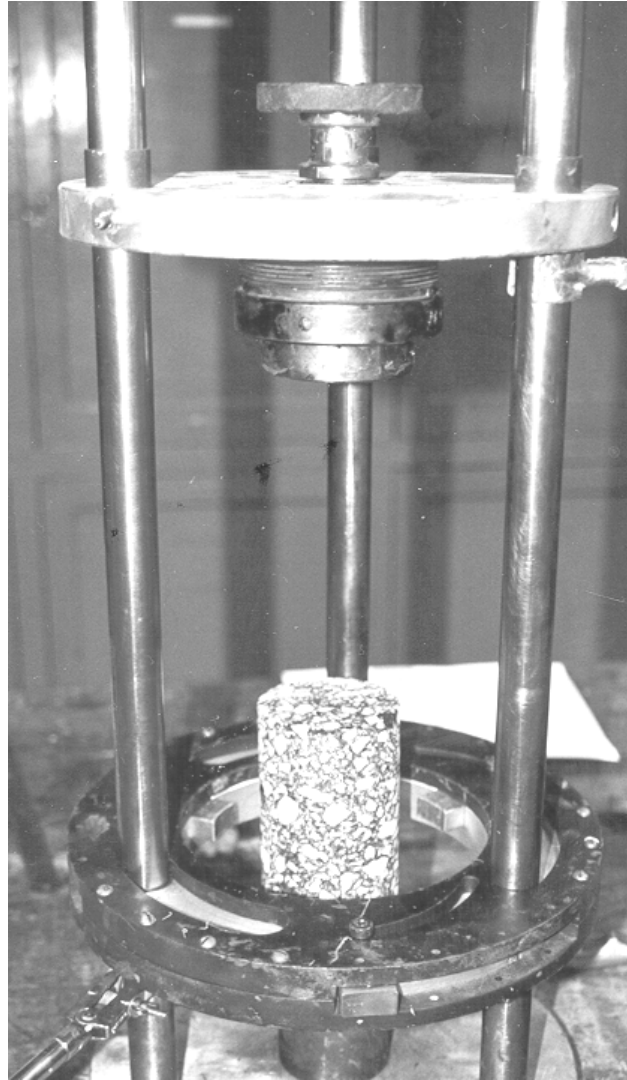


Figure B.4. Gluing jig

*B.2 Testing Systems*



Figure B.5. MTS testing setup



Figure B.6. UTM testing system

### B.3 Specimen Geometry

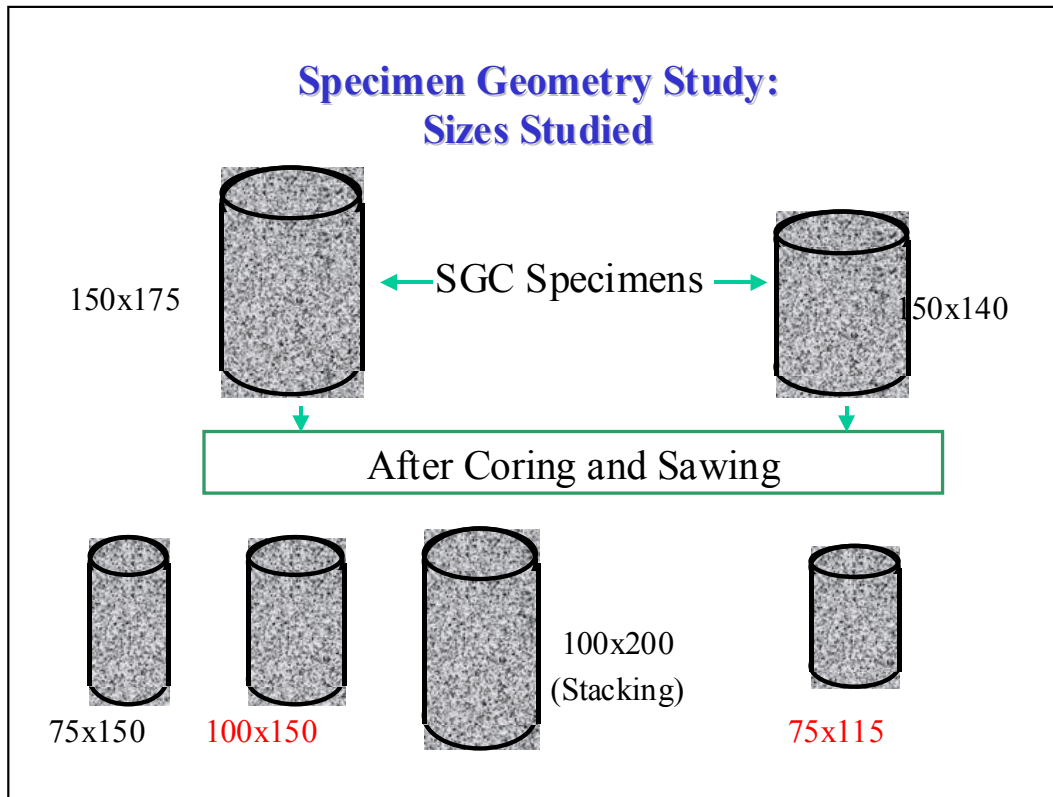


Figure B.7. Geometries used for mechanical testing

**Specimen Geometry Study:  
Air Void Distribution-Typical Cut and Cored  
sections**

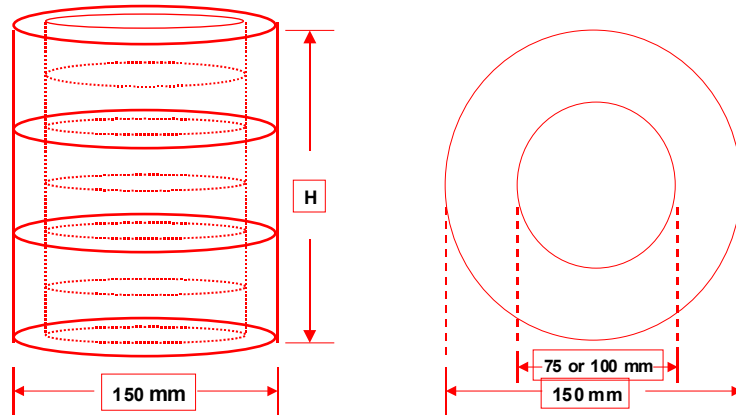


Figure B.8. Specimens cut and cored for air void distribution study



Figure B.9. Wrapping a specimen with Parafilm

#### ***B.4 Measurement Instrumentation***



Figure B.10. GTX LVDT (Left) and XSB LVDT (Front)



Figure B.11. CD LVDTs

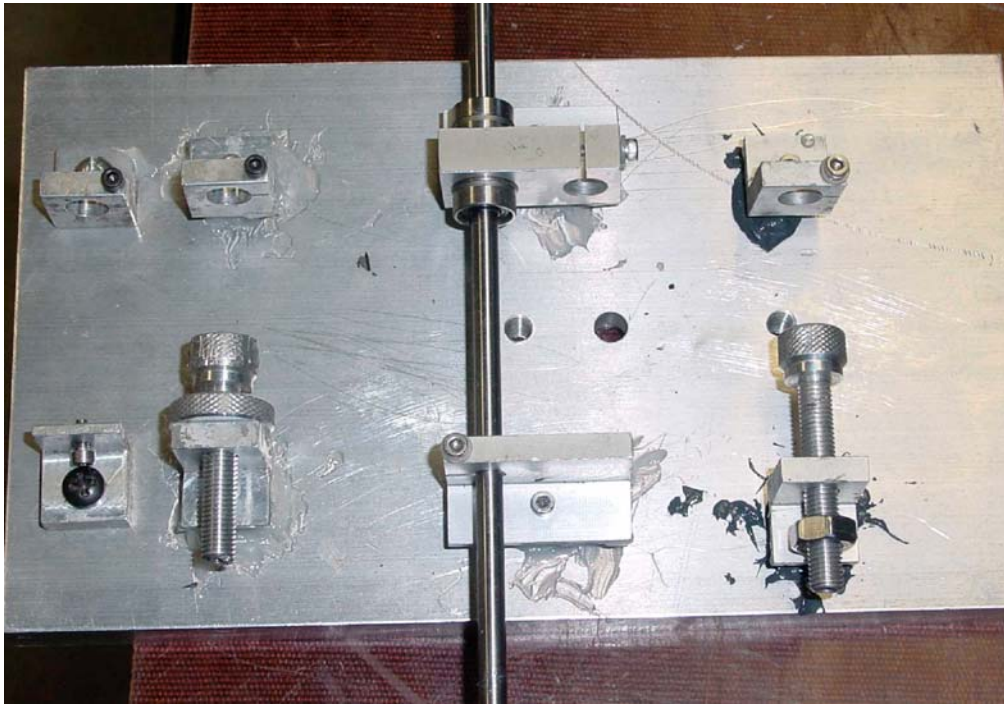


Figure B.12. Different LVDT mounting mechanisms on a horizontal plate to check strain drift

## **Appendix C: Machine Compliance and Measurement Instrumentation**

### ***C.1 Introduction***

Currently, the asphalt industry is moving in the direction of mechanistic design, as evidenced by the development of the Simple Performance Test (SPT) (Witczack 2000) for mix design and the upcoming AASHTO 2002 structural design guide. Fundamental material properties required for the mechanistic design are to be measured in the laboratory under various loading and environmental conditions. Accurate determination of these fundamental material properties is essential in developing a reliable material characterization model. This chapter addresses issues pertaining to machine compliance and measurement instrumentation that affect the measurement of asphalt concrete material properties in the laboratory.

Application and measurement of stresses and strains to obtain the material properties involve both a mechanism by which load is applied and a system to measure the response of the material to the input loading. Loading is applied through a loading frame with either a mechanical system or hydraulic/pneumatic actuator. Loads can be measured using a load cell and displacements can be measured using some type of transformer or gauge. Current technology uses electronically powered devices from which voltages are read and converted to the appropriate units of load or displacement. The electronic signal passes through various filters and conditioners en route to the data acquisition system. The level of accuracy for both the control and measurement sides of

the testing must be adequate to achieve meaningful or appropriate results to extract the desired information from the test.

An FHWA publication (Alavi, et al. 1997) describes procedures to be used in laboratory testing and quality control for resilient modulus testing of unbound materials. Appropriate performance verification of electronic systems should be performed on any laboratory machine at the time of initial setup, as described in the report procedures. The performance verification includes characterizing the frequency response of the system and calibrating the load cell and LVDTs. However, once this performance verification is completed, there are additional issues in testing that arise. This chapter addresses some potential problems with machine compliance and instrumentation that can have a significant effect on experimentally measured material properties and, as a result, the research and design in which they are used. The focus is on both the measurement of complex modulus testing results that are needed for the determination of linear viscoelastic response functions in addition to issues affecting creep and recovery testing results needed for viscoplastic modeling.

## ***C.2 Testing Program***

The research described herein focuses on the testing of asphalt concrete materials using servo-hydraulic closed-loop testing machines and LVDTs for deformation measurements. However, the concepts of machine compliance and various instrumentation issues are applicable to testing with all types of machines on any kind of material. The question is whether these issues are significant enough for a particular application to affect the test results and research.

### **C.2.1 Testing Machines**

The two testing machines used in this research are closed-loop servo hydraulic machines. One is a Materials Testing System (MTS) with 100 kN capacity and the second is a Universal Testing Machine (UTM), made by Industrial Process Controls, Inc. (IPC), with a 25 kN capacity. The MTS system uses a 458 micro-console control system with micro-profiler for function generation. LabView software is used with a National Instrument 16-bit data acquisition board to collect multiple channels of data. The load cell and actuator LVDT signals are conditioned through the micro-console. The UTM system has both computer control and data acquisition systems using UTM software, in addition to LabView data acquisition. The load cell and actuator LVDT signals for the UTM are conditioned through the UTM control and data acquisition system (CDAS).

### **C.2.2 Deformation Measurements**

Deformation measurements were made on both the MTS and UTM systems using various types of LVDTs. All types were used in testing on both the MTS and UTM systems. All of the LVDTs were obtained from IPC and have signal conditioners compatible with the signal conditioners on the UTM load cell and ram LVDT and are powered by the CDAS. For testing on the MTS system, the LVDTs were powered by an IPC power supply. The different LVDT types studied are presented in Table C.1 and shown in Figures B.11 and B.12.

### C.2.3 Materials

The asphalt concrete mixtures are standard North Carolina and Maryland mixtures with 12.5 mm Superpave gradations and PG 70-22 and PG 64-22 asphalt binders, respectively. The actual mixture properties are not as important as the fact that the material is viscoelastic in nature and that certain trends in the measured properties are expected from viscoelastic materials tested under various types of loading. Testing was also performed on an aluminum specimen. Both the asphalt and aluminum specimens were 75 mm diameter and 150 mm tall, based on recommendations by (Chehab, et al. 2000). Specimens were glued to steel end plates with Devcon Plastic Steel Putty using a gluing jig to ensure proper alignment. Testing was performed in uniaxial direct tension.

Table C.1 Summary of LVDT Types

<b>LVDT Name</b>	<b>Type</b>	<b>Signal Cond. Model</b>	<b>Designation</b>
<b>GTX 5000</b>	3/8" Spring-loaded	1020	GTX
<b>099XS-B</b>	3/16" Loose core	661	XSB
<b>CD-100</b>	3/8" Loose core	661 and 1020	CDA and CDB

### C.2.4 Test Methods

Both monotonic (constant crosshead rate) and complex modulus (frequency sweep) tests were performed in this research. Frequency sweep testing was performed in the linear viscoelastic range of the material (no damage induced) and involved applying various frequencies of sinusoidal loading to the specimen and then measuring the strain response to obtain the dynamic modulus and phase angle values. Both tests were described in detail in Chapter 3.

### ***C.3 Machine Compliance***

Monotonic constant crosshead rate tests and cyclic tests (haversine and saw-tooth) conducted on both the UTM and MTS showed that the magnitude of movement of the specimen plates (deformation of specimen itself) is less than that of the actuator. Only when there was no load on the system (i.e., failed specimen or no specimen in the machine) did the plates move the same amount as the actuator. This response suggests that some component or components of the loading system yield under the applied loads. The issue of machine compliance is of concern because it indicates that the specimen does not deform as expected in actuator displacement control tests and that the true material response is not measured by the actuator LVDT during load control tests.

Figure C.1 shows the on-specimen, plate-to-plate, and actuator LVDT strains measured from a monotonic test. In this test, a specimen is pulled apart using a constant crosshead strain rate. Due to the machine compliance, the on-specimen and plate-to-plate LVDT measurements follow a power curve until failure. During this time, the specimen does not experience a true controlled-strain or controlled-stress mode of loading, but rather a mixed mode of loading.

After failure, the plate-to-plate measurements become linear with a rate close to that of the crosshead; the increase of on-specimen strain becomes linear as well, but with a higher rate, due to the difference in gauge length from which strains are calculated. The crosshead and plate-to-plate deformations are divided by the same gauge length (length of the specimen), whereas the on-specimen deformations are divided by a smaller gauge length. For the same deformation measurement, which is the case after failure due to the

development of a single macrocrack, the strain calculated from the on-specimen LVDTs is larger.

Deformations measured from the actuator LVDT and on-specimen LVDTs differ in frequency sweep testing as well. The calculated strains from the actuator LVDT are greater than those calculated from the on-specimen LVDTs due to the machine compliance. This difference transfers to the calculated dynamic modulus values as the same stress amplitude is divided by different strain amplitudes, resulting in a lower dynamic modulus measured from the actuator LVDT. Figure C.2 shows the difference in dynamic modulus and phase angle measurements calculated from the actuator and on-specimen LVDTs for a Maryland mixture specimen tested at 25°C on the UTM. There is an average difference in the phase angle of 20° between the actuator and on-specimen LVDT measurements. The dynamic modulus measured from the specimen is 4.5 times that measured from the actuator at 20 Hz and 1.4 times that measured from the actuator at 0.1 Hz.

Testing performed on an aluminum specimen and asphalt specimens at different temperatures and loading rates showed that the magnitude of the machine compliance depends upon the stiffness of the material being tested. As the stiffness of the material increased, the percentage difference between the end plate movement and the actuator movement increased; i.e., there was a greater contribution from the load train to the overall displacement. Additionally, it was noted that the UTM, a 25-kN machine, exhibited higher compliance than the MTS, a 100 kN machine; this difference could be attributed to a difference in the stiffness of the loading system components.

In frequency sweep tests, the difference between the actuator and specimen end

plate movement becomes larger as the testing frequency increases, as shown by the dynamic modulus values in Figure C.2. Moreover, for monotonic tests, it was observed that the faster the crosshead-rate, the greater the effect of the machine compliance. These differences are due to the viscoelastic nature of the material; the faster the loading is applied, the stiffer the material becomes, and hence, the increased effect of machine compliance. This result is also true with testing at different temperatures; there is a greater contribution from machine compliance at lower testing temperatures.

LVDTs were mounted across various joints on the MTS loading system to determine which components were contributing to the machine compliance by deforming under load (Figure C.3). A series of haversine and saw-tooth cyclic tests in both controlled-strain and controlled-stress modes were performed to measure joint displacements. Several of the threaded connections between adapters and the ram and load cell were found to exhibit appreciable deformation upon loading. It is worthy to note that although all joints are expected to exhibit some deformation during loading, those deformations should be reduced as much as possible when they are close in magnitude to the specimen deformation. This reduction can be accomplished through regular maintenance and cleaning of all connections. Pre-tensioning of the joints can also reduce deflections, but is not practical in testing where the joints need to be locked and unlocked frequently for different test setups.

While the aforementioned suggestions can help reduce the machine compliance, they will never eliminate it. Since there are various sources of deflection along the load path, some of which are inevitable, it is more practical and less time-consuming to measure the displacements from LVDTs mounted on the specimens rather than from the

actuator. When actuator displacement control is required, it is possible to determine a correction factor that, when applied to the crosshead rate, achieves the desired specimen displacement rate.

If deformation attributed to the machine compliance is elastic, then that deformation divided by the load under which the deformation occurs should be a constant for all testing conditions. This constant may be regarded as the stiffness of a spring that characterizes the machine compliance. This phenomenon was investigated for several monotonic test conditions, as shown in Figure C.4. Plate-to-plate strain was subtracted from the crosshead-based strain and the result was divided by the stress. The result is a constant for several rates of crosshead-based strain up to the value of peak stress. After peak stress occurred, macrocracks in the specimen started to develop and plate-to-plate strains could not be used anymore. At the higher test temperature of 40°C, the spring constant increased slightly with crosshead strain. This suggests that, in general, the machine compliance deformations are generally elastic.

#### ***C.4 Measurement Instrumentation: LVDTs, Signal Conditioners, and Mounting Assembly***

##### **C.4.1 Effect on Phase Angle Measurement**

Complex modulus tests on asphalt specimens performed using the MTS machine resulted in an unreasonable trend for the phase angles calculated using on-specimen LVDT measurements. The typical trend is shown by the dashed lines in Figure C.5; the unadjusted phase angle decreases and then increases with faster frequencies, whereas it should have continued to decrease due to the viscoelastic nature of asphalt concrete. This

unexpected pattern for the variation of phase angle with frequency is likely due to a combination of dynamic and electronic effects related to measurement instrumentation. Some of these effects are also identified and discussed with respect to resilient modulus testing of unbound materials (Alavi, et al. 1997). A series of tests were performed on both the MTS and UTM machines using the XSB and GTX LVDTs with various mounting assemblies (L-mount, square mount, hex mount). Testing was performed on an aluminum specimen (elastic response) and on an asphalt specimen. Figure C.6 shows the different mounting assemblies on the aluminum specimen. The different types were tested when mounted to the specimen in some trials and when mounted to the end platens in other trials.

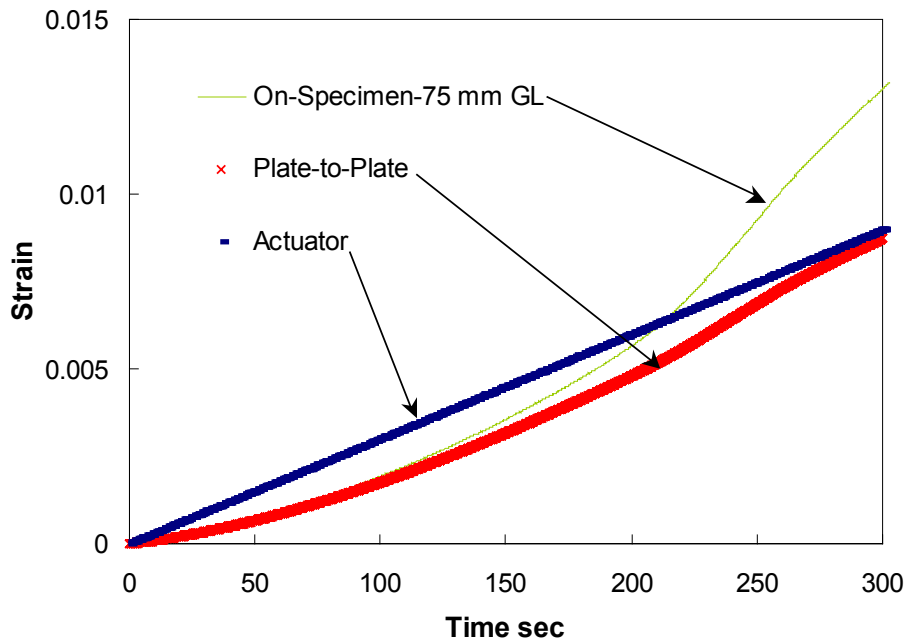


Figure C.1. Stress and strain measurements for constant crosshead-rate test.

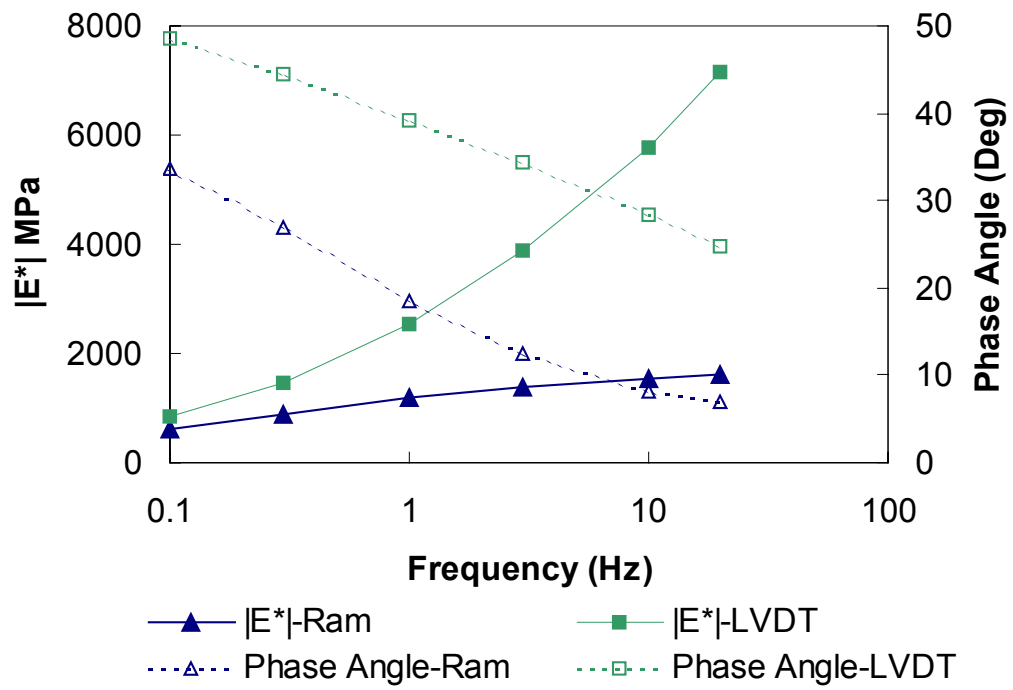


Figure C.2. Comparison of ram and LVDT dynamic modulus and phase angle measurements

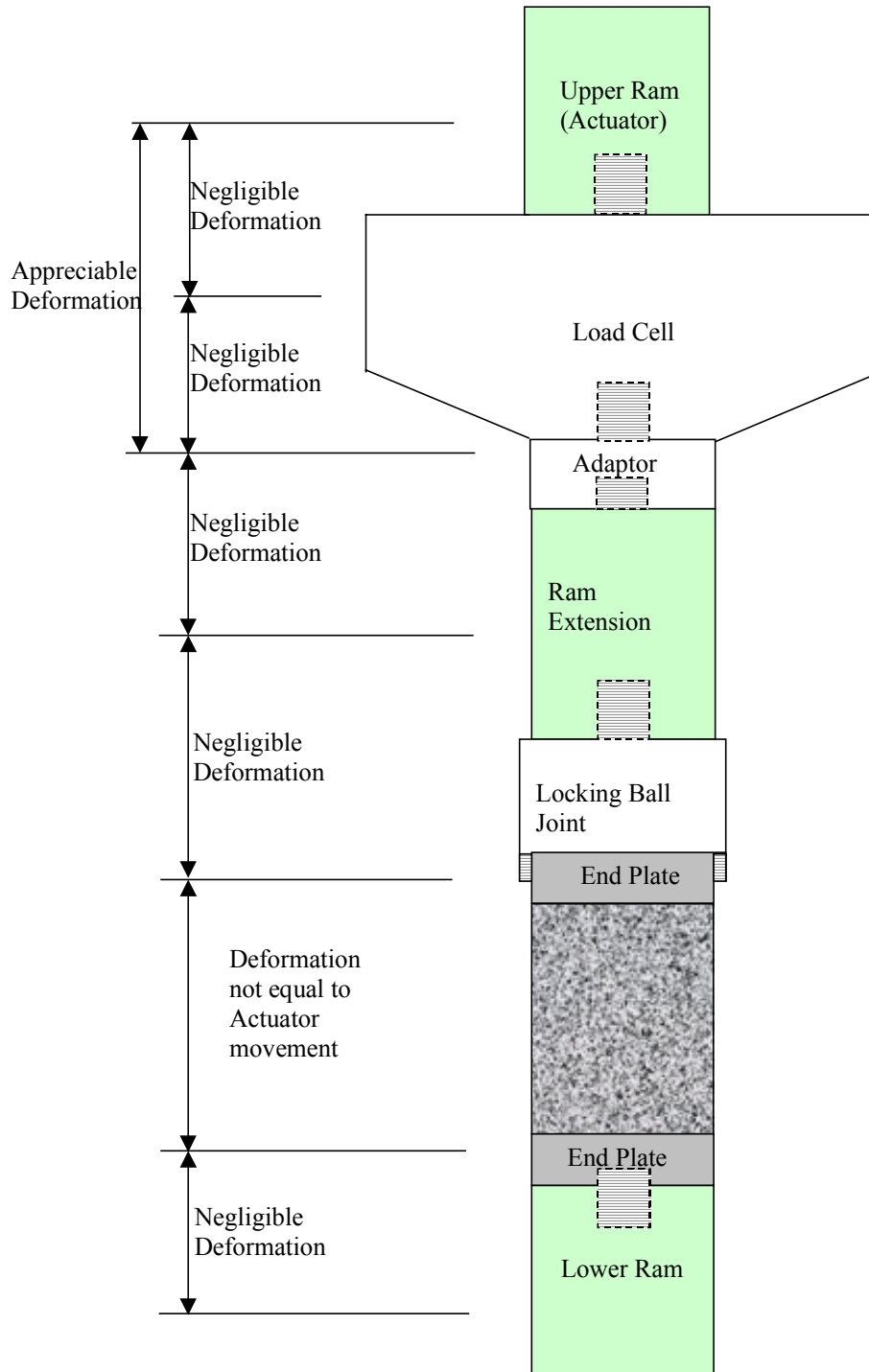


Figure C.3. Measurement of deformations at each joint along the loading train of the MTS loading machine

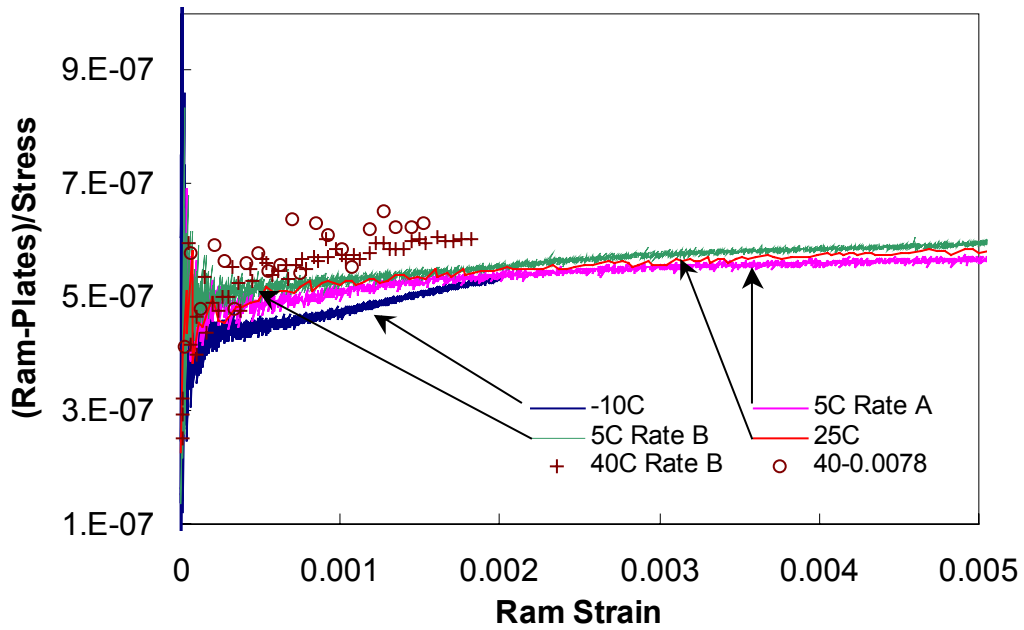


Figure C.4. Machine compliance evaluated at different temperatures and crosshead strain rates for UTM machine.

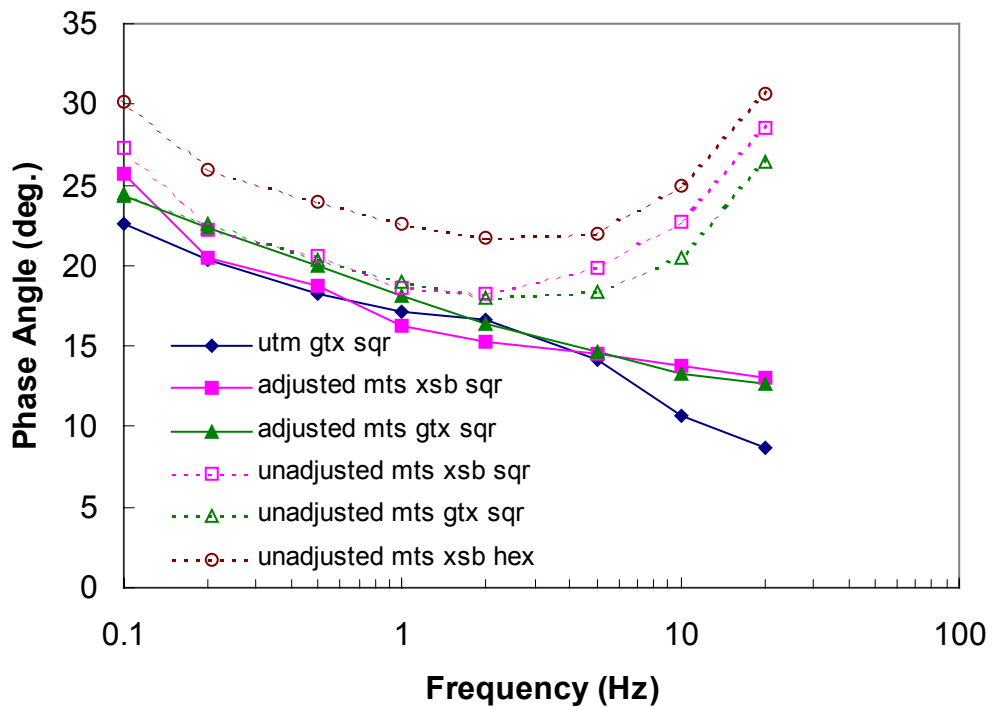


Figure C.5. Adjusted and unadjusted phase angle measurements for various machine,

LVDT, and mount type combinations

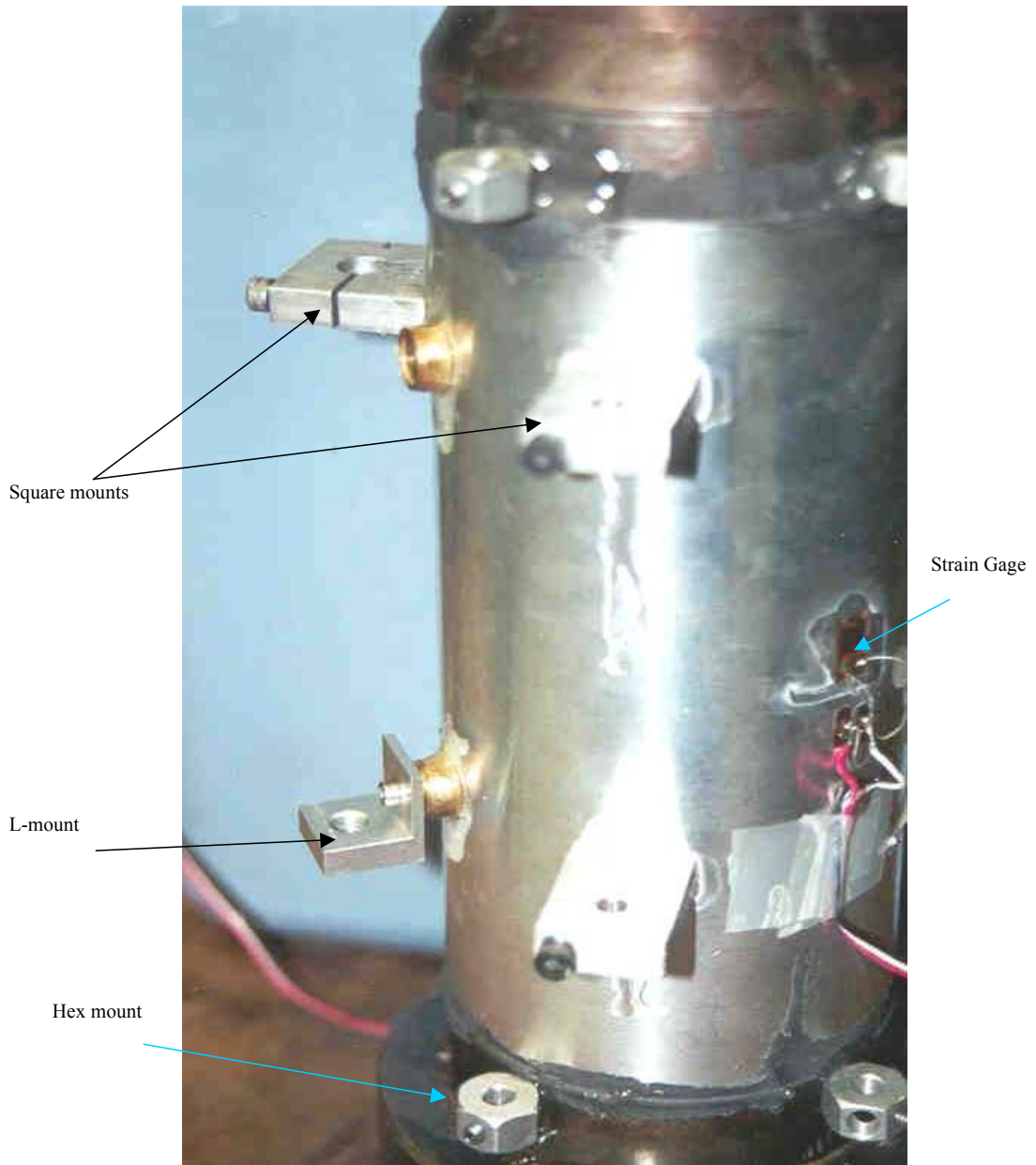


Figure C.6 Different LVDT mount types on aluminum specimen

#### *C.4.1.1 Dynamic effects*

The dynamic effects include the damping of the whole loading system, especially the mass acceleration and hysteresis of the load cell, in addition to the dynamics of the LVDT and its mounting assembly. These effects depend on the type and weight of the LVDT, mounting assembly, and the measurement mechanism (loose core versus spring loaded).

#### System Damping

One source of phase shift is loading path dynamics (damping). The mass-acceleration of the actuator, load cell, and other components on the load path causes a phase when a change of actuator movement direction happens. Load cell hysteresis could also introduce a phase shift. Hysteresis is defined as the difference in load measurement when a load value is approached from the ascending versus the descending direction. Force measurement lead/lag could be hysteresis up to the specification value (0.05% for MTS).

#### LVDT Type

It was concluded that the type of the LVDT does not affect the phase angle. Phase angles measured using GTX LVDTs are similar to those measured from XSB LVDTs using the same mounting mechanism, as seen in Figures C.5 and C.7. It seems that the effect of weight (GTX is heavier than XSB) and measurement mechanism (XSB being a loose core LVDT versus GTX being a spring loaded type LVDT) either cancel each other out or do not significantly affect the phase angle.

## Mounting Mechanism

The mounting mechanism significantly affects the measured phase angle. This finding was especially true for the XSB LVDTs. The LVDTs attached to the hex mounts always recorded phase angles that were higher than those measured using the LVDTs with the L-mount or square mount assemblies, as shown in Figures C.5 and C.7. This could be attributed to the smaller surface area on the hex mount that provides the contact to the specimen and/or to the different mechanism for securing the LVDT in the mount. (The hex mount uses a single locking screw while the other two use a clamping mechanism; see Figure C.6).

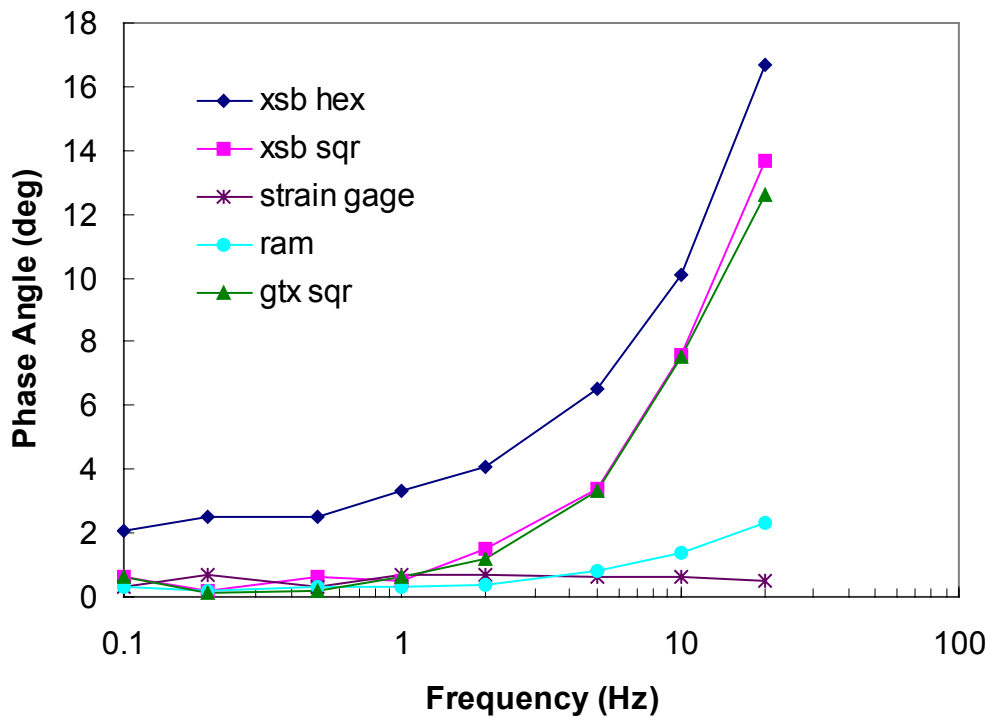


Figure C.7 Phase Angle Measurements from Aluminum Specimen Tested with MTS

#### *C.4.1.2 Electronic Effects*

The signal conditioning and filtering could lead to a phase angle that is measured but is physically non-existent. If the circuitry in the signal conditioner of the load cell is different than that of the LVDTs, an electronic phase angle can result and would be measured by the data acquisition system. The load cell on the UTM machine has a signal conditioner that is compatible with both types of LVDT signal conditioners. The difference between machines became apparent when the GTX LVDTs measured different phase angles when used with the MTS versus the UTM. Using the same LVDT type (CD) with the two different conditioners also resulted in different phase angle values and variations in frequency.

The electronic filtering of signals can also cause a phase angle that is physically non-existent. According to the UTM manufacturer, the control module has a first order low pass filter that gives the controlling transducer (load cell in stress control tests) a phase shift of  $1.2^\circ$  at 10 Hz and  $2.4^\circ$  at 20 Hz. With respect to resilient modulus testing of unbound materials (LTPP Protocol P46), an electronics tolerance of  $1.8^\circ$  is allowed (Alavi, et al. 1997). The electronic effects on phase angle are expected to be greater with the MTS machine because the LVDTs and the load cell are from two different companies, and are not calibrated together.

#### *C.4.1.3 Phase Angle Adjustment*

Although the dynamic and electronic effects have been identified as probable sources of the phase angle problem, they are very difficult and impractical, if not impossible, to eliminate. Therefore, a method must be developed to adjust the measured

phase angle to remove these effects. This was accomplished by performing tests on an aluminum specimen that has no material phase angle (purely elastic). Any phase angle measured from the aluminum specimen must be attributed to the dynamic and electronic effects. To accurately simulate the dynamic effects that occur with an asphalt specimen, an appropriate load level was applied to the aluminum specimen to generate the same strain magnitude (~50 microstrain) as experienced by the asphalt specimen.

Figure C.7 shows the phase angles measured from different LVDTs and mount types on an aluminum specimen tested on the MTS. Immediately noticeable is the fact that a phase angle is measured from the LVDTs and that it increases with increasing frequency. The LVDTs attached to the hex mounts measured a higher phase angle than those attached to the square mounts. There is little difference in the measurements from the GTX and XSB LVDTs. Also shown on this figure are the phase angles measured from the actuator LVDT and from a strain gauge mounted directly on the specimen surface. The actuator phase angle increases slightly at the higher frequencies, which may be attributed to filtering, as mentioned above. The strain gauge, which should exhibit no dynamic effects, shows no phase angle, which is expected since the aluminum is an elastic material.

A comparison between the two signal conditioners on the MTS and UTM machines shows that both signal conditioners measure higher phase angles on the aluminum specimen when used with the MTS machine. The GTX LVDTs show a negligible phase angle when used with the UTM machine. Therefore, use of the GTX LVDTs with L-mounts (or square mounts) on the UTM system will measure the true material response of an asphalt specimen. There is not a mount-LVDT-signal conditioner

combination that eliminates the dynamic and/or electronic effects with the MTS machine and, therefore, an adjustment must be made to obtain the true material response.

Figure C.5 shows the phase angles measured from an asphalt specimen tested in both the UTM and MTS machines using various LVDT and mount combinations. The phase angle is calculated by averaging the responses from two LVDTs. The phase angles from the UTM test show an expected decreasing trend with frequency, while those from the MTS test decrease and then increase. The adjusted MTS phase angles, shown with solid lines, were calculated by subtracting the phase angle of the aluminum specimen from that measured from the asphalt specimen, thereby removing any dynamic and electronic effects. The agreement between the adjusted MTS phase angles and the UTM phase angles (measured from the same asphalt specimen) proves that this approach is valid.

The recommended test protocol for use in any test where phase angles will be measured is to first test an aluminum (or other suitable elastic material) specimen using the same geometry, instrumentation (LVDT, mount, etc), and strain levels to be used in the actual testing to develop a fingerprint of any dynamic and/or electronic effects. These effects can then simply be subtracted from the measurements of the actual test specimen to obtain the true material response.

### ***C.5 Electronic Noise***

The LVDT signal conditioners have low pass filters installed to eliminate noise that consists of all unwanted frequencies above a certain threshold cutoff frequency. The farther the cutoff frequency is from the operating frequency, the greater the noise. To

reduce the amount of noise, the threshold frequency should be decreased. However, this filtering process causes a phase shift; the closer the operating frequency to the threshold cutoff frequency, the greater the shift, as evidenced by the phase angles in Figure C.7. If the operating frequency and the cutoff frequency are the same value, the phase shift will be 45 degrees. To reduce the phase shift, the threshold frequency should be increased. Therefore, there must be a compromise between the acceptable levels of noise and phase shift.

This phenomenon is illustrated in Table C.2 in which the three LVDTs were used in testing the aluminum specimen at a frequency of 20 Hz. The XSB conditioner uses a 200 Hz cutoff frequency, the GTX conditioner uses a 400 Hz cutoff frequency, and the CDA conditioner uses a cutoff frequency greater than 400 Hz. The CDA LVDT exhibits the largest amount of noise (30% of mean signal amplitude) because of the high cutoff frequency and, conversely, the XSB LVDT exhibits the least amount of noise (8 % of mean signal amplitude). The phase angles measured from the aluminum specimen by each of the LVDTs are shown in Table C.3. As expected, the XSB LVDT exhibits the highest phase shift and the GTX and CDA LVDTs exhibit lower phase shift. Also noticeable is that the XSB phase shift increases as the frequency increases and becomes closer to the cutoff frequency.

In determining the dynamic modulus and phase angle values, the deformation (or strain) measurements are fit to a sinusoidal function to account for the noise effect in determining the correct amplitude and phase. Typically, an error minimization technique is utilized such that the fit follows the mean strain value. This works well with the phase angle measurements; however, this may not work to extract the correct strain amplitude

when noise levels are high. This finding is illustrated by the difference in dynamic modulus values measured from the aluminum and asphalt specimens using the CDA, CDB, and GTX LVDTs, shown in Table C.3. There is a 10% error in the modulus value of the aluminum specimen measured with the two different signal conditioners (CDA and CDB LVDTs), whereas the difference between the two LVDTs with the same conditioner (CDB and GTX) is only 3%. Differences of up to 13% in dynamic modulus values from the same asphalt specimen are measured using the different signal conditioners (CDA and GTX LVDTs).

Table C.2. Noise amplitude for different LVDT types

LVDT Type	CDA	CDB	GTX	XSB
Mean strain	70 $\mu\epsilon$	70 $\mu\epsilon$	70 $\mu\epsilon$	65 $\mu\epsilon$
Noise Amplitude	20 $\mu\epsilon$	7 $\mu\epsilon$	8 $\mu\epsilon$	5 $\mu\epsilon$
% of Mean	28.6	10.0	11.4	7.7

Table C.3. Frequency sweep results from aluminum and asphalt specimens

Freq (Hz)	Aluminum Specimen								Asphalt Specimen	
	CDA		CDB		GTX		XSB		E*  MPa	
	E*  (MPa)	Phase (Deg)	E*  (MPa)	Phase (Deg)	E*  (MPa)	Phase (Deg)	E*  (MPa)	Phase (Deg)	GTX	CDA
20.0	76947	0.9	70919	0.9	70067	0.1	72198	12.3	10651	11392
10.0	76317	0.2	71413	0.3	69925	0.4	71891	11.4	9098	9876
3.0	75693	1.1	71239	0.6	70111	0.9	71899	8.0	6605	7261
1.0	76461	0.9	71370	0.7	69258	0.8	72759	7.8	4694	5288
0.3	77073	0.4	70030	1.0	70024	0.6	73901	7.5	3122	3541

### ***C.6 Drift in Strain Measurement***

LVDT measurements were found to drift during static loading and rest periods. Spring loaded GTX LVDTs, used with L-mount assemblies that were glued to the specimen using 5-minute Devcon epoxy, measured increasing axial displacements although no load was applied to the specimen. This displacement corresponds to 40 microstrains after 1000 seconds (100 mm gauge length); such a magnitude is significant relative to strains obtained from linear viscoelastic testing. The specimen was disconnected from the actuator and, thus, had no load applied on it. The positive strain indicates tension; thus, the specimen's self-weight and the weight of the end plate, which would cause compressive strains, are not the causes of this drift. Several possible sources of LVDT drifting during testing could be:

- Faulty LVDTs,
- Error in programming (load was actually applied to specimen during rest),
- Deformation due to thermal stresses,
- Electronic interference, and/or
- Mechanical causes related to LVDT functionality and setup.

The first three possible sources were eliminated through testing with different LVDTs, testing a specimen not connected to the actuator, and testing at constant temperature. No electronic interference from the CDAS or the National Instruments data acquisition board was detected; however, IPC recommended that the in-line signal conditioners on the LVDTs be allowed to warm up for approximately 30 minutes prior to testing to avoid errors in strain measurement due to warming components. After appropriate warm-up time, drifting of the LVDT measurements was still detected, indicating that the drifts are mechanical in nature.

Deformation at the mounts that hold the LVDTs and the connection to the specimen could lead to drift in strains and may be caused by one or a combination of the following:

- Slippage of the LVDT from the mount,
- Deformation (rotation) of the mounts due to force exerted by the LVDT spring on the target mount, and
- Movement of the mount due to the self-weight of the LVDT and its cable.

Ensuring that the LVDT was very tight in place eliminated the possibility of any slippage from the mount. To determine whether the two other possible causes were contributing to the drift, a set of mounts were bolted (not glued) to a horizontal aluminum plate (Figure B.12). After measuring strains overnight, no drift was detected, indicating that the LVDT type and mounting assembly connection were, in fact, contributing to the drift. The mechanical action(s) affecting the drift may be dependent on the type of LVDT, type of mount assembly (its contact area with the specimen), and type of epoxy used to secure the mounts to the specimen. The findings of an experimental study with these variables are shown in Table C.4. The type of mount assembly shows little effect on drifting.

It can be concluded that the major problem lies in the type of LVDT and the type of glue used. It is the spring force and not the weight of the GTX LVDTs that caused the mounts to deform. This is because the same drift is measured regardless of the orientation of the LVDTs (horizontal or vertical). Moreover, when the specimen and LVDT setup is flipped vertically, the drift remains in the same direction (mounts are being pushed away from each other). The XSB LVDTs do not exhibit drift while in the horizontal direction

(no spring force applied to mounts). When the XSBs are in the vertical direction, the drift is sometimes positive and in other times negative, suggesting that both the LVDT and its cable weight (lower mount), in addition to the core and its extension rod (upper mount), cause the deformation of the mounts. It is also clear that the Devcon Plastic Steel Putty should be used instead of 5-minute epoxy to glue the mounts to the specimen. It is important, however, that proper curing time be given (preferably overnight); otherwise the mounts might still deform.

Based on the aforementioned findings, loose core LVDTs with Devcon Plastic Steel Putty is recommended as a deformation measurement system for asphalt mixture testing.

Table C.4 Extent of drift in strains for the different combinations tested

LVDT Type	Mounting assembly	Horizontal		Vertical	
		Devcon 5-minute epoxy	Devcon 2-Ton Plastic steel Putty	Devcon 5-minute epoxy	Devcon 2-Ton Plastic steel Putty
GTX	L-mounts	v. significant <sup>a</sup>	significant	v. significant	significant
	Guided rod assembly	significant <sup>b</sup>	-	significant	significant
	Rectangular mounts	-	-	v. significant	significant
XSB	L-mounts	-	No drift	significant	minimal

<sup>a</sup> indicates more than 10 microns of drift in 3 hours for 100 mm gage length.

<sup>b</sup> indicates 5-10 microns of drift in 3 hours for 100 mm gage length.

Dash indicates that combination was not tested.

There are many potential problems that can affect the values of material properties measured from various tests. The significance of each of these problems

depends upon the type of testing that is being performed and the application of the resulting measured properties. For illustration, consider two tests to measure the linear viscoelastic properties of a material. In a creep and recovery test, the drift of the LVDT measurements would be a serious problem in measuring the strain under a static load over a period of time and then the recovery with time when the load is released. A drift in the LVDT measurements would either underestimate or overestimate both the strain under the load and during recovery, depending upon the testing and drift directions. This could also be critical in repetitive creep and recovery tests conducted for viscoplastic model coefficient determination. However, any phase shift in the signal conditioners would not affect the test results. In a frequency sweep test, any phase shift poses a serious problem in the calculation of phase angles, but drifting of the LVDT measurements does not because the amplitudes, and not the mean values of stresses and strains, are needed for the calculations.

Each individual test setup may exhibit the issues discussed in this paper to varying degrees. The type and capacity of the loading frame, type of measurement devices, compatibility between the measurement devices and the control and data acquisition systems are just a few of the variables that can affect measurement of fundamental material properties. The amount of adjustment that is needed (if any) will be highly dependent upon equipment selection. A particular test system may need few adjustments with one measurement system and many adjustments with another system.